
Doctoral Dissertations

Student Theses and Dissertations

Spring 2015

An integrated study for hybrid composite beam (HCB) structures

Mohamed Abdelkhalik Aboelseoud

Follow this and additional works at: https://scholarsmine.mst.edu/doctoral_dissertations



Part of the [Civil Engineering Commons](#)

Department: Civil, Architectural and Environmental Engineering

Recommended Citation

Aboelseoud, Mohamed Abdelkhalik, "An integrated study for hybrid composite beam (HCB) structures" (2015). *Doctoral Dissertations*. 2371.

https://scholarsmine.mst.edu/doctoral_dissertations/2371

This thesis is brought to you by Scholars' Mine, a service of the Missouri S&T Library and Learning Resources. This work is protected by U. S. Copyright Law. Unauthorized use including reproduction for redistribution requires the permission of the copyright holder. For more information, please contact scholarsmine@mst.edu.

AN INTEGRATED STUDY FOR HYBRID COMPOSITE BEAM (HCB) STRUCTURES

by

MOHAMED ABDELKHALIK ABOELSEUD

A DISSERTATION

Presented to the Faculty of the Graduate School of the
MISSOURI UNIVERSITY OF SCIENCE AND TECHNOLOGY

In Partial Fulfillment of the Requirements for the Degree

DOCTOR OF PHILOSOPHY

in

CIVIL ENGINEERING

2015

Approved

John J. Myers, Advisor

Mohamed Elgawady

Lesley Sneed

Victor Birman

K. Chandrashekhara

© 2015

MOHAMED ABDELKHALIK ABOELSEUD

All Rights Reserved

PUBLICATION DISSERTATION OPTION

This dissertation consists of the following five articles that have been submitted for publication as follows:

The first paper "Hybrid Composite Beam (HCB) Bridge Implementation and Field Monitoring" (pages 25 through 51) was published in Structural Faults & Repair, London, UK, 8th – 10th July 2014. Appendix (A) has been added to supplement the first paper.

The second paper "Finite-Element Modeling of Hybrid Composite Beam Bridges in Missouri" (pages 52 through 83) was published in ASCE Journal of Bridge Engineering ISSN (print) 1084-0702, May 2014. Appendix (B) has been added to supplement the second paper.

The third paper "Analysis Methods for Single-web and Multi-web Hybrid Composite Beam (HCB) Bridges" (pages 84 through 115) is intended for submission to Journal of Composite Structures. Appendices (C, D, E, and F) has been added to supplement the third paper.

The fourth paper "Durability of Hybrid Composite Beam (HCB) Bridges Subjected to Various Environmental Conditioning" (pages 116 through 152) is intended for submission to ASCE Journal of Composites for Construction. Appendix (G) has been added to supplement the fourth paper.

The fifth paper "Design of Hybrid Composite Beam Bridge Superstructures for Thermal Gradient" (pages 153 through 184) is intended for submission to ASCE Journal of Bridge Engineering. Appendix (H) has been added to supplement the fifth paper.

ABSTRACT

The hybrid composite beam (HCB) consists of a self consolidating concrete (SCC) arch that is tied at the end by galvanized strands. The tied arch is encapsulated by a glass fiber reinforced polymer (GFRP) shell. A limited number of researches have studied the essential design methodologies and long-term performance of the HCB. The research presented in this dissertation aimed to more fundamentally understand the structural behavior of this new beam and evaluate its durability. This research study was conducted through four phases. A full-scale bridge load testing was conducted on a single-web HCB bridge during the first phase. The first finite element analysis of an HCB bridge superstructure was conducted. The areas that need more research and investigation were highlighted. In the second phase, double-web HCB Bridge was instrumented by various sensors. Strains induced in HCB's elements during several loading stages were collected. The existing flexural analysis method was unable to estimate accurately the induce strains. Analysis methods for a simply supported HCB and an HCB that is supported on bearing pads were proposed. These methods achieved significant enhancement in estimating the HCB's strains. The HCB's shell was subjected to five aging regimes during the third stage. The existing voids in the laminated shell made the fibers and the interphase regions prone to chemical and moisture attacks. However, the diffusion of the chemical solutions was always found to be confined to the first lamina. This result suggested that the composite shell is able to protect the strands from a moisture attack during the HCB's service life. The last stage clarified that the thermal stresses in an HCB bridge superstructure elements produced by thermal gradients are not critical and can be excluded from the design.

ACKNOWLEDGMENTS

I would like to express my sincere gratitude to my advisor, Dr. John Myers, for his guidance, support, and cordial dealings during the pursuit of my PhD degree.

I would also like to thank my advisory committee members: Dr. Mohamed Elgawady, Dr. Lesley Sneed, Dr. Victor Birman, and Dr. K. Chandrashekhara for their effort to review my dissertation and for their valuable suggestions and recommendations to enhance my work.

I am very grateful to the Egyptian government for sponsoring me and my family for three years providing the opportunity to study at MS&T. I would like also to acknowledge the Missouri Department of Transportation (MoDOT) and the National University Transportation Center (NUTC) at Missouri S&T for co-sponsoring this research.

I would like to thank Mr. John Hillman for providing technical information about the HCB and for responding to all of my questions. I would also like to thank my project mate Ms. C. Renee Earley for her cooperation and help during this research project. I would like to thank Dr. Santosh Mishra for his help and supervision during the preparation of an alkaline solution.

I'm grateful to the staff support from the Dept. of Civil, Architectural & Environmental Engineering, and Center for Infrastructure Engineering Studies (CIES) at Missouri S&T, especially Mr. Brian Swift, Mr. Jason Cox, Mr. Gary Abbott, Mr. Delbert, and Mr. John Bullock.

I would like to thank my parents, my sister, and my brother not only for their encouragement and moral support during my PhD study, but also for their endless support and unconditional love during my life.

Finally, I would like to especially thank my wife for her patience and understanding throughout this challenging journey. She stood behind me and never ceased to offer her love and support throughout my PhD study. Her efforts surpassed all that I could have ever expected.

DEDICATION

To my beloved wife

TABLE OF CONTENTS

	Page
PUBLICATION DISSERTATION OPTION	iii
ABSTRACT	iv
ACKNOWLEDGMENTS	v
DEDICATION	vi
LIST OF ILLUSTRATIONS	xiii
LIST OF TABLES	xviii
SECTION	
1. INTRODUCTION	1
1.1. GENERAL	1
1.2. HYBRID SYSTEMS	2
1.3. PREVIOUS HYBRID-COMPOSITE BEAM RESEARCH PROJECTS	6
1.3.1 IDEA Test Program	7
1.3.2 Testing of Knickerbocker Bridge HCB..	9
1.3.3 Testing Tide Mill Bridge HCBs.	11
1.4. ADVANTAGES OF THE HCB	13
1.5. OBJECTIVE	18
1.6 DISSERTATION ORGANIZATION	21
PAPER	
I. HYBRID COMPOSITE BEAM (HCB) BRIDGE IMPLEMENTATION AND FIELD MONITORING.....	23
ABSTRACT.....	23
INTRODUCTION	24
HCB COMPOSITION	25
FABRICATION OF HCB SHELL.....	27
INSTALLATION SEQUENCE.....	28
BRIDGES DESCRIPTION	30
Bridge B0439	30
Bridge B0478	30

Bridge B0410	31
TESTING MATRIX	32
FLEXURAL DESIGN OF THE HCB	34
MATHEMATICAL CALCULATION OF THE STRAIN	38
EARLY-AGE BEHAVIOR OF B0410	38
RESULTS OF B0410 LOAD TEST	43
CONCLUSIONS.....	44
ACKNOWLEDGMENTS	45
REFERENCES	46
II. FINITE ELEMENT MODELING OF HYBRID COMPOSITE BEAM BRIDGE IN MISSOURI, USA.....	48
Abstract.....	48
Introduction.....	49
Bridge 0439 Description	51
Load Testing of Bridge 0439	52
FE Modeling of Bridge 0439	53
Material Properties	54
<i>FRP Composites</i>	54
<i>Concrete</i>	55
<i>Steel Reinforcement</i>	57
<i>Polyisocyanurate Foam</i>	57
Element Types and Model Simplifications	58
<i>Hybrid Composite Beam (HCB)</i>	58
<i>Bridge Deck</i>	60
Load Modeling	61
Boundary Conditions.....	62
Theoretical Calculations	63
Results Discussion	66
Structural Behavior Analysis	70
Conclusions and Recommendations	75
Acknowledgements.....	76

REFERENCES	77
III. ANALYSIS METHODS FOR SINGLE-WEB AND MULTI-WEB HYBRID COMPOSITE BEAM (HCB) BRIDGES.....	80
Abstract.....	80
Introduction.....	80
Significance of the Current Study.....	81
Experimental Program	82
Bridge 0410	82
Load Testing and Instrumentation of B0410.....	83
Material Properties.....	85
<i>Concrete</i>	86
<i>Steel Reinforcement</i>	86
<i>FRP Composites</i>	86
<i>Polyisocyanurate Foam</i>	87
Finite Element Modeling of B0410	88
<i>Element Types</i>	88
<i>Modeling of Loads</i>	89
<i>Modeling of Boundary Conditions</i>	89
Mathematical Calculations.....	91
Modified Analysis Method	92
Results Discussion	93
Design of a Simply Supported HCB.....	100
Chimney Effect	101
<i>First Approach</i>	101
<i>Second Approach</i>	102
Verification of the Proposed Method.....	103
Results of Simply Supported HCB	105
Conclusions.....	107
Acknowledgements.....	108
REFERENCES	109
IV. DURABILITY OF HYBRID COMPOSITE BRIGES SUBJECTED TO	

VARIOUS ENVIRONMENTAL CONDITIONING.....	111
Abstract.....	111
Introduction.....	112
The current Research Objectives	113
Specimen Details	114
Aging Regimes.....	115
Alkaline Environment Exposure Regime.....	115
Salt Fog Exposure	115
UV-Irradiation and Salt Fog Exposure.....	116
Thermal Cycling and Sustained Stress Regime	116
Natural Weathering and Sustained Stress Regime.	117
Tensile Strength Test	117
Microstructural Analysis.....	118
Results Discussion	119
Control Specimens	119
Alkaline Environment Effects	120
<i>SEM and EDX Tests</i>	120
<i>FTIR Tests</i>	128
Salt Fog, and UV-irradiation and Salt Fog Effects	132
Sustained Stresses and Thermal Cycles Effects	137
REFERENCES	144
V. HYBRID COMPOSITE BEAM BRIDGE SUPERSTRUCTURE DESIGN FOR THERMAL GRADIENT.....	148
Abstract.....	148
Introduction.....	149
Contribution of the Current Research	150
Experimental Program	151
Finite Element Modeling	153
Thermal FE model.....	154
Structural FE model.....	155
Modeling the Thermal Loads	155

Modeling the Boundary Conditions	156
Mathematical Algorithm	157
Correction of Measured Strains	162
Correction of VWSG Measurements	162
Correction of Resistive Strain Gage Measurements.....	163
Material Properties.....	163
Concrete.....	164
Steel Reinforcement	165
FRP Composites	166
Polyisocyanurate Foam	167
Results Discussion	168
Summary and Conclusions	175
Acknowledgements.....	175
REFERENCES	176
SECTION	
2. CONCLUSIONS AND RECOMMENDATIONS.....	181
2.1 SUMMARY.....	179
2.2 CONCLUSIONS AND RECOMMENDATIONS	181
2.3 RECOMMENDATIONS FOR FUTURE RESEARCH.....	184
APPENDICES	
A. FIGURES FOR THE HCB FABRICATION AND SCC MIX DESIGN.....	186
B. MEASURED AND ESTIMATED DEFLECTIONS ALONG B0439 HCBS' LENGTHS	195
C. DERIVATION OF SLOPE-MOMENT EQUATIONS FOR NON- PRISMATIC BEAM.....	206
D. ESTIMATION OF THE STIFFNESSES PROVIDED BY THE CHIMNEY FOR TIDE MILL BRIDGE HCB.....	220
E. MATLAB CODES FOR ESTIMATING THE STRAINS IN HCBS AND HCBS SUPPORTED ON BEARING PADS	235
F. MEASURED AND ESTIMATED STRAINS IN HCB2 OF B0410 AND TIDE MILL BRIDGE SIMULATED HCB	266
G. MECHANICAL TESTING AND MICROSTRUCTURAL ANALYSIS'	

RESULTS OF ENVIROMENTAL EFFECTS ON THE GFRP SHELL.....	292
H. MATLAB CODE FOR ESTIMATING THE THERMAL STRESSES AND STRAINS IN B0410 SUPERSTRUCTURE	325
BIBLIOGRAPHY.....	346
VITA	345

LIST OF ILLUSTRATIONS

		Page
Figure 1.1	Typical Pultruded Composite Cross Sections.....	3
Figure 1.2	Hybrid FRP-Concrete Cross Section.....	4
Figure 1.3	Hybrid FRP-concrete bridge superstructure.....	5
Figure 1.4	Fragmentary Perspective of Hybrid-Composite Beam.....	6
Figure 1.5	Typical cross-section of the HCB tested in AEWCLab.....	10
Figure 1.6	Transportation of eight B0439 HCBs with one truck.....	13
Figure 1.7	Loading of HCBs via small crane.....	14
Figure 1.8	Knickerbocker HCB Bridge in Boothbay, Maine.....	15
Figure 1.9	Pultruded GFRP panel.....	16
Figure 1.10	GFRP sandwich deck panel.....	16
Figure 1.11	Connection of Pultruded bridge decks to beams' flanges using mechanical fasteners.....	17
PAPER I		
Fig. 1	Fragmentary Perspective of Hybrid-Composite Beam.....	28
Fig. 2	B0439, HCB Erection Process.....	31
Fig. 3	Typical Cross Section of B0439 HCB.....	32
Fig. 4	Typical Cross Section of B0478 HCB.....	33
Fig. 5	Typical Cross-Section of Bridge 0410.....	34
Fig. 6	Instrumentation of HCB2, B0410.....	35
Fig. 7	Typical Cross-section of the Composite Hybrid-Composite Beam...	37
Fig. 8	Concrete Temperature during Hydration Process at VWSG/T2.....	41
Fig. 9	Strands Temperature of HCB2, B0410 during and after the Arch Pour.....	42
Fig.10	The strains induced in the strands and FRP shell at sec. (A-A) of HCB2, B0410, during and after the Arch Pour.....	43
Fig. 11	B0410 Shear Strain during and after the Arch Pour.....	44

Fig. 12	Normal Strain in Composite HCB2 due to Stop1 Loads (a) strains in concrete arch (b) strains in FRP shell and strands.....	45
Fig. 13	Shear Strain in Composite HCB2 due to Stop1 Loads.....	46
PAPER II		
Fig. 1	Typical Cross-Section of Bridge B0439.....	53
Fig. 2	Truck Stop Locations and Trucks Dimensions.....	55
Fig. 3	Finite Element Modeling of Hybrid-Composite Beam using SAP2000 V14.2.....	62
Fig. 4	Modeling of the Bridge Deck and the HCBs in ANSYS.....	63
Fig. 5	Comparison of the Bridge 0439 Deflections Measured at Field and Predicted by ANSYS, SAP2000 and Theoretical Calculations.....	69
Fig. 6	The Maximum Tensile and Compressive Stresses Locations in the HCB Concrete Arch of G3 due to (a) stage 2 loading (b) stage 3 loading.....	75
Fig. 7	Stresses in the Lower FRP Flanges of all the Girders due to Stage 3 loading.....	76
Fig. 8	Exaggerated Deformed Shape of HCBs Due to Stop 3 Loads.....	77
PAPER III		
Fig. 1	Typical Cross-Section of Bridge 0410.....	82
Fig. 2	HCB2 Instrumentation.....	83
Fig. 3	Load Testing Truck Stops.....	85
Fig. 4	Finite Element Modeling of Multi-Celled Hybrid-Composite Beam using ANSYS 14.0.....	88
Fig. 5	The measured strains and the estimated strains by the FE model using different C values.....	91
Fig. 6	Strain Values Due to the Concrete Arch Pour (Stage 1).....	94
Fig. 7	Strain Values Due to Stop1 Loads (Stage 3) (a) Concrete arch (b) FRP shell and strands.....	95
Fig. 8	Strain Values Due to Stop3 Loads (Stage 3) (a) Concrete arch and web (b) FRP shell and strands.....	95
Fig. 9	Strain Values Produced by Deck weight (Stage 2) (a) Concrete arch and web (b) FRP shell and strands.....	97

Fig. 10	(a) Strain Profile Due to Stop1 Sec. (A-A) (b) Displacement in X-dir. Due to Stop1 Sec. (A-A).....	98
Fig. 11	Strain Values Due to the Total Loads of the Three Stages (a) Concrete arch and web (b) FRP shell and strands.....	102
Fig. 12	Decoupling of the simply supported HCB into two structural systems.....	103
Fig. 13	Strains along the length of non-composite HCB of B0410 under uniform distributed load (a) concrete arch (b) bottom and top FRP flanges.....	108
Fig. 14	Strains along the length of the composite HCB of B0410 (a) concrete arch (b) bottom and top FRP flanges.....	108
Fig. 15	Strain profiles at the midspan of Tide Mill bridge's HCB (a) Midspan point load (b) 2-quarter point loads.....	109
PAPER IV		
Fig. 1	Typical Cross Section of B0439 HCB.....	115
Fig. 2	Dimensions of the GFRP specimens.....	118
Fig. 3	Comparison between the tensile strength of control specimens (panels 2 and 4) and specimens exposed to alkali, salt fog, UV-salt fog attacks.....	120
Fig. 4	Comparison between the tensile strength of control specimens (panels 1 and 3) and specimens exposed to Sustained stresses with controlled and natural thermal cycles.....	120
Fig. 5	Specimen 4T-C (a) Chemical analysis by EDX (b) Surface morphology by SEM (X1000 = magnified 1000 times).....	122
Fig. 6	(a) SEM micrographs in 4L-Alk (X250) (b) EDX for the circled fiber in (a) (c) SEM for the circled fiber in (a) (X3500).....	123
Fig. 7	(a) SEM micrographs in 4L-Alk (X250) (b) EDX for the circled fiber in (a) (c) SEM for the circled fiber in (a) (X3500) (at distance 0.76 mm (0.03") from the exterior surface).....	124
Fig. 8	Fiber damage and fiber-matrix interface deterioration in (a) 4L-Alk specimens at distance 0.35 mm (0.01") from the exterior surface (first layer) (b) 4T-Alk in the first layer.....	124
Fig. 9	Fiber etching and notching in the first lamina of specimen 4T-Alk (X=2500).....	125
Fig. 10	SEM micrograph in 4-L-Alk (X900) in the first lamina.....	127

Fig. 11	SEM micrograph and EDX for 4L-Alk (X800) at distance > 1 mm (0.04") from the exterior surface (2nd layer).....	128
Fig. 12	SEM micrograph in 4L-Alk.....	129
Fig. 13	Typical FTIR Spectra for 4L-C.....	131
Fig. 14	Typical FTIR Spectra for 4L-Alk.....	132
Fig. 15	Optical Microscope images illustrate existing voids at the exterior surface of control specimens.....	133
Fig. 16	NaOH attack to the fiber through existing voids in outer surface (2L-Alk).....	133
Fig. 17	SEM micrographs in 4L-SF (X400) and EDX analysis.....	135
Fig. 18	SEM micrographs in 4L-SF (X1100).....	135
Fig. 19	SEM micrographs in 4L-UV-SF (X1000) and EDX analysis results.	136
Fig. 20	SEM micrographs in 4L-UV-SF (X250) and EDX analysis results...	137
Fig. 21	NaCl attack to the fiber through existing voids in outer surface (2L-SF).....	137
Fig. 22	Formation of micro cracks in the surface of uncoated specimen (2L-UV-SF) following UV exposure.....	139
Fig. 23	SEM micrographs for specimens subjected to sustained stresses in indoor and outdoor weathering (a) 1T-IN-HW (X1500) (b) 3T-OUT_HW (X 2000).....	141
PAPER V		
Fig. 1	Typical Cross-Section of Bridge 0410.....	153
Fig. 2	Instrumentation of HCB2.....	154
Fig. 3	Finite Element Modeling of B0410 superstructure using ANSYS V14.0	156
Fig. 4	Measured and estimated self-equilibrating strains in HCB2 produced by temperature fluctuations at the same day.....	171
Fig. 5	Measured and estimated self-equilibrating strains in HCB2 produced by temperature fluctuations at different days.....	172
Fig. 6	Strains measured by C3 on August 21st (LC 6 & 7).....	173
Fig. 7	Estimated self-equilibrating stresses in HCB2 produced by AASHTO positive thermal gradient.....	174

Fig. 8	Estimated self-equilibrating strains in HCB2 at Sec. (A-A) produced by AASHTO negative thermal gradient.....	175
Fig. 9	Self-equilibrating stresses at the deck top using different deck and arch depths, and tension reinforcements.....	176

LIST OF TABLES

		Page
PAPER II		
Table 1	Material properties used for modeling the FRP shell.....	59
Table 2	Material properties used for modeling the Polyisocyanurate Foam.....	62
PAPER III		
Table 1	Material Properties Used for Modeling the FRP Shell.....	91
Table 2	Material Properties Used for Modeling the Polyisocyanurate Foam...	91
Table 3	Measured and Estimated Strains Under Stop1 Loads.....	100
Table 4	Estimated Rotational and Extensional Stiffnesses For Tide Mill Bridge Simulated HCB's Chimney.....	109
PAPER IV		
Table 1	Ratio for OH/CH for control and conditioned specimens.....	131
PAPER V		
Table 1	Average Measured Temperature at B0410 Superstructure Elements °C.....	155
Table 2	Material Properties Used for Modeling the FRP Shell.....	169
Table 3	Material Properties Used for Modeling the Polyisocyanurate Foam.	170

1. INTRODUCTION

1.1. GENERAL

The transportation infrastructure in the United States can be considered the backbone of America due to its effect on nation's economy as well as citizens' lifestyle. Bridges are considered to be a vital part of the infrastructure system. However, the number of deficient bridges continues to increase. According to the National Bridge Inventory (2012), 11% of America's bridges (67000 out of 607000 bridges) are deficient. That means these bridges are not unsafe but must be closely monitored and inspected or repaired. The spans in these bridges are vital to motorists, who take 210 million trips daily across them. The need for innovative construction materials that can significantly prolong bridges' lifetime has led to the extensive use of fiber reinforced polymer (FRP) composites in bridge applications. These composites possess favorable properties (e.g. high strength-to-weight ratio, corrosion resistance, dimensional stability, good durability, transparency to electromagnetic radiation, and low-to-moderate tooling costs) making them ideal alternatives for resolving a number of problems, particularly corrosion and deterioration. However, fully composite FRP structural members fail to be cost competitive when compared to traditional concrete and steel members in civil engineering applications. The increased initial cost can be traced directly to the FRP composites' raw material costs and low stiffness. The most effective use of the FRP (as main load carrying members) is in the form of hybrid systems that combines both FRP and traditional construction materials (Mirmiran, 2001).

Hillman conceived a new hybrid composite beam (HCB) in 1996 that was used commercially for the first time in 2008 (Hillman, 2012). The HCB is comprised of three main sub-components: a composite shell, a compression reinforcement, and a tension reinforcement. The shell is comprised of a glass fiber reinforced polymer (GFRP) box. The compression reinforcement consists of self-consolidating concrete (SCC) that is poured into a classical arch shape. The tension reinforcement consists of galvanized high strength (HS) steel tendons anchored at each end within the end blocks. The concrete and steel are tucked inside the durable fiberglass shell, and the voids are filled with a Polyisocyanurate

(polyiso) foam. This new HCB can be constructed rapidly and possesses increased durability.

Three recently constructed bridges in Missouri incorporated HCBs in conjunction with traditional reinforced concrete deck systems. HCB is, however, quite novel. At this moment, a limited number of researches have studied the essential design methodologies of the HCB. This research study performed experimental tests and investigations, along with, theoretical and numerical analyses to more fundamentally understand the flexural and thermal behaviors of this new beam. It also examined the durability of the FRP shell that supplements the environmental protection of the beam components.

1.2. HYBRID SYSTEMS

The use of FRP composites as construction materials in structural engineering has grown significantly over the past decade (Bank, 2006). These composites have apparent advantages over conventional construction materials (e.g., concrete and steel). Their high strength-to-weight ratio, corrosion resistance, dimensional stability, good durability, and high dielectric strength make them promising and valuable materials for use in both new construction and existing infrastructures.

Although FRP composites are ideal alternatives for resolving a number of problems that face highway bridges (particularly corrosion and deterioration), their initial cost is relatively high when compared to more traditional materials used in civil engineering applications. This increased initial cost is largely due to current design approaches that use FRP composites in common linear shapes, such as I-sections and rods. These shapes do not take advantage of the inherent in-plane stiffness and strength of laminated composites (Keller, 2002). The use of FRP composites in construction industry can be optimized by combining the composites with hybrid structural systems. These hybrid systems either combine GFRPs with CRFPs or integrate FRPs with conventional construction materials in structural members. The advantages of hybrid systems include their cost-effectiveness and the ability to optimize the structure based on constituent material properties.

Several researchers have applied the hybrid FRP-concrete design concept to flexural members. The concept of using concrete with common GFRP composite sections (such as illustrated in Figure 1.1) emerged to conquer the shortcomings involved with using

these sections independently as flexural members. These shortcomings include the following:

- The compressive flange is considerably weaker than the tensile flange. This difference is attributed to both the local buckling phenomena and GFRP's low compressive strength (relative to its tensile strength).
- Because GFRP is linear elastic up to failure, GFRP structures' failure is catastrophe.
- Owing to the low stiffness of GFRP sections, obviously larger sections are used to satisfy the design codes' serviceability requirements.

A number of researchers have sought to overcome these issues. They replaced the upper GFRP flange with a layer of concrete to utilize its high compressive strength in resisting the compression zone stresses. At the same time, the concrete's high stiffness contributes to the overall stiffness of the member. In some cases, however, a thin layer of externally bonded CFRP was added to the hybrid section's tension zone. Owing to the CFRP's low ultimate strain, the addition of this layer intended to make the CFRP collapse first, providing warning of imminent failure. The high stiffness, excellent creep behavior, and excellent fatigue resistance of CFRP also increase the member's rigidity and enhance its resistance to both sustained and fatigue stresses. Finally, part of the cross-section was used as formwork for the wet concrete to minimize the fabrication costs. An illustration of a hybrid FRP-concrete cross section is given in Figure (1.2).

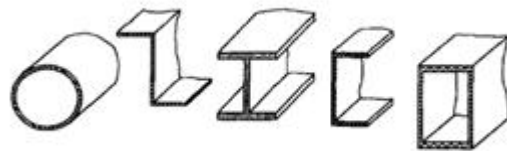


Figure 1.1. Typical Pultruded Composite Cross Sections

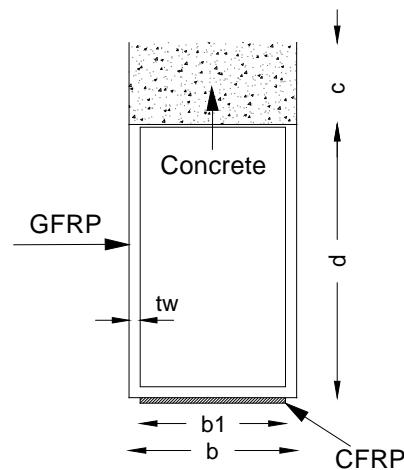


Figure 1.2. Hybrid FRP-Concrete Cross Section

Deskovic et al. (1995) investigated a hybrid FRP-concrete beam. This beam consisted of a filament-wound GFRP box section that was combined with a layer of concrete and a CFRP laminate in the compression and tension zone, respectively. They concluded that their proposed design concept resulted in cost-effective hybrid members that possess many desirable mechanical behavioral characteristics (e.g. such as pseudo-ductility, high strength, and increased stiffness) while maintaining a low weight. Van Erp et al. (2002) proposed a hybrid FRP-concrete beam similar to the system proposed by Deskovic et al. (1995). This beam consisted of a GFRP box section, a layer of concrete (bonded on the GFRP box section by a high quality epoxy adhesive), and a fiber reinforcement that was added to the box section's tensile flange. The weight of the hybrid beam was claimed to be approximately one-third that of a similar reinforced concrete beam.

Aref et al. (2005) proposed a hybrid FRP-concrete bridge superstructure in an attempt to attain corrosion-resistance, cost-effectiveness, lightweight, prefabrication, short construction period, and local deformation reduction under loading points. They formed a one-lane superstructure by fabricating three trapezoidal GFRP box sections individually. These trapezoidal components were then bonded together and wrapped with an FRP laminate to produce an integral structural system. Finally, concrete was poured into

appropriate cavities within the upper flange (Figure 1.3) .A further review on hybrid structures can be found in Mirmiran (2001).

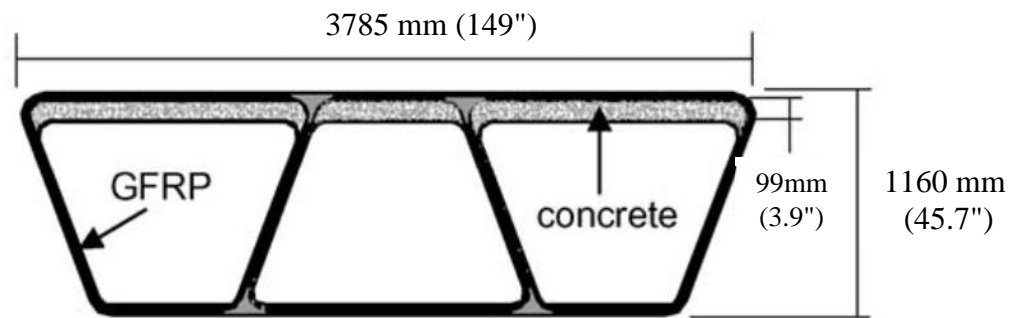


Figure 1.3. Hybrid FRP-concrete bridge superstructure (Aref et al., 2005)

Hai et al. (2010) incorporated CFRP and GFRP in hybrid FRP composite beam to utilize the superior stiffness and strength of the CFRP and the low cost of the GFRP. They were also combined to achieve the “hybrid effect” phenomena. An essential observation of the hybrid effect is that the failure strain of the carbon fiber becomes greater in a hybrid composite than it is in an all-carbon fiber composite (Hai et al., 2010). Observation of the hybrid effect was first credited to Hayashi (1972). It has subsequently been reported by several other researchers. This hybridization also offers better fatigue performance by incorporating an appropriate amount of CFRP/GFRP in hybrid composite (Dickson et al., 1989; Shan and Liao, 2002). A review on studies conducted on hybrid carbon–glass composites can be found in Summerscales and Short (1978).

This current work investigated a new type of HCBs that were recently used to construct three bridges in Missouri. The underlying concept of the HCB was conceived by Hillman in 1996 (Hillman, 2012). This HCB incorporates traditional construction materials (steel and concrete) with FRP composites in a new configuration to optimize the beam's structural performance. Each HCB consists of SCC that is poured into a classical arch shape

and tied at the ends by conventional prestressing strands. The concrete and steel are tucked inside a durable fiberglass shell, and the voids are filled with polyiso foam. The orientation of these sub-components is further evident as demonstrated graphically in Figure 1.4.

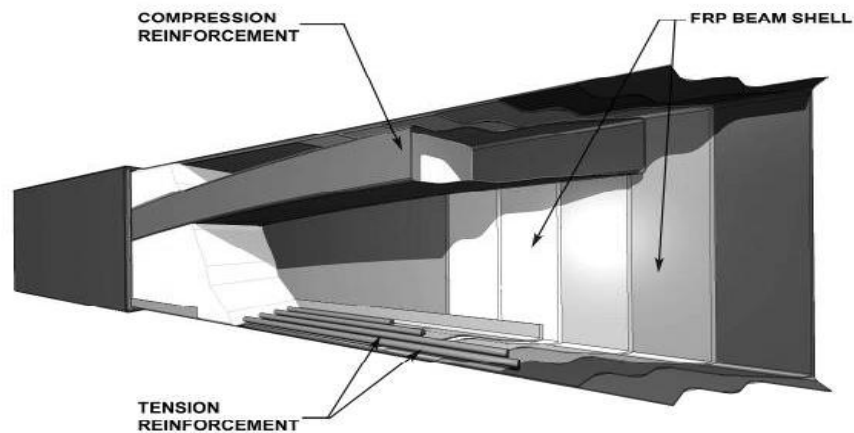


Figure 1.4. Fragmentary Perspective of Hybrid-Composite Beam

1.3. PREVIOUS HYBRID-COMPOSITE BEAM RESEARCH PROJECTS

Only three research projects were conducted on HCBs. Hillman (2003; 2008) implemented the first research project, as a part of innovations deserving exploratory analysis (IDEA) programs, before the first commercial use of the HCB in bridge applications. The second project was executed by University of Maine before the construction of the Knickerbocker HCB Bridge in Maine (Snape and Lindyberg, 2009). The last project was conducted by Virginia Tech University before the construction of the Tide Mill HCB Bridge in Virginia (Ahsan, 2012; Mascaro and Moen, 2012; Nosdall, 2013).

1.3.1 IDEA Test Program. The IDEA test program consisted of two studies. The first study addressed the HCB cost metrics that are associated with a railroad bridge construction, the materials selection for the beam's components, and the HCB fabrication process. This study also tested experimentally the first prototype HCB and established the preliminary design methodologies. The second study examined the application of the HCB as a framing system in railroad bridges.

Hillman (2003) compared the cost of HCBs to the cost of steel, prestressed concrete, and cast-in-place (CIP) concrete beams to evaluate the feasibility of the proposed HCB for railroad applications. He noticed that most of the obsolete class-1 road rail bridges were wood bridges with spans less than 6.1 m (20 ft). Typically, these obsolete bridges were replaced with longer prestressed beams that doubled the new bridges' span. As a result, Hillman's (2003) feasibility study focused on span ranges that were between 6.1 and 15.2 m (20 to 50 ft), with the target market at 9.1 m (30 ft). He estimated that the initial construction cost per linear foot of an HCB railroad bridge superstructure was \$6594/m (\$2010/ft). This cost was based on a 3.7 m (12-foot) wide deck comprised of eight 9.1 m (30-foot) HCBs. The cost of a similar built-up plate girder bridge was found to be nearly the same. Prestressed and CIP concrete bridges had a cost of \$4265/m and \$4921/m (1300 and \$1500/ft), respectively. Hillman (2003) concluded that HCB spans shorter than 9.1m (30 ft) were uneconomical. Life-cycle costs including operation, maintenance, repair, and disposal costs as well as the rapid advancements in the composite industry are expected to reduce the cost difference between the HCB beam and the concrete beams. The unique attributes of HCB, however, can make it more favorable than other competing beams at spans range from 9 to 37 m (30 to 120 ft).

The first prototype HCB was 6.6 m (19 ft) long, 61 cm (24 in) deep, and 30.5 cm (12-in) wide. The experimental program included applying nine load cases, via two 67 metric tons (150 kips) hydraulic actuators, to simulate the effects of Cooper E-80 locomotives. One of these tests included the application of cyclic loading (200,000 cycles) to simulate repeated Cooper E-80 axle load traveling across the bridge. The beam's elements were instrumented with strain and rosette gages. Six linear variable differential transformers (LVDTs) were used to measure the beam's deflections, and three LVDTs were used to measure the rotations at one beam end (Hillman, 2003).

Measured deflections under design service and factored loads were higher than the deflections that were calculated mathematically. The compression reinforcement of this prototype beam was formed using Portland cement grout. Because of the high aggregate stiffness, the typical Portland cement concrete has slightly higher stiffness than the Portland cement grout. Hillman (2003) attributed the higher measured deflection to the grout's lower stiffness. The beam exhibited almost a linear elastic behavior, up to the ultimate loading. This behavior was anticipated because the HCB's design was driven by its stiffness. No degradation in the beam's stiffness was observed after 200,000 fatigue cycles (Hillman, 2003).

During flexural tests, Hillman (2003) noticed that, in general, strains in the compression and tension reinforcements were maximum at the midspan and dropped significantly at the beam's ends. Hillman concluded that the HCB behaved like a beam rather than a tied arch because the strains in the two elements did not remain constant along their lengths. According to Hillman's interpretation, the forces in the compression and tension reinforcements at the beam's ends were transferred through shear in the shell webs to the supports (Hillman, 2003).

When the actuators' loads exceeded 40 kips, during flexural testing, the beam behaved like a tied arch with more uniform distributions of forces in the compression and tension reinforcements. Hillman (2003) suggested that a redundant load path was created, at high loads, and these loads were distributed from the FRP webs to the compression and tension reinforcing. Hillman (2003) concluded that a perfect beam behavior is valid up to the factored design loads. Whereas, at higher loads, the arching action offers a redundant load path making the beam behaves in a manner that is similar to a tied arch.

The second study, performed through the IDEA testing program, involved the construction and field-testing of a prototype HCB railroad bridge. This bridge was 9.1 m (30 ft) long and consisted of eight HCBs. These HCBs were divided into two four HCB units. The girders in each unit were tied together with threaded rods (Hillman, 2008). The concrete, which was used to form the concrete arch of the first HCB, had a 20 cm (8-in) slump, 34.5 MPa (5 ksi) precast concrete mix design. Because of the difficulty experienced during casting this concrete into the arch cavity of the first HCB, the remaining (seven) arches were shaped using SCC (Hillman, 2008). A 10 cm (4 in) slab, along with ballast

curbs were cast with typical 41.4 MPa (6 ksi) concrete. A track was then placed slightly off-center. The outside rail was approximately 10 cm (4 in) higher than the inside rail. The bridge's instrumentation included strain gages at different locations within both the HCBs and the bridge's slab. Several LVDTs were used to measure the relative displacement between the HCBs and the overlay. String pots were used to measure deflection at the girders' midspan. Static and dynamic load tests were performed on the bridge using heavily loaded coal cars. The train's speed was between 2 and 45 mph, during the dynamic load tests. The estimated strains and deflections were corrected to account for the track's superelevation and eccentricities as well as the train's velocity (Hillman, 2008).

Overall, the predicted deflections and the strains at lower FRP flanges (estimated via Hillman's model) correlated well with the measured values. In contrast, the estimated concrete strains did not correlate with the measured strains as accurately. The LVDTs placed at the bridge corners measured displacements that were on the order of a few thousandths of an inch. Based on these very small displacements along with the good correlation between the measured and predicted strains and deflections, Hillman (2008) concluded that, it is acceptable to assume a full composite action between the deck and HCBs during the design.

1.3.2 Testing of Knickerbocker Bridge HCB. The Knickerbocker bridge in Maine was constructed in 2010. Testing was performed prior to the construction in the Advanced Engineering Wood Composite (AEWC) lab at University of Maine. The test program included static and fatigue tests performed on a full-scale HCB that was compositely connected to a CIP deck. The program also tested the mechanical properties and the durability of the HCB's shell through macroscopic-level tests. The durability was tested by subjecting test specimens to two UV-irradiation exposure regimes.

The HCB tested in the AEWC lab had a height of 84 cm (33 in) with one layer of forty-two 13-mm (1/2 in) diameter seven-wire strands. The beam was connected, via shear connectors, to a concrete deck that was 17.8 cm (7 in) deep and 121.9 cm (48 in) wide. The top lid of the Knickerbocker HCB was infused in segments and spliced together. A typical cross-section of the tested beam is illustrated in Figure 1.5 (Snape and Lindyberg, 2009).

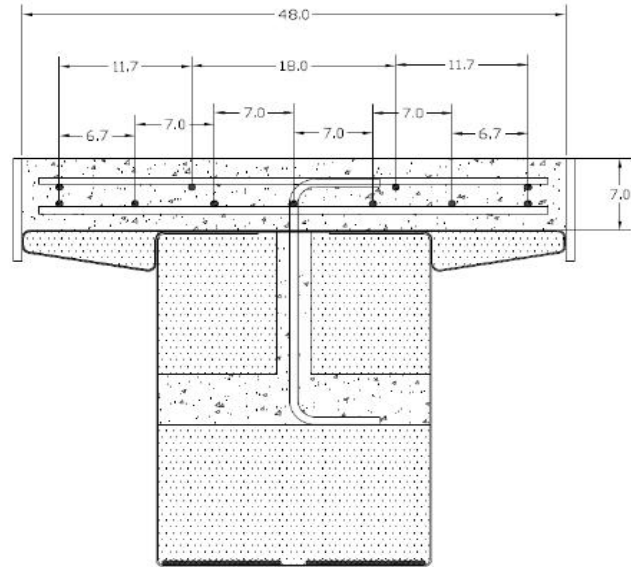


Figure 1.5. Typical cross-section of the HCB tested in AEW lab (Snape and Lindyberg, 2009)

The initial deflection measurements under both the self-weight of the fluid arch concrete and the fluid deck concrete correlated well with the design calculations base on Hillman's model. The beam had a negative camber of approximately 3.5 cm (1 3/8 in) at the mid-span approximately three days after the deck pour. Snape and Lindyberg (2009) attributed this negative camber to the design equations. These equations neither considered the FRP shell's self-weight nor the shrinkage of the arch and the deck's concrete.

Initial static shear and bending tests demonstrated that the HCB is linear-elastic under non-factored design loading conditions. The beam also exhibited a linear-elastic behavior under factored design shear and bending loads. Neither deterioration nor degradation was observed in the beam's flexural stiffness after 2,000,000 fatigue bending cycles (Snape and Lindyberg, 2009).

The composite wings were found to provide stiffness and stability to the tested beam when the arch was cast. The splicing technique used to transfer load across the joint in the top plate and wings was largely ineffective, buckling under the load until the joint

closed in compression. Although some ties were excessively stressed, the composite cross-ties (spacers) prevented the local buckling of shell webs under the fluid concrete load (Snape and Lindyberg, 2009).

Nearly all of the composite shell's mechanical properties increased after completing the UV exposure; the in-plane shear modulus, however, did not. These results indicate that the UV inhibitors that were included in the resin effectively resisted the UV irradiation. Subsequently, the UV irradiation's effects were limited to fading and discoloration of the surface. This increase in the mechanical properties was attributed to residual cross-linking of the polymeric structure (Snape and Lindyberg, 2009).

These tests demonstrated that, overall, Hillman's model predicted the beam's behavior accurately under service loads. The tested beam was instrumented by 35 strain gages. The study, however, presented strain and deflection results under the applied service loads at the midspan only. Moreover, it did not present any results under the applied factored design loads. The HCB was loaded up to failure at the end of the testing program. Here, failure took place when the tension reinforcement anchors broke free, damaging the FRP shell at its end.

1.3.3 Testing Tide Mill Bridge HCBs. The Tide Mill Bridge testing program was executed by Virginia Tech University. This program consisted of three phases. The first phase was conducted on HCBs before casting the concrete arch (FRP shell and prestressing tendons only). Both distributed and concentrated loads (at the midspan and the quarter points) were applied manually by placing steel angles at the top of the FRP lid. The second phase tests were performed on non-composite HCBs (complete HCBs including the compression reinforcement, before the deck was poured). In this phase, a hydraulic static actuator was used to apply concentrated loads at the HCB's midspan and quarter points. A full-scale laboratory HCB bridge was tested during the final phase. This 13.4 m (44 ft) single-span bridge consisted of three HCBs that were incorporated with traditional, skewed, reinforced concrete deck. Different load cases that simulate tire loading of a HL-93 truck on a bridge's deck were implemented (Ahsan, 2012).

The HCB elements behaved linear-elastically during service level tests. Predicted deflections and strains (via Hillman's model) in the HCB elements were often found to be

conservative when compared to measured results (Ahsan, 2012). The neutral axis locations observed from testing were in general agreement with the predicted locations (Ahsan, 2012). Strain profiles constructed from the strain measurements of each component during the last two phases revealed that the arch's behavior was inconsistent with the overall HCB's behavior (Ahsan, 2012; Nosdall, 2013). Overall, comparisons between the experimental measurements and the theoretical calculations illustrated that Hillman's model predicted the strains in both the strands and the FRP shell with acceptable accuracy. Whereas, the model provided a poor prediction for the concrete arch's strains (Ahsan, 2012; Nosdall, 2013).

Nosdall (2013) suggested that an HCB can be decoupled into an FRP shell and a tied arch (consisting of the concrete arch and the tension reinforcement). At the same time he concluded that there is a strain compatibility between the FRP bottom shell and the strands. The measured strains along with his proposed analysis procedure revealed that the tied arch carried approximately 80% of the total load for the non-composite HCB. The concrete arch fell below the neutral axis after the deck placement. At this phase, the concrete arch's strain gages provided unexpected results. Nosdall (2013) assumed that the arch was cracked and that the sensors' measurements became erratic. Thus, he didn't include the arch during the beam's stiffness calculations. For this composite case, Nosdall (2013) concluded that the FRP shell and prestressing strands resisted approximately 85% of the applied load. The bridge deck carried the remaining 15%.

Close-range Photogrammetry was used to detect out-of-plane movement of the FRP web during the first and second load testing phases. This Photogrammetry was also used to detect any movements of the arch within the FRP shell under the applied loads during the second phase. Significant lateral displacement at the midspan of the HCB was measured during the first two phases. This displacement indicates that beam was flexible laterally and prone to lateral displacement, especially when it was not connected to a bridge system. The Photogrammetry showed also that the arch moved within the FRP shell during the second phase (Mascaro and Moen, 2012).

1.4. ADVANTAGES OF THE HCB

The HCB attains apparent advantages that allow this new technology to be a better alternative for prestressed and steel beams in many bridge applications. These advantages are:

➤ *Light weight*

For most typical applications, the HCB is transported and erected before the concrete arch pour. This makes the weight of an HCB, during transportation and erection, is approximately one fifth of the weight of a similar conventional steel beam and approximately one tenth of the weight of a similar precast prestressed concrete beam. Thus, four to eight HCBs can be placed on a single truck as opposed to a single beam for a precast concrete box beam. In most cases, a HCB can be safely set with 30-50 cranes instead to 150-300 ton cranes. The transportation and unloading of B0439 HCBs are illustrated in Figures 1.6 and 1.7, respectively.



Figure 1.6. Transportation of eight B0439 HCBs with one truck



Figure 1.7. Loading of HCBs via small crane

The weight of the complete HCB (after pouring the concrete arch and web) ranges from approximately one fourth to one third the weight of a similar prestressed concrete beam. This minimizes the weight of a bridge's superstructure and, subsequently, minimizes the cost of the substructure. This light weight allows using existing infrastructures when a deteriorated superstructure being replace. It also makes this technology well suited to accelerated bridge construction (ABC).

➤ *Increased durability*

The expected age of an HCB is 100 years versus a target life for highway bridges of 75 years according to AASHTO (2012) bridge design specification (Hillman, 2003). This potentially long service life together with the low maintenance requirements of the

HCB may reduce the frequency and duration of roadway and lane closure, thus, minimizing the impact to traffic and reducing the potential of work zone accidents. The increased durability of the HCB made it the best available solution to replace the deteriorated Knickerbocker bridge in Boothbay, Maine. The Knickerbocker bridge (Figure 1.8) is an eight-bay bridge with a total length equals 165 m (540 ft) and a width equals 9.8 m (32 ft).

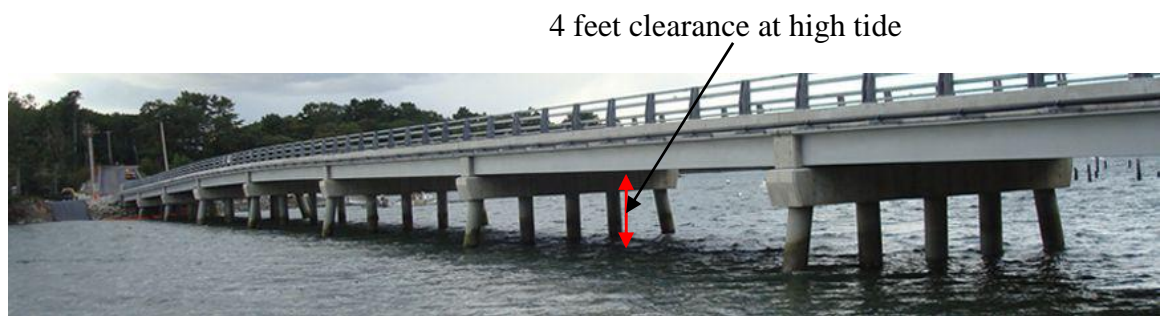


Figure 1.8. Knickerbocker HCB Bridge in Boothbay, Maine

➤ *Economic Solution*

As discussed earlier in sec. 1.3.1, the HCB is cost competitive with the traditional structural members.

➤ *Compatible with the FRP decks*

FRP decks were recently used in the bridge applications to overcome the deck's reinforcement corrosion problem. These bridge decks can be subdivided into two groups: Pultruded profiles and sandwich panels. Figures 1.9 and 1.10 illustrate Pultruded and sandwich panels, respectively. Figure 10 illustrate one of the most recent proposed sandwich deck panels for bridge applications. This panel was fabricated by the VARTM technique to reduce the cost of the FRP deck (Tuwair et al., 2014).



Figure 1.9. Pultruded GFRP panel



Figure 1.10. GFRP sandwich deck panel (Tuwair et al., 2014)

In most applications these decks are connected to either steel or FRP girders via mechanical fasteners (e.g. shear studs, bolts, or dowels) or adhesive bonding. Connection systems between an FRP deck and supporting beams via bolts is depicted in Figure 1.11. The integration of the FRP decks with steel girders shifts the corrosion problem from the deck to the girder. Whereas, FRP girders failed to compete with the conventional structural members in the construction industry because of their cost. The HCB is more durable than

the steel girders, cheaper than the FRP girders, and its exterior composite skin provides an advantage over the concrete beams. This HCB can be adhesively bonded to the FRP decks. For FRP composites, adhesive bonding is more suitable connection method than bolted connections because larger surfaces can be linked together, thus, ensuring reduced stresses at the connection interface (Schollmayer, 2009). The adhesive bond is also cheaper and requires less effort and time to be implemented than a bolted connection. Previous studies showed that adhesive bonding always provided full composite action between FRP decks and steel girders even when flexible polyurethane adhesives with a layer thickness up to 50 mm (2 in.) was used (Gürtler, 2004; Keller and Gürtler, 2005, 2006). The advantages offered by the HCB over the conventional girders makes this new beam one of the most convenient elements that can be integrated with the FRP decks to eliminate the corrosion dilemma in the bridge applications.

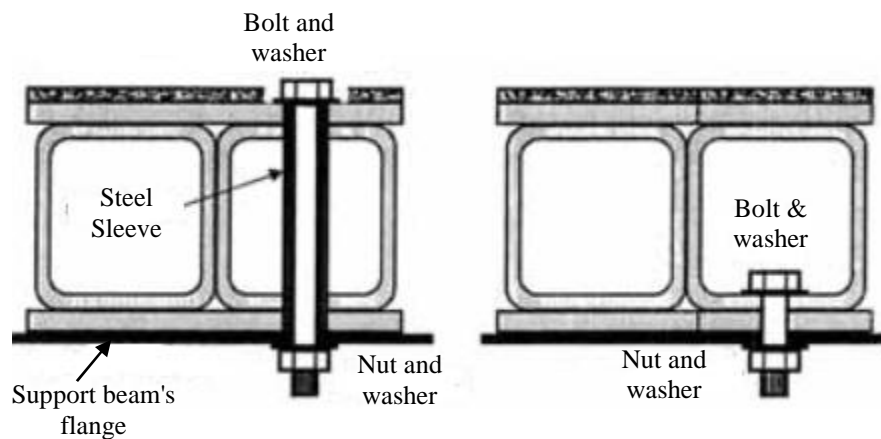


Figure 1.11. Connection of pultruded bridge decks to beams' flanges using mechanical fasteners

➤ *Eco-friendly Technology*

The production of concrete and the fabrication of steel produces significant amount of greenhouse gases. An HCB uses only 10% of the concrete of a prestressed concrete beam.

1.5. OBJECTIVE

The main objectives of this research were to conduct the first finite element (FE) analysis of an HCB bridge superstructure, investigate the HCB's flexural behavior, propose new flexural analysis methods, evaluate the HCB's durability performance, and analyze the HCB's thermal behavior. This research program was conducted through main four phases. Each phase achieved one of the main objectives.

Phase 1: The finite element modeling of an HCB bridge superstructure

None of the researches that were conducted on HCBs performed FE analysis to these beams. Owing to its uncertain behavior, the FE analysis work is indispensable to provide better understanding of the HCB's structural behavior. The FE modeling of the HCB bridge is unconventional because of the novelty of the HCB, its unique configuration, and its hybrid nature. As well, evaluating the accuracy of current model in estimating the HCB deflection is as important as understanding its structural behavior. This importance can be attributed to the fact that the HCB's design, to-date, is driven by its stiffness. Subsequently, the FE analysis of an HCB bridge superstructure was conducted to achieve the following goals:

- a. Establish a method for applying computer modeling to HCBs and testing its accuracy in predicting the behavior of the HCB under static loads.
- b. Provide a better understanding of the HCB's structural behavior.
- c. Highlight the areas that need further research and investigation.
- d. Evaluate the accuracy of the existing design method in estimating deflection along HCBs under static load cases.

Phase 2: An investigation of HCB's flexural behavior

The literature review clarified that understanding the HCB's flexural behavior is challenging. The FE analysis results, obtained in the first stage emphasized the need for analyzing the flexural behavior of the HCB and indicated that the current flexural design method needs to be improved. Consequently, this phase thought to achieve the following goals:

- a. Analyze the flexural behavior of in-service HCBs under service loads.

- b. Evaluate the performance of the current flexural analysis method.
- c. Propose flexural analysis methods for both simply-supported HCBs and HCBs supported on bearing pads to achieve better estimation of the strains in the beam's elements.

Phase 3: An assessment of HCB's durability performance

The main concept of the HCB is to acquire its strength and stiffness mainly from cheap construction materials (i.e. steel and concrete), while the environmental protection is provided by a more expensive, however, relatively more durable material (i.e. GFRP composite). Subsequently, the composite shell must possess not only sufficient strength and stiffness to withstand the self-weight and applied loads, but also relevant physical and in-service properties that can endure the aggressive environmental conditions into which the girder may be placed. These properties are of primary importance in relation to the durability of the FRP composite shell and hence the HCB as a whole.

The objectives of this phase were to: subject the FRP shell to environmental conditioning regimes that reflect the natural weathering conditions in Missouri, perform microstructural analysis to understand the stress corrosion mechanisms under different environmental exposures, and propose recommendations to enhance the HCB's durability.

The durability of the HCB was evaluated in terms of changes in the ultimate tensile strength under different conditioning regimes. The GFRP shell was subjected to the following aging regimes:

- a. Salt fog exposure regime for 3072 hours (128 days).
- b. UV-irradiation exposure for 3072 hours followed by 6048 hours of salt fog exposure (totally 380 days).
- c. Immersion in a concrete pour simulated solution for 80 days.
- d. Sustained stress, along with 350 different thermal cycles, in a computer-controlled environmental chamber (75 days).
- e. Sustained stress along with indoor ambient controlled weathering and outdoor natural weathering (240 days).

The microstructural analysis was achieved via: optical microscopy (OM), scanning electron microscopy (SEM), Energy-dispersive X-ray (EDX) analysis, and Fourier transform infrared (FTIR) spectroscopy. These tools allowed observing: the diffusion of aggressive ions into the laminated shell, matrix cracking, matrix hydrolysis, fiber-matrix interface debonding, and fiber deterioration. The mechanical testing and the microstructural analysis provided fundamental insight into the durability and stress corrosion mechanisms of the examined GFRP shell under different environmental effects. This information is valuable to enhance the GFRP shell's durability.

Phase 4: An analysis of HCB's thermal behavior

Variations in environmental conditions result in two thermal cycles in bridge structures: seasonal cycle, and diurnal cycle (Gross, 1999). The seasonal temperature cycle leads to uniform temperature changes, while the daily cycle results in thermal gradient throughout a structure cross-section. Axial bridge deformations under uniform temperature changes are well understood and are accounted for by providing expansion joints and/or flexible supports, such as sliding plates and elastomeric bearing pads. Thermal gradients through the depth of a bridge superstructure, however, presents a more complex engineering problem (Mahama et al., 2009). Thermal strains and tresses may lead to cracks formation. Typically, the ultimate strength of a typical concrete bridge superstructure is not affected by this thermal cracking. However, the thermal cracks result in corrosion of the reinforcing steel bars affecting significantly the serviceability of the structure (AASHTO, 1998). AASHTO (2012) specifications for bridges design include the temperature gradient in various service limit state load combinations. AASHTO (2012) (Provision C3.12.3) states "*If experience has shown that neglecting temperature gradient in the design of a given type of structure has not lead to structural distress, the owner may exclude temperature gradient*". To-date, neither the thermal behavior of an HCB bridge superstructure was studied nor a thermal analysis method for this new type of bridges was proposed. Therefore, this phase endeavored to accomplish the following goals:

- a. Study the thermal behavior of an HCB bridge superstructure under ambient temperature fluctuations.
- b. Establish a design method of HCB bridge superstructures for thermal gradient.

1.6 DISSERTATION ORGANIZATION

The research outcome of this study is presented by publication dissertation option. All the findings and conclusions of this research study have been submitted to technical journals and conference proceedings. The thesis is divided mainly into three sections: Introduction, paper, and conclusions and recommendations.

INTRODUCTION: this section presents an introduction and literature review about the use of the hybrid systems in civil engineering applications. The section then introduces the previous researches that were implemented on HCBs and summerizes their conclusions. Finally, the section explains the main objectives of this dissertation and the motivations of these objectives.

PAPER: this section is the main body of the thesis. It consists of five technical papers.

First paper: The first paper introduces the HCB for the reader as a new structural element that can be implemented in bridge applications. This paper details the elements of the HCB and their functions. It illustrates the fabrication process of the GFRP shell and the installation and construction sequences of an HCB. The paper also explains the instrumentation of a double-web HCB with various sensors. Finally, it presented the early-age behavior of the HCB and analyzed the strain levels that induced in the GFRP shell during this stage.

Second paper: The second paper explains in detail the FE modeling of an HCB bridge superstructure via two commercial FE analysis software packages: *ANSYS 13* and *SAP2000 14*. The paper evaluates the performance of the FE models and the current analysis methods in estimating the HCB's deflection. The evaluation is achieved by comparing the estimated deflections to deflections measured during a full-scale bridge testing. Finally, the paper analyzes the structural behavior of the HCB and highlightes the areas that need further research and investigation.

Third paper: The third paper studies the flexural behavior of the HCB. This paper presents the strains that induced in HCB elements during different loading stages. The paper compares the measured strains to the strains calculated by FE analysis and the current design method. Finally, analysis methods are presented and evaluated for both simply supported HCBs and HCBs that are supported on bearing pads.

Fourth paper: The fourth paper evaluates the HCB's durability. The durability is evaluated in terms of the change in the ultimate tensile strength under five aging regimes. The paper also presents micro structural analysis results for control and exposed specimens. The micro structural analysis was performed using scanning electron microscopy (SEM), energy dispersive spectroscopy (EDS) analysis, and Fourier transform infrared (FTIR) spectroscopy. Finally, the paper provides conclusions about the damage mechanisms of the GFRP shell under different environmental conditions. It also provides recommendations to optimize the shell's resistance to environmental effects.

Fifth paper: The fifth paper introduces a mathematical algorithm for estimating the stresses that can induce in an HCB bridge superstructure under temperature fluctuations. The paper takes the first step toward gaining an experience about the thermal behavior of this new type of bridges. The paper also compares between the strains estimated by the proposed algorithm, thermo-structural FE analysis, and the experimentally measured strains. This paper demonstrates that the proposed algorithm is effective and of practical applicability in predicting the stress and strain levels induced by thermal gradients.

CONCLUSIONS AND RECOMMENDATIONS: This section summarizes the work that was accomplished in this dissertation. It also presents the key findings of all experiments and theoretical analyses, which were executed during this research study. Finally, it gives recommendations for future research on the HCB.

PAPER**I. HYBRID COMPOSITE BEAM (HCB) BRIDGE IMPLEMENTATION AND
FIELD MONITORING****M.A. Abeol Seoud¹ and Prof. J.J. Myers²**¹Graduate Research Assistant²Professor

Missouri University of Science and Technology (Missouri S&T)

Center for Infrastructure Engineering Studies (CIES)

Department of Civil, Arch., & Envir. Engineering

Rolla, MO 65409

USA

Corresponding Author: jmyers@mst.edu

KEYWORDS: FRP, hybrid composite beam (HCB), Bridge superstructure, Finite element analysis, Structural design.

ABSTRACT

This project involves the field evaluation of three Hybrid-Composite Girder Bridges in Missouri, USA. These hybrid composite beams (HCB)s are comprised of three main sub-components: a composite shell, compression reinforcement, and tension reinforcement. The shell is comprised of a fiber reinforced polymer (FRP) box beam. The compression reinforcement consists of self-consolidating concrete (SCC) which is pumped into a profiled conduit within the shell. The tension reinforcement consists of galvanized steel tendons anchored at the compression reinforcement ends. Due to the novelty of the HCB and its unclear behavior, an integrated study is under implementation to evaluate the recently constructed hybrid bridge superstructures. To achieve the goals of this study, a series of load tests was applied to the three bridges and the HCBs deflections were measured. HCB elements have been instrumented with various sensors and the induced strains were recorded at several stages and under the applied test loads. Finite element (FE) models were constructed via *ANSYS 13.0* and *SAP2000 14.2* commercial softwares. Mathematical calculations were performed to predict the deflections and the strains using the existing design methodology. The study showed that the new HCB is a promising

technique in the bridge applications. The HCB unique configuration optimizes its performance and leads to lightweight, cost-effective, and durable member. The existing design procedure is simple and suites the bridge designers. However, it needs some refinements. This paper presents briefly the work achieved to date and highlights the concluded remarks. The fabrication and construction sequencing of the HCB is also presented.

INTRODUCTION

A new type of hybrid composite beams (HCB)s used recently to construct three bridges in Missouri, USA. The underlying concept of the HCB was conceived by Hillman in 1996, and the first commercial use was in June 2008. Hillman supposed that if a concrete arch were tied at the ends and encapsulated in a fiber reinforced polymer (FRP) shell, the embodiment would become a lightweight, strong, and corrosion resistant structural member. This unique configuration that combines conventional materials into FRP components creates a structural member that utilizes the inherent benefits of each material in such a manner as to optimize the overall performance of the beam. Since FRP materials, are generally too expensive and too flexible when arranged in a homogeneous form, the strength and stiffness are provided by an efficient use of the steel purely axial tension, and the concrete in purely axial compression.

Due to the novelty of the HCB, an integrated field evaluation program of the recently constructed HCB bridges in Missouri is under implementation by Missouri University of science and technology (MS&T). The program aims to develop a quality control / quality assurance testing of the bridge members, analyze the structural behavior of the HCB, examine the design methodology and assumptions, evaluate the thermal effects in the HCB, test its durability, and assess the potential serviceability and maintenance challenges. In order to achieve these goals, a series of load tests was applied to the three bridges, beam elements have been instrumented with various sensors, FE models were generated for two HCB bridges, and theoretical predictions for the beams deflections and strains were carried out using the current design methodologies.

This paper introduces the HCB as a new structural element that can be implemented as a framing system in the bridge applications. The paper explains: the HCB composition,

fabrication and installation sequencing, the recently constructed HCB bridges, and the current flexural design methodology. It also analyzes a sample of strain data recorded during several loading stages of B0410.

HCB COMPOSITION

The HCB elements are demonstrated graphically by figure 1. This figure was constructed by the commercial software *SAP2000 14.0* during the finite element analysis of B0439 superstructure (Aboelseoud and Myers, 2014). A brief discussion about these elements and their functions follows:

Compression Reinforcement: it consists of concrete poured into classical arch shape. As indicated by the name, the selection of the arch shape aims to subject the concrete to pure compressive stresses under the service loads, hence optimizing the usage of the concrete. The concrete arch ends with two concrete shafts (chimneys). The main function of the chimney is to transfer the horizontal forces from the HCB to the cast-in-place (CIP) diaphragms. Another function of the chimney is to enable the tension reinforcement to tie the arch without the need for an anchorage device. Due to the constricted and inaccessible cavity provided for the compression reinforcement, the use of highly flowable concrete is substantial. Subsequently, self-consolidating concrete (SCC) was used to form the HCB arches of the three constructed bridges.

Tension Reinforcement: the function of the tension reinforcement is to tie the concrete arch and contribute to the flexural stiffness of the HCB. The tension and compression reinforcing are the primary load carrying elements of the HCB. They also provide the greatest contribution to the beam stiffness. During the design process, the amount of the tension reinforcement is increased until the deflection limit is satisfied. Therefore, the material selected for this component must have a very high tensile strength and a very high modulus of elasticity. Based on these requirements, the conventional prestressing tendon seems the most convenient element to serve as tensile reinforcement of the HCB. In the current project, prestressing strands were used to tie the HCBs arches.

FRP Shell: the main goal of the FRP box is to protect the HCB elements from the environmental effects, hence increasing its lifetime. It also serves as a formwork during the concrete arch pour and contributes to the girder stiffness and nominal capacity.

The standard laminate composition of the HCB shell is typically a quad weave glass reinforcing fabric infused with a vinylester resin matrix. Generally the quad-weave or "triaxial weave" fabrics that used in HCB comprised of multiple layers of glass rovings with varying percentages of the fibers oriented in the 0° , 90° and $\pm 45^\circ$ directions relative to the longitudinal axis. This type of fabrics with multidirectional fibers enhances the efficiency of a composite subjected to shear strains as well as longitudinal and transverse strains. Another benefit of the multidirectional weaves is that with the proper orientation of fibers, the composite begins to behave somewhat "quasi-isotropic" which can simplify preliminary designs.

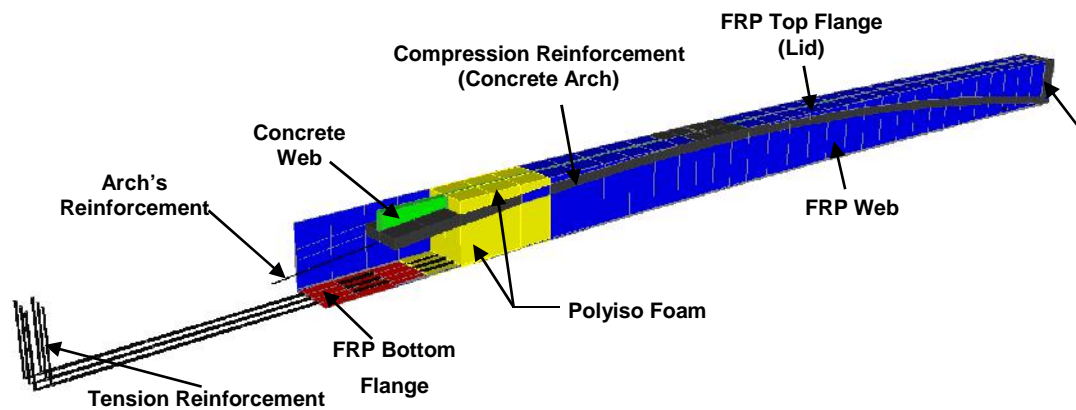


Fig. 1. Fragmentary Perspective of Hybrid-Composite Beam

HCB Core: the core material fills the voided space within the beam shell. Polyisocyanurate (polyiso) foam was selected to serve as the core material due its lightweight, low cost, available sizes and its tremendous low thermal conductivity. The core plays two important roles during the fabrication and the service life of the HCB. First, the core serves as interior form that helps the beam maintain its shape during the fabrication process. Without the

core, the other beam elements would implode under the vacuum process. Second, it provides lateral stability to the FRP webs increasing their buckling strength.

Concrete Web: the web can be considered as a part of the compression reinforcement. Its main function is to transfer the loads from the lid to the concrete arch and subsequently to the tension reinforcement.

Shear Connectors: they are intended to transfer the load from the bridge deck to the arch achieving a full composite action between the HCB and deck slab. The connectors also increase the shear capacity of the arch.

FABRICATION OF HCB SHELL

The first step in manufacturing the HCB is the fabrication of the FRP box and steel strands. The bottom shell of the beam (FRP bottom flange and webs), complete with tension reinforcing are fabricated in one mold. While the top flange is fabricated in a separate mold. The shell is fabricated using the Vacuum Assisted Resin Transfer Molding (VARTM) process. VARTM is an adaptation of the resin transfer molding (RTM) process and it is very cost-effective in making large structures (Mazumdar, 2001). Although the fabrication and construction sequencing of HCB are not unique and deviate slightly from project to another, the main steps of the fabrication of the HCBs can be summarized as follow:

A three-sided box is fabricated to the dimensions of the beam. Along the centerlines of the flange, slots are made to install channels. These channels act as a line source for the resin infusion and vacuum. The layup of the shell consists of placing one layer of a surface veil over the entire mold surface, followed by one layer of a distribution media, and finally the glass fiber layers. In addition to the UV inhibitors contained in the resin, the surface veil and distribution media provide extra protection for the fiber layers against the UV degradation. The two layers also ease the resin transfer and provide a resin rich layer on the outer surface of the shell.

Seven-wire high strength tendons are then placed on the top of the bottom flange fiber layers with ends running up vertically to anchor the compression reinforcement. Once the post-tensioning bars are positioned, polyisocyanurate foam blocks are placed within

the mold forming arch shape. A bag is placed on the foam blocks and inflated to keep a cavity for the compression reinforcement. Spacers and clamps are used to tie the shell webs and ensure the dimensions of the cavity. Upper layer of foam blocks is placed on the top of the bag while still leaving a cavity to accommodate the concrete web.

The entire mold is completely enclosed in layers of vacuum bagging film sealed with tacky tape. Vacuum is then applied through the vacuum ports. After evacuating all of the air, the vinyl ester resin is pulled into the form by the vacuum pressure and the mold is kept under vacuum. The FRP lid (top flange) is fabricated in a separate mold with the same procedure.

Before attaching the top flange to the bottom shell, seven-wire strands (generally two strands) are installed in the bottom of the arch and run the full length of the beam. Tie wires are attached to the strands to lift them up during installation of the shear connectors.

The FRP lid is glued to the bottom shell using methyl methacrylate adhesives (MMA). The MMA adhesives provide strong bond that ensure that the lid acts compositely with the bottom shell during the arch pour and the erection of the HCB. Self-tapping stainless steel screws are used to further connect the two elements. The screws are important to arrest any crack that might propagate through the adhesive bond.

Finally, holes are drilled into the lid and the bottom legs of the shear connectors are then developed below the loose strands.

INSTALLATION SEQUENCE

Once fabricated, the HCB shells are shipped and erected on the supports. SCC is then pumped into a profiled conduit within the shell through preset slots in the top flange. The slots are drilled into the lid at the midspan, quarter points, and above the chimneys. Pouring the concrete arch may be executed prior to erection or even before shipment of the beams as occurred in B0410. Casting the arch after installation of the beams facilitates significantly the shipment process and allows using small cranes for the beams placement. For example, the fifteen HCBs fabricated for B0439 were shipped using only two trucks rather than fifteen trucks needed for similar prestressed girders. On the other hand, casting the arch before beams shipment allows the concrete arch to gain strength while other construction activities take place, hence reducing the construction time, and yet the weight

of the full HCB is about one third to one fourth the similar prestressed girders. It should be noted that once the beams are filled with concrete, they must be lifted from the ends. This can be achieved by placing strand lifting loops in the chimneys prior to casting the arch. These loops are then removed once the HCB units installed on the substructure. Figure 2 displays the placement of B0439 HCBs.



Fig. 2. B0439, HCB Erection Process

Once cured, the concrete arch acts compositely with the complete shell and the concrete of the deck and parapets can be placed. There are many different ways to place a concrete deck on top of an HCB framed bridge. The deck slab is typically filled in-place, however, it may also be precast prior to erection. Though casting the concrete arch and deck slab prior to erection reduces the lightweight advantage of this technology, this technique allows constructing a bridge superstructure in one day, resulting in substantial congestion relief.

BRIDGES DESCRIPTION

Bridge B0439

The first HCB bridge (B0439) constructed in Missouri was completed in November 2011 and opened to traffic shortly thereafter. This three-span bridge is approximately 55 m (2160 in) long, and its overall width is 9.3 m (368 in). The B0439 bridge consists of five simply supported HCBs in each span for a total of fifteen HCBs. Each of these HCBs is 84 cm X 62 cm (33 in X 24.4 in) and consists of SCC arch that is 12.7 cm (5 in) deep and 56 cm (22 in) wide. The concrete arch is reinforced with two 13-mm (1/2 in) galvanized steel strands Grade 1,860 MPa (270 ksi) and is tied via 36 13-mm (1/2 in) strands of the same type. To further expedite the superstructure construction, this bridge incorporated the use of precast stay-in-place deck forms spanning between the beams, spaced at 1.9 m (76 in) to accommodate the 9.3 m (368 in) out-to-out dimension of the deck. A typical cross section of B0439 HCB is shown in figure 3.

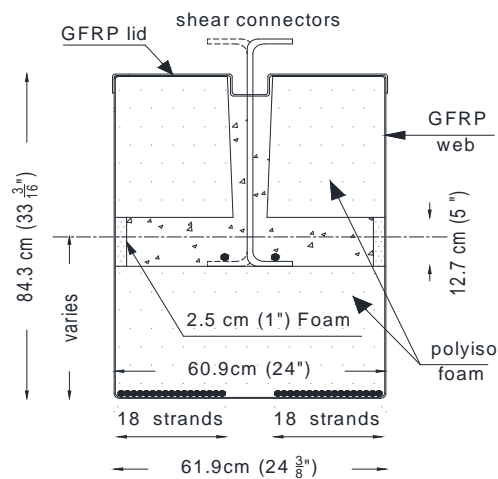


Fig. 3. Typical Cross Section of B0439 HCB

Bridge B0478

The third bridge (B0478) constructed in Missouri is two-span bridge. The bridge overall length is 30.1 m (1148 in) and its out-to-out dimension of the deck is 8.1 m (320 in). The

bridge consists of twelve HCBs, six simply supported HCBs in each span. The configuration of HCBs used in this project is similar to those used in B0439 with slight changes in the dimensions and tension reinforcements. Figure 4 illustrates the composition of each HCB. To meet the Accelerated Bridge Construction initiatives, instead of precast planks, this bridge used a six-beam cross section with composite overhanging flanges. Subsequently, the HCB units were placed at 1.3 m (52 in) centers rather than the 1.9 m (76 in) spacing on the B0439. As a result, the only deck forming required was for overhangs at the fascia girders, which was done using standard overhang brackets and walkways.

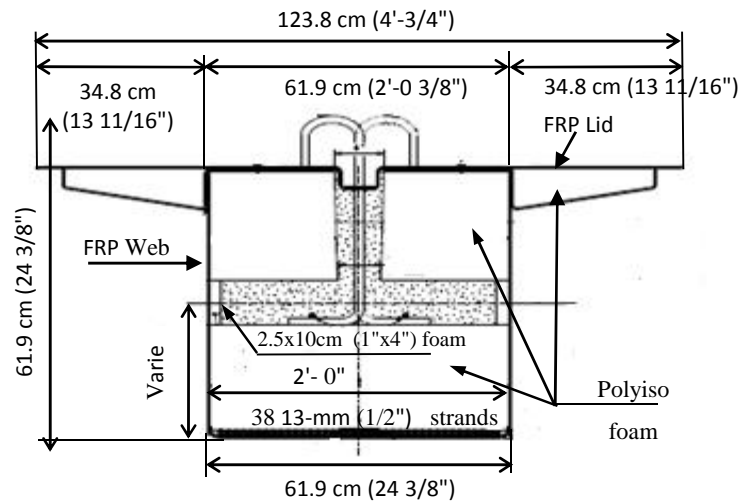


Fig. 4. Typical Cross Section of B0478 HCB

Bridge B0410

The second bridge (B0410) constructed in Missouri spans 31.7 m (1248 in) and its out-to-out dimension of the deck is 9.35 m (368 in). The single-span bridge consists of three HCBs. Since the lengths of the HCBs are relatively long, the beams were fabricated as multi-celled, double-web beams. This was intended to significantly reduce the time of fabrication and erection. The multi-celled HCBs require a slight increase in lay-up time;

however, the infusion time is the same due to additional infusion ports for each cell of the beam. The entire process can still be performed in one day. The reduction in erection time was due to the contractor only handling three girders instead of six.

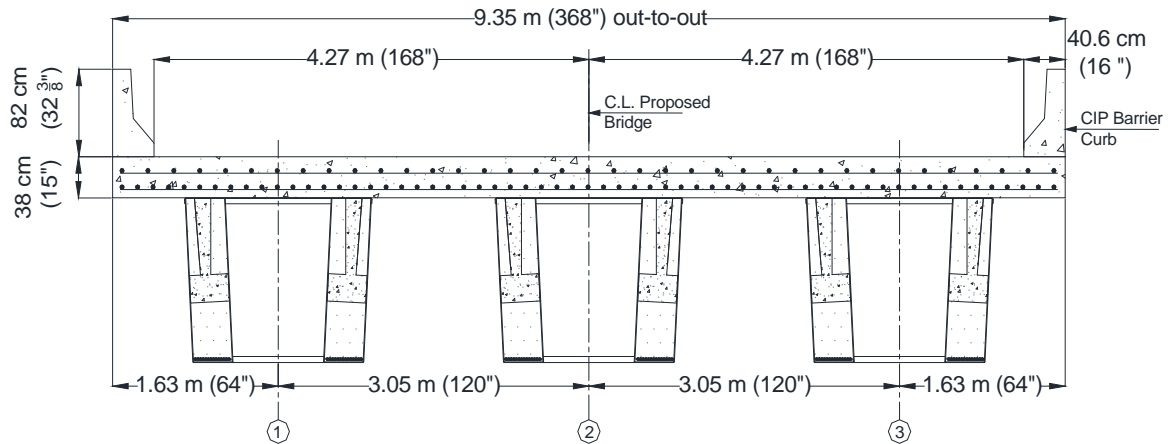


Fig. 5. Typical Cross-Section of Bridge 0410

Each multi-celled HCB has an overall depth 152.4 cm (60 in) and varying width ranging from 167.6 cm (66 in) at the bottom to 182.9 cm (72 in) at the top. Each single HCB consists of SCC arch that is 25.4 cm (10 in) deep and 26.7 cm (10.5 in) wide. The concrete arch is reinforced with two 13-mm (1/2 in) diameter, 1,680 MPa (270 ksi) seven-wire galvanized steel strands, and is tied by and fort four 13-mm (1/2 in) strands of the same type. A typical cross section of B0410 is shown in figure 5.

TESTING MATRIX

The tests performed to date on the three bridges included quality control / quality assurance (QC/QA) tests of the HCB concrete pour, and deflection and strains monitoring during a series of load tests performed on the bridges superstructures. A total station and prisms were used to measure the deflection at different locations of each girder of the three bridges under the applied loads. While the strain data was collected only from B0410. The

structural elements of one of B0410 girders (HCB2) were instrumented with different strain gauges. The instrumentation (figure 6) consisted of resistive strain gages on the FRP shell and strands, vibrating wire strain gages/thermistors in the concrete arch, and thermocouples on the strands.

The data collection for the early-age behavior of HCB2 was performed by recording the strain for 25 hours started an hour before the beginning of the concrete arch pour. After the bridge construction, two three-axle dump trucks performed three stops to produce maximum bending moments and shear forces in HCB2. The induced strains in the different elements due to the three stops were recorded. In the current work samples of the strain data recorded during the arch pour and the load test are presented and discussed.

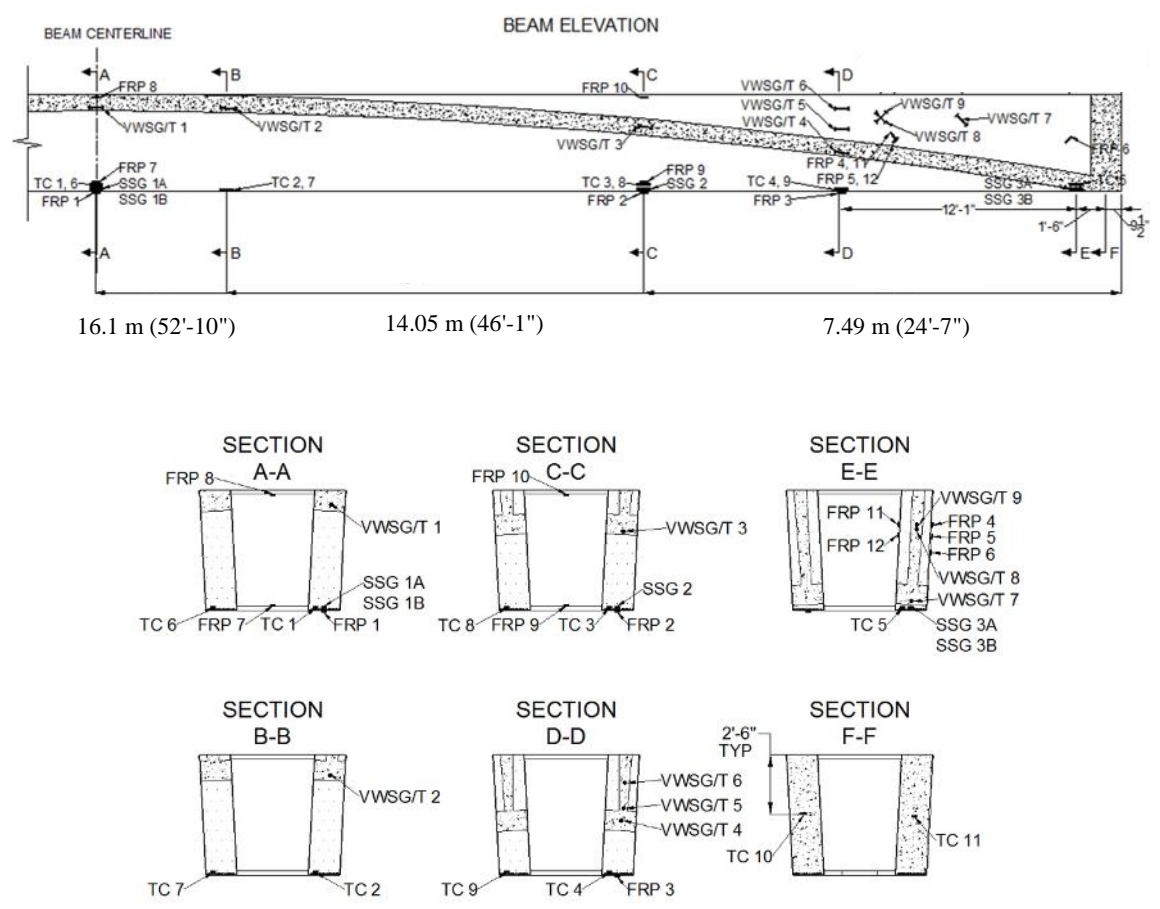


Fig. 6. Instrumentation of HCB2, B0410

FLEXURAL DESIGN OF THE HCB

A typical composite HCB cross-section is displayed in figure 7. In real bridges, the actual elements may deviate slightly from those shown in this figure. The current flexural design methodology uses the same assumptions as the reinforced concrete beam to calculate the nominal bending moment capacity of the HCB. Based on bridges designed and constructed to date, the failure mode for the HCB is crushing of the concrete rather than failure of the laminate or ductile failure of the strands (Hillman, 2012). By considering the HCB to be over-reinforced, the design process, for the nominal bending capacity, starts with considering the strain at the extreme upper fiber of concrete equals to the ultimate concrete strain. Using the strain compatibility approach, the strains in the different components are related to the concrete strain as follow

$$v_i(x) = \frac{v_{cu} \times (y_i(x) - \overline{y_p}(x))}{h_c - \overline{y_p}(x)} \quad (1)$$

where $v_i(x)$ is the strain of the component i at distance x from the beam end, v_{cu} is the ultimate strain of the concrete and is assumed -0.003 (ACI, 2011), $y_i(x)$ is the distance from the c.g. of the component i to the extreme lower fiber of the beam at distance x from the beam end, $\overline{y_p}(x)$ is the distance from the plastic neutral axis (PNA) of the composite section to the extreme lower fiber of the beam at distance x , and h_c is the total depth of the composite section.

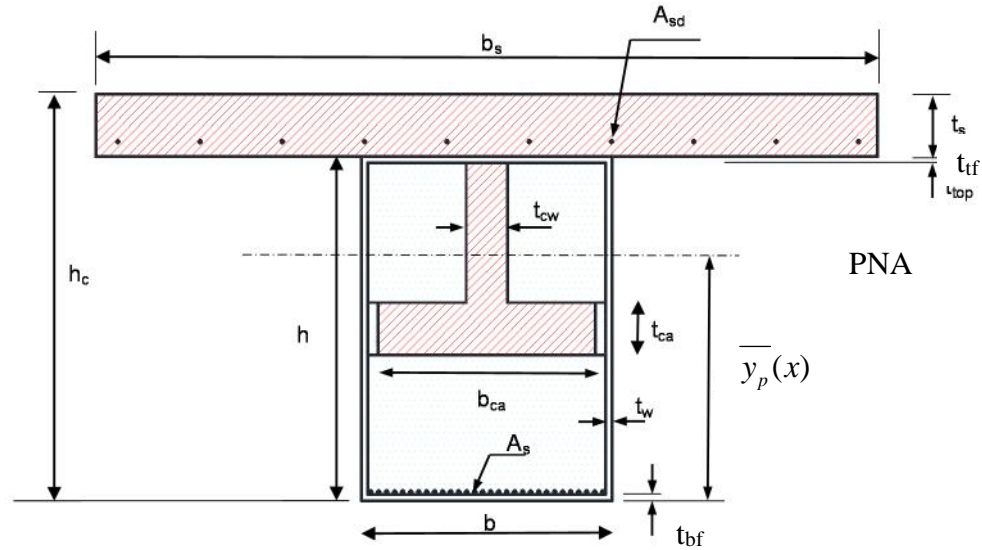


Fig. 7. Typical Cross-section of the Composite Hybrid-Composite Beam

The force in the FRP elements, strands, and the deck reinforcement, $F_i(x)$, can be calculated as follow

$$F_i(x) = E_i v_i(x) A_i \quad (2)$$

where E_i is elastic modulus of the component i, and A_i is the cross-sectional area of the component i.

By assuming the PNA, at distance x from the beam end, to be within the concrete web, the force in the concrete components can be calculated as follow

$$F_{cs}(x) = 0.85 f'_{cs} t_s b_s \quad (3)$$

$$F_{cw}(x) = 0.85 f'_{ca} S_1 (h - t_{tf} - \bar{y}_p(x)) t_{cw} \quad (4)$$

$$F_{ca}(x) = 0 \quad (5)$$

where $F_{cs}(x)$, $F_{cw}(x)$, and $F_{ca}(x)$ are the forces in the deck slab, concrete web, and concrete arch respectively, f'_{cs} and f'_{ca} are the compressive strength of the deck and arch concrete respectively, t_s , t_{cf} , and t_{cw} are the thicknesses of the deck slab, top FRP flange, and concrete web respectively, b_s is the effective slab width, h is the depth of the FRP box, and S_1 is a factor that relates the depth of the equivalent stress block to the actual stress depth. The value of S_1 can be found in (ACI, 2011).

The PNA location can be calculated by equilibrating the horizontal forces

$$\sum_{i=1}^n F_i(x) = 0 \quad (6)$$

where n is the number of the HCB elements. However, the PNA may lie within the deck slab, concrete web, concrete arch, or below the concrete arch. Subsequently, identifying the PNA location requires using a trial and error method.

Once the PNA is identified, the reduced nominal moment capacity of the composite section can be estimated by summing the moments around the PNA location and applying the reduction factor

$$WM_n(x) = 0.81 \left(\sum_{i=1}^n F_i d_i(x) \right) \quad (7)$$

where $d_i(x)$ is the distance from the component i force to the PNA (moment arm), and W is the reduction strength factor. Though, ACI (2012) recommends a strength reduction factor equals 0.65 for the reinforced concrete compression controlled member, Hillman (2012) uses the factor recommended by ACI (2012) for tension controlled members (0.9) multiplied by other reduction factor (0.9) that compensates for including FRP laminates in the HCB.

Finally, the reduced nominal moment should satisfy the following equation

$$wM_n(x) \geq M_u(x) \quad (8)$$

where $M_u(x)$ is the factored bending moment. For highway bridge applications, the factored moment shall be estimated using the design loads provided by (AASHTO, 2012).

It should be noted that the compression forces calculated in the concrete components using Whitney stress block (equations 3 and 4) are approximate forces. Because Whitney stress block method is applied for concrete elements that subjected to strains range from zero to the ultimate concrete strain. For example, eq. (4) overestimates the concrete force in the web because the strain at the top of the concrete web is less than 0.003.

Hillman (2003) proposed second methodology that achieves more accurate estimation of the nominal bending capacity of the HCB. Instead of assuming a uniform stress in the compression block, the actual stress relative to the strain in the concrete is used based on a parabolic stress-strain curve for concrete. The most common curves that are used to relate the concrete compressive stress to its strain are: modified Hognestad curve (Hognestad, 1951), Todeschini curve (Todeschini et al., 1964), and Thorenfeldt, Tomaszewicz, and Jensen curve (Thorenfeldt et al., 1987). A brief discussion about these curves can be found in (Wight and MacGregor, 2012).

Once, the stress is related to the strain in the concrete components, the axial force in each component, $F_{Ci}(x)$, can then be calculated by

$$F_{Ci}(x) = b_i \int_{y_{li}}^{y_{ui}} f_i(x, y) dy \quad (9)$$

where b_i is the width of the concrete component i , y_{ui} and y_{li} are the distances from the extreme upper and lower fibers of the component i to the extreme lower fiber of the beam at distance x respectively, and $f_i(x, y)$ is the stress of the concrete component i at the location (x, y) .

MATHEMATICAL CALCULATION OF THE STRAIN

The strains in the different HCB elements of B0410 due to the applied loads were calculated using the second design methodology presented in the previous section. However, the concrete subjected to tensile stress was assumed to contribute to the strength and stiffness of the HCB up to the modulus of rupture of the concrete. This aimed to allow the comparison between the tensile strains captured by some sensors in the arch and the estimated strains. It should be noted also that, under the applied loads the strain at the upper concrete fiber cannot be assumed to equal the ultimate concrete strain.

A MATLAB code was implemented to calculate the PNAs at the sensor locations using iterative procedure. The process assumes initial value for the PNA at distance x . Thereafter, the axial forces of the different components are calculated. If the forces don't equilibrate the code moves the PNA upward or downward based on the forces' values, and the process is repeated until convergence is achieved.

However, the strains obtained from the mathematical procedure are found in the elastic ranges of all the constituting materials. Consequently, the strains under the applied loads can be calculated in one-step by

$$v_i(x) = \frac{M(x)(\bar{y}(x) - y_i(x))}{I(x)E_w} \quad (10)$$

where $M(x)$ is the bending moment in the HCB at distance x due to the applied loads, $\bar{y}(x)$ is the distance from the elastic neutral axis (ENA) to the extreme lower fiber of the HCB at distance x , E_w is the elastic modulus of the shell web, and $I(x)$ is the transformed moment of inertia, with respect to the elastic modulus of the shell web, about the ENA at distance x .

EARLY-AGE BEHAVIOR OF B0410

Figure 8 displays the change in the concrete temperature at sec. (B-B) (thermistor 2) during the first 24 hours after the beginning of the concrete arch pour. The hydration of Portland cement is highly exothermic process. Mindess and Young (1981) and Lachemi et al. (1997)

divided the Portland cement hydration process into five phases. In Phase 1, the heat is rapidly evolved for a short period during the initial mixing. Thereafter, a dormant period (Phase 2) starts for several hours. During this phase, the concrete remains plastic. Once the dormant period ends, a vigorous reaction between the calcium silicate in the cement and the water begins until a maximum rate of heat evolution is reached. Final set occurs during this acceleration phase (Phase 3). Then, the heat generation continues but with slow rate. The concrete temperature rises slowly during this phase (phase 4) until the peak hydration temperature is reached by its end. During the final phase (Phase 5), the heat generation is minimal and the concrete loses heat until a state of equilibrium is reached with the surrounding environment.

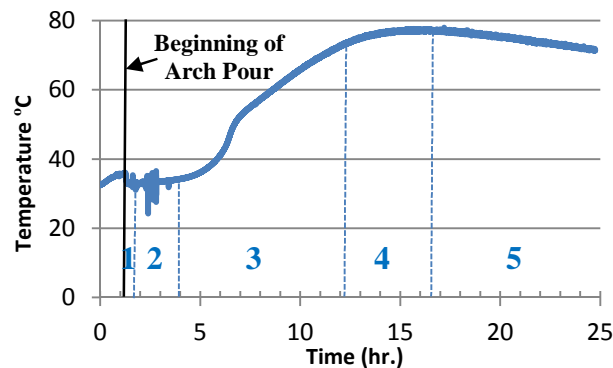


Fig. 8. Concrete Temperature during Hydration Process at VWSG/T2

The occurrence of the five phases during the arch pour is demonstrated graphically by figure 8. The temperature changes captured by the remaining thermistors were similar to what recorded by T2. Since the hydration development was not almost affected by the ambient temperature, the hydration curves were similar to what might be expected under adiabatic conditions. The maximum temperature rise (around 55 °C) was captured by T4 at sec. (D-D), while the minimum temperature increase (around 23 °C) occurred close to the beam end (T10). Though it was expected that the concrete close to the end would

experience the highest temperature rise due to the relatively large amount of concrete in the chimney, the low temperature rise at the beam ends may be attributed to the large number of the tendons tied the concrete arches. These tendons might work as temperature sink that reduced the concrete temperature at the beam end. Figure 9 illustrates that, the temperature of the strands during the 24 hours was maximal at the beam ends and decreased as we move toward the midspan. These results support the conclusion that the strands absorbed the concrete temperature at the beam end. Moreover, the holes drilled at the chimneys, quarter points, and midspan, to allow casting the concrete, might slightly reduce the concrete temperature at these locations relative to the temperature at sec. (D-D).

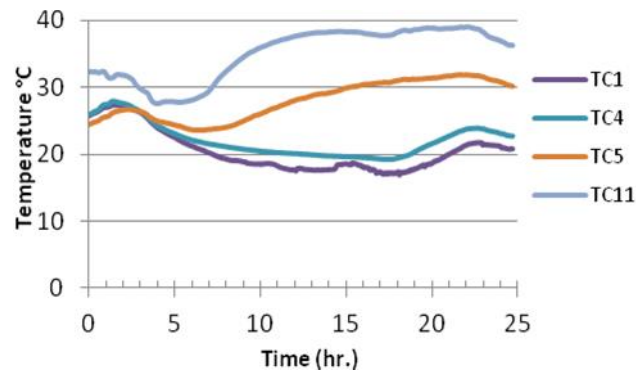


Fig. 9. Strands Temperature of HCB2, B0410 during and after the Arch Pour

The maximum temperature rise (55 °C) matches the ACI Committee 363 (1992) suggestion that the temperature rise during hydration for high-strength concretes ranges from 6 to 8 °C per 100 lb/yd³ of cement.

Figure 10 shows the strain data recorded at the midspan of HCB2 during and after the concrete pour. The strain increased gradually at all the gauges up to the end of the concrete pour. By the end of the cast, the strain at FRP8 is found about three times the strain at FRP1 suggesting that the NA located about one-fourth the depth of the shell from the beam lower

fiber. This is expected, because with the absence of the compression reinforcement, the tension reinforcement significantly moves the NA downward. Once the pour ended, the strain remained almost constant for several hours. As the concrete temperature began to rise at the top of the beam (sec. A-A), tensile strains induced at the upper fibers, while compressive ones took place at the lower fibers. The magnitude of the induced strains due to the thermal effects seem to be compatible with the NA location at this stage. When the concrete started to cool, reversed strains induced in the shell elements.

Since concrete is known to go through a phase of expansion during the plastic state followed by a phase of drying shrinkage during the hardened state. The strains induced in the FRP shell and strands, after the concrete pour, are expected to result not only from the thermal effects, but also from the concrete volumetric changes due to the physical and chemical reactions of the concrete with its internal and external environment.

Figure 10 clarifies that there is no strain compatibility between the strands and the bottom FRP shell (SSG1A and FRP1), unlike to what was expected. This indicates that, in spite of the simultaneous infusion with resin, the two elements separated allowing each element to suffer different levels of stress. The figure also demonstrates that, the maximum normal strain occurred during the concrete pour (FRP8) was about 7% of the ultimate compressive strain (0.012 in/in). While the maximum tensile strain was less than 1% of the ultimate tensile strain (0.026 in/in).

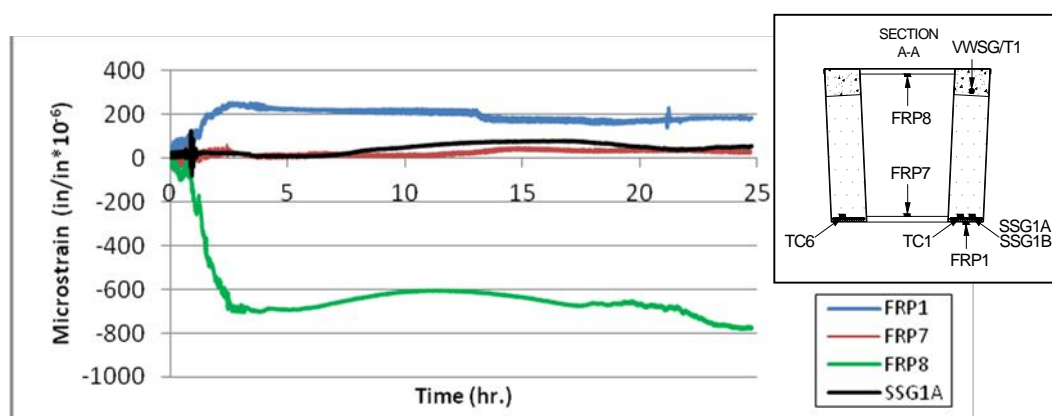


Fig. 10. The strains induced in the strands and FRP shell at sec. (A-A) of HCB2, B0410, during and after the Arch Pour

Figure 11 displays the shear strains induced in the FRP shell due to the concrete pour. Gauge FRP 6, which is located at distance 76.2 cm (30 in) (half the shell depth) from the centerline of the support, captured the highest shear strain. Gauges FRP 4 and 5 were adhered on the exterior shell, while gauges FRP 11 and 12 were placed at the same locations as FRP 4 and 5 but on the interior shell of the girder. However, the exterior gauges (4 and 5) read lower strains than those read by the interior ones (11 and 12) rather than similar strains as expected. This behavior is unexplained; however, the exterior webs suffered slight outward deformation (buckling) during the concrete pour which might affected the exterior gauges readings.

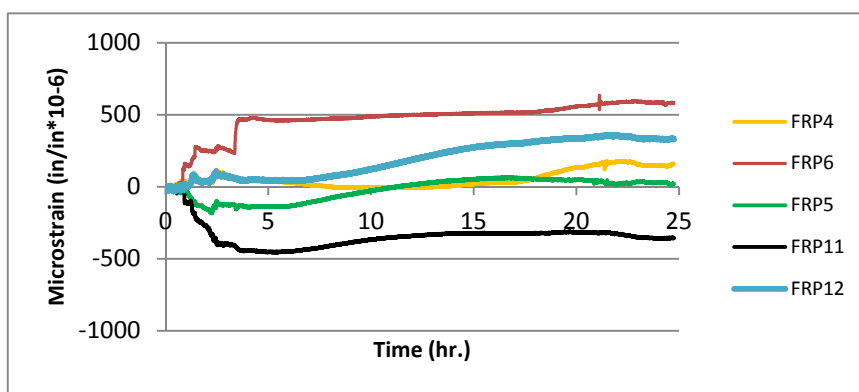


Fig. 11. B0410 Shear Strain during and after the Arch Pour

The maximum shear strain captured after the concrete pour was about 600 \sim v with corresponding shear stress equals about 35% of the ultimate shear strength 22.8 MPa (3.3 ksi). These results indicate that the shear and wrinkling of the shell webs are the most critical criteria during the design of the shell. It should be noted that the stress corresponding to the shear strain was calculated via multiplying the shear strain by the shear modulus. In other words, the FRP was assumed isotropic and neither the Poisson's ratio nor the coupling effects were included in that calculation. It is worth mentioning also

that by the end of this stage the deflection of the HCB due to its self-weight was found about half the expected deflection. This forced increasing the depth of the B0410 deck slab to eliminate the excessive camber.

RESULTS OF B0410 LOAD TEST

Figure (12) presents the measured and calculated normal strains in HCB2 elements due to stop 1 loads. Figure (12-a) demonstrates that the existing flexural design methodology is unable to accurately identify the strains in the concrete arch. The figure also shows that the maximum compressive strains occurred close to the junction of the arch and the chimney. This suggests that there was negative bending moment at the beam end that might be combined with axial compressive force through the beam length. This conclusion interprets the significant overestimation of the tensile strains in the FRP shell, strands, and the arch midspan by the existing methodology. Figure (12-b) illustrates the normal strains measured by the gauges (SSG1A and SSG1B) are significantly lower than the strains measured by (FRP1) assuring that there is no strain compatibility between the two elements, as observed during the arch pour phase.

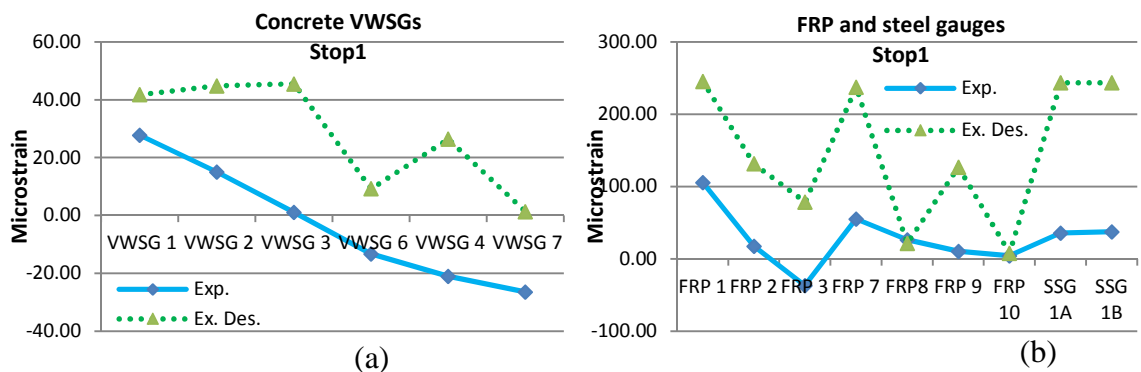


Fig. 12. Normal Strain in Composite HCB2 due to Stop1 Loads
 (a) Strains in concrete arch (b) Strains in FRP shell and strands

Figure (13) displays the measured shear strains due to the same stop. This figure illustrates that the exterior (FRP4 and FRP5) and interior (FRP10 & FRP11) shell webs suffered similar levels of the shear strains as it was expected and unlike to what observed during the concrete pour. The figure also clarifies that the shear strains induced due to the service loads are significantly lower than those induced due to the arch pour. This is compatible with Aboelseoud and Myers (2014) observation that, the majority of the shear strains induce in the shell webs occur during the concrete arch pour stage. Generally, the measured normal and shear strains in the GFRP shell due to the concrete pour and the service loads stages indicate that the shell can maintain a long-term durability.

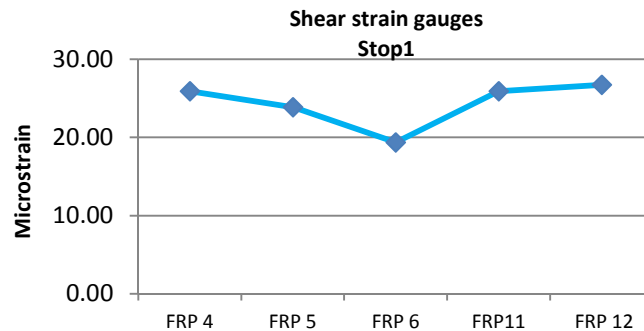


Fig. 13. Shear Strain in Composite HCB2 due to Stop1 Loads

CONCLUSIONS

A new type of hybrid composite beams (HCB)s used recently to construct three bridges in Mo, USA. An integrated study on the HCB is under implementation by Missouri University of science and technology. The study aims to evaluate the girder's in-service behavior and the theoretical design methodologies. Based on the work achieved to date, the following conclusions can be drawn

- The unique configuration of the HCB optimizes the load carrying behavior and maintains the gross section properties under the service loads.
- HCB possesses a sufficient flexural and shear rigidity.
- The strain levels experienced by the GFRP shell due to different load stages suggests that the shell can maintain long-term durability increasing the overall lifetime of the HCB.
- The shell webs are the most critical elements in shell. Attentiveness needs to be paid to their elastic buckling and shear stresses during the design process.
- The existing flexural design methodology is simple and suites the daily design process. However, it needs some improvements to overcome its flaws.

ACKNOWLEDGMENTS

The authors gratefully acknowledge the Missouri Department of Transportation (MoDOT) and the National University Transportation Center (NUTC) at Missouri S&T for sponsoring this research study. The staff support from the Dept. of Civil, Architectural and Environmental Engineering and Center for Infrastructure Engineering Studies (CIES) at Missouri S&T are also greatly appreciated.

REFERENCES

- Aboelseoud, M. A. and Myers, J. J. "Finite Element Modeling of Hybrid Composite Beam Bridge in Missouri, USA." *Journal of Bridge Engineering*, ISSN (print) 1084-0702, May 2014.
- ACI. "Building Code Requirements for Structural Concrete (ACI 318-11) and Commentary." American Concrete Institute, 2011.
- ACI, Committee 363. "State-of-the-Art Report on High-Strength Concrete." ACI 363R-92. Detroit, American Concrete Institute, 1992.
- Ansys 13.0. [computer software], Canonsburg, PA, Ansys.
- Hillman, J. R. "Hybrid-Composite Beam (HCB®) Design and Maintenance Manual." The Missouri Department of Transportation, 2012.
- Hillman, J. R. "Investigation of a Hybrid-Composite Beam System." High Speed Rail IDEA Program, Transportation Research Board of National Academies, Chicago, HSR Project Report 23, 2003.
- Hognestad, E. "Study of combined bending and axial load in reinforced concrete members." University of Illinois at Urbana Champaign, College of Engineering. Engineering Experiment Station, Champaign, Illinois, 1951.
- Lachemi, M., Lessard, M. and Aitcin, P. "Early-Age Temperature Developments in a High-Performance Concrete Viaduct." *ACI Special Publication*, Vol. 167, No., 1997.
- AASHTO "AASHTO LRFD bridge design specifications." American Association of State Highway and Transportation Officials Washington, DC. 2012.
- Mazumdar, S. "Composites manufacturing: materials, product, and process engineering." CRC press, 2001.
- Mindess, S. and Young, J. F. "Concrete, Prentice Hall." Englewood Cliffs, NJ, pp. 481, 1981.
- Sap2000 14.2 [computer software], Berkeley, CA, Computers and Structures.
- Thorenfeldt, E., Tomaszewicz, A. and Jensen, J. "Mechanical properties of high-strength concrete and application in design." *Proceedings of the Symposium Utilization of High Strength Concrete*, 1987.
- Todeschini, C. E., Bianchini, A. C. and Kesler, C. E. "Behavior of concrete columns reinforced with high strength steels." *ACI Journal Proceedings*, 1964.

Wight, J. K. and Macgregor, J. G. "Reinforced concrete: mechanics and design." Pearson Education Inc., Upper Saddle River, NJ, 2012.

PAPER

II. Finite Element Modeling of Hybrid Composite Beam Bridge in Missouri, USA

Mohamed A. Aboelseoud¹ and John J. Myers, F.ASCE²

Abstract

Three bridges were recently constructed in Missouri, USA using a new type of Hybrid-Composite Beam (HCBs) incorporated within traditional reinforced concrete deck systems. These HCBs are comprised of three main sub-components: a composite shell, compression reinforcement, and tension reinforcement. The compression reinforcement is a self-consolidating concrete (SCC) arch that is tied at the ends by high strength galvanized steel strands. The compression and tension reinforcements are encapsulated in glass fiber reinforced polymer (GFRP) box and the voids are filled with polyisocyanate (polyiso) foam. This unique configuration aims to optimize the structural performance of the HCB constituents and hence optimizing the overall performance of the beam. However due to the novelty of the HCB, its structural behavior has not been completely understood yet. Consequently, the finite element modeling of this new type of beams is crucial for providing deeper insight of its structural behavior and validating the current design assumptions. It is, therefore, the main goal of this study is to examine the accuracy of linear finite element (FE) analysis in predicting the static behavior of the HCB under service loads. This paper explains in detail the finite element modeling of the superstructure of one of the recently constructed HCB bridges using two commercial FE analysis packages; *ANSYS 13.0* and *SAP2000 14.2*. A field load test that simulates several load cases was applied to the bridge and the deflections of the HCBs were measured at different locations. A simple analytical procedure that is based on the transformed area method is also used to predict the HCBs deflections. The comparison between measured deflections and predicted deflections show that the FE analysis can predict the HCB bridge behavior with acceptable accuracy, while the theoretical procedure overestimates significantly the beams' deflections. Finally, the two finite element (FE) models are used to analyze the behavior of the HCB.

CE Database of subject headings: Hybrid-Composite Beam (HCB); finite element analysis; Bridge superstructure; Structural behavior analysis; FRP composites; Full-scale bridge testing.

Introduction

The use of fiber reinforced polymer (FRP) composites as construction materials has increased significantly over the last two decades (Bank, 2006). The advantageous characteristics of the FRP composites such as high strength-to-weight ratio, corrosion resistance, dimensional stability, excellent durability, high dielectric strength and low to moderate tooling costs make them valuable materials for the use in structural applications and ideal alternatives for resolving a number of problems that face highway bridges, especially corrosion and deterioration problems. However the use of structural members fabricated entirely of FRP in bridge applications has faced some obstacles that precluded the wide spread use of this technology. The most important reason is the high initial cost of the FRP members, which prevents them from being cost competitive with traditional concrete and steel members. The increased cost can be traced directly to the raw material costs and to the low stiffness of the FRP composites. Another disadvantage of fully FRP structural members is their catastrophic failure nature because FRP composites are almost linear elastic up to failure. The last disadvantage is their poor compressive behavior especially for glass fiber reinforced polymer (GFRP) composites. This low compressive strength combined with the local buckling phenomena make the compressive flange considerably weaker than the tensile flange (Deskovic et al., 1995). Keller (2002) attributed the high cost of the fully composite FRP members to current design approaches that use them in common linear shapes, such as I-sections and rods, which do not take advantage of the inherent in-plane stiffness and strength of laminated composites.

To overcome the previous shortcomings, several researchers have used the FRP composites in hybrid systems. The proposed hybrid systems combined either GFRP with carbon fiber reinforced polymer (CFRP) or other FRP composites with traditional materials such as concrete and steel. A number of studies on hybrid carbon–glass composites have been reviewed by Summerscales and Short (1978), while an overview review on the

combination of FRP with traditional materials in structural members can be found in the paper by (Mirmiran, 2001).

This investigation studies a new type of hybrid composite beams (HCBs) that incorporate traditional construction materials, concrete and steel, in conjunction with GFRP composites. The underlying concept of the HCB was conceived by John Hillman in 1996. The HCB consists of SCC that is poured in classical arch shape and anchored at ends by high strength tendons. Both the SCC and the high strength tendons are tucked inside durable, fiberglass composite shell. The unique configuration of the HCB aims to subject the concrete to pure compressive stresses and the steel to pure tensile stresses and exploit the durability of the GFRP to produce a structural member that can last more than one hundred years.

A very limited number of research studies have been conducted on the HCB. The experimental results of these studies demonstrate that the behavior of the HCB has not been completely understood. The HCB was thought to behave like a tied arch beam; however, during testing of the first HCB-prototype, (Hillman, 2003) concluded that the HCB behaves like a beam element rather than tied arch. During the same testing program, Hillman found that when the actuator load exceeded certain limit, the HCB behaved more similar to a tied arch. He suggested that at high loads, a redundant load path was created and the load was distributed from the FRP webs to the compression and tension reinforcing. A more recent study was performed at Virginia Tech on the HCB before its use in the Tide Mill Bridge (Ahsan, 2012). Results of this study demonstrated that under some load cases the concrete above the neutral axis was subjected to tensile stresses, where compressive stresses were expected to exist. They also found that the concrete arch has high compressive stress close to the junction with the chimney (concrete end block). At this location, the concrete was very close to the neutral axis and was supposed to have very small stresses. Finally, the researchers concluded that Hillman's model is unable to determine the strains and consequently the stresses in the concrete arch.

Three bridges were recently constructed in Missouri, USA using the new HCB in conjunction with reinforced concrete systems. Due to the uncertain behavior of the HCB, the FE analysis work is fundamental to improving the understanding of the HCB behavior. The finite element modeling of the HCB bridge is unconventional due to the novelty of the

HCB, its unique configuration and its hybrid nature. It is, therefore, the main goals of this study to: examine the accuracy of finite element analysis for predicting the static behavior of the HCB under service loads, provide a better understanding for the HCB structural behavior, and highlight the areas that need more research and investigation.

Bridge 0439 Description

B0439 is the first HCB bridge constructed in the State of Missouri. Its construction was completed in Nov. 2011. B0439 is a three-span bridge. The first and last spans are 18.03 m (59'-2") long, while the middle span is 18.29 m (60'-0"). The overall width of the bridge is 9.35 m (30'-8"). A typical cross-section of B0439 is shown in Figure 1.

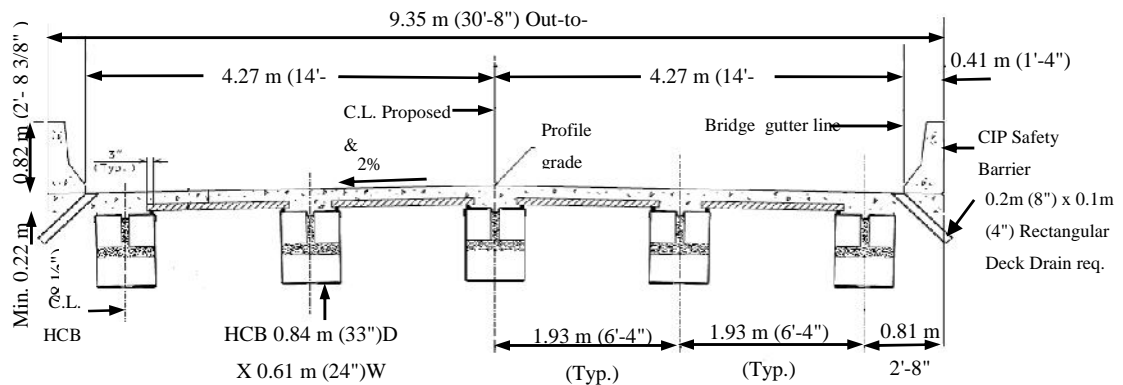


Fig. 1. Typical cross-section of bridge B0439

The bridge consists of fifteen HCBs, five simply supported HCBs in each span. Each HCB is 83.8 cm x 61.9 cm (33-in. x 24.375-in.). The HCB consists of SCC arch with 12.7 cm (5-in.) depth and 55.9 cm (22-in.) width. The concrete arch is reinforced with two 13-mm (1/2-in.) diameter 1,860 MPa (270 ksi), seven-wires, galvanized steel tendons and is tied via thirty six 13-mm (1/2-in.) diameter tendons of the same type. The concrete arch is connected to the upper GFRP flange with SCC web with varying width. The concrete arch is reinforced also with 15 mm (0.625-in.) galvanized shear connectors to

develop composite action between the deck and beam. The voided spaces between the arch and the FRP shell are filled with polyiso foam.

Load Testing of Bridge 0439

A load test of B0439 was carried out by a research team from Missouri University of Science and Technology (MS&T) on March 26, 2012. A Leica total station and 19 prisms were used to measure the deflection along each girder. An additional three prisms were used as control points to make sure the total station did not move during the testing.

Two Missouri Department of Transportation (MoDOT) three-axle trucks were used to perform three stops simulating three different load cases on the first span of the bridge. The front tires load (p1) of the first truck (T-6732) is 6.9 metric tons (15.2 kips) and the rear axle load (P2) is 15.9 metric tons (35 kips); the front load (P1) of the second truck (T-7627) equals 7 metric tons (15.5 kips) and the rear load (P2) equals 14.6 metric tons (32.2 kips). The truck stops, distribution of the rear tires load and the trucks configuration are displayed in Figure 2.

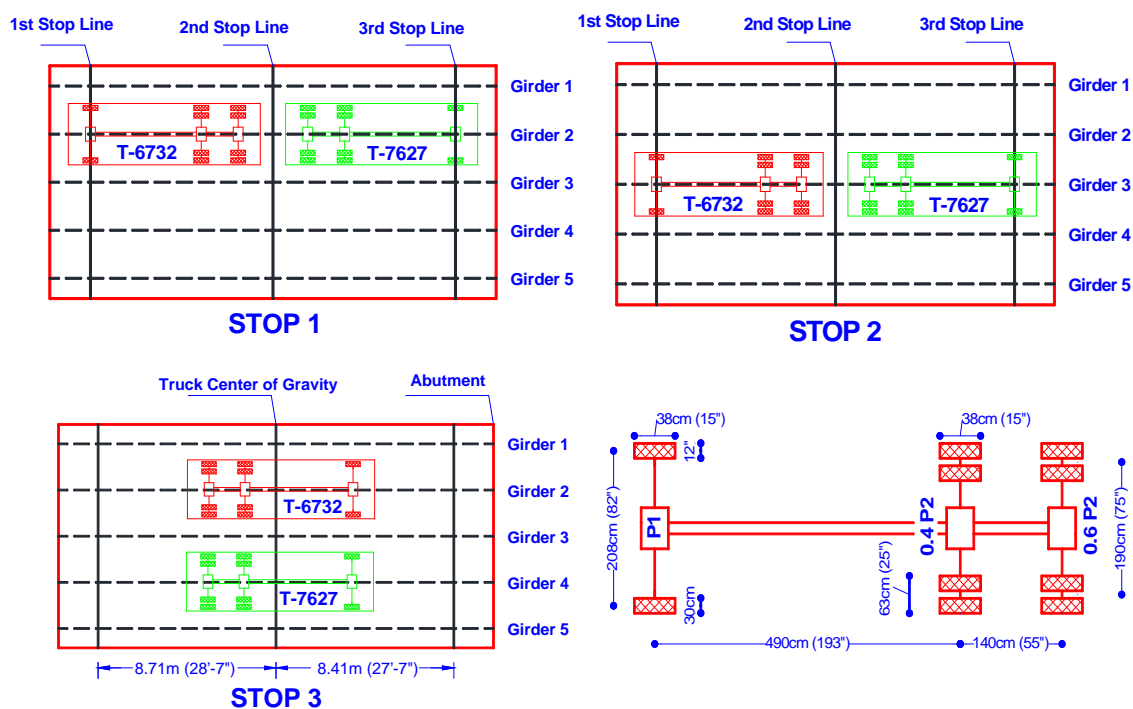


Fig. 2. Truck stop locations and trucks dimensions

FE Modeling of Bridge 0439

Two FE models were constructed to model the superstructure of B0439. A FE model with a very fine mesh was constructed using ANSYS V13.0. This FE model consists of 75032 elements and 54698 nodes. The second FE model has a coarse mesh relative to the first one and was constructed via SAP2000 V14.2. The FE model consists of 13595 elements and 10896 nodes.

The maximum deflection measured during the load test of B0439 was 0.13 cm (0.0508-in.) and occurred at stop 3. This very small value indicated that there is no need to perform nonlinear geometric analysis. It also gave an indication that all the materials may behave within their linear elastic range at service loads. Consequently, the first FE analysis trial represented all of the materials as linear elastic in the two models. The results obtained from the FE models prove that the linear behavior assumption is valid at the service loads. However, the ultimate strength prediction of the HCB requires nonlinear FE analysis.

Material Properties

FRP Composites

The FRP composites are anisotropic materials; that is; their properties are not the same in all directions (Gibson, 2011). However, the unidirectional laminates that have fibers with circular cross-section can be assumed as transversely isotropic, because the properties of these composites are almost the same in any direction perpendicular to the fibers. For transversely isotropic materials, the strain tensor can be related to the stress tensor via the compliance matrix $[S]$ as follows (Lubarda and Chen, 2008):

$$\begin{Bmatrix} V_{xx} \\ V_{yy} \\ V_{zz} \\ X_{xy} \\ X_{xz} \\ X_{yz} \end{Bmatrix} = \begin{bmatrix} S_{11} & S_{12} & S_{12} & 0 & 0 & 0 \\ S_{12} & S_{22} & S_{23} & 0 & 0 & 0 \\ S_{12} & S_{23} & S_{22} & 0 & 0 & 0 \\ 0 & 0 & 0 & S_{44} & 0 & 0 \\ 0 & 0 & 0 & 0 & S_{44} & 0 \\ 0 & 0 & 0 & 0 & 0 & 2(S_{11} - S_{12}) \end{bmatrix} \begin{Bmatrix} \dagger_{xx} \\ \dagger_{yy} \\ \dagger_{zz} \\ \dagger_{xy} \\ \dagger_{xz} \\ \dagger_{yz} \end{Bmatrix} \quad (1)$$

where V_{ii} is the normal strain in the direction i , X_{ij} is the shear strain in the plane ij , \dagger_{ii} is the normal stress in the direction i , \dagger_{ij} is the shear stress in the plane ij , $i, j = x, y, z$ and $i \neq j$. In equation (1), the axis of isotropy is along the X-direction (direction of fibers). Equation (1) indicates that $E_y = E_z$, $\nu_{xy} = \nu_{xz}$, $\nu_{yz} = \nu_{zy}$, $G_{xy} = G_{xz}$, and $G_{yz} = E_y / 2(1 + \nu_{yz})$, and hence resulting in five independent elastic constants, where E_i is the young's modulus in the direction i , G_{ij} is the shear modulus in the plane ij , ν_{ij} is the Poisson's ratio.

The standard laminate composition of the HCB FRP shell is typically a quadweave glass reinforcing fabric infused with a vinylester resin matrix. The woven fabrics used in the FRP shell of B0439 are comprised of multiple layers of glass rovings with varying percentages of the fibers oriented in the 0° , 90° , and $\pm 45^\circ$ directions relative to the longitudinal axis. The multidirectional fabrics can be assumed to have isotropic properties

to simplify preliminary designs. However for more accurate modeling of the shell, it was assumed orthotropic transversely isotropic. The shell's manufacturer performed experimental tests on the shell webs, at the macroscopic level, to identify the elastic constants of the FRP laminate. These tests identified the tensile and the compressive in-plane moduli of elasticity (E_x^+ , E_x^- , E_y^+ , E_y^-), the in-plane shear modulus (G_{xy}), the effective longitudinal compressive and tensile strengths (S_L^+ , S_L^- , respectively), effective transverse compressive and tensile strengths (S_T^+ , S_T^- , respectively), and the effective shear strength (S_{LT}). The test results enable the calculation of only three elastic constants, in order to calculate the remaining two constants, ν_{xy} was assumed 0.26 and ν_{yz} was assumed 0.30 (Kachlakev et al., 2001). A summary for material properties used for modeling the FRP shell is listed in Table 1.

Table 1. Material properties used for modeling the FRP shell

Property	Strength MPa (ksi)	Stiffness GPa (Msi)	Shear Modulus GPa (ksi)
Tensile properties	$S_L^+ = 372(54)$	$E_x^+ = 27.6(4)$	$G_{xy} = 6.3(919)$
	$S_T^+ = 124(18)$	$E_y^+ = 15.7(2.3)$	$G_{xz} = 6.3(919)$
	$S_{LT} = 21(3)$	$E_z^+ = 15.7(2.3)$	$G_{yz} = 3.7(530)$
Compressive properties	$S_L^- = 138(20)$	$E_x^- = 8.96(1.3)$	$G_{xy} = 6.3(919)$
	$S_T^- = 152(22)$	$E_y^- = 9.5(1.4)$	$G_{xz} = 6.3(919)$
	$S_{LT} = 21(3)$	$E_z^- = 9.5(1.4)$	$G_{yz} = 3.7(530)$
Density kg/m^3 (lb/ft^3)	$\rho = 1682(105)$		

Concrete

Concrete is a quasi-brittle material with different compression and tension behaviors. In compression, the stress-strain relation is linearly elastic up to 30% of the maximum compressive strength (Kachlakev et al., 2001). In tension, the stress-strain curve is approximately linearly elastic up to the maximum tensile strength. However, the tensile

and compressive moduli of elasticity are almost the same in the elastic linear range. In B0439, self-consolidating concrete (SCC) was used to form the compression reinforcement of the HCB. SCC is a new category of high-performance concrete, which can flow easily into tight and constricted spaces with minimum or no vibration needed (Khayat, 1999).

The original design documents for the three HCB bridges specified a minimum compressive strength of 41.4 MPa (6 ksi) for the concrete arch in the HCB. However, quality control/quality assurance (QC/QA) tests showed that the compressive strength of the concrete arches of the HCBs used in the second and third bridges (B0410 and B0478) had an average 28 day-compressive strength that was much higher than the specified minimum. Unfortunately, no QC/QA field data was available regarding the compressive strengths of the HCBs used in B0439. In this study, the compressive strength of the HCBs concrete arches was assumed to equal the average of the compressive strength of the HCB concrete arches of the second and third bridges, which is 68.9 MPa (10 ksi). The concrete of the deck was assumed to have an average compressive strength for the precast prestressed panels and the cast in place concrete equals to 41.4 MPa (6 ksi).

(Domone, 2007) analyzed data from more than 70 recent studies on the hardened mechanical properties of SCC to produce comparisons to the properties of equivalent strength normally vibrated concrete (NVC). Domone (2007) concluded that, the design rules and practice for NVC developed over many decades can be used for structures cast with SCC. He also found that the elastic modulus of SCC can be significantly lower than that of NVC at low compressive strengths. Based on Domone (2007) study, the elastic modulus of 70 MPa (10.1 ksi) SCC is about 10% lower than the elastic modulus of NVC with the same strength and as the strength increases the difference decreases, while the modulus of rupture of both types is almost the same. On the other hand, the mix design of the concrete arches of B0439 contained 272 kg (600 lb.) cement and 90.7 kg (200 lb.) fly ash per 0.76 cubic meters (1 cubic yards) and the load testing was performed more than 150 days after casting of the concrete arches. A number of studies have been conducted, to derive models that can predict the compressive strength development of fly ash concrete (Han et al., 2003; Hwang et al., 2004). These studies showed that the average compressive strength of different mixes of fly ash concrete at 150 days is approximately 30% higher than the strength at 28 days. Since the exact value of the compressive strength of the HCBs

concrete arches of B0439 is not known, the elastic modulus and the maximum tensile strength were, conservatively, calculated via the following ACI 318-11 equations (2011) without modifications:

$$E_c = 57000\sqrt{f'_c} \quad (2)$$

$$f_r = 7.5\sqrt{f'_c} \quad (3)$$

where f'_c is the compressive strength of concrete, f_r is the modulus of rupture of concrete, and E_c is the elastic modulus. In equations 2 and 3 E_c , f_r , and f'_c are in psi.

Steel Reinforcement

Two types of reinforcement bars were used in B0439. Typical steel reinforcing bars were used in the deck, while seven wires, conventional prestressed concrete strands (1,860 MPa class) (Grade 270) were used in the HCBs. Both types were assumed to have identical behavior in tension and compression. The high strength tendons were assumed to have Young's modulus equal to 196,500 MPa (28,500 ksi), while the typical steel bars are assumed to have a Young's modulus equal 199,948 MPa (29,000 ksi). The two types were assumed to have 0.3 Poisson's ratio and 7849 kg/m³ (490 lb/ft³) density.

Polyisocyanurate Foam

Polyiso foam is a 32 kg/m³ (2.0 lb/ft³), rigid, closed cell foam supplied as blocks with 61 cm (24-in.) width. The tensile and compressive elastic moduli, and the shear modulus were provided by the manufacturer in the longitudinal and perpendicular directions. In this study, the foam was assumed to behave as transversely isotropic material. Poisson's ratios ν_{yz} were calculated based on the provided moduli, while ν_{xy} and ν_{xz} were assumed to be 0.33 (Friis et al., 1988). A summary for material properties used for modeling the polyiso foam is listed in Table 2.

Table 2. Material properties used for modeling the Polyisocyanurate Foam

Property	Elastic Modulus kPa (psi)	Poisson's ratio	Shear Modulus kPa (psi)
Tensile properties	$E_x^+ = 8440(1225)$	$\nu_{xy} = 0.33$	$G_{xy} = 1516(220)$
	$E_y^+ = 3190(463)$	$\nu_{xz} = 0.33$	$G_{xz} = 1516(220)$
	$E_z^+ = 3190(463)$	$\nu_{yz} = 0.308$	$G_{yz} = 1219(177)$
Compressive properties	$E_x^- = 4823(700)$	$\nu_{xy} = 0.33$	$G_{xy} = 1516(220)$
	$E_y^- = 2301(434)$	$\nu_{xz} = 0.33$	$G_{xz} = 1516(220)$
	$E_z^- = 2301(434)$	$\nu_{yz} = 0.226$	$G_{yz} = 1219(177)$

Element Types and Model Simplifications

Hybrid Composite Beam (HCB)

Since the GFRP shell of the HCB has very small thickness relative to its length and width, it was modeled using two-dimensional space elements; shell181 element in ANSYS and traditional shell element in SAP2000. Both elements are four-node elements with six degrees of freedom (DOFs) at each node. Shell 181 element in ANSYS is based on first-order shear deformation theory. In SAP2000 model, thick-plate formulation is selected for the traditional shell element. This formulation was selected because it includes the effects of transverse shearing deformation. The compressive FRP properties were assigned to FRP webs and upper flange elements while the tensile FRP properties were assigned to the lower flange elements. The concrete web was also modeled using shell181 element in ANSYS and traditional shell element in SAP2000.

The concrete arch was modeled using solid65 element in ANSYS and traditional solid element in SAP2000. The polyiso foam was modeled using solid185 element in ANSYS and traditional solid element in SAP2000. Solid elements in both models are defined by eight nodes, each node has three translational DOFs. Foam tensile properties were assigned to the elements below the concrete arch, while the compressive properties were assigned to the elements above the concrete arch. For the upper and lower foam, axis of isotropy was taken along the gravity direction (y-dir. in ANSYS and z-dir. in SAP2000).

The HCB strands are modeled using beam188 element in ANSYS and traditional beam element in SAP2000. The tension reinforcement lies directly on the lower FRP flange. Previous experimental tests performed by Snape and Lindyberg (2009) showed that, due to the simultaneous infusion with resin, there is perfect bond between the strands and the lower flange resulting in the strands reinforcing the bottom flange. However, recent experimental test executed by the authors on B0410 showed a significant difference in the strains of the two elements, indicating that they have indicated slip/separation from each other (Earley et al., 2013). Consequently, the bridge under study (B0439) is conservatively assumed to have strain incompatibility between the strands and the lower flange, similar to B0410. Since the strands are modeled using one-dimensional space elements in both models, if they are modeled directly on the lower flange, the flange will behave as if it is reinforced with these strands. In order to achieve the strain incompatibility assumption between the two components, the strands were modeled in two layers separated from the lower flange and from each other with 1.27 cm (0.5-in.). Modeling the 36 strands via 36 separate beam elements would complicate the meshing; consequently, the 36 strands were represented by 6 beam elements, 3 per each layer. The total cross-sectional area of the 6 beam elements is equal to the area of the 36 strands.

Based on experimental testing, it is found that the shell webs are stiffened by a resin bond to both the concrete arch and polyiso foam (Hillman, 2003). This bond allows the webs to reach the allowable shear strength of the GFRP within the service load limits without suffering elastic buckling. It is, therefore, acceptable to assume perfect bond between the shell webs with the compression reinforcement and the polyiso foam. Generally, a perfect bond between all the components of the HCB is assumed in the FE analysis of B0439. This was achieved in the two FE models by maintaining the same mesh for all the constituents. Maintaining the same mesh guaranteed that the joints of any component coincide with the joints of other components that are in intimate contact with this component, consequently achieving the assumption of the perfect bond. The HCBs of bridge B0439 were manufactured with an initial 13.34 cm (5.25-in.) camber to equilibrate the downward deflection of the beams when subjected to the full dead loads. This camber was presented in the FE models. Figure 3 displays the finite element modeling of HCB using SAP2000.

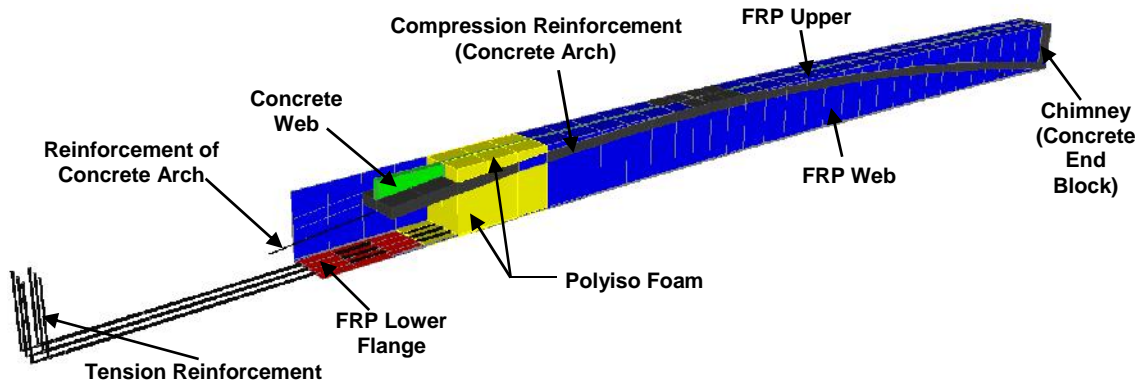


Fig. 3. FE modeling of hybrid-composite beam using SAP2000 V14.2

Bridge Deck

The bridge slab was modeled using solid65 element in ANSYS and traditional solid element in SAP2000. Two solid elements were used throughout the slab depth, to allow modeling of the reinforcement bars. The reinforcement bars in longitudinal and transverse directions were modeled using beam elements in both models. The parapet was poured simultaneously with the slab, and its reinforcement extended in the deck. A previous study by Myers et al. (2008) showed that when a composite action is achieved between the slab and the parapet, the deflection is significantly decreased. Consequently, the parapet was included in the FE models and simulated using solid65 element and traditional solid element in the ANSYS and SAP2000 respectively. Although, some states do not allow taking into consideration the contribution of the parapet to the stiffness of the bridge superstructure, representing the parapet in the FE models aimed to simulate the actual behavior of the bridge superstructure and allow realistic comparison between the measured and predicted data. A previous study (Hillman 2008) proved that the shear connectors of the HCB achieve full composite action between the bridge deck and the HCBs. In the FE

analysis, a perfect bond is assumed between the deck components and between the deck and the HCBs. Figure 4 displays modeling of B0439 superstructure in ANSYS.

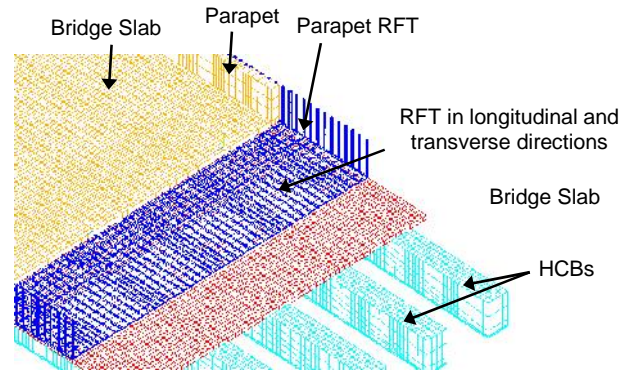


Fig. 4. Modeling of the bridge deck and the HCBs in ANSYS

Load Modeling

A time dependent analysis was performed to account for the stress history of the HCBs resulting from casting the concrete arch and the bridge slab in addition to the dead and live loads. The time dependent analysis was performed through three stages:

Stage 1: In this stage, the permanent stresses induced in the strands and the GFRP shell, due to pouring the concrete arch, were calculated. Consequently, the HCB was modeled without the concrete arch and web. The self-weight of the HCB components were included in the analysis, while the weight of the concrete arch and web were applied as distributed load on the upper face of the lower foam elements (the foam below the concrete arch). Neither the dynamic effects nor the lateral stresses that may occur during pumping the concrete were included in the analysis because these stresses are considered to be temporary.

Stage 2: As it is shown in Figure 1, B0439 incorporated the use of precast stay-in-place deck forms to expedite the construction process. Consequently, the deck was not shored during the construction. This stage calculated the stresses induced in the complete HCB due to casting the bridge slab and barriers. This is achieved by applying the weight

of the bridge slab and barriers as uniform distributed load on the upper FRP shell elements. The self-weight of the HCB components was not included in this stage, since it was considered in the first stage.

Stage 3: In this stage, complete models for B0439 superstructure were constructed. Only the wearing surface weight, which was assumed 2.54 cm (1-in.), and the truck loads were applied on the composite section. Both the dead and live loads were applied as uniform pressure on the upper surface of the slab elements. The tire loads were modeled as distributed loads instead of point loads, because using 3D elements is non-consistent with the concentrated loads. When applied to 3D elements, the concentrated loads may result in a stress singularity, as the element size become smaller and smaller as the stress increases and tends to infinity, hence mesh convergence cannot be achieved.

Finally, linear superposition was performed between the three stages to obtain the total stresses induced in the different constituents of the HCBs. The principle of the superposition was used because the HCBs did not undergo large deformations in all the three stages and the different materials were found to behave within their linear elastic ranges. Moreover, the total maximum stresses obtained from the time dependent analysis, which will be presented later, were found within the elastic ranges of all the materials.

Boundary Conditions

The HCBs of B0439 are supported on the bridge piers through steel-laminated neoprene bearing pads, each of which are 20.3 cm X 55.9 cm X 1.9 cm (8-in X 22-in X 3/4-in). Generally, the elastomeric bearing pads are designed to allow horizontal deformations of the beams due to thermal changes, applied loads and time-dependent concrete changes. For that reason, it is common to model bridge girders as simply supported beams that have a pin support at one end and a roller support at the other end. However many researches proved that the actual bridges are stiffer than their theoretical models due to neglecting the restrained forces at the beam-pad interface. Tests on twenty six bridges in Canada proved that bridges are generally stiffer than theoretical assumptions (Yazdani et al. 2000). Yazdani et al (2000) predicted translational and rotational stiffness values that can simulate the bearing restraint effect. The predicted stiffnesses were found to be very close to the calculated stiffnesses based on AASHTO specifications (1996). However, when they used

the calculated stiffnesses during finite element modeling of prestressed I-beam bridge in Florida, USA, the maximum deflection and tensile strain at mid span were found to be significantly larger than the measured values. Even when the bearing pad was assumed to have shear modulus equals 25 times the maximum shear modulus that is required by the AASHTO specifications to simulate the effect of aging and cold, the maximum deflection and maximum tensile strain were found to be higher than the field test data by about 19% and 25% respectively.

Based on the previous studies, it is thought that modeling the HCB using pin supports at each end may provide more realistic predictions for the deflections. Consequently, pin supports were applied to the lower flanges at the locations of the bearing pads. Due to the continuity of the bridge slab, the edge of the slab over the interior bent is restrained from translation and rotation in all directions. While over the abutment, the edge of the slab is restrained from translation in all direction.

The bridge incorporated the use of concrete diaphragms that span between the HCBs ends and rested directly on the interior and exterior bents. These diaphragms were simulated by applying supports that restrain the lateral translation of the HCBs at the contact areas between the diaphragms and the beams.

Theoretical Calculations

In order to calculate the deflection of the HCBs, the first step is to define the beam stiffness. In calculating the section properties of the HCB, two factors should be considered. The first factor is the different constitutive properties of the different materials used. Hillman's design methodology (Hillman, 2003; Hillman, 2012) uses the transformed area technique to transform the different constituents of the HCB to equivalent amounts of the GFRP of the webs. The other factor is the fact that the HCB sections are not prismatic along the length of the beam due to the parabolic profile of the concrete arch. As a result, Hillman's model calculates the section properties at 1/10th points along the beam length. Hillman proposed that his model is sufficient only for simply supported structures under conventional live loads. The HCBs of B0439 are simply supported. However, the deck is continuous over the three spans. In this study, the efficiency of a mathematical algorithm, similar to Hillman's model, to detect the deflection in B0439 is tested.

Hillman's methodology accounts for the composite properties of the HCB with the concrete deck. However, the model ignores the foam, concrete web and the reinforcement bars of the deck during the calculations. In the present study, these components were included in the calculations and the section properties were calculated at 1/20th points along the beam length.

The calculation of the beam stiffness starts with calculating the transformation factor, modular ratio, n_i

$$n_i = \frac{E_i}{E_w} \quad (4)$$

where E_w is the modulus of elasticity of the FRP web and E_i is the modulus of elasticity of the constituent i that need to converted to equivalent amount of GFRP.

The FE analysis validated the assumption that all the materials behaved within their elastic range under the test loads. It also clarified that the concrete did not crack under these loads. Subsequently, the beam's moment of inertia at each section was calculated based on the elastic neutral axis (ENA) location at that section. The moment of inertia at each section can be determined by equations (5) through (7) as follows:

$$A_{ij}(x) = n_i \times A_j(x) \quad (5)$$

$$\bar{y}_j(x) = \frac{\sum_{i=1}^n A_{ij}(x) \cdot y_{ij}(x)}{\sum_{i=1}^n A_{ij}(x)} \quad (6)$$

$$I_j(x) = \sum_{i=1}^n \left(I_{ij}(x) + A_{ij}(x) \left(y_{ij}(x) - \bar{y}_j(x) \right)^2 \right) \quad (7)$$

where $A_{ij}(x)$ = cross-sectional area of the component i at section j , $A_{tij}(x)$ = transformed area of the component i at section j , $y_{ij}(x)$ = distance from the center of gravity (CG) of the component i to the extreme lower fiber of the beam at point j , $\bar{y}_j(x)$ = distance from the ENA of the composite section to the extreme lower fiber of the beam at section j , $I_{ij}(x)$ = transformed moment of inertia of the component i with respect to its CG at section j , $I_j(x)$ = moment of inertia of the composite section at section j , n is the total number of HCB components and $j = 1, 2, \dots, 21$. In this work, a MATLAB R2012a code was constructed to calculate the stiffness of the HCB at each section.

The second step in calculating the deflection is identifying the load distribution factor for each girder under the applied loads. In this study, the lever rule provided by AASHTO LRFD (2012) was used to determine the load distribution factors for the exterior HCBs. While the load distribution factor, g , for the interior beams was determined by the following AASHTO (2012) equations:

$$g = \left(\frac{S}{3.0} \right)^{0.35} \left(\frac{Sd}{12.0L^2} \right)^{0.25} \quad (8)$$

$$g = \left(\frac{S}{6.3} \right)^{0.6} \left(\frac{Sd}{12.0L^2} \right)^{0.125} \quad (9)$$

where S = spacing of the beams in feet (1 ft = 304.8 mm); d = depth of the beam in inches (1 in. = 25.4 mm), and L = span of beam in feet. Eq. (8) was used when one lane was loaded, while eq. (9) was used when two lanes were loaded. Eq. (8) includes the multiple presence factor for loading one-lane (which is 1.2). Consequently, it was divided by 1.2 to allow realistic comparison with the applied loads.

Finally, the deflection was calculated by modeling each HCB in SAP2000 using twenty non-prismatic elements.

Results Discussion

A sample of the experimental measured deflections and the predicted deflections by the two FE models and theoretical calculations is given in Figure 5. The deflection was measured and predicted at the quarter, mid and three quarter points of each girder span. Generally, the results demonstrate a good agreement between the two FE models predictions and the field measured data and an excellent agreement between the two FE models results. The differences between the measured data and the FE analysis predictions can be attributed to the common error sources such as the deviation of the real dimensions of the bridge elements from the dimensions provided by the drawings, FE model assumptions and simplifications, unknown material properties and experimental errors.

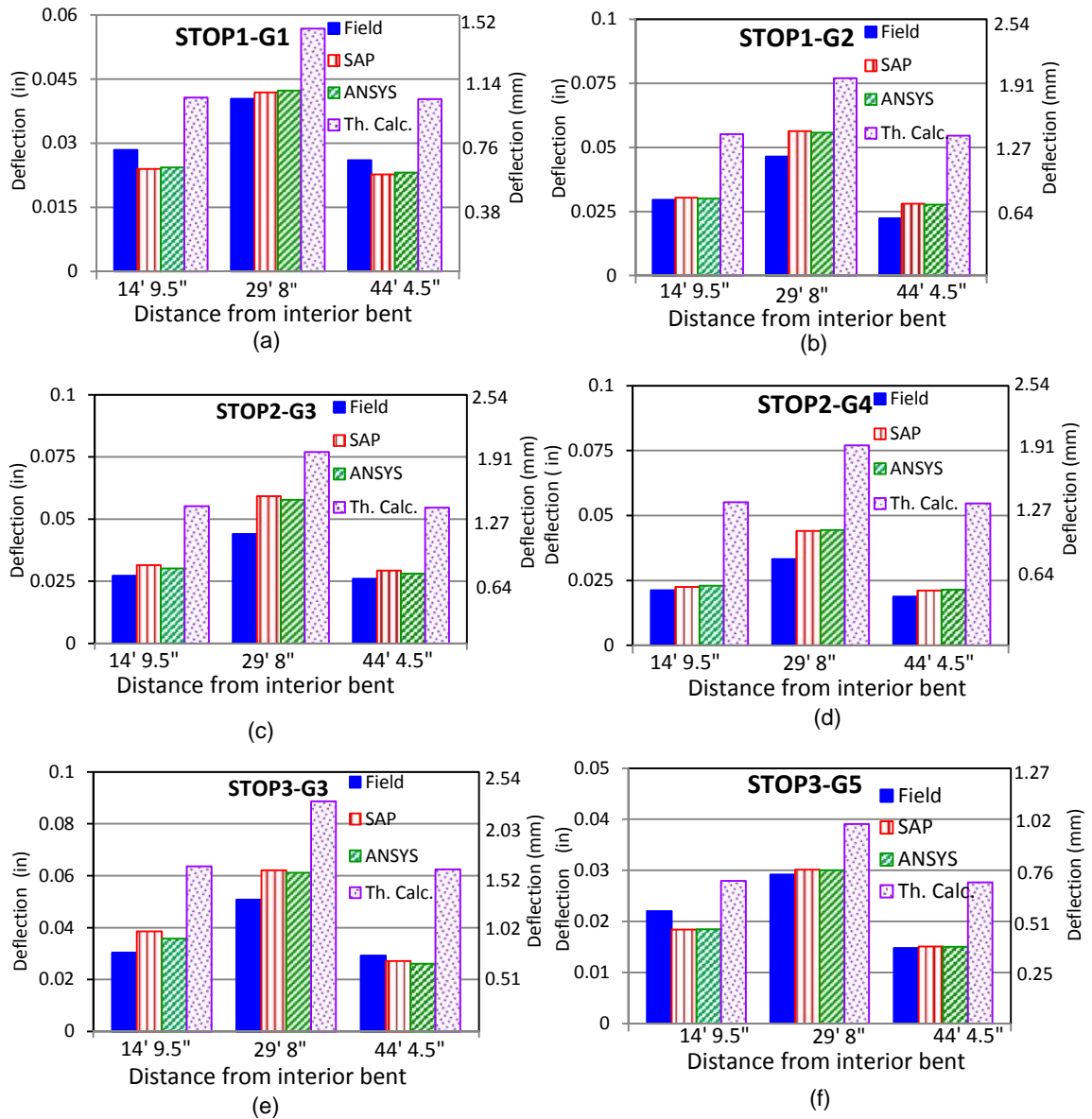


Fig. 5. Comparison of the bridge 0439 deflections measured at field and predicted by ANSYS, SAP2000 and theoretical calculations

In a previous study, Myers et al. (2008) found that the experimental errors in bridges field tests led to the following deflection deviations: a transverse shift in the truck stop location by 30.48 cm (12-in.) changed the deflection by 10%, a longitudinal shift in the truck stop location by 30.48 cm (12-in.) changed the deflection by 5%, 2.27 metric tons (5 kips) error in truck weight reporting altered the deflection by 7%. They also concluded that the sensitivity of the total station equipment is ± 0.013 cm (0.005-in. Some of these errors were incarnated in stop 2. As it is shown in Figure 2 the two trucks loads are symmetric about the longitudinal centerline of the bridge, consequently deflections are expected to be the same along girders 1 and 5 as well as girders 2 and 4. However, the experimental data revealed that the average deflections through girder 2 (G2) were larger than those through G4 by an average value of 28% and that the average difference between G1 and G5 measurements was 12%, indicating that the two trucks shifted transversely toward G1 and G2.

Figure 5 clarifies that the two FE models overestimated the deflection at the mid-span of the five girders in all of the stops. In addition to the aforementioned error sources, the thermal changes effect is another suspected factor that may contribute to the overestimation of the mid-span deflection. The bottom surfaces of the HCBs are not only close to the river surface but also unexposed to the sun, which may reduce their temperature. In contrast, because the deck is exposed to the sun during the daytime, subsequently it can gain temperature from the sun's radiation. This thermal ingredient causes upward deflection, consequently reducing the total deflection at mid-span. According to Radolli and Green (1976), the stresses induced through the depth of the structure due to diurnal cycles can, in some instances, exceed the live loading. Initial and final measurements were recorded by the total station for the bridge, without the trucks loads, at morning and afternoon, respectively. The measurements showed that at the final no-load test the HCBs suffered negative deflections at all the prisms' locations with deflection equals -0.23 mm (-.009-in.) at the mid-span of G3. This indicates that maximum deflection in the last stop was reduced by about 15%. However, since the temperatures of the different superstructure elements were not measured at the time of each load test, a correction for the thermal effects could not be performed.

The average difference between the measured deflections and the ANSYS FE model results was found 15.8%, while the average difference between the field deflections and the SAP2000 FE model results was found 16.5%. The ANSYS FE model overestimated the maximum deflection resulted at the mid-span of G3, under stop 3 loads, by 21%, and the SAP2000 FE model overestimated the maximum deflection by 22%. These results validate the modeling assumptions and simplifications and demonstrate that the linear FE analysis predicted the behavior of the hybrid composite superstructure of B0439 under the applied service loads with acceptable accuracy; hence, it can be used to analyze the HCB behavior.

The results presented in Figure 5 demonstrate that the theoretical calculation procedure highly overestimated the deflections in the three load cases. The theoretical method predicted higher deflections than those predicted by the FE analysis and consequently than the measured data for several reasons. First, the tire loads were distributed to all the bridge girders using the load distribution factors and the lever rule provided by AASHTO LRFD (2012). The sum of the load distribution factors of the five girders was found to exceed 100% in all of the stops. For example in stop 3, the sum of the load distribution factors was 1.1, which means that the applied loads to the girders exceeded the real ones by 10%. Second, the theoretical procedure ignores the effect of the parapet on the deflection. Similar to what was observed by Myers et al. (2008), it was found in this study that the parapet significantly reduces the deflections of the bridge girders. The effect of the parapet was found to be dependent on the load and girder locations. When the bridge was modeled by ANSYS without including the parapets, G1 suffered deflections higher than the deflections of the original FE model by 59%, under stop1 loads. This difference reduced gradually as we moved inward until almost no difference was observed on the deflections of G4 due to removing the parapets from the model. In stop 3, it was found that after excluding the parapets, the average deflections of G1 and G5 increased by about 49%, the average deflections of G2 and G4 increased by 15%, and the average deflections of G3 increased by 8%. Similar differences to those observed due to stop 3 were occurred under stop 2 loads. These differences are based on the average deflection of the quarter, midspan and three quarter points, but the differences of the maximum deflections at the midspan points were higher than the mentioned values. Third, the HCB

was simulated in the theoretical calculations by beam elements, while, it was modeled in the FE analysis by a combination of solid elements, shell elements and beam elements. Since the beam element is more flexible than the shell and solid elements, it is expected that the predicted deflections by the theoretical analysis will be higher than the actual ones. Finally, in the theoretical analysis, the continuity of the slab over the interior bent was not considered, while in the FE model, fixed supports were applied to the slab edge over the pier to account for deck continuity.

Consequently, the mathematical procedure, which was implemented in the current study, can be used as a simple method for the preliminary design of the HCB in continuous structures. While for more accurate prediction of the HCB deflection in continuous structures, a sophisticated analysis is recommended. It is worth mentioning that the complex FE models constructed in this study aimed to predict the stresses in the different components of the HCB and analyze its structural behavior. However, the authors believe that a simpler FE model can predict the deflection of the HCB in the continuous structures with acceptable accuracy.

Since the design of the HCB is stiffness-driven, a study was performed to examine the accuracy of the design/analysis of HCB in case of assuming isotropic properties for the FRP and polyiso foam. In this study, the FRP and foam were assumed isotropic materials with different moduli of elasticity in compression and tension equal to E_x^- and E_x^+ listed in Tables 1 and 2, respectively. The study illustrated that this simplification can result in a deviation of the deflection calculations not more than 10% in stage 1, 7.5% in stage 2, and 5% in stage 3. These results validate that it is acceptable to assume isotropic behavior for the multidirectional FRP and polyiso foam to simplify preliminary design/analysis of the HCB.

Structural Behavior Analysis

The stresses obtained by the two FE models were similar to each other; however, the stresses obtained by the ANSYS model were found higher than those obtained by the SAP2000 model. This can be attributed to the difference in mesh densities between the both models. Because the ANSYS model has finer mesh, all stress results presented in the following sections were extracted from this model. The presented stresses of the different

HCB components are the major stresses in the longitudinal direction of the beams (X-direction). These stresses are the stresses induced in G3 due to the total loading of the three stages with stop 3 loads included in the third stage. This stop was found to produce maximum stresses among the three stops.

The maximum compressive stress induced in the concrete arch of G3 was found 14.2 MPa (2060 psi) which is less than 30% of the compressive concrete strength of 68.9 MPa (10 ksi). Stage 3 loads induced tensile stresses in the concrete arch. However, when these tensile stresses were added to the stresses resulted from stage 2 loading, the arch was found to be subjected to pure compressive stresses. The maximum stress in the tensile reinforcement of the HCB was found to be 37.8 MPa (5480 psi), which is much lower than the yield stress of the tendons. The maximum compressive stress in the lower FRP shell was 27.4 MPa (3980 psi) and the maximum tensile stress was 12.9 MPa (1875 psi), which are much lower than the effective longitudinal tensile and compressive strengths of the GFRP given in Table 1, respectively. The stresses in the FRP upper flange and webs were found lower than the stresses in the lower flange, while the maximum shear stress in the FRP shell was 9.0 MPa (1300 psi). This occurred in the shell web as it was expected. About 80% of this stress occurred during stage 1, while after hardening of the concrete arch; significantly, lower shear stresses took place in the web. The stresses in the bridge deck were also found to be within the elastic range of the concrete and reinforcement bars. These values assured that all of the materials behaved within their linear elastic ranges. They also indicate that the total loads of the three stages are much lower than the HCB's capacity. The maximum measured deflection 0.127 cm (0.05-in.) due to stop 3 is much lower than the allowable live load deflection provided by the AASHTO (2012) of span length/800, which is 2.25 cm (0.89-in.). This is compatible with the stress indication that the applied loads are much lower than the ultimate capacity of the HCBs.

A study was performed to compare between, the HCB behavior under the actual truck loads used in the implemented load testing, and the notional loads recommended by AASHTO (2012) for the optional live load deflection evaluation. The study started by identifying the design truck axels spacing, the trucks orientations in the longitudinal and transverse directions of the bridge, and the load case that produce maximum deflection. The results clarified that two design trucks with all axels spaced 4.27 m (14'-0"), oriented

symmetrically about G3 in the transverse direction, produce maximum deflection in G3. The total load of one design truck, including the dynamic load allowance, is 43.5 metric tons (95.8 kip), which is about twice the average load of the trucks used in the load test. However, the HCB was found to still behave within the elastic ranges of its constituents. The maximum tensile stress in the concrete arch due to the fictitious truck loads in addition to the second stage load was found to be 248 kPa (36 psi), which is much lower than the modulus of rupture of the concrete. This small stress indicates that the HCB can maintain the gross section properties under significantly higher loads than the notional loads provided by AASHTO (2012). The maximum deflection predicted by the ANSYS model due to the design trucks loads was found to be 3.8 mm (0.15-in.). This deflection is also much lower than the allowable live load deflection provided by AASHTO (2012).

Figure 6 shows the locations of the maximum tensile and compressive stresses in the concrete arch of G3 due to the loads of stages 2 and 3. In stage 2, the maximum compressive stress took place close to the junction of the arch with the chimney. Since, the non-composite HCB is simply supported, according to the current design methodology by Hillman, a small bending moment close to zero is supposed to occur at this location. Moreover, the location of the maximum compressive stress is below the ENA of the HCB. Consequently, a very small tensile stress is expected to take place at this location. This location of the maximum compressive stress in the arch is compatible with the literature (Ahsan, 2012) and contradicts the current design methodology. While in this stage, the maximum tensile stress was found to occur at the concrete web close to the junction of the concrete web with the chimney. These results indicate that, though the non-composite HCB is simply supported, negative bending moment might take place at the end of the beam. The maximum compressive stress in the concrete arch not only took place at the lower extreme fiber but also was higher than the compressive stress at the extreme upper fiber of the arch at the same location. Moreover, the stress in the upper FRP flange at this location was found to be tensile stress, while the stress in the lower FRP flange at this location was found to be compressive one. These results support that the moment at the end of the HCB is in fact negative. An explanation of this behavior is that the chimney provides partial fixation to the beam resulting in negative moment at its end.

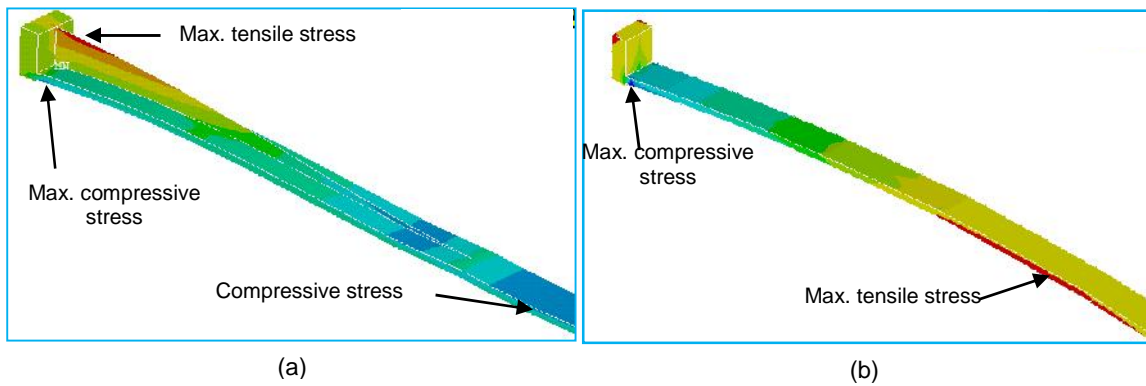


Fig. 6. The maximum tensile and compressive stresses locations in the HCB concrete arch of G3 due to a) stage 2 loading b) stage 3 loading

In stage 3, the results also indicated that there is negative moment at the end of the beam. During this stage, the maximum tensile stress occurred close to the midspan at the lower fiber of the arch. Figure 7 displays the stresses in the lower FRP flanges of all the girders under stage 3 loads. The compressive stresses are displayed with the grey color in the ANSYS model and with the purple color in the SAP model. Compressive stresses induced in the lower FRP flange in the three stages at the same locations as in Figure 7. It is clear from this figure that significant portions of the lower flanges were subjected to compressive stresses, According to the current design methodology, it is expected that all the lower flanges be subjected to tensile stresses only.

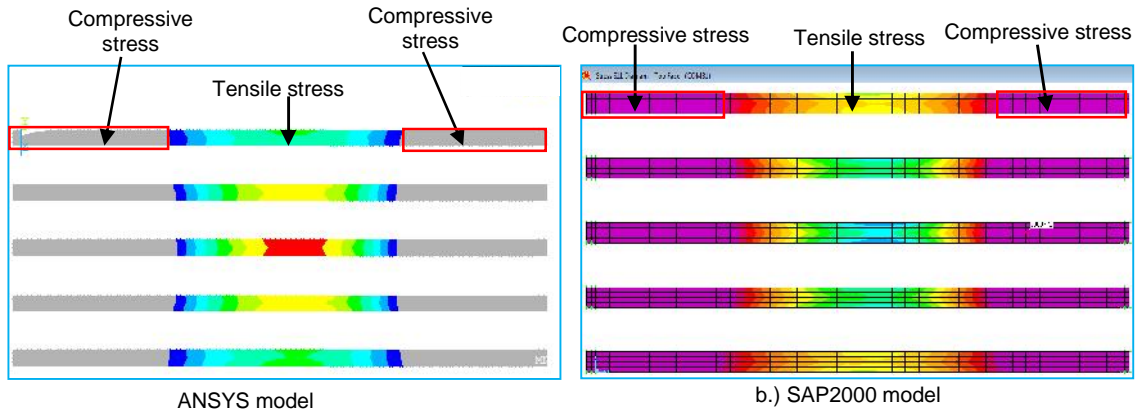


Fig. 7. Stresses in the lower FRP flanges of all the girders due to stage 3 loading

To verify these results a comprehensive study was performed in which the HCB was modeled individually and as a framing system in B0439. The HCB was modeled in each case with two boundary conditions; hinge-hinge, and roller-hinge. Finally, the HCB was modeled individually with camber and without camber. In all the cases, the concrete arch and the lower FRP shell under different applied loads suffered stresses similar to what illustrated by Figures 6 and 7.

The findings of this paper indicate that the current design methodology may need some refinements. An experimental investigation is recommended to assure the stress results obtained from the FE models. Regardless the design methodology and assumptions, the results proved that the classic arch shape optimizes the use of the concrete and preserves the HCB overall stiffness under the service loads.

The FE models results showed that the HCBs underwent lateral and rotational deformations under the vertical truck loads of the three stops. The value of the maximum lateral displacement occurred in FRP webs in G1 and G5 and was found approximately 20% of the maximum vertical deflection in the three load cases. Because, this may indicate that the HCB has weak lateral and torsional stiffness, field measurements need to be performed to verify the FE models observation. Figure 8 displays the lateral and rotational deformations of the HCBs due to stop 3 loads.

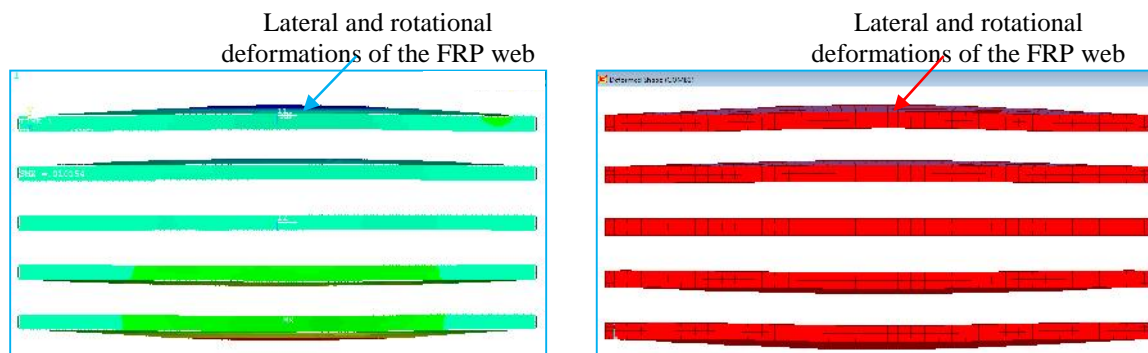


Fig. 8. Exaggerated deformed shape of HCBs due to stop 3 loads

An analytical study was performed to identify the contribution of the polyiso foam to the lateral stiffness of the HCB. When the foam was removed from the HCBs, the FRP webs underwent very large deformations. Consequently, the exact contribution of the foam to the lateral stiffness could not be precisely determined. Nevertheless, this study proved that the foam plays an important role for the stability of the FRP shell because it prevents the local buckling of the FRP webs and provide lateral stability to them.

Conclusions and Recommendations

This paper studied the structural behavior of a new type of the HCB that has been recently used in the construction of three bridges in Missouri, USA. Two FE models were constructed for bridge 0439 superstructure using the commercial packages ANSYS V13 and SAP2000 V14.2. The FE models demonstrated that the linear FE analysis can predict the behavior of the HCB under service loads with acceptable accuracy. A simple analytical procedure, based on the transformed area method, was found significantly conservative in predicting the HCB's deflection. This can be mainly attributed to ignoring the continuity of the bridge deck. However, it can be used as a simple conservative method during the preliminary design/analysis of the HCB in continuous structures.

The FE analysis proved that the classical arch shape of the compression reinforcement optimizes the use of the concrete and preserves the overall stiffness of the HCB under service loads. The maximum measured deflection due to different load cases is found less than 6% of the permissible live load deflection provided by AASHTO LRFD

(2012). The numerical simulation illustrated that the maximum deflection due to the notional loads provided by AASHTO LRFD (2012) is expected to be approximately 17% of the permissible live load deflection. These deflections and the predicted stresses clarify that the HCB possesses a sufficient flexural and shear rigidity that avoids excessive deflections under service loads. In addition, the low stress carried by the FRP shell under the service loads, maintains the ability for long-term durability of the shell, hence increasing the lifetime of the HCB as a whole.

Although the HCB seems to be a promising technology in the bridge applications, this study suggests that the current design methodology of the HCB has room for improvement and may need refinements. It also points out that the HCB may suffer lateral and rotational deformations under the vertical loads. Experimental investigations are recommended to verify these theoretical observations.

Acknowledgements

The authors would like to acknowledge the Missouri Department of Transportation (MoDOT) and the National University Transportation Center (NUTC) at Missouri S&T for sponsoring this research study. The staff support from the Dept. of Civil, Architectural and Environmental Engineering and Center for Infrastructure Engineering Studies (CIES) at Missouri S&T are also greatly appreciated.

REFERENCES

- AASHTO. (1996). *Standard specifications for highway bridges*, American Association of State Highway and Transportation Officials, Washington, DC.
- AASHTO, LRFD. (2012). *AASHTO LRFD bridge design specifications*, American Association of State Highway and Transportation Officials, Washington, DC.
- ACI. (2011). *Building Code Requirements for Structural Concrete (ACI 318-11) and Commentary*, American Concrete Institute.
- Ahsan, S. (2012). "Evaluation of Hybrid-Composite Beam for Use in Tide Mill Bridge." M. S. thesis, Virginia Polytechnic Institute and State University, Blacksburg, VA.
- Ansys 13.0. [computer software], Canonsburg, PA, Ansys.
- Bank, L. C. (2006). *Composites for construction: Structural design with FRP materials*, John Wiley & Sons Inc., Hoboken, New Jersey, pp.1-27.
- Deskovic, N., Triantafillou, T. C., and Meier, U. (1995). "Innovative design of FRP combined with concrete: short-term behavior." *Journal of Structural Engineering*, Vol. 121, No. 7, pp. 1069-1078.
- Domone, P. L. (2007). "A review of the hardened mechanical properties of self-compacting concrete." *Cement and Concrete Composites*, Vol. 29, No. 1, pp. 1-12.
- Earley, C. R., Aboelseoud, M. A., and Myers, J. J. (2013). "Early-Age Behavior and Construction Sequencing of Hybrid Composite Beam (HC Beam) Bridges in Missouri, USA." FRPRCS-11 – 11th International Symposium on Fiber Reinforced Polymer for Reinforced Concrete Structures, Guimarães, Portugal (CD-ROM).
- Friis, E. A., Lakes, R. S., and Park, J. B. (1988). "Negative Poisson's ratio polymeric and metallic foams." *Journal of Materials Science*, Vol. 23, No. 12, pp. 4406-4414.
- Gibson, R. F. (2011). *Principles of composite material mechanics*, Taylor & Francis Group, Boca Raton, FL, pp. 64-84.
- Han, S. H., Kim, J. K., and Park, Y. D. (2003). "Prediction of compressive strength of fly ash concrete by new apparent activation energy function." *Cement and Concrete Research*, Vol. 33, No. 7, pp. 965-971.
- Hillman, J. R. (2003). "Investigation of a Hybrid-Composite Beam System." High Speed Rail IDEA Program, Transportation Research Board of National Academies, Chicago, HSR Project Report 23.

- Hillman, J. R. (2008). "Product Application of a Hybrid-Composite Beam System." IDEA Program Final Report, Transportation Research Board of National Academies, Chicago, HSR - 43.
- Hillman, J. R. (2012). "Hybrid-Composite Beam (HCB®) Design and Maintenance Manual." The Missouri Department of Transportation, Mo.
- Hwang, K., Noguchi, T., and Tomosawa, F. (2004). "Prediction model of compressive strength development of fly-ash concrete." *Cement and Concrete Research*, Vol. 34, No. 12, pp. 2269-2276.
- Kachlakev, D., Miller, T., Yim, S., Chansawat, K., and Potisuk, T. (2001). "Finite element modeling of reinforced concrete structures strengthened with FRP laminates." Final Report SPR. 316: 2001.
- Keller, T. (2002). "Overview of fibre-reinforced polymers in bridge construction." *Structural Engineering International*, Vol. 12, No. 2, pp. 66-70.
- Khayat, K. H. (1999). "Workability, testing, and performance of self-consolidating concrete." *ACI Materials Journal*, Vol. 96, No., pp. 346-353.
- Lubarda, V. A., and Chen, M. C. (2008). "On the elastic moduli and compliances of transversely isotropic and orthotropic materials." *Journal of Mechanics of Materials and Structures*, Vol. 3, No. 1, pp. 153-171.
- Mirmiran, A. (2001). "Innovative combinations of FRP and traditional materials." *FRP Composites in Civil Engineering, Proceedings of the International Conference on FRP Composites in Civil Engineering*.
- Myers, J. J., Holdener, D. J., Merkle, W. and Hernandez, E. (2008). "Preservation of Missouri transportation infrastructures: validation of FRP composite technology through field testing—in-situ load testing of bridges P-962, T-530, X-495, X-596 and Y-298." Report No. OR09-007, MoDOT, Mo.
- Radolli, M. and Green, R. (1976). "Thermal Stresses in Concrete Bridge Superstructures under Summer Conditions." *Transportation Research Record*, No. 547.
- Sap2000 14.2 [computer software], Berkeley, CA, Computers and Structures.
- Snape, T. and Lindyberg, R. (2009). "Test Results: HC Beam for the Knickerbocker Bridge." *Advanced Structures & Composites Center conducts, AEWG Report 10-16*, University of Maine, Orono, ME.
- Summerscales, J and Short, D. (1978). "Carbon fibre and glass fibre hybrid reinforced plastics." *Composites*, Vol. 9, No. 3, pp. 157-166.

Yazdani, N., Eddy, S. and Cai, C. S. (2000). "Effect of bearing pads on precast prestressed concrete bridges." *Journal of Bridge Engineering*, Vol. 5, No. 3, 2000, pp. 224-232.

PAPER

I. Analysis Methods for Single-web and Multi-web Hybrid Composite Beam (HCB) Bridges

Mohamed A. Aboelseoud¹ and John J. Myers, F.ASCE²

Abstract

A new hybrid composite beam (HCB) was recently used to construct three bridges in Missouri. Each HCB consists of self-consolidating concrete (SCC) that is poured into a classical arch shape and tied at the ends by galvanized steel tendons. Both the concrete and the steel are tucked inside a durable fiberglass shell, and the voids are filled with Polyisocyanurate (polyiso) foam. One of the recently constructed HCBs was instrumented with various sensors. The axial strains induced in the HCB elements during different loading stages were measured experimentally. The current analysis method could not accurately predict the axial strains along the concrete arch's length. A commercial finite element (FE) analysis software package was used to construct an FE model and simulate the instrumented beam. The FE analysis predicted the measured strains with acceptable accuracy. It also clarified that the HCB neither behaved like a tied arch nor a traditional beam. Analysis methods were proposed and tested to estimate the strains in simply supported HCBs and HCBs supported on bearing pads. These methods achieved enhancements in estimating the strains under service loads.

CE Database of subject headings: Hybrid composite beam; Full-scale bridge testing; Flexural analysis methods; Bridge superstructure; Finite element analysis; FRP composites.

Introduction

A new type of hybrid composite beams (HCBs) was recently used to construct three bridges (B0439, B0410, and B0478) in Missouri. The underlying concept of the HCB, conceived by Hillman in 1996 (Hillman, 2012), consists of a self-consolidating concrete (SCC) arch

that is tied at the ends with high-strength galvanized steel strands. The concrete and steel, which represent the compression and tension reinforcement, respectively, are encased inside a durable fiberglass composite shell. This unique configuration allows the glass fiber reinforced polymer (GFRP) box to protect the steel and concrete from environmental effects. The composite box also serves as a formwork when the concrete arch is poured. The beam's strength and stiffness are provided by an efficient use of steel in purely axial tension and concrete in purely axial compression. This configuration also produces a lightweight member that can be transported easily and erected rapidly making this technology well suited to accelerated bridge construction.

The HCB was thought to behave like a tied arch. After testing the first HCB prototype, however, Hillman (2003) concluded that a perfect beam behavior is valid up to the factored design loads. He suggested that the arching action offers a redundant load path at higher loads, causing the beam to behave in a manner that is similar to a tied arch. Hillman (2003) established a flexural analysis method that assumes a perfect beam behavior. Snape and Lindyberg (2009) demonstrated that Hillman's model predicted the beam's behavior accurately under service loads. Virginia Tech University (Ahsan, 2012; Nosdall, 2013) concluded that Hillman's model provides a poor prediction for the concrete arch's strains. Nosdall (2013) suggested decoupling the HCB into an FRP shell and a tied arch during the flexural analysis. Aboelseoud and Myers (2014) recently conducted a finite element (FE) analysis on an HCB bridge superstructure. They noticed significant negative bending moment at the HCB's end, even when the beam was simply supported. They concluded that the current flexural analysis method needs to be improved.

Significance of the Current Study

Studies that were conducted on the HCB clarified that its flexural behavior is not completely understood. Therefore, the objectives of the current study were as follows:

1. Analyze the flexural behavior of the HCB
2. Examine the accuracy of the current flexural analysis method when estimating the strains in the HCB's elements under service loads

- Propose flexural analysis methods for both simply-supported HCBs and HCBs supported on bearing pads to achieve better estimation of the strains in the beam's elements

Experimental Program

Bridge 0410

Bridge 0410 (B0410) was the second HCB bridge to be constructed in Missouri. This single span bridge is 31.7 m (1248 in.) long and 9.35 m (368 in.) wide. It is the longest span HCB bridge in the United States. The roadway deck is supported by three lines of double-web HCBs. These beams were fabricated as multi-cell (double-web) beams to reduce the time of fabrication and erection. A typical cross-section of B0410 is depicted in Figure 1. The dimensions of B0410 HCB are illustrated in Figure 2.

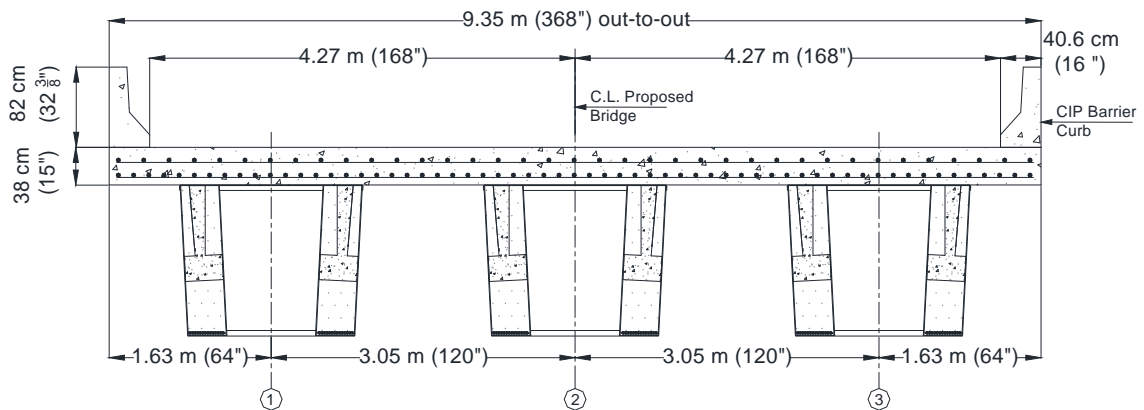


Fig. 1. Typical cross-section of bridge 0410

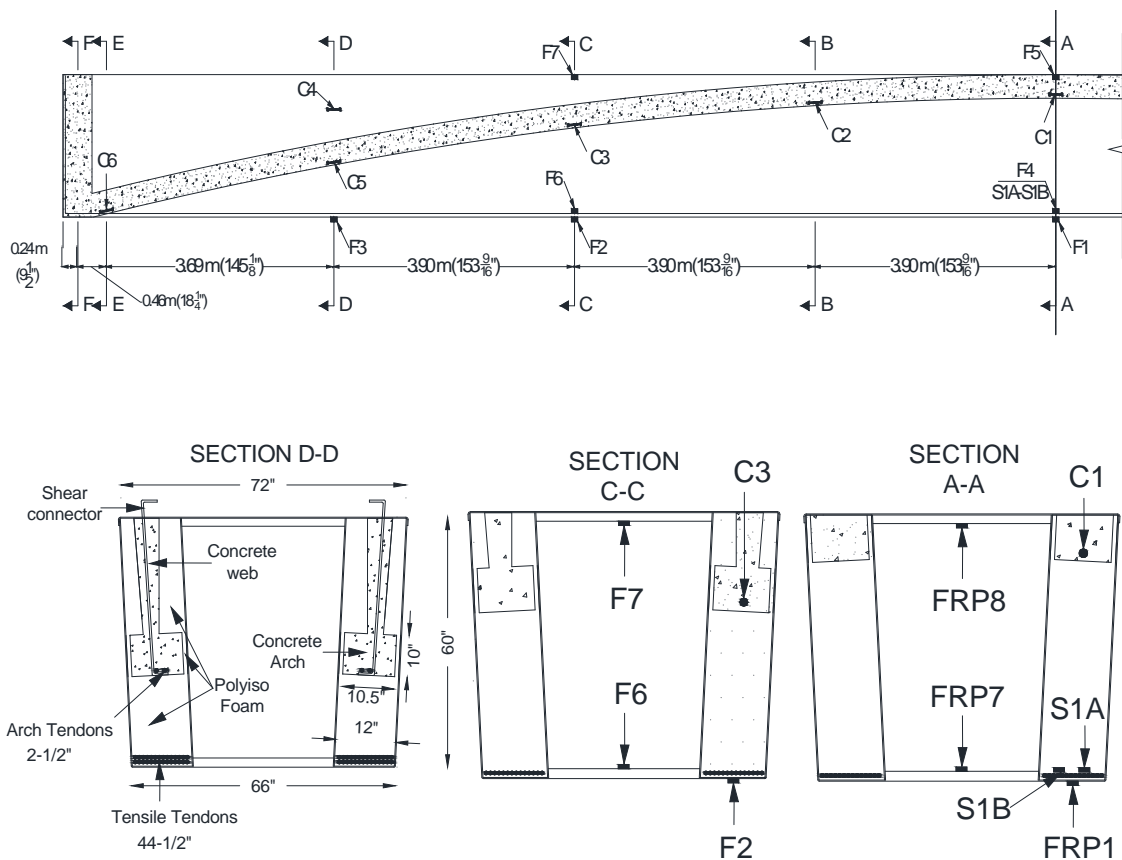


Fig. 2. HCB2 instrumentation

Load Testing and Instrumentation of B0410

Structural elements of HCB2 (the middle beam in Figure 1) were instrumented with strain gages to allow for the evaluation of the HCB analysis methods. These sensors also allowed for the monitoring of both short-term and long-term behaviors. Four electrical resistance strain gages were attached to tension strands. A concrete arch and its web (in HCB2) were instrumented by nine vibrating wire strain gages (VWSGs) / thermistors (seven gages to measure axial strains and two gages to measure shear strains). Twelve electrical resistance strain gages were adhesively bonded to the fiber reinforced polymer (FRP) shell; seven sensors to measure axial strains and five to measure shear strains. Twelve thermocouples were also placed at various locations.

All but the FRP shell's sensors were placed during the shell fabrication at Harbor Technologies in Maine. Researchers from Missouri University of Science and Technology (Missouri S&T) placed strain gages on the shell before the concrete arch was poured at a precast plant in Virginia. The GFRP shell was fabricated using vacuum assisted resin transfer mold (VARTM) process. Following fabrication, data collection indicated that two strand strain gages and two VWSGs within the concrete arch were not functioning properly. These sensors could have been damaged during the transportation and erection processes. They may have also been exposed to very high temperatures during the resin infusion process. The sensors' locations within the member are depicted in Figure 2. Only the functional, normal strain sensors are displayed in this figure. The VWSGs that were placed in the concrete are denoted by C, the FRP gages are denoted by F, and the strand gages are denoted by S.

The B0410 HCBs were subjected to three stages of dead and live loading. Both the GFRP shell and the strands were subjected to stresses from casting the concrete arch and web during the first stage. The non-composite HCB (complete HCB including the arch) was subjected to a load when the deck and barriers were poured during the second stage. The composite HCB (HCB connected to the deck) was subjected to in-service traffic during the third stage.

Strain readings were taken one hour before the concrete arch was poured. These readings continued for 25-hours. The initial strain data was subtracted from the strain readings that were recorded after the arch had been poured. These estimated strains are the strains induced in the shell and the strands under stage 1 loads. Unfortunately, no data was collected while the deck was being poured (stage 2).

A load test was conducted with 2 fully loaded, 10-wheel, 3-axle trucks to simulate the live loading in stage 3. These trucks performed three stops (Figure 3), simulating three different load cases. The first truck's (T-1995) axle load (P1) was 7.5 metric tons (16.5 kip). The middle axle load (P2) was 7.1 metric tons (15.6 kip), and the rear axle load (P3) was 11.1 metric tons (24.4 kip). The P1 of the second truck (T-2406) equalled 7.5 metric tons (16.4 kip). The P2 equalled 9.3 metric tons (20.5 kip), and the P3 equalled 9.1 metric tons (20.0 kip). The traffic was stopped, and strain measurements for the unloaded bridge were recorded. These strains served as a baseline and were subtracted from the strains

produced by each stop. Hence, the strains induced in the HCB2 elements under pure live loading were obtained.

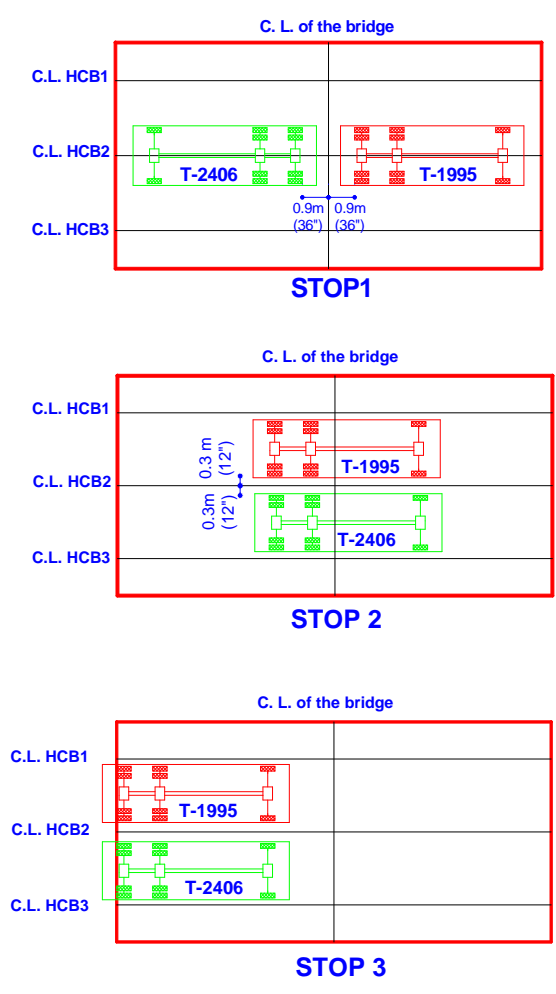


Fig. 3. Truck stop locations stops

Material Properties

The strains measured during the first and third stages clarified that all of the materials behaved within their linear elastic ranges. The numerical estimations of the strains that

were induced during the three stages were in agreement with the experimental observations. Consequently, only the linear properties of the constituent materials are presented in the following sections.

Concrete

SCC was used to form the HCB's compression reinforcement. The field tests revealed that the average compressive strength of the HCBs' concrete arches was approximately 76 MPa (11 ksi) after 28 days. Based on a previous study (Domone, 2007), the traditional ACI (2011) equations used with the normally vibrated concrete were used in the current study to calculate the SCC properties.

Steel Reinforcement

Two types of reinforcement bars were used in B0410. Typical Grade 60 mild steel reinforcing bars were used to reinforce the bridge deck, and seven wire strands [conventional, prestressed concrete strands (1860 MPa class, Grade 270)] were used to reinforce the HCBs. The Young's modulus of the strands and the typical mild steel were assumed to be 196,500 MPa (28,500 ksi), and 199,948 MPa (29,000 ksi), respectively.

FRP Composites

The FRP shell of B0410 consists of woven glass reinforcing fabrics. These fabrics consist of varying percentages of the fibers oriented in the 0° , 90° , and $\pm 45^\circ$ directions relative to the longitudinal axis. RTM-80545 vinylester resin was used to infuse the fibers. The shell was assumed to behave as a transversely isotropic material. The manufacturer provided the mechanical properties of the shell. The Poisson's ratio $[\nu_{xy}]$ was assumed to be 0.26, and $[\nu_{yz}]$ was assumed to be 0.30 (Kachlakev et al., 2001). A summary of the material properties used for modeling the FRP shell is listed in Table 1. Here, the x-axis is oriented in the warp (longitudinal) direction. The z-axis is oriented in the fill (crosswise) direction. The y-axis is oriented through the shell's thickness.

Table 1. Material properties used for modeling the FRP shell

Times	Strength MPa (ksi)	Elastic Modulus GPa (Msi)	Shear Modulus GPa (ksi)
Tensile properties	$S_x^+ = 423(61.4)$	$E_x^+ = 25.8(3.8)$	$G_{xy} = 7.8(1130)$
	$S_z^+ = 138(20)$	$E_y^+ = 18.3(2.7)$	$G_{xz} = 7.8(1130)$
	$S_{xz} = 26.2(3.8)$	$E_z^+ = 18.3(2.7)$	$G_{yz} = 3.6(520)$
Compressive properties	$S_x^- = 157(22.8)$	$E_x^- = 13.7(2)$	$G_{xy} = 7.8(1130)$
	$S_z^- = 152(19.1)$	$E_y^- = 9.3(1.4)$	$G_{xz} = 7.8(1130)$
	$S_{xz} = 26.2(3.8)$	$E_z^- = 9.3(1.4)$	$G_{yz} = 3.6(520)$

Polyisocyanurate Foam

Polyisocyanurate (polyiso) foam is a 32 kg/m³ (2.0 lb/ft³), rigid, closed cell foam. The elastic moduli and shear moduli were provided by the manufacturer. In this study, the foam was assumed to behave as a transversely isotropic material. Since the compression and tension moduli are close to each other, the tension properties were used for modeling the foam. The Poisson's ratios (ν_{xy} and ν_{xz}) were assumed to be 0.33 (Friis et al., 1988). A summary of the material properties used to model the polyiso foam is listed in Table 2. In this table, the x-axis is the axis of isotropy.

Table 2. Material properties used for modeling the polyisocyanurate foam

Elastic Modulus kPa (psi)	Poisson's ratio	Shear Modulus kPa (psi)
$E_x^+ = 8440(1225)$	$\nu_{xy} = 0.33$	$G_{xy} = 1516(220)$
$E_y^+ = 3190(463)$	$\nu_{xz} = 0.33$	$G_{xz} = 1516(220)$
$E_z^+ = 3190(463)$	$\nu_{yz} = 0.308$	$G_{yz} = 1219(177)$

Finite Element Modeling of B0410

The bridge superstructure was modeled via the commercial FE analysis software *ANSYS 14.0*. The y-axis was oriented in the gravity direction, the x-axis was oriented in the longitudinal direction of the bridge, while the z- axis was oriented in the lateral direction of the bridge.

Element Types

A combination of one, two and three-dimensional space elements was used to model the HCB. The shell181 element was used to model both the GFRP shell and the concrete web. The solid65 element was used to model the concrete arch, and element solid185 was used to model the polyiso foam. Element link180 was used to model the HCB strands. A perfect bond between all of the components of the HCB were assumed. The FE model of the HCB via *ANSYS 14.0* is depicted in Figure 4.

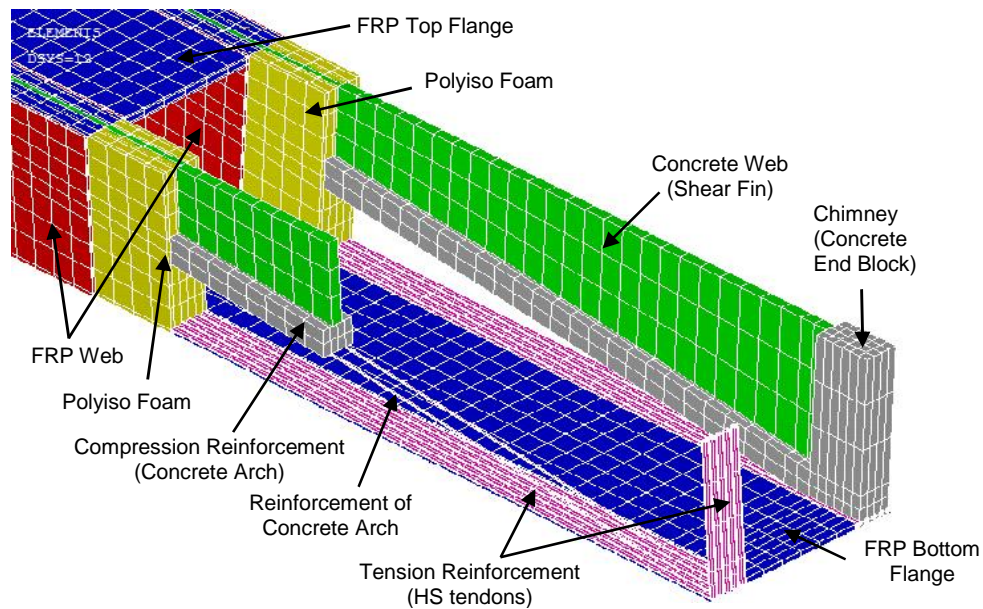


Fig. 4. FE modeling of multi-celled hybrid-composite beam using *ANSYS 14.0*

Solid65 elements were used to model the bridge's concrete slab. Three solid elements were used throughout the slab's thickness to allow the upper and lower reinforcement bars to be modeled via link180 elements. The parapet was poured simultaneously with the slab, and its reinforcement extended into the deck. Previous studies (Myers et al., 2008; Aboelseoud and Myers, 2014) showed that the bridge girder's deflection and stress are decreased when composite action is achieved between the slab and the parapet. Consequently, the parapet was included in the FE model and simulated by solid65 elements. Hillman (2008) demonstrated that the shear connectors of the HCB achieved full composite action between the bridge deck and the HCBs. A perfect bond was assumed to exist between the deck components and between the deck and the HCBs during the FE analysis.

Modeling of Loads

The FE analysis accounted for the stress history of the HCB resulting from the construction sequence of an HCB bridge. The weight of the concrete arches and webs was applied as a uniform load on the lower foam elements (the foam elements below the concrete arch, see Figure 4) during the first stage. The deck's weight was applied as a uniform load on the upper flange elements of the non-composite HCB during the second stage. The truck's axle loads were applied as uniform distributed loads over each tire's contact area, on the upper surface of the deck elements, during the third and final stage.

Modeling of Boundary Conditions

Each end of the B0410 HCBs was supported on two steel-laminated neoprene bearing pads. Each elastomeric bearing pad, located underneath the chimney, was 30.5 cm X 30.5 cm X 1.9 cm (12 in. X 12 in. X 0.75 in.). These bearing pads were simulated by roller supports, and translational and rotational springs. The translational stiffness of the bearing in the x-dir. (k_{xb}) and the rotational stiffness about the z-axis (k_{rzb}) were estimated as follows (Yazdani et al., 2000):

$$k_{xb} = \frac{CGA_{xz}}{H} \quad (1)$$

$$k_{rzb} = \frac{CE_b I_z}{H} \quad (2)$$

where A_{xz} is the area of the bearing in the xz plane, H is the total thickness of the bearing, I_z is the moment of inertia of the bearing about the z -axis, E_b is the stiffness of the bearings, G is the shear modulus of the bearing, and C is a factor that represents the effects of aging and cold temperatures on the elastomer's stiffness. According to AASHTO (2012), the elastomer should have a shear modulus between 0.7 MPa (95 psi) and 1.4 MPa (200 psi). In the current work, the shear modulus of the elastomer was assumed to be 1 MPa (145 psi).

Both aging and temperature can increase the elastomer's stiffness up to 50 times the original stiffness (Roeder et al., 1989). Yazdani et al. (2000) simulated the bearing pads, during the FE modeling of a prestressed I-beam bridge in Florida, via translational and rotational springs. They found that the maximum deflection and tensile strain at the midspan significantly larger than the measured values. The maximum deflection and tensile strain were found higher than the field test data by approximately 19 and 25%, respectively, when the value of (CG) was increased up to 34.5 MPa (5000 psi). Based on their study, two values for C were used here to estimate the translational and rotational stiffnesses: 12 and 25. The strains estimated when C was assumed to be 12 closely mirrored the experimental measurements. Consequently, C was assumed here to be 12. A comparison between the measured strains in the concrete arch under stop 1 loads and the strains estimated by the FE model using two values for C is illustrated in Figure 5.

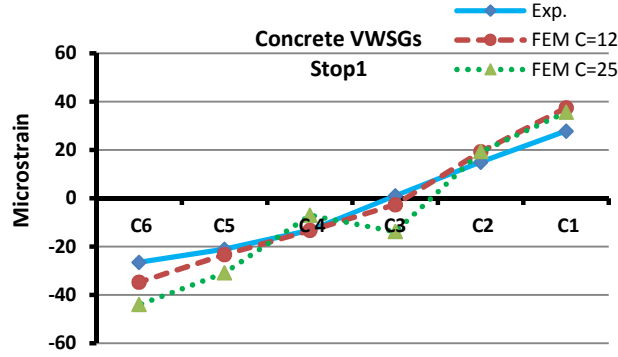


Fig. 5. The measured strains and the estimated strains by the FE model using different C values

Mathematical Calculations

The existing analysis method (Hillman, 2003; Hillman, 2012), models the HCB as a straight, simply supported beam with varying sectional properties along the beam's length. Hillman's model assumes a perfect beam behavior. This method divides the HCB into ten elements to account for the beam's non-prismatic nature. The transformed area technique is then used to estimate the geometric properties at each section. All of the materials in this study behaved within their linear elastic ranges. Consequently, the strains were estimated as:

$$v_{ij} = \frac{M_j(\bar{y}_j - y_{ij})}{I_j E_w} \quad (3)$$

where v_{ij} is the axial strain (in x-direction) of component i at section j , M_j is the bending moment at section j , y_{ij} is the distance from the center of gravity (c.g.) of component i to the extreme lower fiber of the beam at point j , \bar{y}_j is the distance from the elastic neutral axis (ENA) of the composite section to the extreme lower fiber of the beam at section j , E_w is the modulus of elasticity of the FRP web, and I_j is the transformed moment of inertia of the composite section with respect to E_w , about the ENA, at section j .

Modified Analysis Method

Two modifications were applied to the existing analysis method to enhance the strain estimation in the different HCB's components. One modification was applied to the beam's geometry, and the other was applied to its boundary condition.

Both horizontal movements and axial forces are expected to induce through the beam's length (x-dir.) due to the compression reinforcement's parabolic profile. Consequently, the axial stresses and strains are expected to be sensitive to the type of translational restraint in the x-dir. at the beam's end. The current analysis method models the HCB as a straight, simply supported beam. Therefore, neither axial force induces through the beam length nor the model is sensitive to the restrained translational DOFs in the longitudinal direction. The ENAs of both the non-composite and composite HCB (stages 2 and 3) were found to continuously form a curved path. Therefore, the first proposed modification was to model the HCB as a curved beam based on the ENAs' locations rather than as a straight beam.

The second proposed modification was to model the supports at each end with a roller support, a translational spring in the x-dir., and a rotational spring about the z-axis. The concrete arch is expected to perform both horizontal and vertical movements under static vertical loads. The concrete arch's longitudinal deformation is partially restrained by the strands at the beam end. The longitudinal movement of the overall beam is partially restrained by the bearing pads at each end. The arch is the primary cause of the beam's movement in the longitudinal direction. Subsequently, it may be acceptable to simulate the restrained horizontal forces at each end of the beam, under static vertical loads, using a translational spring with the following stiffness:

$$K_x = K_{xb} + K_{xs} \quad (4)$$

where K_x is the translational spring stiffness at the end of the HCB in the x-dir., K_{xb} is the stiffness presented by the bearing pad, given by Equation (1), and K_{xs} is the stiffness provided by the strands.

It can be shown that K_{xs} is given by the following equation:

$$K_{xs} = \frac{2E_s A_s}{L} \quad (5)$$

where E_s and A_s are the elastic modulus and the cross-sectional area of the strands, respectively, and L is the beam length.

The bearing's stiffness has been documented to significantly affect the bridge girder's behavior (Yazdani et al., 2000; Cai and Shahawy, 2003). Thus, Equation (2) was used to calculate the stiffness of the rotational springs at the HCB's ends. The strains were, then, estimated by modifying Equation (3) to account for the axial force in the beam:

$$v_{ij} = \frac{M_j(\bar{y}_j - y_{ij})}{I_j E_w} + \frac{N_j}{A_j E_w} \quad (6)$$

where N is the axial force, A is the transformed cross-sectional area of the composite section.

The proposed modifications were applied only to the second and third stages. The ENA location was constant along the beam's length during the first stage (the HCB, without compression reinforcement). Consequently, the beam was modeled as a straight beam without modifying the existing method.

Results Discussion

The measured and the estimated strains that were produced by the weight of the concrete arches and webs (stage 1) are illustrated in Figure 6. Both the FE model and the current design method estimated the strains in the shell with acceptable accuracy during this stage. The FE model estimated the maximum compressive and tensile strains in the shell (F5 and F1, respectively) with errors less than 10%. The errors produced by the mathematical model estimations were less than 18%. The FE analysis overestimated the strains in the strands by approximately 30%. The strands' strain gages were attached to individual spiral wires. It is expected that these sensors captured angled strains rather than longitudinal strains because of the helical nature of the wire. Ahsan (2012) performed an experimental study to quantify the error's level that can occur during measuring the axial strain in a wired

strand. This study (Ahsan, 2012) concluded that measuring angled strain of an individual spiral wire underestimates the axial strain by approximately 18%. Subsequently, the FE model error is expected to be less than 15%.

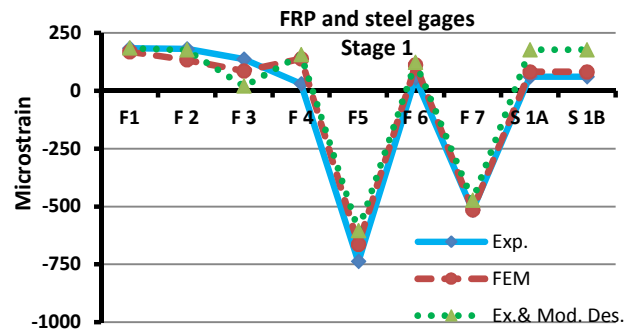


Fig. 6. Strain values due to the concrete arch pour (stage 1)

The measured and the estimated strains that were produced by the truck loads during stops 1 and 3, respectively (stage 3) are illustrated in Figures 7 and 8. Table 3 also lists the measured and the estimated strains under the truck loads during stop1. Both, the measured and the estimated strains under stop 2 loads were very close to the measured and the estimated strains under stop 3 loads. The FE model errors in estimating the strains under stop3 loads were also within the same range of errors as in the first and the second stops. The FE model predicted higher strains in the concrete arch than the measured strains, as it is illustrated in Table 1. The arch may have gained strength higher than that was used in the FE model because the mix design of the concrete arch of B0410 contained fly ash. Previous studies (Han et al., 2003; Hwang et al., 2004) clarified that the fly-ash concrete achieves a significant increase in strength after 28 days. This increase continues at the long-term due to the pozzolanic reaction. The strength used in the FE model was obtained from standard cylinder tests performed after 28 days from the concrete pour. While, the load test was performed approximately 6 months after the concrete pour. The increase in the strength

of the concrete arches during this period could be as high as 35% according to Han et al. (2003) and Hwang et al. (2004) studies. Additional factors that may produce discrepancies between the FE model and the measured data during full-scale bridge testing were presented by Myers et al. (2008) and Aboelseoud and Myers (2014). In general, the FE model estimated the strains under this stage loads with acceptable accuracy. Consequently, the FE model was used to provide a better understanding of the HCB's flexural behavior.

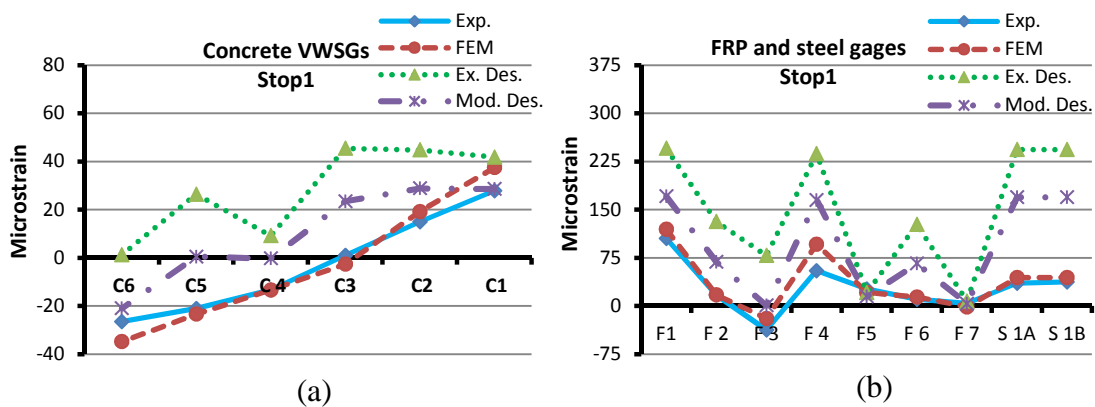


Fig. 7. Strain values due to the stop1 loads (stage 3)
 (a) Concrete arch (b) FRP shell and strands

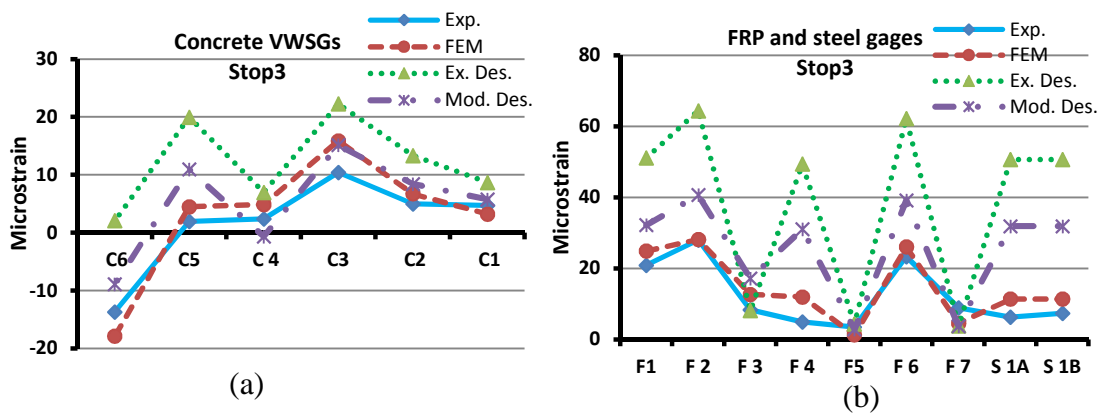


Fig. 8. Strain values due to stop3 (stage 3)
 (a) Concrete arch (b) FRP shell and strands

Table 3. Measured and estimated strains under stop1 loads

STOP 1	Experimental	FE model	Mod. Meth.	Ex. Meth.
F1	106	120	171	246
F 2	17	18	69	132
F 3	-37	-19	1	79
F 4	55	97	165	238
F5	27	21	15	21
F 6	11	14	66	127
F 7	4	-1	4	8
S 1A	36	44	170	244
S 1B	37	45	170	244
C1	28	37	29	42
C2	15	19	29	45
C3	1	-3	24	46
C 4	-13	-13	0	9
C5	-21	-23	1	26
C6	-27	-35	-21	1

The maximum compressive strain in the concrete arch was found very close to the junction of the arch with the chimney during the three stops. VWSG (C6), instrumented at this location, captured the maximum normal compressive strains during all of the truck's stops (see, Figures 7a, and 8a). The same behavior was predicted by the FE model. According to the existing analysis method, C6 was located below the ENA and the bending moment was small at this location during all of the stops. Consequently, the current method always predicted very small tensile strains at C6. The FRP strain gage F3 captured compressive strains during stop 1 (Figure 7b) and stop 2 (not shown here). These results assure that the HCB was subjected to a negative bending moment at the support locations. This negative moment can be attributed mainly to the restrained moments at the beam-pad interface. Consequently, no definite conclusion regarding the chimney's effect could be drawn from the experimental strains measured in HCB2. The negative moment may have been combined with an axial compressive force along the beam's length due to the compression reinforcement's parabolic profile.

In general, the comparison that was made between the field strains and the current analysis procedure's strains reveals that the current method could not predict the maximum compressive strain at the concrete arch end during stage 3. It was also significantly conservative when predicting the FRP shell and strands' strains. The same trends were observed in the second stage (based on the FE model estimations, see Figure 9). The existing method was also conservative when estimating the concrete arch's strain at the midspan during stage 2. These defects can be attributed mainly to neglecting the negative moment at the beam end and the axial force through the beam length.

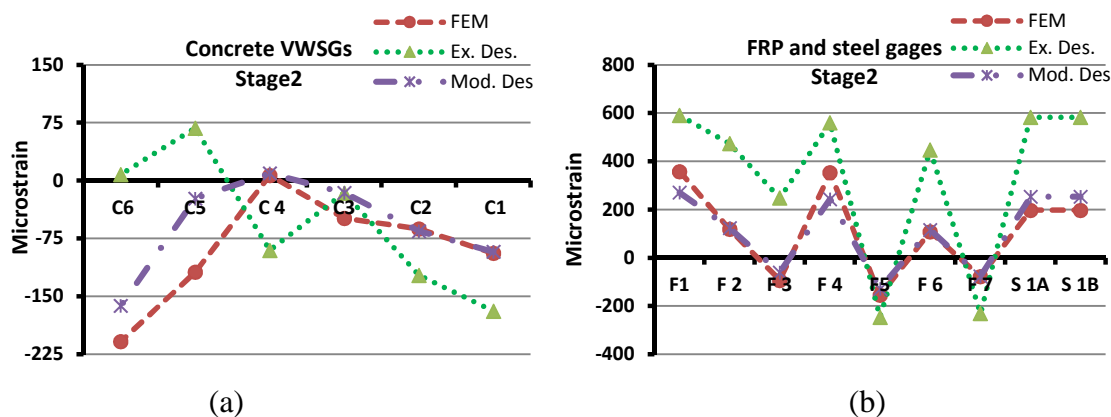


Fig. 9. Strain values produced by deck weight (stage 2)
(a) Concrete arch (b) FRP shell and strands

Figures 7b and 8b illustrate that the measured strains at the strands' midspan (S1A and S1B) were significantly lower than the bottom flange strains at the same location (F1). If the HCB had a perfect beam-behavior, then strains in both the strands and the bottom flange would have been very close to each other. However, the FE model detected strain differences that were similar to those that were measured experimentally. These differences indicated that some of the design assumptions may be invalid. Thus, the FE model results were used to develop strain profiles throughout the thickness of the composite and non-composite HCB to verify the design assumptions.

The strain profile (based on the FE model estimations) at section (A-A), due to stop 1 loads, is illustrated in Figure 10a. This figure also illustrates the strain profile obtained by the modified method (which assumes a perfect beam behavior). The strain profile clarified that the strain compatibility assumption is invalid. This strain incompatibility between the HCB components can be attributed to the polyiso foam's low shear moduli. This foam behaves as a flexible shear connection, allowing differential vertical and horizontal displacements between the HCB elements. The longitudinal displacement (x-dir.) of the composite HCB elements, at the beam's midspan, under stop 1 loads is illustrated in Figure 10b. The FE model also detected vertical differential movements between the HCB components. Mascaro and Moen (2012) observed relative vertical movements between the concrete arch and the FRP shell via two experimental methods: close-range photogrammetry and LVDT measurements. Their experimental investigations agree with the current FE model's results. Due to the relative movements between the HCB elements: the strain distribution throughout the deck, concrete arch, and concrete web is linear (because of the rigid connection between them), the strain distribution through the GFRP shell components is linear but with different slope, while the strain in the strands is independent. The effect of the flexible shear connections on the strain throughout girder's depth has been documented by many researchers among them (Keller and Gürtler, 2006).

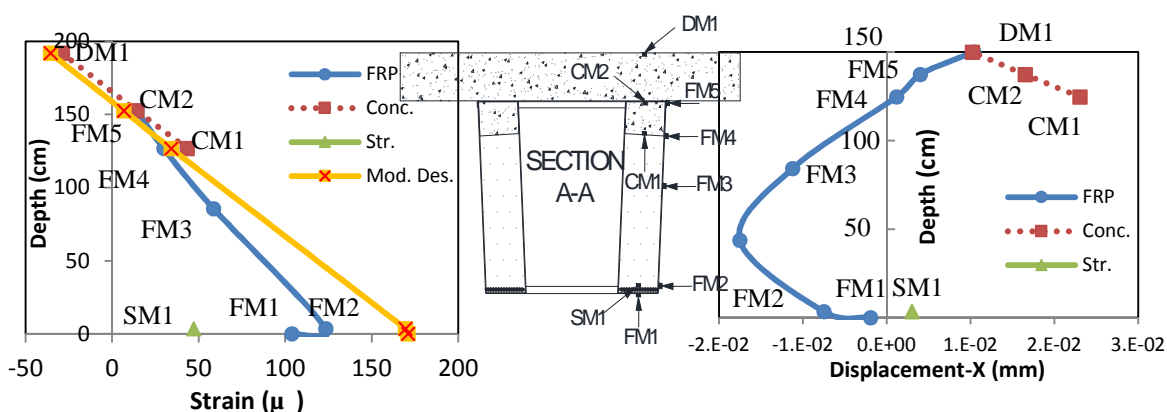


Fig. 10. (a) Strain profile (b) Displacement in X-dir. due to stop1 sec. (A-A)

The FE model's results demonstrated that the stress was not constant along the strand's length. Hillman (2003) observed the same behavior while testing the first HCB prototype. He concluded that the HCB behaves like a beam rather than a tied arch. The strands examined in the current study, however, were continuously subjected to tensile stresses, even where the FRP lower shell had compressive stresses close to the beam end. This behavior demonstrates that the strands were subjected to an axial force at the HCB's end. Consequently, they worked as a tie for the concrete arch restraining its longitudinal movements, while, at the same time, contributing to the beam's flexural rigidity. The FE model observations prove that the HCB has no perfect beam behavior even under relatively small service loads. Because the concrete arch and the strands are integrated with other elements (i.e., FRP shell and deck), the HCB does not also behave like a perfect tied arch.

Figures 7, 8 and 9 and Table 3 illustrate that the modified method was conservative when estimating the strains in the FRP shell and the strands during stage 3. This method was also unable to accurately identify the strain at some locations through the arch's length during the second and the third stages. The modified method underestimated the maximum compressive strain by 25% and 27% under stage 2 and total loading, respectively (see, Figures 9 and 11). The FE model illustrated that there was a strain concentration region at the junction of the arch with the chimney. This strain concentration led to the inability of the modified method to accurately estimate the maximum compressive strain. In general, Figure 11 clarifies that, although a perfect beam behavior was assumed, the modified analysis method achieved an acceptable accuracy when identifying axial strains in the HCB elements under different stages of service loading.

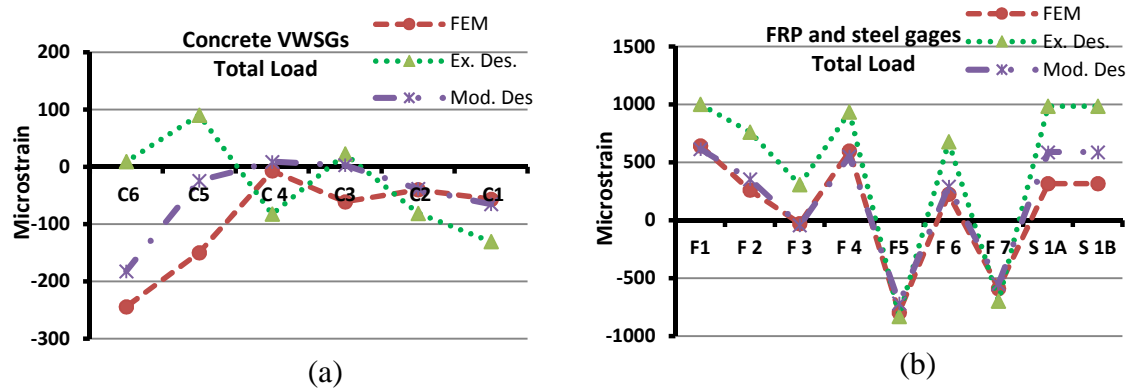


Fig. 11. Strain values due to the total loads of the three stages
(a) Concrete arch (b) FRP shell and strands

Design of a Simply Supported HCB

Designers often ignore the bearing pad's effects when designing a bridge's beam. A mathematical method is proposed here for use when designing a simply supported HCB. Understanding the flexural behavior of a simply supported HCB will also aid in evaluating the chimney's effect at the beam's end.

The concrete arch in a typical HCB is connected to a chimney at each end. A layer of foam separates both the arch and the chimney from the FRP shell. Subsequently, the chimney is expected to provide localized partial fixity to the arch rather than the overall beam. The HCB beam was decoupled into two structural components to apply different boundary conditions for the HCB's elements. The first structural component consisted of the FRP shell. This component was modeled as a straight, simply supported beam. The second component consisted of the concrete arch and web, and the strands (in addition to the deck in case of composite HCB). This component was modeled as a curved beam. The chimney's effect was represented at the curved beam's end by translational and rotational springs. The load was divided between the two components (straight and curved beams) based on their contributions to the flexural rigidity of the overall system. The proposed mathematical model is depicted in Figure 12.

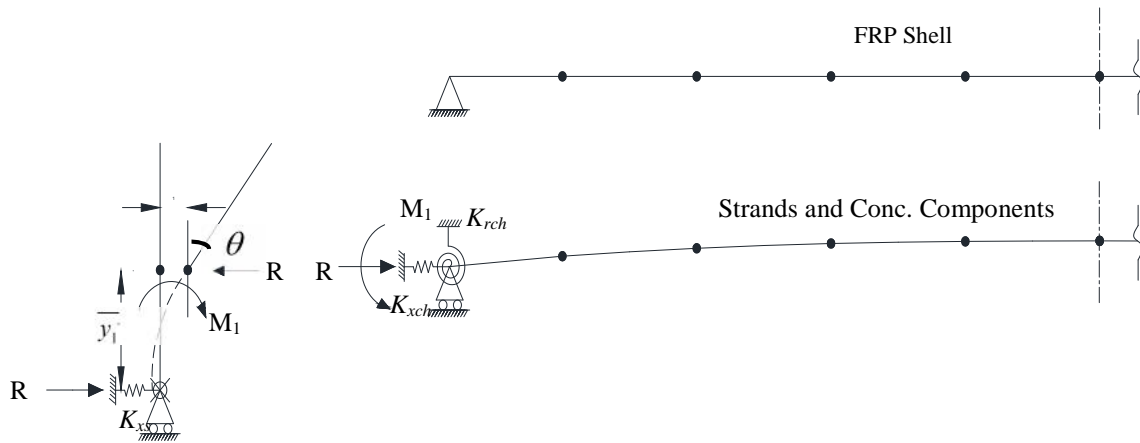


Fig. 12. Decoupling of the simply supported HCB into two structural systems

Chimney Effect

The chimney was expected to suffer small rotation at its base because the chimney's rotation was restrained by a relatively large number of strands on one side (the HCBs implemented in bridge applications to-date were always over-reinforced, Hillman 2012) and a concrete arch on the other side. This rotation was neglected in the current study, and the chimney was assumed fixed against rotation at its base. Two approaches were proposed to estimate the chimney's effect at the curved beam's end.

First Approach

This approach is an approximate approach that neglects the horizontal reaction (R) at the end of the curved beam assuming that bending moment is only transferred from the beam to the chimney. This assumption was made because the beam has a small curvature producing small horizontal reaction in the X-dir. Based on this approach, the translational stiffness at the arch end is assumed to equal (k_{xs}), while the rotational stiffness provided by the chimney was be estimated as:

$$K_{rch} = E_c I_{ch} / \bar{y}_1 \quad (7)$$

where E_c is the elastic modulus of the arch's concrete, and I_{ch} is the chimney's moment of inertia.

Second Approach

The slope-deflection method was used to estimate the translational and rotational stiffnesses the chimney provides at the curved beam end. The following equations were derived for estimating the moment of a non-prismatic, five-element beam with a fixed support at end A and a hinged support and a rotational spring (K_{rB}) at end B:

$$M_{AB} = \frac{25E}{L_{AB}} \left(\frac{e}{ae - cd} \right) {}^n_A + \frac{25E}{L_{AB}} \left(\frac{d}{ab - cd} \right) {}^n_B + \frac{25E}{L_{AB}^2} \left(\frac{d + e}{cd - ae} \right) \Delta_{AB} + FEM_{AB} \quad (8)$$

$$M_{BA} = \frac{25E}{L_{AB}} \left(\frac{a}{ab - cd} \right) {}^n_B + \frac{25E}{L_{AB}} \left(\frac{c}{ae - cd} \right) {}^n_A + \frac{25E}{L_{AB}^2} \left(\frac{a + c}{cd - ae} \right) \Delta_{AB} + FEM_{BA} \quad (9)$$

The moment of inertia of the non-prismatic beam changed from I_{AB1} at end A to I_{AB6} at end B, where

$$a = 0.2/I_{AB5} + 0.8/I_{AB4} + 1.8/I_{AB3} + 3.2/I_{AB2} + 7/3I_{AB1} \quad (10)$$

$$b = 0.2/I_{AB2} + 0.8/I_{AB3} + 1.8/I_{AB4} + 3.2/I_{AB5} + 7/3I_{AB6} \quad (11)$$

$$c = 1/6I_{AB1} + 0.8/I_{AB2} + 1.2/I_{AB3} + 1.2/I_{AB4} + 0.8/I_{AB5} \quad (12)$$

$$d = 1/6I_{AB6} + 0.8/I_{AB5} + 1.2/I_{AB4} + 1.2/I_{AB3} + 0.8/I_{AB2} \quad (13)$$

$$e = b + 25E/K_{rB}L_{AB} \quad (14)$$

The fixed end moments at A and B (FEM_{AB} and FEM_{BA} , respectively) for a uniform load (w) distributed on the overall length of the beam, and a point load (p) at the midspan, were derived as:

$$FEM_{AB} = \frac{wL^2}{25} \left(\frac{bw_2 - dw_1}{ae - cd} \right), FEM_{BA} = \frac{wL^2}{25} \left(\frac{aw_1 - cw_2}{ae - cd} \right) \quad (15)$$

$$FEM_{AB} = \frac{pL}{5} \left(\frac{bp_2 - dp_1}{ae - cd} \right), FEM_{BA} = \frac{pL}{5} \left(\frac{ap_1 - cp_2}{ae - cd} \right) \quad (16)$$

$$w_1 = 2/I_{AB2} + 6/I_{AB3} + 9/I_{AB4} + 8/I_{AB5}, w_2 = 2/I_{AB5} + 6/I_{AB4} + 9/I_{AB3} + 8/I_{AB2} \quad (17)$$

$$p_1 = 1/2I_{AB2} + 2/I_{AB3} + 3/I_{AB4} + 2/I_{AB5}, p_2 = 1/2I_{AB5} + 2/I_{AB4} + 3/I_{AB3} + 2/I_{AB2} \quad (18)$$

Equations 8 and 9 can be used to solve for the moment and the reaction at the beam's end as functions in the chimney's stiffnesses. The rotational and translational stiffnesses can, then, be estimated by:

$$K_{xch} = R / \Delta_{ch} \quad (19)$$

$$K_{rch} = 2EI_{ch}M_1 / \left(2M_1\bar{y}_1 + R\bar{y}_1^{-2} \right) \quad (20)$$

Alternatively, Equations 8 and 9 can be used to solve the beam with the chimneys as one frame. The stiffnesses can be estimated next.

Verification of the Proposed Method

The non-composite and composite HCBs of B0410 were remodeled as simply supported beams via *ANSYS 14.0*. Different load cases were applied to the non-composite HCB. These cases simulated the loads that may be produced during the deck pour. The truck's

loads that were produced during the three stops were applied to the simply supported B0410. The strains obtained by the proposed model were then compared to the FE analysis estimations.

The proposed model was also verified using results that were obtained from laboratory experimental tests performed by Virginia Tech University (Ahsan, 2012). Two load cases were applied on single-web, simply supported HCBs: a point load at the midspan and two equal point loads at the quarter points. The HCB tested by Virginia Tech University was 13.1 m (516-in.) long, simulating the Tide Mill bridge HCBs. Ahsan (2012) provided detailed description for this experimental work.

The stiffnesses provided by the Tide Mill bridge simulated HCB's chimney at the curved beam's end under different load cases were calculated via the two proposed approaches. A comparison between the results obtained by the two approaches is presented in Table (4). Here, the differences between the stiffnesses as estimated by the two approaches were small leading to insignificant changes in the strains. These small differences can be attributed to the beam's small curvature. Thus, the first approach was used to estimate the rotational stiffnesses provided by the chimneys of the examined HCBs.

Table 4. Estimated rotational and extensional stiffnesses for Tide Mill Bridge simulated HCB's chimney

Load case	Stiffness	First approach	Slope-def. approach	Dif. %
Midspan Load	K_{rch} MN.in/rad (Kip.in/rad)	275 (2.437E+06)	281 2.484E+06	-1.9
	K_{xch} MN/in (Kip/in)	63 (359)	67 (383)	-6.2
2-Quarter Point Loads	K_{rch} MN.in/rad (Kip.in/rad)	275 (2.437E+06)	279 2.472E+06	-1.4
	K_{xch} MN/in (Kip/in)	63 (359)	69 (392)	-8.4
Distributed Load	K_{rch} MN.in/rad (Kip.in/rad)	275 (2.437E+06)	280 2.474E+06	-1.5
	K_{xch} MN/in (Kip/in)	63 (359)	68 (389.5)	-7.8

Results of Simply Supported HCB

The strains estimated by the existing and the proposed analysis methods, as well as the FE analysis along the length of the non composite and composite HCBs of B0410 are illustrated in Figures 13 and 14. The existing method's performance in estimating the concrete arch's strain was poor for both the non-composite and composite HCBs. The method is fairly accurate when estimating the shell and the strands' strains for the non-composite HCB. Whereas, it is conservative when estimating the bottom FRP shell and the strand strains for the composite HCB. The proposed model's results correlated well with the FE model estimations during stage 2 (non-composite beam). The HCB's behavior had become more challenging to predict after the deck being poured. However at this stage, the proposed method estimated the maximum strains with good accuracy. The proposed model was unconservative when estimating the maximum compressive strain at the arch's end during both the second and the third stages. This can be attributed to a strain concentration at the junction of the arch with the chimney. The proposed model was unconservative by approximately 18%, when estimating the strain at the arch's end during the second stage. The proposed method for HCBs that are rested on bearing pads underestimated the strain at the arch's end by 25% during the second stage. The FE analysis clarified that as the degree of fixity at the HCB's end increased as the strain concentration increased. Thus the difference in the error presented in the two cases (simply supported and rested on pads HCBs) can be attributed to an increase in the strain concentration.

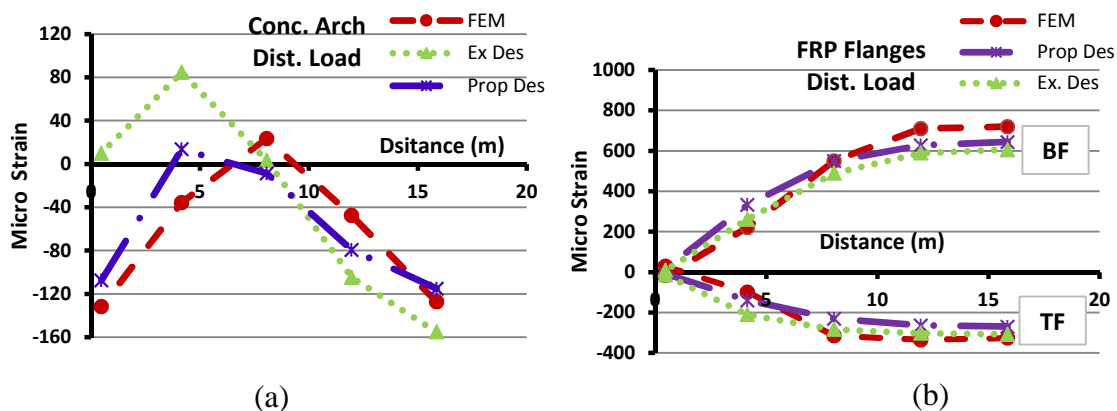


Fig. 13. Strains along the length of non-composite HCB of B0410 under uniform distributed load (a) concrete arch, and (b) bottom and top FRP flanges

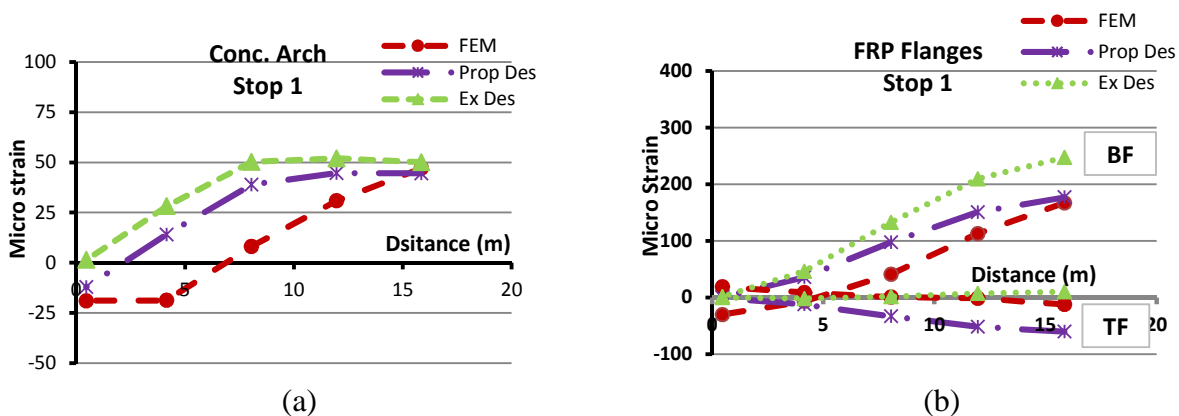


Fig. 14. Strains along the length of the composite HCB of B0410 (a) concrete arch, and (b) bottom and top FRP flanges.

The comparison between the proposed model's results and the measured strains by Ahsan (2012) reveals that decoupling the HCB into two main components enabled estimating, with good accuracy, different strains in the HCB elements that are at the same level (Figure 15). The proposed model was unconservative when estimating the strands' strains (Figure 15) for the non-composite HCB. The same behavior was observed when the strains of the non-composite HCB of B0410 were estimated (based on the FE model

results). However, the model was conservative when estimating the strains of B0410 strands during the last stage. This reduced the error of the mathematical model, with respect to the FE analysis, to less than 5%.

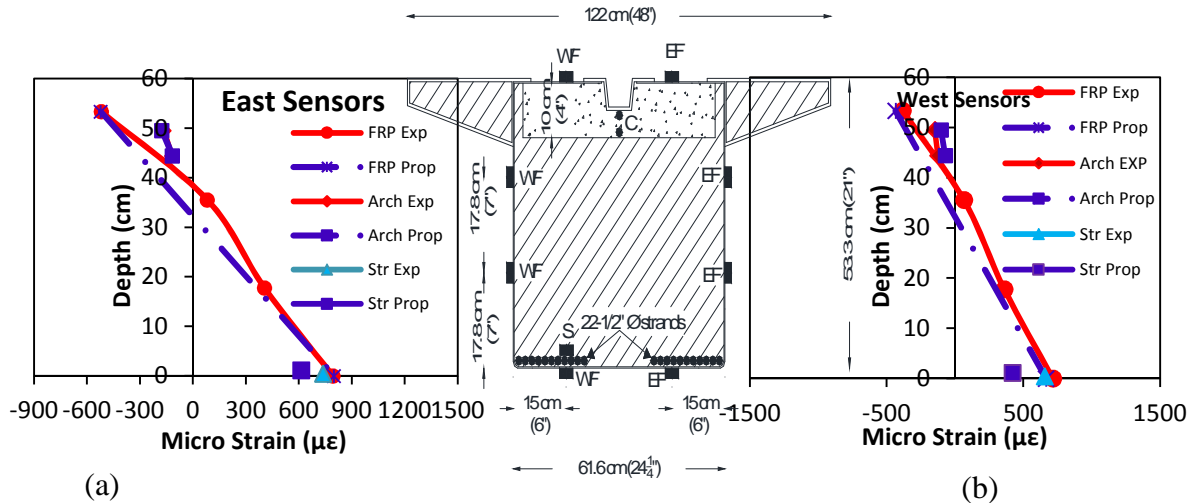


Fig. 15. Strain profiles at the midspan Tide Mill bridge's HCB's depth (a) Midspan point load (b) 2-quarter points loads

Conclusions

The following conclusions were drawn from the results gathered during this study:

- The flexural behavior of the HCB
 - The HCB neither exhibits a perfect beam behavior nor behaves like a tied arch.
 - The polyiso foam works as a flexible shear connection. In doing so, this foam achieves partial composite action between the different HCB elements, allowing them to suffer differential deformations. Subsequently, the different components, at the same level, have different strains.
 - The chimney at the beam's end provides partial fixity. This effect, however, is localized to the concrete components.

- The existing flexural analysis method
 - The existing flexural analysis method exhibits a poor performance in predicting the strains along the length of the concrete arch in both the non-composite and composite HCBs that either supported on bearing pads or are simply supported.
 - The method is also significantly conservative when calculating the strains in the FRP shell and the strands for the HCBs supported on bearing pads and for the composite, simply supported HCBs.
- The proposed flexural analysis methods
 - The proposed flexural analysis method predicts the non-composite HCB's behavior with acceptable accuracy. However, after the deck being poured the proposed methods provide less accurate estimations for the HCBs strains.
 - The proposed methods are unconservative when predicting the compressive strain at the concrete arch's end.

In general, the proposed flexural analysis methods were more accurate than the existing method in predicting the strains in the HCB elements. Nevertheless, the major limitation of the current work is that only service loads were used to examine the proposed methods. Future research should investigate the applicability of these methods to the design of the ultimate flexural strength of the member.

Acknowledgements

The authors would like to acknowledge the Missouri Department of Transportation (MoDOT) and the National University Transportation Center (NUTC) at Missouri S&T for sponsoring this research study. The staff support from the Dept. of Civil, Architectural and Environmental Engineering, and Center for Infrastructure Engineering Studies (CIES) at Missouri S&T are also greatly appreciated.

REFERENCES

- AASHTO, LRFD. (2012). *AASHTO LRFD bridge design specifications*, American Association of State Highway and Transportation Officials, Washington, DC.
- Aboelseoud, M. A. and Myers, J. J. (2014). "Finite Element Modeling of Hybrid Composite Beam Bridge in Missouri, USA." *Journal of Bridge Engineering*, ISSN (print) 1084-0702.
- ACI. (2011). *Building Code Requirements for Structural Concrete (ACI 318-11) and Commentary*, American Concrete Institute.
- Ahsan, S. (2012). "Evaluation of Hybrid-Composite Beam for Use in Tide Mill Bridge." M. S. thesis, Virginia Polytechnic Institute and State University, Blacksburg, VA.
- Cai, C. S. and Shahawy, M. (2003). "Predicted and measured performance of prestressed concrete bridges." *Journal of Bridge Engineering*, Vol. 9, No. 1, pp. 4-13.
- Domone, P. L. (2007). "A review of the hardened mechanical properties of self-compacting concrete." *Cement and Concrete Composites*, Vol. 29, No. 1, pp. 1-12.
- Friis, E. A., Lakes, R. S., and Park, J. B. (1988). "Negative Poisson's ratio polymeric and metallic foams." *Journal of Materials Science*, Vol. 23, No. 12, pp. 4406-4414.
- Han, S. H., Kim, J. K., and Park, Y. D. (2003). "Prediction of compressive strength of fly ash concrete by new apparent activation energy function." *Cement and Concrete Research*, Vol. 33, No. 7, pp. 965-971.
- Hillman, J. R. (2003). "Investigation of a Hybrid-Composite Beam System." High Speed Rail IDEA Program, Transportation Research Board of National Academies, Chicago, HSR Project Report 23.
- Hillman, J. R. (2008). "Product Application of a Hybrid-Composite Beam System." IDEA Program Final Report, Transportation Research Board of National Academies, Chicago, HSR - 43.
- Hillman, J. R. (2012). "Hybrid-Composite Beam (HCB®) Design and Maintenance Manual." The Missouri Department of Transportation, Jefferson City, MO.
- Hwang, K., Noguchi, T., and Tomosawa, F. (2004). "Prediction model of compressive strength development of fly-ash concrete." *Cement and Concrete Research*, Vol. 34, No. 12, pp. 2269-2276.

- Kachlakev, D., Miller, T., Yim, S., Chansawat, K., and Potisuk, T. (2001). "Finite element modeling of reinforced concrete structures strengthened with FRP laminates." Final Rep. SPR 316, Oregon DOT, ResearchGroup, Salem, OR.
- Keller, T., and Gürtler, H. (2006). "Design of hybrid bridge girders with adhesively bonded and compositely acting FRP deck." *Composite Structures*, Vol. 74, No. 2, pp. 202-212.
- Mascaro, M. G., and Moen, C. D. (2012). "Out-of-Plane Web Deformation and Relative Arch Movement of Hybrid-Composite Beams Based on Photogrammetry." Virginia Polytechnic Institute and State University, Report CE/VPI-ST-12/08, Blacksburg, VA.
- Myers, J. J., Holdener, D. J., Merkle, W., and Hernandez, E. (2008). "Preservation of Missouri transportation infrastructures: validation of FRP composite technology through field testing—in-situ load testing of bridges P-962, T-530, X-495, X-596 and Y-298" Report No. OR09-007, Missouri DOT, Jefferson City, MO.
- Nosdall, S. V. (2013). "Experiments on a Hybrid Composite Beam for Bridge Applications." M. S. thesis, faculty of the Virginia Polytechnic Institute and State University, Blacksburg, VA.
- Roeder, C. W., Stanton, J. F., and Feller, T. (1989). "NCHRP Report 325: Low Temperature Behavior and Acceptance Criteria for Elastomeric Bridge Bearings." TRB, National Research Council, Washington, DC.
- Snape, T., and Lindyberg, R. (2009). "Test Results: HC Beam for the Knickerbocker Bridge." Advanced Structures & Composites Center Conducts, AEWG Report 10-16, University of Maine, Orono, ME.
- Yazdani, N., Eddy, S., and Cai, C. S. (2000). "Effect of bearing pads on precast prestressed concrete bridges." *Journal of Bridge Engineering*, Vol. 5, No. 3, pp. 224-232.

PAPER**IV. DURABILITY OF HYBRID COMPOSITE BEAM (HCB) BRIDGES
SUBJECTED TO VARIOUS ENVIRONMENTAL CONDITIONING****Mohamed A. Aboelseoud¹ and John J. Myers, F.ASCE²****Abstract**

The hybrid composite beam (HCB) is a novel idea that combines conventional construction materials (i.e., steel and concrete) with fiber reinforced polymer (FRP) composites in a new configuration. This hybridization aims to optimize the beam's structural performance and produce a structural element that is more durable than conventional members. This study examined the durability of a commercial glass FRP (GFRP) laminate that was used to encase the HCB elements in a recently constructed HCB bridge. The E-glass/vinylester laminate was subjected to five aging regimes. These conditioning regimes simulated an alkaline attack, a salt attack, a salt attack that was preceded by UV-irradiation exposure, and sustained stresses that were accompanied by controlled thermal cycles and natural weathering. The durability of the E-glass/vinylester laminate was examined in terms of changes that were occurred in the ultimate tensile strength. A microstructural analysis was performed on both unconditioned and conditioned specimens via optical microscopy (OM), scanning electron microscopy (SEM), energy-dispersive X-ray (EDX) analysis, and Fourier transform infrared (FTIR) spectroscopy. The microstructural analysis revealed that the hydroxide and chloride ions penetrated the laminate through the existing voids and cracks without causing hydrolysis to the vinylester resin. Both the alkaline and the salt solutions caused fiber-matrix debonding and reduced the glass fibers load-bearing through physico-chemical processes (leaching and the dissolution of fibers). The tensile strength was reduced greatly under the alkali attack. Mechanical testing and microstructural analysis provided fundamental insight into the durability and stress corrosion mechanisms of the examined GFRP shell under different environmental effects. This information is valuable to enhance the GFRP shell's durability.

CE Database of subject headings: Durability; GFRP composites; Hybrid composite beam; Synergistic effects; Microstructural analysis; Alkaline environment; Salt fog; Sustained stress.

Introduction

A new hybrid composite beam (HCB) was recently used to construct three bridges in Missouri. This HCB consists of a self-consolidating concrete (SCC) arch that is tied at the ends by conventional galvanized prestressing tendons. The tied arch is tucked inside a glass fiber reinforced polymer (GFRP) shell. The voids within the shell are filled with polyisocyanurate (polyiso) foam. This configuration is used to optimize the beam's performance based on the mechanical and physical properties of each component. The beam's strength and stiffness are mainly provided by cheap construction materials (i.e., steel and concrete). Whereas, the environmental protection is provided by more expensive, however, relatively more durable material. Subsequently, the composite shell must possess not only sufficient strength and stiffness to withstand the self-weight and the expected loads but also relevant physical and in-service properties that can endure the aggressive environmental conditions. These properties are of primary importance in relation to both the durability of the fiber reinforced polymer (FRP) composite shell and the HCB as a whole. A typical cross-section of the HCB used in bridge 0439 (B0439) is illustrated in Figure (1). This bridge was the first HCB bridge to be constructed in Missouri.

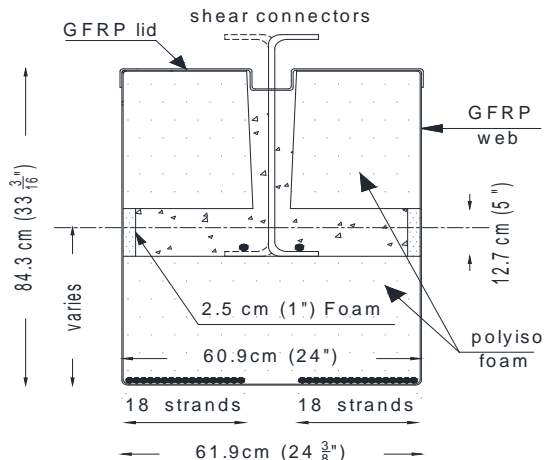


Fig. 1. Typical cross section of B0439 HCB

The HCB's GFRP shells, which were either deployed in real bridge applications or used in laboratory testing, were fabricated by Harbor Technologies LLC., Maine. Several studies have examined the HCB's structural behavior (Hillman, 2003; Hillman, 2008; Snape and Lindyberg, 2009; Ahsan, 2012; Mascaro and Moen, 2012; Nosdall, 2013; Aboelseoud and Myers, 2014b). None of these studies, however, performed a realistic evaluation of the HCB's durability. Snape and Lindyberg (2009) subjected the HCB shell to UV-irradiation testing regime. This exposure regime did not reflect the actual weathering conditions to which the HCB will be subjected.

The current Research Objectives

The primary objectives of this research were as follows:

1. Perform a factual assessment of the HCB shell's durability under different conditioning regimes that simulate actual environmental weathering in Missouri.
2. Conduct microstructural scale tests to identify the damage mechanisms under different environmental exposures.
3. Provide recommendations for enhancing the shell's durability and thus the HCB's durability.

Specimen Details

Harbor Technologies LLC., Maine provided four panels for testing purposes. These panels were similar to the shell webs used in Missouri bridge B0439 HCBs. They were fabricated via the vacuum assisted resin transfer molding (VARTM) process. Each panel consisted of the following layers (listed from the exterior surface inward): a layer of surface veil, a layer of continuous flow media (CFM), a layer of off-axis knit fabric with +/- 45 degree plies (E-BXXS 2410), and a layer of quad knit fabric with 0, 90 and +/-45 degree plies (E-QX 10200). Both the veil and the CFM layers facilitate the resin transfer and provide a resin rich layer on the beam shell's outside perimeter. The first layer (E-BXXS 2410) was 0.76 mm (0.03 in) thick and weighted 1172.10 g/m² (34.6 oz/yd²). The second layer (E-QX 10200) was 2.03 mm (0.08 in) thick and weighed 3426 g/m² (101 oz/yd²). The fiber content (by weight) in the E-QX 10200 was 68%. Fifty percent of the rovings in this layer were oriented in the warp (longitudinal) direction (0°); fourteen percent were oriented in the fill (transverse) direction (90°). The remaining fibers were equally oriented by +/- 45° angles.

A CCP Stypol 040-8086 resin was used to infuse the glass fabrics of B0439. This matrix is a Bisphenol-A, epoxy vinylester resin that is generally combined with styrene to lower the viscosity for infusion. The resin contained a pigment that included inhibitors for ultraviolet (UV) irradiation. The veil and CFM layers provided an extra layer for UV protection. Two panels (designated 3 and 4) were painted with a post-applied gel coat comprised of a UV inhibiting paint. This paint was roller applied to the exterior surfaces of the B0439 fascia HCBs (Hillman, 2012). Panels 1 and 2 remained uncoated.

Water jetting technology were used to cut all four panels into 120 coupon specimens in both the longitudinal and the transverse directions. The specimen's configuration of the specimens is illustrated in Figure (2). Eight specimens (four in the longitudinal direction and four in the transverse direction) from each of panels 2 and 4 were used as control specimens. Six specimens (three in the longitudinal direction and three in the transverse direction) from each of panels 1 and 3 were used as control specimens. The remaining specimens were subjected to different aging regimes.

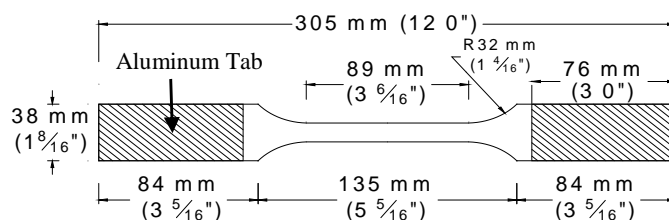
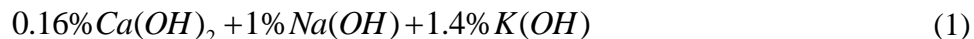


Fig. 2. Dimensions of the GFRP specimens

Aging Regimes

Alkaline Environment Exposure Regime

A concrete pore solution is highly alkaline with a pH between 10 and 13.5 (Diamond, 1981; Taylor, 1987). Sixteen specimens were immersed in a simulated concrete pore solution at room temperature (24°C, 75°F) for 80 days. These specimens were taken from panels 2 and 4 (Four in the longitudinal direction and four in the transverse direction from each panel). The following percentages by weight of calcium, sodium, and potassium hydroxides were dissolved into distilled water to produce a simulated concrete pore solution (Micelli and Nanni, 2004).



The prepared solution had a pH of 13.25. A pH meter was used to measure the solution's pH each two weeks. The solution was replaced with a freshly prepared solution after 40 days, so that the pH remained higher than 13 throughout the exposure period.

Salt Fog Exposure

A total of 12 specimens (panels 2 and 4) were exposed to continuous salt fog cycles for 128 days according ASTM B117. The salt solution contained 5% (by weight) Sodium

Chloride (NaCl). The chamber's temperature was maintained at 35°C (95°F) via chamber heaters throughout the test.

UV-Irradiation and Salt Fog Exposure

A total of 12 specimens (panels 2 and 4) were subjected to UV-irradiation for 128 days. This regime consisted of continuously repeated cycles. Each cycle consisted of 4 hours of UV exposure that were followed by 4 hours of condensation (dark period). Fluorescent lamps with an irradiance of 0.89 W / (m².nm) were used to subject the specimens to UV-irradiation at 340 nm. The temperature during the 4 hours of UV exposure was maintained at 60 ± 2.5°C (140 ± 5°F). The temperature was maintained at 50 ± 2.5°C (122 ± 5°F) during the black period. The specimens were subjected to salt fog for 252 days according to ASTM B117 when the UV exposure was complete.

Thermal Cycling and Sustained Stress Regime

Twenty-four specimens (panels 1 and 3) were subjected to sustained stresses in conjunction with a series of thermal cycles in a computer-controlled chamber. These thermal cycles continued for 75 days to simulate seasonal effects in the mid-west United States. The specimens in the environmental chamber were subjected first to 50 freeze-thaw cycles. The temperature was between -20°C and 10°C (-4°F to 50°F) during these cycles to simulate the winter season effects. The summer season effects were then simulated by 300 cycles. These 300 cycles consisted of three identical groups of 50 high temperature cycles alternated with three different groups of 50 high relative humidity (RH) cycles. The temperature during the high temperature cycles was between 20°C and 50°C (68°F and 122°F). The RH varied between 60% and 95% at a constant temperature of 20°C (68°F) during the first 50 RH cycles, to simulate the humidity and rain that occur during the night. The second group of RH cycles simulated the humidity and rain that occur during the day. The RH varied between 60% and 95% at a constant temperature of 25°C (77°F) during these cycles. The third group of RH cycles simulated the heat that may emit from the bridge deck during rain, causing the nearby air temperature to rise to a higher level. In these cycles, the RH varied from 60% to 95% at a constant temperature of 40°C (104°F).

Two holes were drilled at the top and bottom of the GFRP coupons so that sustained stresses could be applied to the specimens. Each specimen was then hung on a wide bar; a concrete block was attached to the bottom of each specimen. The concrete blocks had two different weights: heavy weight (HW) blocks with an average weight of 48 kg (106 lb) and lightweight blocks (LW) that had an average weight of 25 kg (55 lb). The HW blocks produced stress levels of 4.4% and 7.4% of the ultimate tensile strength of the longitudinal and transverse specimens, respectively. The LW blocks produced stress levels of 2.3% and 3.9% of the ultimate strength of the longitudinal and transverse specimens, respectively. These stress levels were used to simulate the shell's in-service stress levels (Aboelseoud and Myers, 2014a; Aboelseoud and Myers, 2014b).

Natural Weathering and Sustained Stress Regime.

A total of 24 specimens were subjected to the same stress levels as those in the previous regime in both outdoor and indoor weathering, for 240 days. Twelve specimens taken from panel 3 were subjected to these sustained stresses in natural outdoor weathering. Twelve specimens taken from panel 1 were subjected to the sustained stresses at room temperature.

Tensile Strength Test

The GFRP shell's durability was quantified in terms of changes that occurred in the ultimate tensile strength in both the longitudinal and the transverse directions. An MTS880 test machine was used to conduct tensile strength tests. Changes that took place in the ultimate tensile strength under the different aging regimes are illustrated in Figures 3 and 4. The percentage of change in the tensile strength of the exposed specimens, relative to the control specimens, is written above each bar. The alkali exposure regime caused significant loss in the GFRP shell's tensile strength (up to 37%). Whereas, the reduction of the tensile strength under the other conditioning regimes was less than 21%. Consequently, the alkali effects on the GFRP laminate receive more discussion for the remainder of this paper.

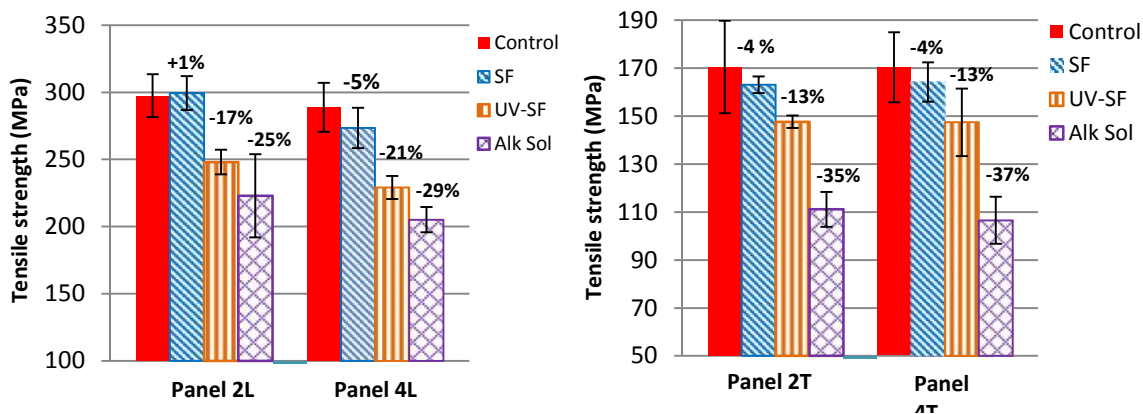


Fig. 3. Comparison between the tensile strength of control specimens (panels 2 and 4) and specimens exposed to alkali, salt fog, and UV-salt fog attacks

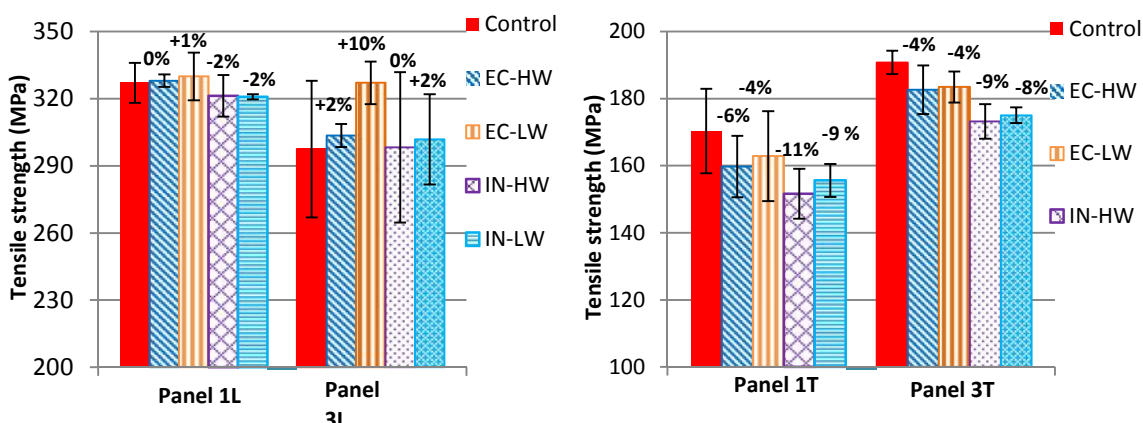


Fig. 4. Comparison between the tensile strength of control specimens (panels 1 and 3) and specimens exposed to Sustained stresses with controlled and natural thermal cycles

Microstructural Analysis

Microstructural analysis was performed in an effort to better understand the damage mechanisms of the examined GFRP composite under different environmental conditions. Understanding the damage mechanisms was achieved by observing: the diffusion of harmful ions into the GFRP laminate, matrix cracking, matrix hydrolysis, fiber-matrix debonding, and fiber deterioration.

Energy dispersive X-ray (EDX) analysis was performed to detect the diffusion of any aggressive ions into the composite shell. Scanning electron microscopy (SEM) images in conjunction with EDX analysis were used to identify fiber degradation. First, SEM micrographs were used to identify the damaged fibers. The EDX analysis was then performed so that any change that occurred in the fiber's chemical composition could be detected. This analysis helped with differentiating between a fiber that may have been damaged during the specimen preparation process (grinding and polishing processes) or one that was damaged by a chemical attack. Highly magnified SEM images were used to identify the fiber-matrix interface deterioration and the matrix micro-cracking. Fourier transform infrared (FTIR) spectroscopy was used to examine the matrix hydrolysis. An Optical microscope (OM) was also used to inspect the formation of voids and micro-cracks on surfaces of control and conditioned specimens.

Results Discussion

Control Specimens

Both a micrograph and the EDX analysis results for a control sample, taken from panel 4 in the transverse direction (4T-C), are illustrated in Fig 5). The fibers had variable diameters; with average diameter was 20 μm . The energy dispersive spectroscopy (EDS), did not detect zirconium dioxide (ZrO_2) as illustrated in Figure 5b. Thus, the fibers that reinforced the HCB's shell were normal E-glass and not alkali resistance (AR) fibers. This result was expected because the alkali attack significantly reduced the tensile strength. The percentage of silica (SiO_2) detected during the EDX analysis (62%) indicated that these fibers were boron free E-glass (did not contain Boron trioxide, B_2O_3)

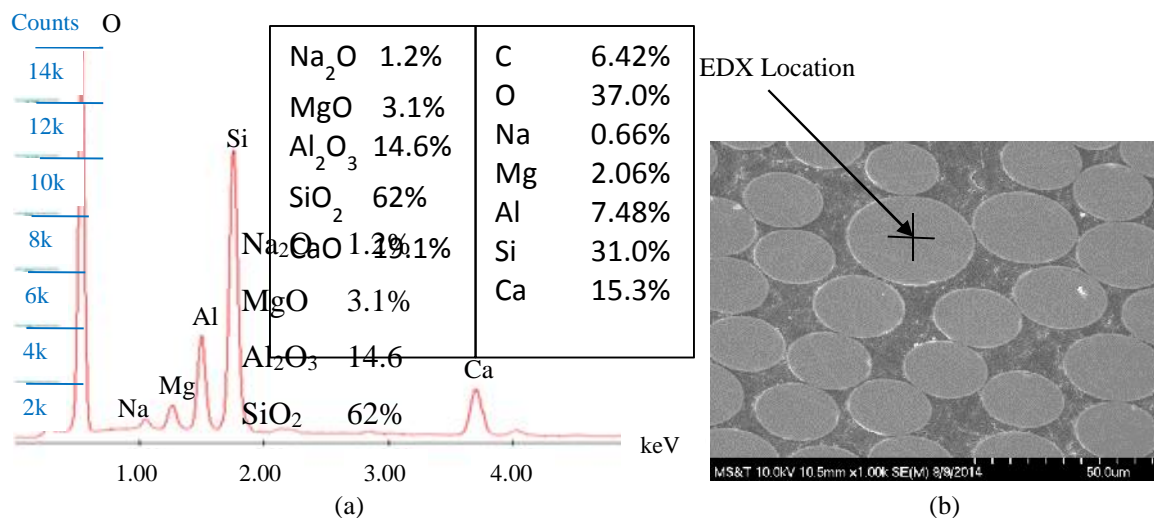


Fig. 5. Specimen (4T-C) (a) Chemical analysis by EDX
(b) Surface morphology by SEM (X1000 = magnified 1000 times)

Alkaline Environment Effects

SEM and EDX Tests

The SEM micrographs of exposed specimens that were taken from panel 4 in the longitudinal direction (4L-Alk) are illustrated in Figures 6 and 7. These figures contain images of fibers that were located in the first knit fabric layer (E-BXXS 2410). The EDX analysis revealed that the sodium (Na^+) percentage increased from approximately 1% in the control specimen to approximately 12% in the conditioned specimens. The calcium (Ca^{+2}) content in the fiber was reduced significantly and no potassium (K^+) ions were detected in the inspected fibers. These results demonstrate that only the sodium ions were able to penetrate the GFRP laminate. This can be attributed to the higher diffusivity of the sodium because of its smaller size than the calcium and potassium atoms. The hydroxide ion (OH^-) was absent in the elemental analysis results because it is a light ion that cannot be detected by EDX analysis. In general, the EDS cannot detect either elements or ions that are lighter than sodium (Mufti et al., 2007). However, the significant increase of the Na^+ ions in the inspected fibers is an evidence of the diffusion of the OH^- ions together with the Na^+ ions. The diffusion of the aggressive OH^- ions into the laminate is expected to maintain the charge neutrality of the Na^+ ions.

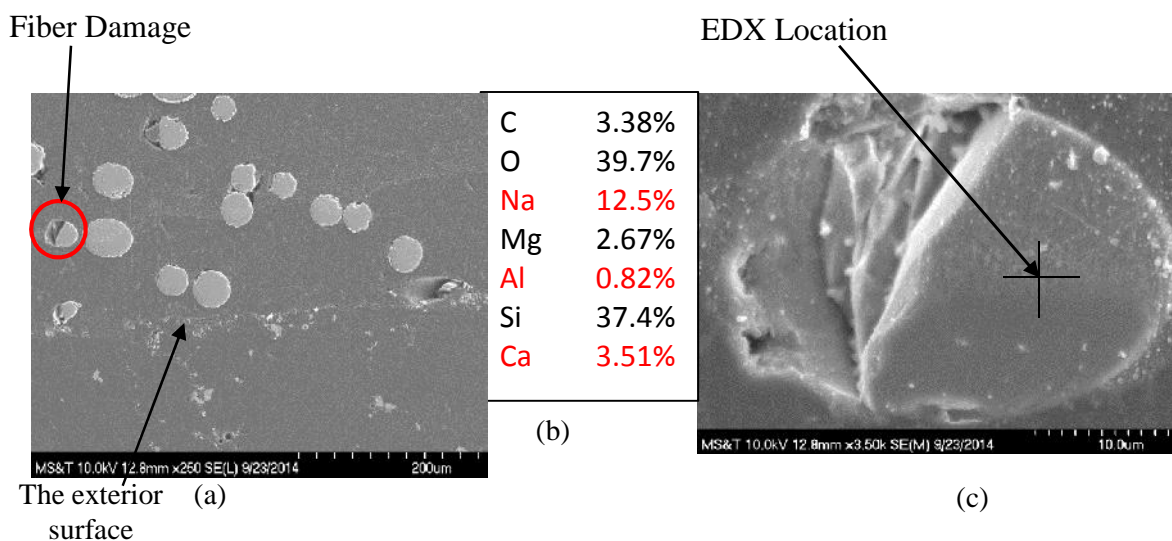


Fig. 6. (a) SEM micrographs in 4L-Alk (X250), (b) EDX for the circled fiber in (a) (c) SEM for the circled fiber in (a) (X3500)

The EDX results illustrated in Figures 6 and 7 clarify that the aluminum (Al^{+3}) ions were decreased from approximately 7% to less than 1%. The Ca^{+2} ions were reduced from approximately 15% to less than 4%. These results illustrate that the penetration of $NaOH$ led to ion exchange process and, thus, leaching of the inspected fibers. The diffusion of metalloids and alkali earth ions (Al^{+3} and Ca^{+2} , respectively) out of the glass structure led to a loss in the cross-sectional area of the attacked fibers. The SEM images illustrated in Figures 6 through 9 show clear cases of fiber damage and fiber-matrix interface deterioration.

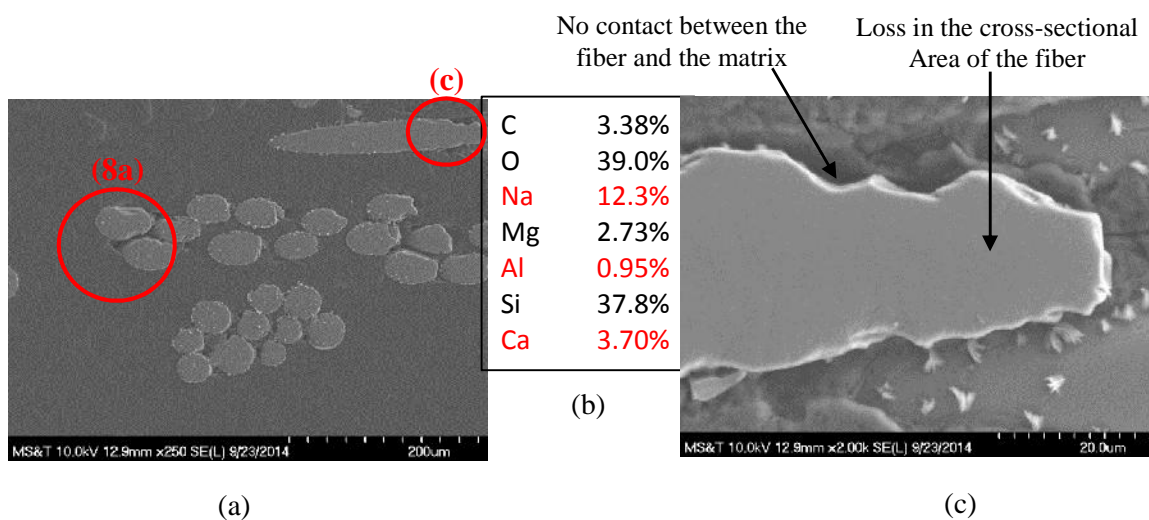


Fig. 7. (a) SEM micrographs in 4L-Alk (X250), (b) EDX for the circled fiber in (a) (c) SEM for the circled fiber in (a) (X3500) (at distance 0.76 mm (0.03 in) from the exterior surface)

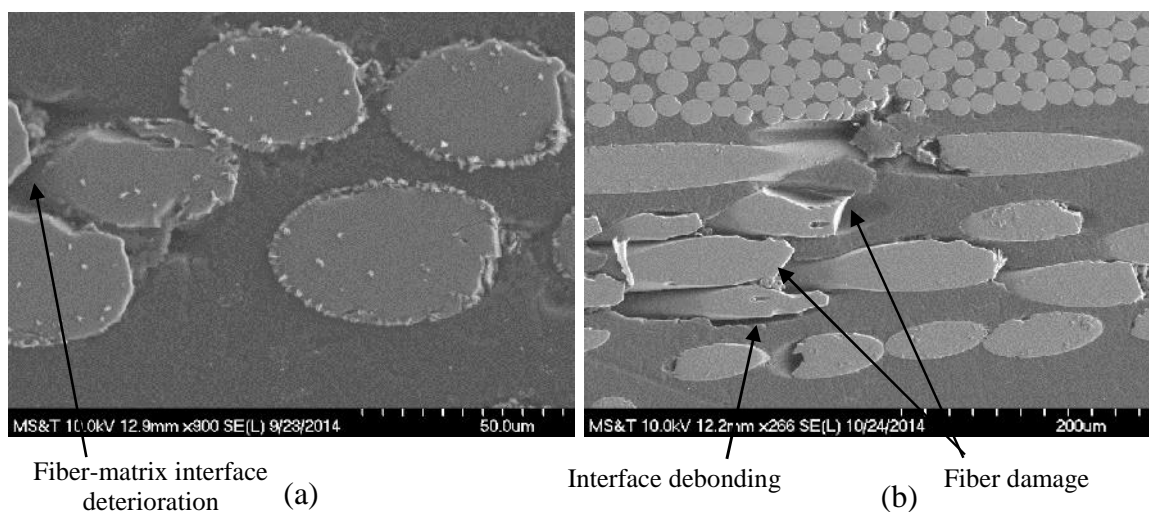


Fig. 8. Fiber damage and fiber-matrix interface deterioration in (a) 4L-Alk specimens at distance 0.35 mm (0.01 in) from the exterior surface (first layer) (b) 4T-Alk in the first layer

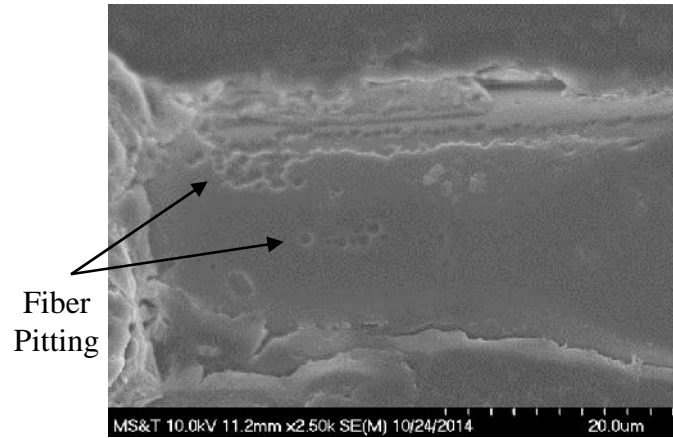
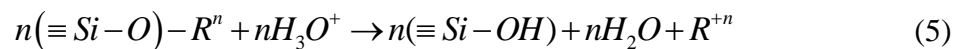
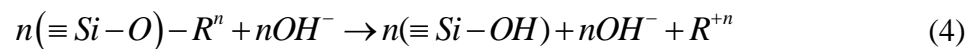
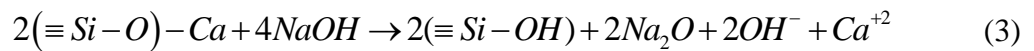
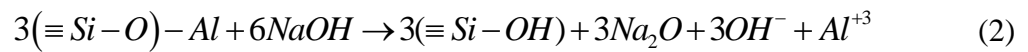
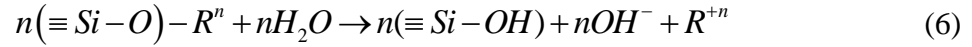


Fig. 9. Fiber etching and notching in the first lamina of specimen 4T-Alk

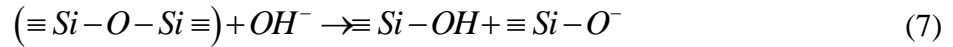
The chemistry of the fiber degradation in an alkaline environment has been studied extensively (Cox, 1976; Lewis, 1989; Sonawala and Spontak, 1996; Chong, 1998; Nkurunziza et al., 2005; Onofrei, 2005; Kamal, 2011). The microstructural analysis and the mechanical testing results gathered during this study together with the results gathered from previous studies, indicate that the following reactions were responsible about the fiber's deterioration under the current alkali exposure regime:

Ion-Exchange (leaching)





Overall Network Dissolution



The solution reacts chemically with individual fibers when an alkaline solution penetrates the resin and contacts the glass fibers. The first chemical reaction that takes place is the diffusion of the alkali, the earth alkali, and/or the metalloids out of the glass structure (Equations 2 and 3). This process is referred to as leaching (dissolution) of the glass fibers (Nkurunziza et al., 2005). The $Si-O-R$ bond (R is the alkali, the earth alkali, or the metalloids ions in the glass structure) dissociates during this process (Cox, 1976; Lewis, 1989). This bond dissociation can take place as a result of either the chemical reaction between the glass and the $NaOH$ (Equations 2 and 3) or the free OH^- , H^+ , or H_3O^+ (Hydronium) ions in the alkaline solution (Equations 4 and 5). The free ions are able to react (to a higher degree) with the fiber and matrix than the other ions (Tannous and Saadatmanesh, 1999). Glass fiber leaching can be produced by not only an alkali attack but also a moisture attack, as shown in Equation 6. The leaching process continues as long as the alkali, earth alkali, or metalloids ions are available in the glass fibers. The EDX analysis revealed that significant reductions occurred in the Al^{+3} and Ca^{+2} percentages to less than 1% and 4%, respectively.

The OH^- ions that are produced by leaching (Equations 2 to 6) increases the pH of the alkaline environment around the fibers. $Si-O-Si$ bonds, as well as the $Si-O-R$ bonds are broken when the pH of the alkaline environment exceeds nine (Cox, 1976; Sonawala and Spontak, 1996), as illustrated in Equation 7. The gel byproduct $SiOH$ (silicon hydroxide) is formed during all of the fiber degradation processes (Equations 2 to 7). This gel layer is less dense than the original glass structure. It is able to transport the water and the alkali ions easily, accelerating the deterioration mechanism (Tannous and Saadatmanesh, 1998). Finally, the OH^- ions attract the fibers' surface generating cracks which, subsequently, degrade the fibers' strength (Nkurunziza et al., 2005).

The formation of white material at the glass interface produced by the alkali attack is illustrated in Figure 10. The crystalline shape of this material suggested that it was not $SiOH$. An EDX analysis was performed to part of this material. The result of this analysis (Figure 10) suggested that this material was produced by the interaction of the alkali solution with either the coupling agent or the glass fiber. Coupling agents used for glass fiber reinforcement are basically organo-silanes. Silane coupling agent has a silicon end that bonds well to glass fibre and an opposing organic end that bonds well to resins (Kamal, 2011). Another degradation mechanism that results from the reaction of the silica with the sodium hydroxide produces sodium metasilicate (Na_2SiO_3). The (Na_2SiO_3) is also known as the water glass or liquid glass. This degradation takes place as follows:

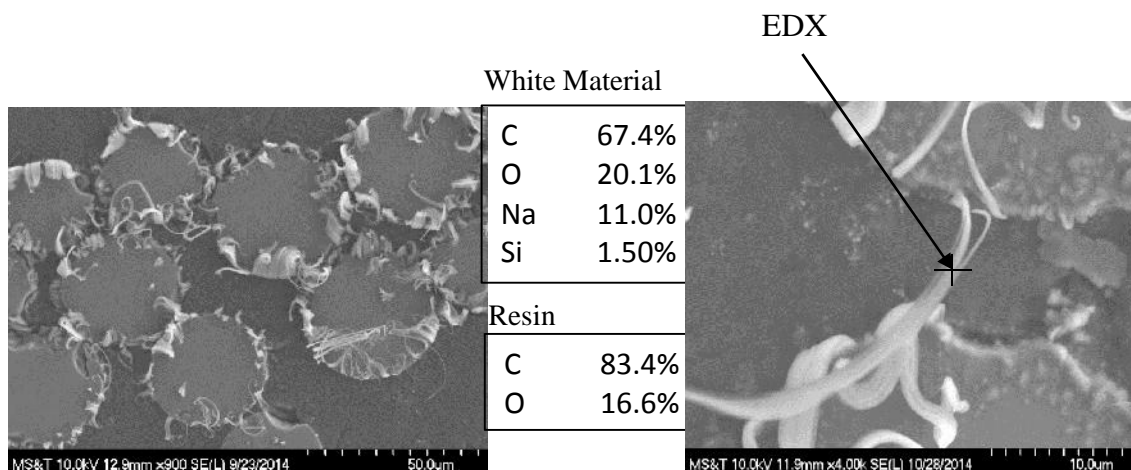


Fig. 10. SEM micrograph in 4-L-Alk (X900) in the first lamina

Both the SEM micrograph and the EDX analysis results for fibers at a distance greater than approximately 1 mm (0.04 in) from the exterior surface are illustrated in Figure 11. This SEM image does not contain any signs of either fiber damage or fiber-matrix debonding. The EDX result is in agreement with the surface morphology, clarifying that

the OH ions did not attack the fibers and fiber leaching did not occur. These results demonstrate that the alkali attack was confined in the first lamina, while the fibers in the second lamina remained unaffected. The microstructural analysis illustrated that the fibers that were very close to the specimen's interior surface (in the second lamina) remained as well unaffected. All the specimens were placed in two containers such that they were rested through the interior surfaces directly on the container's base. Therefore, the containers likely protected the specimen's interior surfaces from the alkali attack.

Sonawala and Spontak (1996) found that a vinylester/E glass laminates suffered a higher loss in tensile strength under an alkali attack after two different surface veils were added to the laminates. They concluded that the two types of surface veil facilitated $NaOH$ wicking through the resin leading to, a greater reduction in the tensile strength. Consequently, the surface veil that was used in the examined laminate herein may have facilitated the $NaOH$ diffusion through the exterior face. The effect of this surface veil on the laminate durability needs to be tested.

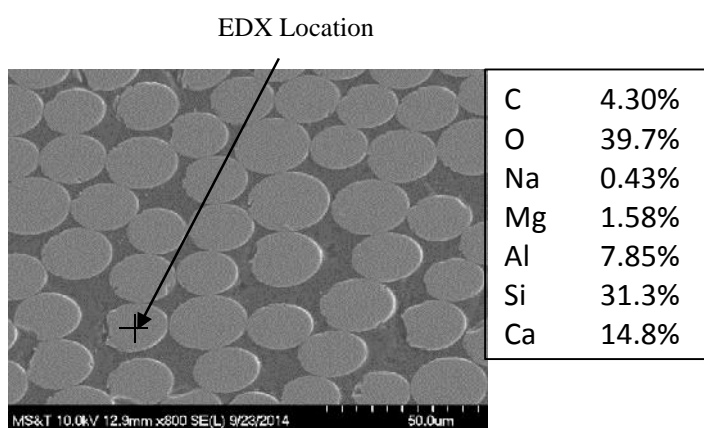


Fig. 11. SEM micrograph and EDX for 4L-Alk (X800) at distance > 1 mm (0.04 in) from the exterior surface (2nd layer)

The fiber-matrix interphase is a critical region that affects not only the properties of an FRP composite but also the degradation of these properties. Adhesion between the fibers and the matrix is achieved by mechanical interlocking between the surface features on the fibers and the matrix, a wetting of the fibers by the matrix, and a chemical bonding

between the fibers and the matrix (Barkatt, 2001). The interphase region is vulnerable to aqueous solution ingress and, subsequently, to degradation because of the relative weakness of the bonds in this region (Barkatt, 2001). Kamal (2011) suggested that the degradation of a GFRP composite in an alkaline environment begins at the fiber-matrix interphase. Fiber degradation can, in some cases, begin before the fiber-matrix interphase begins to deteriorate. Fibers in the first ply are illustrated in Figure 12. An EDX analysis to these fibers provided results that are similar to those displayed in Figures 6 and 7, indicating that these fibers began to leach. The attacked fibers have perfect contact with the matrix; no signs of fiber-matrix debonding are visible. Similar cases were observed in SEM micrographs, demonstrating that the degradation process is not always initiated at the fiber-matrix interphase. Fiber leaching did, however, begin at the fiber's surface. Consequently, fiber leaching will weaken the mechanical interlocking between the fiber and the matrix. Complete debonding will occur after a significant loss takes place in the fiber's cross-sectional area.

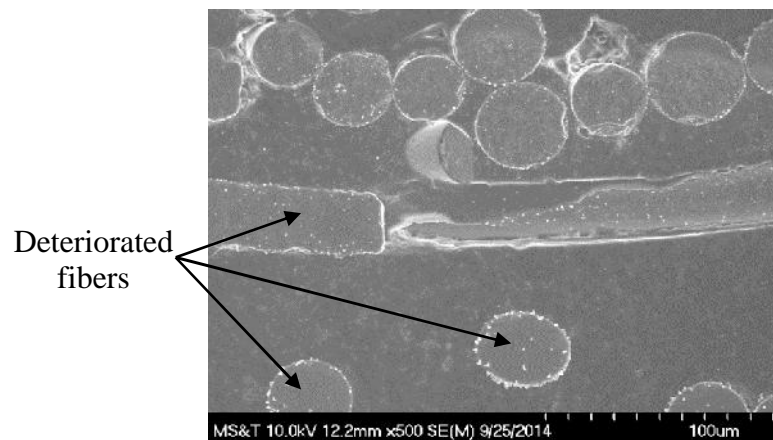
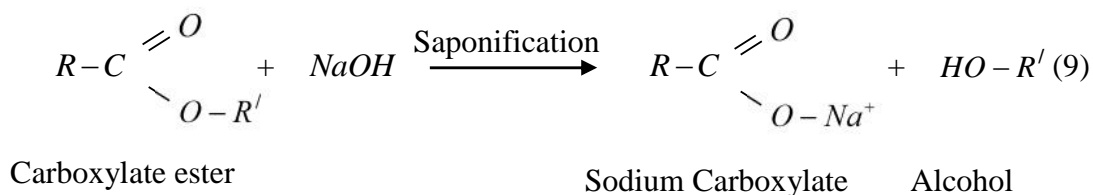


Fig. 12. SEM micrograph in 4L-Alk

FTIR Tests

The chemical nature of the long molecular chains within a polymeric matrix largely controls polymer's durability. All resins have ester bonds in their molecular structures. These bonds are the weakest links in a polymer's chain (Mufti et al., 2007; Kamal, 2011). The hydrolysis of the matrix' ester linkages in an alkaline environment is illustrated in Equation 9 (Carey and Sundberg, 2007).

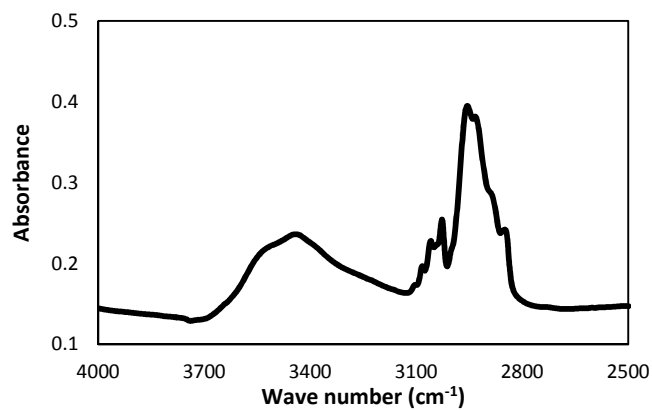


Changes in the amount of hydroxyl groups (*OH*) within the polymer matrix provide information on the extent of the polymer hydrolysis. The *CH* (carbon-hydrogen group) content in a polymeric resin is assumed to be constant. Subsequently, any change in the *OH/CH* indicates polymer hydrolysis. If the matrix of a conditioned sample is deteriorated, the *OH/CH* of this sample is expected to be higher than the *OH/CH* of an unconditioned sample. The maximum of the band corresponding to *OH* groups was at 3440 cm^{-1} ; the maximum of the band corresponding to *CH* groups was at 2955 cm^{-1} , in the current study.

The *OH/CH* content for both the control and the conditioned specimens under different exposure regimes is listed in Table (1). Typical FTIR spectra graphs for the control specimen (4L-C) and the conditioned specimen in the alkaline solution (4L-Alk) taken from panel 4 in the longitudinal direction are illustrated in Figures 13 and 14, respectively. The two graphs are almost identical clarifying that, though the *NaOH* diffused into the laminate, it didn't cause significant hydrolysis to the vinylester resin.

Table 1. Ratio for OH/CH for control and conditioned specimens

Specimen	OH/CH
1T-C	0.79
1T-IN-HW	0.79
3L-C	0.77
3L-EC-LW	0.77
3T-OUT-HW	0.77
4L-C	0.79
4L-Alk	0.72
4T-Alk	0.78
4L-UV-SF	0.82
2L-UV-SF	0.86

**Fig. 13.** Typical FTIR Spectra for 4L-C

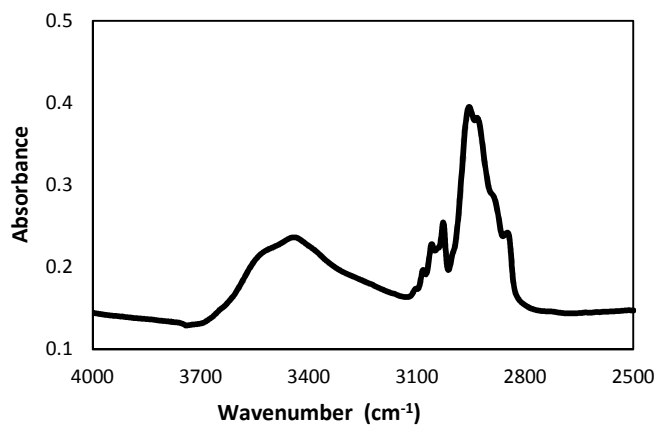


Fig. 14. Typical FTIR Spectra for 4L-Alk

A large number of voids were visible in all the specimens. An OM micrograph that illustrates the existing voids at the exterior surface of control specimens is illustrated in Figure 15. The OM images clarified that the penetration of the alkali solution took place through the existing voids in the matrix. An image that depicts the alkali attack to the fibers through the existing voids is illustrated in Figure 16. The inspection of conditioned specimens' surfaces didn't show any formation of micro-cracks on these surfaces. This finding is compatible with the FTIR, confirming that the resin did not react chemically with the alkali solution.



Fig. 15. Optical Microscope images illustrate existing voids at: outer surface (left image) and inner surface (right image) of control specimens

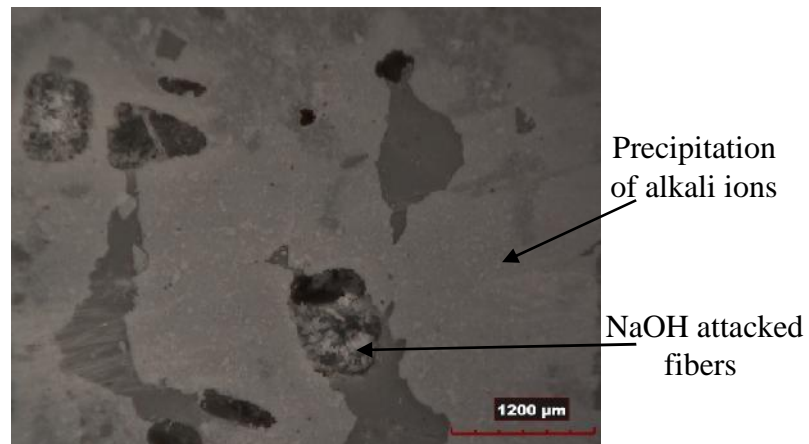


Fig. 16. NaOH attack to the fiber through existing voids in outer surface (2L-Alk)

Damage Mechanism under Alkali Attack

The microstructural analysis results indicate that the following stress degradation mechanism occurred:

- The sodium hydroxide penetrated the vinylester resin through the existing voids due to fabrication imperfections.

- The penetration was then facilitated by both capillary effects through the matrix and wicking along the fiber-matrix interface (Lewis, 1989; Sonawala and Spontak, 1996).
- When the solution contacted the glass fibers it reacted chemically with individual fibers causing them to leach and dissolve. The leaching process started at the surface of the fiber reducing the cross-sectional area of the fiber and decreasing the fiber load-bearing.
- Dissolution of the surface layer destroyed the retarding effect for this layer and opened up a larger area of unaffected glass for the surrounding alkali to attack.
- Fiber-matrix interface debonding took place either before the fiber deterioration due to breaking the covalent bond between the fiber and the matrix or after the fiber deterioration due to the reduction in the fiber's cross-sectional area.
- Both the interface debonding and the fiber damage lead to significant reduction in the tensile strength of the conditioned specimens, though the penetration was limited to the first ply.

Salt Fog, and UV-irradiation and Salt Fog Effects

Figures 17 and 18 show SEM micrographs and EDX analysis for specimens (taken in the longitudinal direction of panel 4) exposed to salt fog for 4 months (4L-SF). As it is shown by the EDX analysis, the percentage of the Na^+ ions in the examined fibers increased to approximately 12% assuring the diffusion of the $NaCl$ into the laminate. The EDS clarified that all the fibers within the first ply were attacked by the salt solution. Similar to the alkali exposure regime, no Na^+ ions were detected in the second ply. The salt fog apparatus sprayed the salt solution mainly on the exterior surface. Consequently, no penetration from the interior surface was also detected.

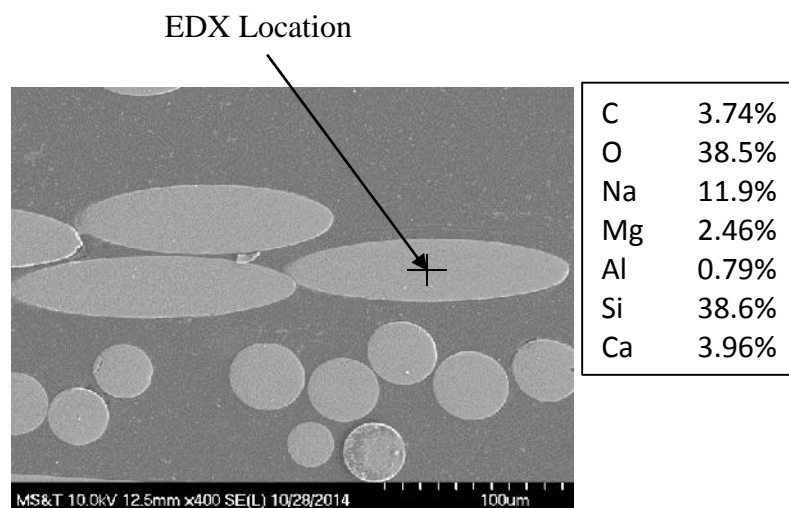


Fig. 17. SEM micrographs in 4L-SF (X400) and EDX analysis

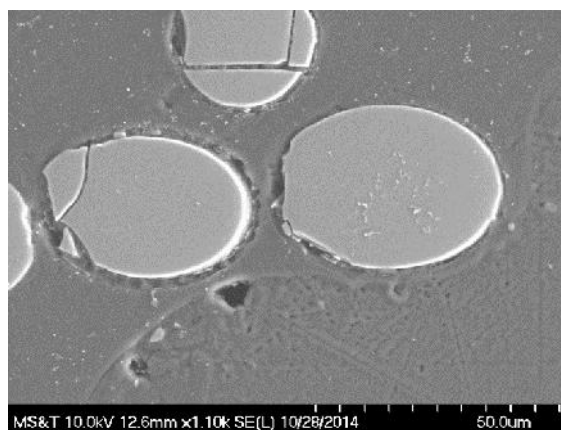


Fig. 18. SEM micrographs in 4L-SF (X1100)

The Al^{+3} and Ca^{+2} in the attacked fibers decreased to almost the same percentages as under the alkali attack. However, the surface morphology by SEM illustrated that the majority of the attacked fibers had perfect interface with the resin (see Figure 17). Moreover, the most of attacked fibers neither were damaged nor suffered loss in the cross-sectional area. Only, a limited number of the attacked fibers were damaged and/or interface

debonding occurred around these fibers, as illustrated in Figure 18. The EDX analysis indicates that the $Si-O-R$ bond of the attacked fibers was broken due to chemical reactions similar to the reactions presented by equations 2 and 3 (with $NaCl$ instead of $NaOH$), equation 4 (with Cl^- instead of OH^-) as well as equation 6. The tensile testing showed that the maximum strength loss under this exposure regime was 5%. This result together with the surface morphology suggests that the OH^- ions produced by the dissolution of fibers in water (equation 6) did not increase the alkalinity around the fibers beyond nine during four months of exposure. Subsequently, $Si-O-Si$ bonds of the majority of the fibers in the first lamina were not broken resulting in insignificant reduction in the tensile strength.

The fibers in specimens, which were subjected to UV irradiation followed by salt fog solution, suffered the same chemical composition changes as in the previous two regimes (Figure 19). After eight months of exposure to the saline solution, the Na^+ penetration was also limited to the first lamina. However, when the exposure time increased from four to eight months, the interface debonding and the fiber damage were more severe and similar to what experienced under the alkali attack (Figure 20). The FTIR results clarified that the vinyl ester resin didn't react with the saline solution (Table 1). Figure 21 illustrate the attack of the $NaCl$ to the fibers through the existing voids similar to the alkali attack.

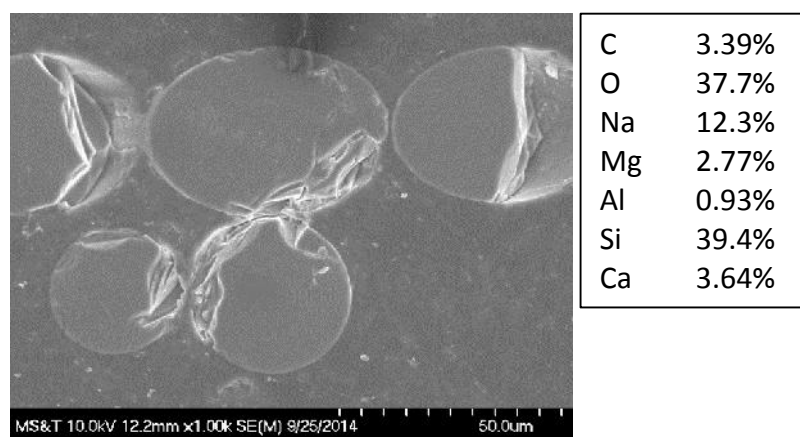


Fig. 19. SEM micrographs in 4L-UV-SF (X1000) and EDX analysis results

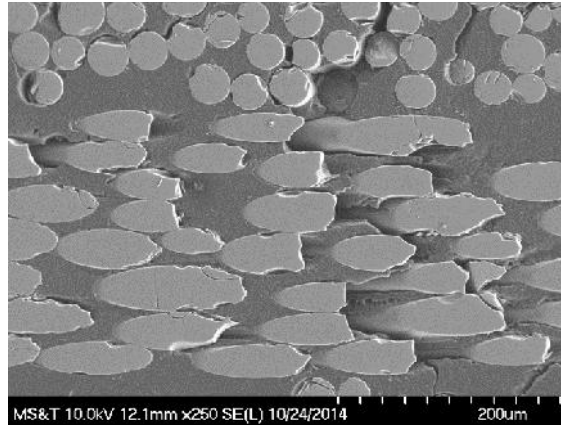


Fig. 20. SEM micrographs in 4L-UV-SF (X250) and EDX analysis results

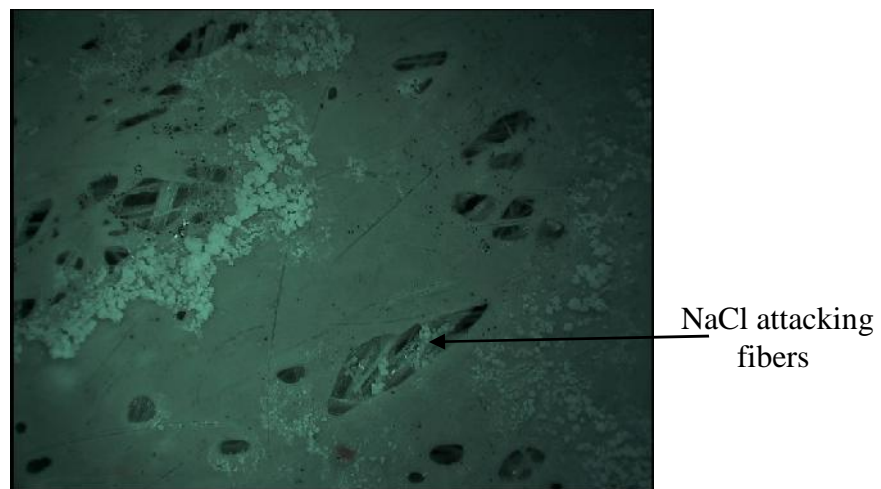


Fig. 21. NaCl attack to the fiber through existing voids in outer surface (2L-SF)

The microstructural analysis demonstrated that the stress corrosion mechanism of the examined GFRP laminate under the salt attack was similar to the degradation mechanism under the alkali attack. However, the higher reduction in the mechanical properties under the alkali attack can be attributed to:

1. The diffusion rate of the OH^- ions is higher than the diffusion rate of the Cl^- ions due to the higher mobility of the OH^- ions. Subsequently, it is expected that the

alkali solution contacted all the fibers within the first lamina and started to react with them during shorter time than that was needed for the salt solution to contact the same number of fibers.

2. The high alkalinity of the concrete pore simulated solution resulted in dissolution of the SiO_2 network shortly after the contact between the solution and the fibers. However, in the case of the saline solution, the pH of the solution around the fibers remained below nine for long time. This retarded the active dissolution of the SiO_2 network.
3. It is expected that the OH^- ions had more deleterious effect than the Cl^- ions not only on the fibers but also on the covalent bond between the fiber and the matrix.

Following the exposure to UV-irradiation, the exposed surfaces of coated and uncoated specimens (panels 4 and 2, respectively) were inspected by the OM. The post applied gel layer were removed from the coated specimens before the inspection. Figure 22 illustrate the formation of micro-cracks in the surface of uncoated specimen. Whereas, no micro cracks were observed in the surfaces of the coated specimens. This clarified that the post applied paint protected the laminate surface from the deleterious effect of the UV-irradiation. Previous researches reported that the UV-irradiation effect is confined to the FRP specimen's surface and leads to insignificant changes in its mechanical properties (Liau and Tseng, 1998; Karbhari et al., 2003). The UV exposure reportedly has an indirect effect on the durability although the induced micro-cracks can clearly facilitate the ingress of the liquids and chemicals; consequently reduce the mechanical properties of the composite. However, the mechanical tests showed that the coated shell suffered similar or higher reduction in the tensile strength than the uncoated specimens under the synergistic UV-SF conditioning regime (Figure 3). This can be attributed to the large number of the existing voids in the examined shell. Thus, the formed cracks likely did not cause significant increase in the ingress of the salt solution into the laminate.

Micro cracks



Fig. 22. Formation of micro cracks in the surface of uncoated specimen (2L-UV-SF) following UV

Sustained Stresses and Thermal Cycles Effects

At low temperature, the polymeric matrix becomes stiffer. Subsequently, the composite behavior that is matrix dominated, such as the torsional stiffness, improves. However, the polymeric resin coefficient of thermal expansion is generally an order of magnitude higher than that of the fiber. This significant mismatch can induce, at low temperatures, stresses in the matrix high enough to initiate the formation of microscopic cracks. When these cracks develop to a certain density and size, they will tend to coalesce to form macroscopic matrix cracks that diffuse in the resin or stroll around the matrix-fiber interface (Wang, 1986).

High temperatures that are close to the polymer glass transition temperature, T_g , may free volumes, which can be filled by other molecules as the matrix tries to reach equilibrium stage. Subsequently mechanical properties of the composite may change at these temperatures (Silva and Biscaia, 2008). Vitrification of the polymer may also take place at high temperatures. This phenomenon is an early form of decomposition of the matrix where the material become amorphous (Caceres et al., 2002). Another phenomenon

that may occur at higher temperatures is hydrolysis decomposition of the molecular structure of the polymer, which is harsh form of plasticization. The high temperature exposure does not always harm the FRP elements, especially as long as the temperature is significantly below the T_g of the matrix. In some cases, the high temperature results in beneficial post cure of the resin. This post cure increases the cross-linking of the polymer and thus increases the strength of the polymeric molecular structure.

When a sustained stress is applied to FRP composite, the composite's mechanical properties decreases with time. As the ratio of the sustained tensile stress to the short-term strength of the FRP laminate increases, the reduction in the mechanical properties increases. It is also well established that the different environmental conditions such as freeze-thaw cycles, high temperature, wet and dry, UV radiation exposure, or high alkalinity can accentuate the creep effect and decrease the endurance time (ACI440.2R-08, 2008). When the level of sustained stress is sufficiently low, the visco-elastic behavior of the resin prevents the formation of the micro-cracks (Devalapura et al., 1997).

The FTIR results showed that the matrix did not plasticized under the RH and high temperature cycles either in the environmental chamber (EC) or in the outdoor (OUT) exposure. Following the exposure regime in the environmental chamber, the specimens (1L and 3L) showed an increase in the tensile strength (Figure 3). This increase indicated that the high temperature cycles resulted in residual cross-linking of the polymeric resin. The images that were taken by both the SEM and OM (not shown here) for these specimens (1L-EC and 3L-EC) clarified that no micro-cracks were formed in the resin. This behavior clarified that the freeze/thaw cycles had no deleterious effect on the examined specimens. It also illustrated that applied stress levels for the longitudinal specimens were less than the stress threshold below which the micro-cracking in the matrix does not take place.

All (3L) specimens that were subjected to sustained stresses by HW or LW blocks either outdoor or in the environmental chamber showed an increase in the tensile strength with maximum increase equalled 10%. The coefficient of variation (COV) of the control specimens (3L) was found to be the highest COV (10.3%) among the COVs of the four panels' control specimens in the longitudinal direction. Consequently, SEM images were taken in the control specimen that had the lowest tensile strength among the three control specimens of (3L). The images illustrated that this specimen had relatively large number

of voids due fabrication imperfections (Figure 23). Though, similar voids were noticed in control and conditioned samples, the diameter and number of the voids in this control specimen were larger than those in all of the other inspected specimens. This indicated that the average tensile strength of (3L) was less than the normal due to the limited number of the tested control specimens (3 specimens).

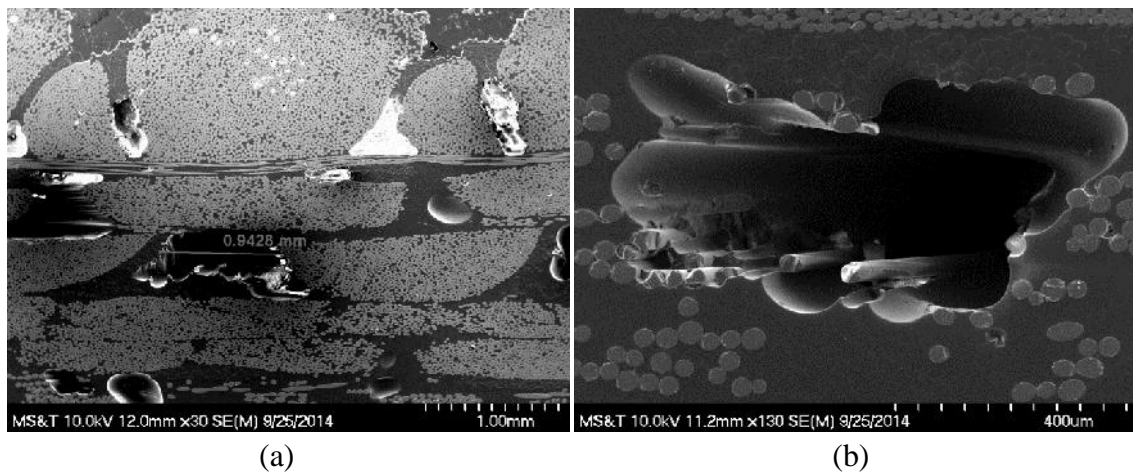


Fig. 23. Existing voids in specimen (3L-C) (a) SEM micrograph (X30)
(b) SEM micrograph (X130)

The comparison between the residual strength of the specimens that were subjected to sustained stresses in outdoor and indoor (IN) environments (Figure 4) demonstrated that the natural thermal cycles had no effect on the examined specimens. All the transverse specimens (1T and 3T) suffered higher reduction in the strength than the longitudinal ones (1L and 3L) after the exposure to sustained stresses in the EC, or indoor and outdoor weathering. This can be attributed to the fact that the creep effects are dominated by the matrix dependent properties (Karbhari et al., 2003). Consequently, the sustained stresses had more significant effect on the strength of the transverse specimens because of the low percentage of fibers oriented in the direction of the applied load. SEM micrographs for specimens (1T and 3T) that were subjected to sustained stresses are shown in Figure (24).

As it is shown in this figure, interface debonding, matrix cracking, and fiber damage were produced by the sustained stresses. Since the resin has higher Poisson's ratio than the fibers. The transverse shrinkage of the resin under sustained tensile stresses can result in fiber-matrix debonding or matrix cracking. As the stress level and/or the duration of the sustained stress increase the gap between the resin and the fiber increases. The damaged fibers were found to be accompanied by interface debonding, as shown in Figure (24). This suggests that these fibers were damaged after the occurrence of the interface debonding due to deficiency in the stress transfer between these fibers and the matrix.

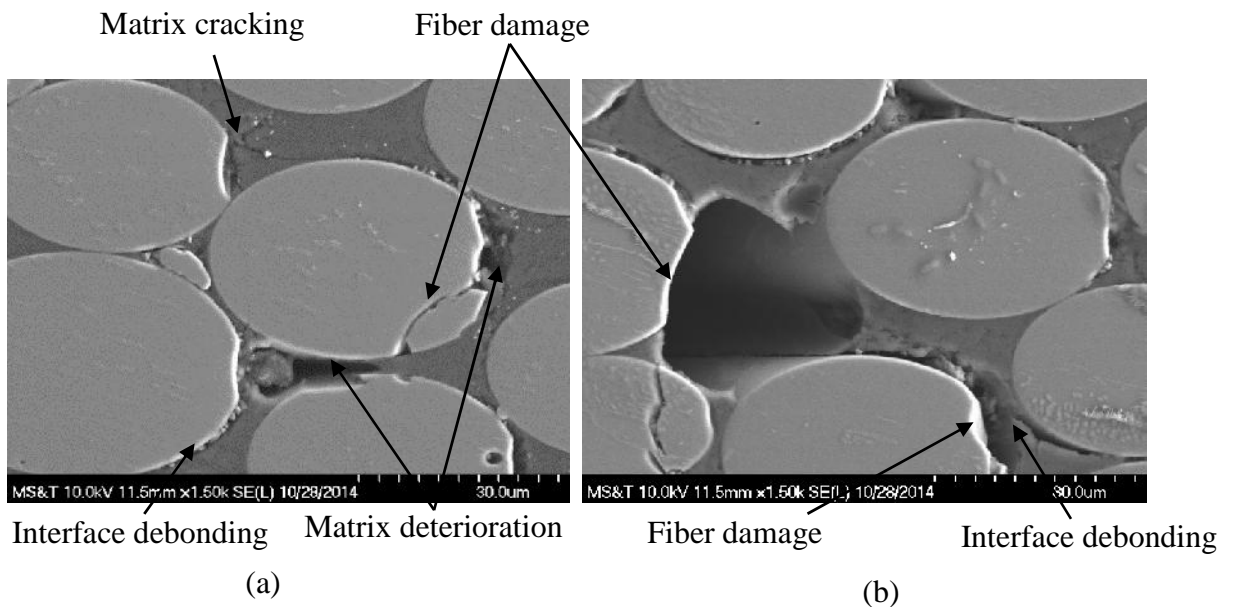


Fig. 24. SEM micrographs for specimens subjected to sustained stresses in indoor and outdoor weathering (a) 1T-IN-HW (X1500) (b) 3T-OUT_HW (X 2000)

Conclusions and Recommendations

The results obtained from the current study allow making a number of conclusions and recommendations regarding the durability of the E-glass/vinylester laminated shell tested herein as well as the overall HCB.

- The stress corrosion mechanism under chemical attacks was dominated by diffusion rate of the aggressive ions, active SiO_2 network dissolution, and interface debonding.
- The stress corrosion mechanism of the conditioned specimens under sustained stresses was dominated by fiber-matrix interface debonding, matrix cracking, and fiber damage.
- The most common alkaline solution that simulated the concrete pore solution during FRP durability tests consisted of 11.8% $Ca(OH)_2$ and 0.09% KOH mixed in deionized water (Benmokrane and Rahman, 1998; Benmokrane et al., 2002). The findings of the current study confirm that the $NaOH$ can, in some cases, diffuse alone into the FRP composite when either the $Ca(OH)_2$ or KOH cannot. Therefore, a concrete pore simulated solution should contain $NaOH$.
- The vinyl ester resin used to infuse the HCB shell was intrinsically resistant not only to chemical attacks but also thermal cycling effects. None of these environmental effects caused significant matrix hydrolysis. Vinyl ester resins, however, are moisture sensitive. This resulted in a significant number of voids in the examined shell during the fabrication. These voids made the glass fibers as well as the interphase regions prone to the chemical and moisture attacks.
- It is suggested that the mold and all of the shell's layers be heated to 150°C prior to the lay up, to reduce the percentage of voids. It is also advisable that the vinyl ester be degassed before vacuum infusion, such that the entrapped air bubbles be removed (Mohamed et al., 2014).
- Polyurethane resins have better mechanical properties, and chemical and impact resistance than vinyl ester resins (Connolly et al., 2006, Tuwair et al., 2014). Therefore, using polyurethane resins in the HCB applications is recommended.
- The post-applied gel layer that was applied to the exterior surfaces of panels 2 and 4 protected the resin from the UV-irradiation and prevented the formation of

micro-cracks at the laminate surface. Applying this layer to the fascia HCBs is recommended. However, in the current study, the effect of this layer on the residual strength was absent because of large number of voids existed in the composite shell.

- Though the alkali attack resulted in relatively substantial reduction in the tensile strength of the shell, this is expected not to affect significantly the durability of the HCBs constructed to date. The GFRP webs are protected from the exposure to the concrete pore solution via a thin layer of polyiso foam, as it is shown in Figure 1. Only the GFRP top flange is subjected to concrete pore solution during the concrete arch and the deck pour. However, from both the mechanical and environmental points of view, this is the less critical element in the GFRP shell. As soon as the deck is poured, this element no longer contributes to the environmental protection of the HCB elements. It also becomes close to the neutral axis of the composite section and, thus, be subjected to low stresses. It is recommended that the FRP webs be always separated from the concrete arch by a layer of foam. If such protection is not achieved, AR glass fibers should be used in the shell's webs.
- The GFRP composite shell's contribution to the HCB's strength and stiffness is small. The main function of the shell is to protect the strands from the environmental attack. The chemicals and the moisture were not able to diffuse into the second lamina after exposure regimes extended up to eight months. Thus, it is expected that the GFRP polymer will protect the strands from the moisture attack. Subjecting a complete HCB to different synergistic environmental effects including harsh moisture attack is recommended, to assure the ability of the shell in protecting the strands from corrosion.
- The effect of the service veil layer used in the examined GFRP shell on the moisture uptake needs to be tested.
- The expected in-service stress levels in the shell maintain the ability for long-term durability of the shell, thereby, the HCB as a whole.

Acknowledgements

The authors would like to acknowledge the Missouri Department of Transportation (MoDOT) and the National University Transportation Center (NUTC) at Missouri S&T for sponsoring this research study. The authors would like also to thank the MoDOT chemical laboratory director and staff for their help in performing the UV and SF exposure regimes. The staff support from the Dept. of Civil, Architectural and Environmental Engineering, and Center for Infrastructure Engineering Studies (CIES) at Missouri S&T are also greatly appreciated.

REFERENCES

- Aboelseoud, M.A. and Myers, J. J. (2014a). "Hybrid composite beam (HCB) bridge implementation and field monitoring." Structural Faults & Repair London, UK.
- Aboelseoud, M. A. and Myers, J. J. (2014b). "Finite Element Modeling of Hybrid Composite Beam Bridge in Missouri, USA." Journal of Bridge Engineering, ISSN (print) 1084-0702.
- ACI440.2R-08 (2008). *Guide for the design and construction of externally bonded frp systems for strengthening concrete structures*, American Concrete Institute, Farmington Hills, USA.
- Ahsan, S. (2012). "Evaluation of hybrid-composite beam for use in Tide Mill Bridge." M.S. thesis, VirginiaTech, Blacksburg, VA.
- Barkatt, A. (2001). *Issues in predicting long-term environmental degradation of fiber-reinforced plastics*, Corrosion Technology-New York and Basel, Vol. 15, No., pp. 419-458.
- Benmokrane, B. and Rahman, H. (1998). "Durability of fiber reinforced polymer (FRP) composites for construction." 1st. Int. Conf. on Durability of FRP composites for construction, Sherbooke, Quebec.
- Benmokrane, B., Wang, P., Pavate, T. and Robert, M. (2006). "Durability of FRP composites for civil infrastructure applications." Durability of Materials and Structures in Building and Civil Engineering, pp. 300-343.
- Benmokrane, Brahim, Wang, Peng, Ton-That, Tan Minh, Rahman, Habib and Robert, Jean-Francois (2002). "Durability of glass fiber-reinforced polymer reinforcing bars in concrete environment." Journal of Composites for Construction, Vol. 6, No. 3, pp. 143-153.
- Caceres, Arsenio, Jamond, Robert M, Hoffard, Theresa A. and Malvar, L. Javier. (2002). "Salt-fog accelerated testing of glass fiber reinforced polymer composites." DTIC Document.
- Carey, Francis A. and Sundberg, Richard J. (2007). *Advanced organic chemistry: Part a: Structure and mechanisms*, Springer Science+Bussnieus Media, LLC, NY.
- Chong, KP. (1998). "Durability of composite materials and structures." Durability of Fibre Reinforced Polymer (FRP) Composites for Construction–Proceedings of the first International Conference (CDCC).

- Connolly, Michael, King, JP, Shidaker, TA and Duncan, AC. (2006). "Processing and characterization of pultruded polyurethane composites." Proceedings of the 8th World Pultrusion Conference, European Pultruders Technical Association.
- Cox, B. (1976). "Advances in corrosion science and technology." Vol. 5 Plenum, New York, pp. 173.
- Devalapura RK, Gauchel JV, Greenwood ME, Hankin A and T., Humphrey (1997). "Long-term durability of glass-fiber reinforced polymer composites in alkaline environments." 3rd International Conference on Fibre-Reinforced Plastics for Reinforced Concrete Structures FRPRCS-4, Baltimore, MD.
- Diamond, S. (1981). "Effects of two danish flyashes on alkali contents of pore solutions of cement-flyash pastes." Cement and Concrete Research, Vol. 11, No. 3, pp. 383-394.
- Hillman, J. R. (2003). "Investigation of a hybrid-composite beam system." High Speed Rail IDEA Program, HSR Project Rep. 23, Transportation Research Board of National Academies, Chicago.
- Hillman, J. R. (2008). "Product application of a hybrid-composite beam system." IDEA Program Final Rep. HSR-43, Transportation Research Board of National Academies, Chicago.
- Hillman, J. R. (2012). "Hybrid-composite beam (HCB) design and maintenance manual." Missouri DOT, Jefferson City, MO.
- Kamal, A. M. (2011). "Towards a better understanding of the mechanisms controlling the durability of frp composites in concrete." PhD Dissertation, University of Saskatchewan, Saskatchewan, Canada.
- Karbhari, VM, Chin, JWal, Hunston, D, Benmokrane, B, Juska, T, Morgan, R, Lesko, JJ, Sorathia, U and Reynaud, D. (2003). "Durability gap analysis for fiber-reinforced polymer composites in civil infrastructure." Journal of Composites for Construction, Vol. 7, No. 3, pp. 238-247.
- Lewis, Michael H. (1989). *Glasses and glass-ceramics*, Chapman & Hall, New York, pp. 1-38.
- Liau, WB and Tseng, FP. (1998). "The effect of long-term ultraviolet light irradiation on polymer matrix composites." Polymer Composites, Vol. 19, No. 4, pp. 440-445.
- Mascaro, Margaret Grace and Moen, Cristopher D. (2012). "Out-of-plane web deformation and relative arch movement of hybrid-composite beams based on photogrammetry." Virginia Polytechnic Institute and State University, VirginiaTech, Blacksburg, VA.

- Micelli, Francesco and Nanni, Antonio (2004). "Durability of FRP rods for concrete structures." *Construction and Building Materials*, Vol. 18, No. 7, pp. 491-503.
- Mohamed, M., Vuppalapati, R. R., Bheemreddy, V., Chandrashekhara, K., and Schuman, T. (2014). "Characterization of polyurethane composites manufactured using vacuum assisted resin transfer molding." *Advanced Composite Materials*, (ahead-of-print), 10.1080/09243046.2014.909975.
- Mufti, AA, Onofrei, M, Benmokrane, B, Banthia, N, Boulfiza, M, Newhook, JP, Bakht, B, Tadros, GS and Brett, P. (2007). "Field study of glass-fibre-reinforced polymer durability in concrete." *Canadian Journal of Civil Engineering*, Vol. 34, No. 3, pp. 355-366.
- Nkurunziza, Gilbert, Debaiky, Ahmed, Cousin, Patrice and Benmokrane, Brahim (2005). "Durability of GFRP bars: A critical review of the literature." *Progress in Structural Engineering and Materials*, Vol. 7, No. 4, pp. 194-209.
- Nosdall, S. V. (2013). "Experiments on a hybrid composite beam for bridge applications." Master of Science, faculty of the Virginia Polytechnic Institute and State University, Blacksburg, VA.
- Onofrei, M. (2005). "Durability of gfrp reinforced concrete from field demonstration structures." *ISIS Canada*, University of Manitoba, Winnipeg, Man, pp. 195.
- Silva, Manuel AG and Biscaia, Hugo (2008). "Degradation of bond between FRP and RC beams." *Composite structures*, Vol. 85, No. 2, pp. 164-174.
- Snape, T., and Lindyberg, R. (2009). "Test results: HC beam for the Knickerbocker Bridge." *AEWC Rep. 10-16*, Univ. of Maine, Orono, ME.
- Sonawala, S. P. and Spontak, R. J. (1996). "Degradation kinetics of glass-reinforced polyesters in chemical environments." *Journal of materials science*, Vol. 31, No. 18, pp. 4745-4756.
- Tannous, Fares E. and Saadatmanesh, H. (1998). "Environmental effects on the mechanical properties of e-glass frp rebars." *ACI Materials Journal*, Vol. 95, No. 2.
- Taylor, Harry F. W. (1987). "A method for predicting alkali ion concentrations in cement pore solutions." *Advances in Cement Research*, Vol. 1, No. 1, pp. 5-17.
- Tuwair, H., Hopkins, M., Volz, J., ElGawady, M., Mohamed, M., Chandrashekhara, K. and Birmand, V. (2014). "An experimental study on static behavior of structural polyurethane foam infill for GFRP bridge deck panels". 1st International Conference on Mechanics of Composites, Long Island, New York.

Wang, A.S.D. (1986). "On fracture mechanics of matrix cracking in composite laminates."
Proc. Int. Symp. on Composite Materials and Structures, Beijing. 576-584.

PAPER**V. HYBRID COMPOSITE BEAM BRIDGE SUPERSTRUCTURE DESIGN FOR THERMAL GRADIENT****Mohamed A. Aboelseoud¹ and John J. Myers, F.ASCE²****Abstract**

The hybrid composite beam (HCB) is an innovative idea that incorporates traditional construction materials (i.e., steel and concrete) with fiber reinforced polymer (FRP) composites in an efficient configuration to optimize the beam constituents' performance. The HCB is comprised of three main sub-components: composite shell, compression reinforcement, and tension reinforcement. The shell is comprised of a glass fiber reinforced polymer (GFRP) box. The compression reinforcement consists of self-consolidating concrete (SCC) that is pumped into a profiled conduit within the shell. The tension reinforcement consists of galvanized steel tendons anchored at the compression reinforcement ends. The HCB is a promising technology in bridge applications because it has several advantages over the conventional structural members (e.g., a prolonged lifetime and a lighter weight). Few studies, however, have focused on studying HCB's essential design methodologies. An integrated research program is working at Missouri University of Science and Technology (MS&T), to understand the structural behavior of this new beam. This project involves proposing a thermal design method for HCB bridge superstructures. Beam elements from one of the constructed bridges were instrumented with various strain gages and thermocouples. The constituting elements' temperatures and the corresponding induced strains were recorded through six months. The proposed algorithm (which is based primarily on Imbsen model) was used to predict the induced strains. A two-step thermo-structural finite element analysis (FE analysis) was performed to further evaluate the proposed algorithm's performance. The results of this study showed that the proposed algorithm was able to predict, with acceptable accuracy, the thermal stresses and strains in an HCB bridge superstructure. Subsequently, this algorithm is

recommended as a useful tool for designing and analyzing HCB bridges that are undergoing environmental thermal effects.

CE Database of subject headings: Hybrid composite beam (HCB); Thermal design; Thermo-structural analysis; FRP composites; Finite element modeling; Bridges; Temperature effects.

Introduction

Bridge structures are regularly subjected to environmental thermal effects. Priestley and Buckle (1979), El Badry and Ghali (1983), and Mirambell and Aguado (1990) studied the parameters that affect the bridge superstructure's thermal response (e.g., solar radiation, wind speed, daily and annual range of day temperature, and presence of asphalt cover). Variations in environmental conditions produce two thermal cycles in a bridge structure: the seasonal cycle, and the diurnal cycle (Gross, 1999). The seasonal temperature cycle produces uniform temperature changes while the daily cycle produces a thermal gradient throughout a structure's cross-section. The deck heats up more quickly on a sunny day than the bridge's underside, resulting in a positive thermal gradient. In contrast, because the surface of a bridge deck is typically larger than the rest of the superstructure, it releases heat more quickly, resulting in a negative gradient (Imbsen et al., 1985).

Axial bridge deformations under uniform temperature changes are well understood. It is accounted for these axial deformations by providing expansion joints and/or flexible supports, such as sliding plates and elastomeric bearing pads. However, thermal gradients throughout the depth of a bridge superstructure present a more complex engineering problem (Mahama et al., 2009). Thermal strains may lead to cracks formation. Typically, the ultimate strength of a conventional concrete bridge superstructure is not affected by this thermal cracking. These cracks do, however, lead to corrosion in the reinforcing steel bars, significantly affecting the structure's serviceability (AASHTO, 1998).

In 1985, the National Cooperative Highway Research Program (NCHRP) provided guidelines for considering the thermal gradients during the design of concrete bridges (Imbsen et al., 1985). They recommended that all concrete bridges be designed to accommodate the stresses and movements produced by fluctuations in the effective bridge

temperature. The first AASHTO specifications that addressed thermal gradients were introduced in 1989 (AASHTO, 1998). AASHTO (2012) recommends that the temperature gradient be included in service limit state load combinations unless the previous data suggested not to perform this thermal analysis. The design approach to thermal gradients that is presented in AASHTO (2012) is a modified version of the Imbsen model (Imbsen et al., 1985) that accounts for the use of steel girders in a bridge superstructure.

Contribution of the Current Research

Hillman conceived a new hybrid composite beam (HCB) in 1996 (Hillman, 2012). This HCB consists of a self-consolidating concrete (SCC) arch that is tied at the ends by galvanized steel strands. Both, the concrete and steel are encased inside a laminated fiberglass composite shell. The voids within the shell are filled with Polyisocyanurate (polyiso) foam. The main concept of the HCB is to use a composite box that protects the beam constituents from environmental effects. In doing so, it increases the beam's serviceability. Moreover, the HCB's unique configuration optimizes its structural performance, resulting in a lightweight structural member.

Since its first use in Illinois in 2008, the HCB has been deployed in highway bridges in New Jersey, and Maine. They were also incorporated into traditional cast in place (CIP) reinforced concrete (RC) decks to construct three bridges in Missouri. A number of studies have examined HCB's structural behavior (Hillman, 2003; Hillman, 2008; Snape and Lindyberg, 2009; Ahsan, 2012; Mascaro and Moen, 2012; Nosedall, 2013; Aboelseoud and Myers, 2014; Myers et al., 2014). These studies neither examined the thermal behavior of HCB bridges nor proposed a design method for the environmental thermal effects. Hillman (2012) released a guide for the design of an HCB bridge superstructure. This design manual does not also include a thermal design method for an HCB bridge superstructure. Allowing an HCB bridge's deck to crack under thermal effects will negate this new technology its primary advantage of creating a durable bridge superstructure. Therefore, the goals of this study are to initiate the first investigation for an in-service HCB bridge superstructure's behavior under temperature fluctuations, and propose a design method for thermal gradients.

Experimental Program

Beam elements of a recently constructed single-span bridge (B0410) were instrumented with various sensors during the fabrication process in an attempt to investigate the thermal behavior of an HCB bridge superstructure. This bridge, which carries MO 97 over Sons Creek in Dade County, spans 31.7 m (104 ft) from center-of-bearing to center-of-bearing. The roadway deck is 38 cm (15 in.) thick and 9.35 m (368 in.) wide. The cast in place deck is supported by three lines of double-web (box) HCBs. A typical cross-section of B0410 is illustrated in Figure 1.

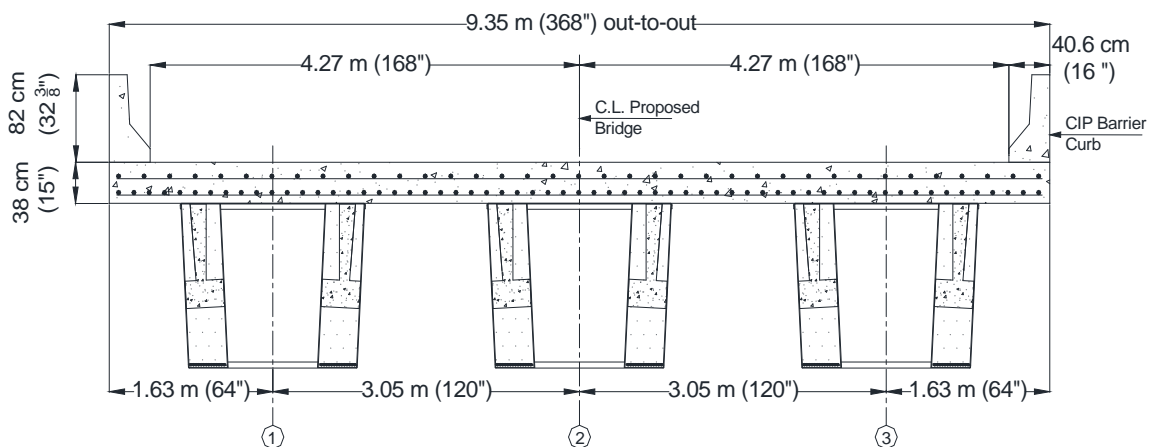


Fig. 1. Typical cross-section of bridge 0410

Nine vibrating wire strain gages (VWSGs) / thermistors were placed in a concrete arch and its web to measure normal and shear strains. Twelve thermocouples and four electrical resistive strain gages were placed at various locations on the prestressing strands. The VWSGs, thermocouples, and resistive strain gages were instrumented during the fabrication of the composite shell of HCB2 (middle beam, Figure 1) at Harbor Technologies Inc., Maine. Twelve electrical resistive strain gages were adhesively bonded to the FRP shell one day before the pour of the concrete arches, at a precast plant in

Virginia, to capture normal and shear strains. The functional strain sensors, located in their corresponding members, are displayed in Figure 2 (the FRP shear strain gages are not illustrated). The VWSGs placed in the concrete are denoted by C, the FRP gages are denoted by F, the thermocouples are denoted by TC, and the strand gages are denoted by S.

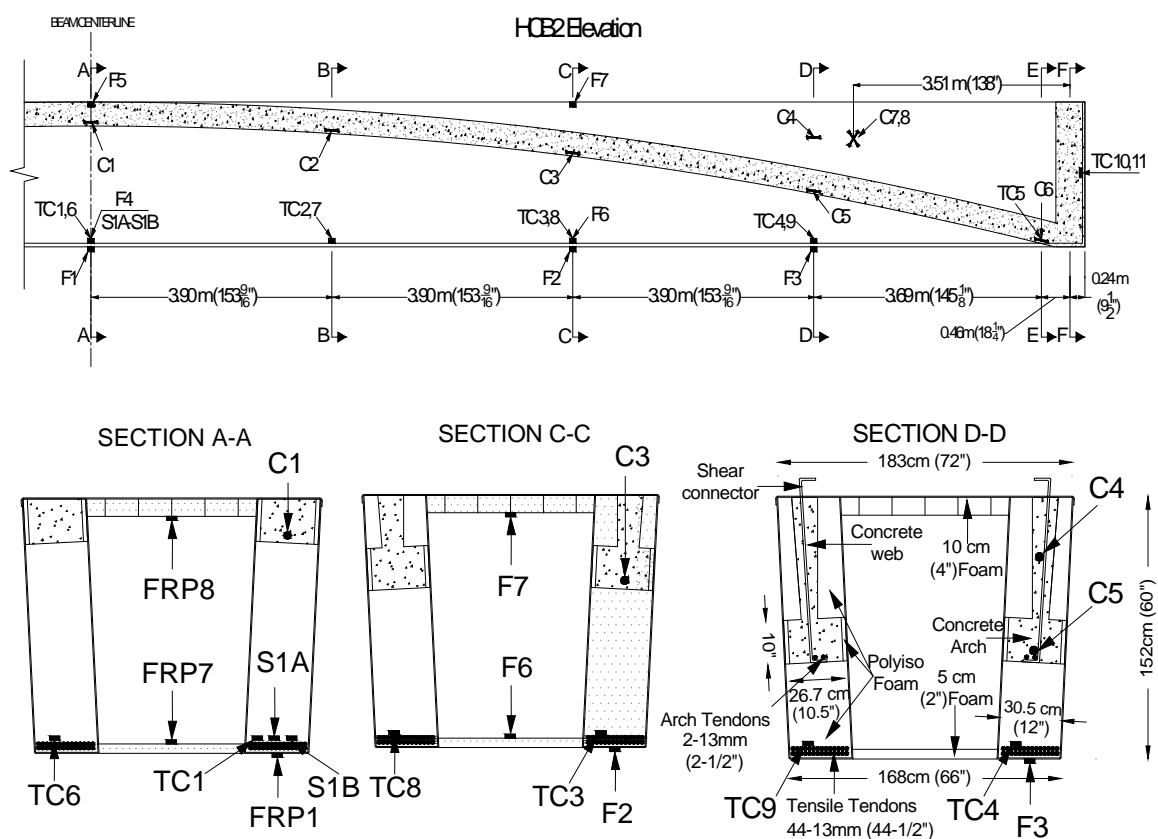


Fig. 2. Instrumentation of HCB2

The B0410 elements' temperatures and the corresponding strains were recorded at different times for six months. The instrumented gages allowed measuring only the concrete arch's and the strands' temperatures. For that reason, a temperature gun was used

to measure the temperature at the top and bottom of the concrete deck, and the interior (inside the box) and exterior FRP shell at different sections during the data collection. A sample of the measured temperature is presented in Table 1.

Table 1. Average Measured Temperature at B0410 Superstructure Elements °C

Structural element	LC1	LC2	LC3	LC4	LC5	LC6	LC7
	Mar. 5 th (10am)	Apr. 10 th (10am)	Apr. 10 th (4 pm)	Jun. 17 th (9 am)	Jun. 17 th (4 pm)	Aug. 21 st (9 am)	Aug. 21 st (4pm)
Top of deck	-1	23.0	30.5	30.8	44.1	32.2	47.9
Bottom of deck	-5	14.2	19.4	24.6	29.7	27.6	31.7
Bot. FRP shell	-2.8	17.7	21.7	24	30.4	26.5	33
Interior shell	-4.3	15.5	18.7	27.8	26.4	31.1	30.2
Concrete arch	-1.5	13.8	14.4	26.7	26.7	31.1	26.7
Strands	-1.0	14.0	16.0	23.3	26.1	26	30.1

Finite Element Modeling

Both thermal and structural finite element (FE) models of B0410 superstructure were constructed via the commercial FE analysis software package *ANSYS 14.0*. Only a quarter of the bridge superstructure was modeled as a result of the symmetry of B0410's geometry, loading, and boundary conditions. The thermal model consisted of 55966 elements and 53103 nodes. The structural model used a slightly larger number of elements and nodes to model the bearing pads by spring elements. The FE model of a quarter of the B0410 superstructure is displayed in Figure 3. Each of the elements used in each model are described in the following sections.

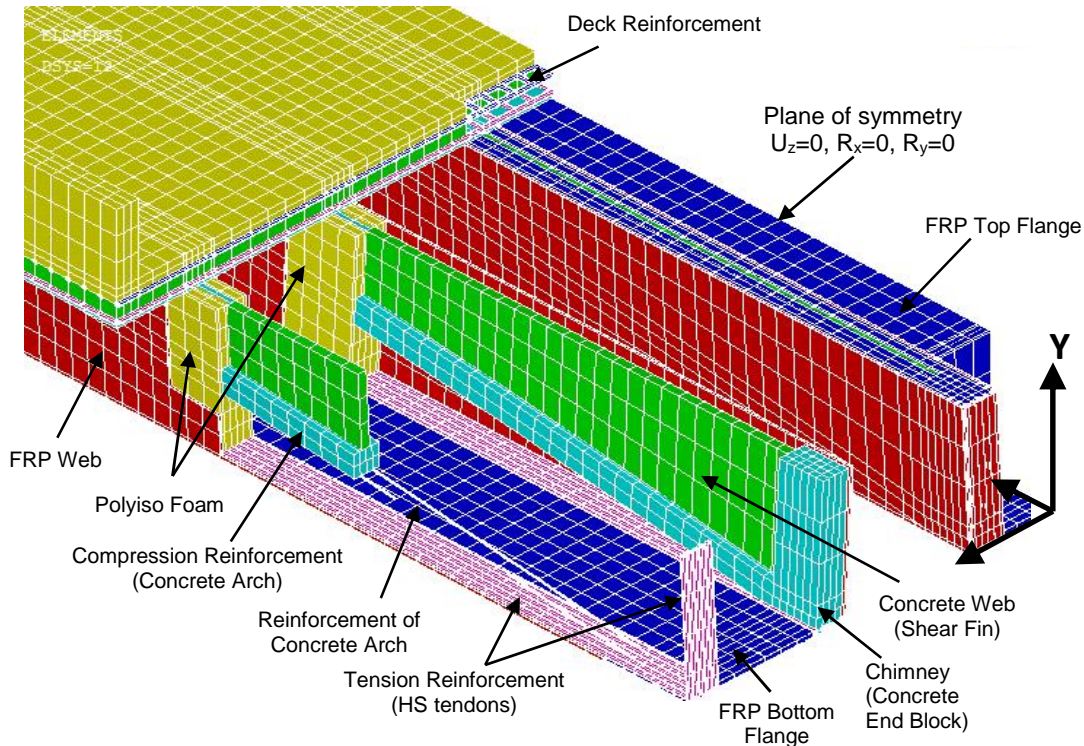


Fig. 3. Finite Element Modeling of B0410 superstructure using ANSYS V14.0

Thermal FE model

A three-dimensional space element (SOLID70) was used to model the concrete arch, the polyiso foam, and the bridge slab. SOLID70 has a 3-D thermal conduction capability. The element has eight nodes with a single degree of freedom (DOF) (temperature) at each node. A two-dimensional space element (SHELL131) was used to model both the GFRP shell and the concrete web. SHELL131 has in-plane and through-thickness thermal conduction capabilities. It is capable of modeling 3-D layered composite shell elements. This element has four nodes with up to thirty-two temperature DOFs at each node. The high-strength strands and the deck reinforcement bars were modeled by the one-dimensional space element, LINK33. LINK33 is a 2-node element that can to conduct heat between its nodes. The element has a single temperature DOF at each node.

The bridge parapet was poured simultaneously with the deck. Subsequently, it was included in the model and simulated using SOLID70 element (Myers et al., 2008; Aboelseoud and Myers, 2014). A perfect bond was assumed to exist between all of the superstructure's elements.

Structural FE model

The thermal elements were converted to equivalent structural elements so that a structural analysis of B0410 can be performed. The SOLID70 elements of the concrete arch and deck were converted to SOLID65 elements. The SOLID70 elements of the polyiso foam were converted to SOLID85 elements. Both structural elements are 8-node elements that have three translational DOFs at each node. The SHELL131 elements were converted to SHELL181 elements. SHELL181 is a four-node element that has six (DOFs) at each node. It is based on the first-order shear deformation theory and can be used for modeling 3-D layered composite shells or sandwich construction. The LINK33 elements were converted to LINK180 elements. LINK180 element is a 2-node element with three translational DOFs at each node.

Modeling the Thermal Loads

The measurements recorded by the VWSGs revealed that temperature was almost constant throughout the concrete arch and web depth. This finding can be attributed to the slab's large thickness above the HCBs. Moreover, the SCC was encapsulated in the GFRP shell and surrounded by foam that had very poor thermal conductivity. Consequently, the temperature measured by a VWSG at each section was applied as DOF constraints throughout the arch and the web's nodes at this section. The measured temperatures at the deck's top and bottom, FRP shell, and strands were also applied as DOF constraints. A steady-state thermal analysis was then executed so that the temperature distribution throughout the bridge elements could be obtained. The nodal temperatures obtained from this analysis were exported to the structural model and applied as thermal loads. Finally, a linear structural analysis was performed so that the induced stresses and strains could be obtained under different thermal effects.

Modeling the Boundary Conditions

Steel-laminated neoprene bearing pads were used in B0410 to allow horizontal movements under temperature fluctuations, applied loads, and time-dependent concrete phenomena. A large number of researches, however, have established that in-situ bridges are significantly stiffer than their idealized mathematical models. These researchers attributed the increased stiffness to restrained movements that occur at the beam-pad interface (Bakht, 1988; Bakht and Jaeger, 1988; Ramachandran, 1994; Yazdani et al., 2000; Cai and Shahawy, 2003). As a result, in a previous study, the bearing pads of B0410 were simulated by roller supports, translational springs, and rotational springs (Myers et al., 2014). The formulas proposed by Yazdani et al. (2000) were used to derive the springs' stiffnesses:

$$k_{xb} = \frac{CGA_{xz}}{H} \quad (1)$$

$$k_{rzb} = \frac{CE_b I_z}{H} \quad (2)$$

where k_{xb} is the translational stiffness of the bearing in the longitudinal direction of the beam (x-dir), k_{rzb} is the rotational stiffness about z-axis (the axis through the beam width), A_{xz} is the area of the bearing in the xz plane, H is the total thickness of the bearing, I_z is the moment of inertia of the bearing about z-axis, G is the shear modulus of the elastomer, E_b is the elastic modulus of the bearing, and C is a factor that presents the effects of aging and cold temperatures on the elastomer stiffness. C was assumed to equal 12, and G was assumed to be 1 MPa (145 psi) (Myers et al., 2014).

AASHTO (1996) provided simplified equation that can be used to detect the bearing's stiffness. This equation is based on the shear modulus and the shape factor (P):

$$E_b = 6GP^2 \quad (3)$$

The shape factor of a rectangular elastomer layer can be obtained with (AASHTO, 2012)

$$P = \frac{LW}{2h_{ri}(L+W)} \quad (4)$$

where L is the bearing length, W is the bearing width, and h_{ri} is the thickness of a single elastomer layer.

The springs' stiffnesses provided by equations (1and2), achieved good agreement between measured strains under static loads and analytical strains estimated by a structural FE model and mathematical calculations (Myers et al., 2014). Subsequently, these stiffnesses were used in the structural FE model and the mathematical algorithm proposed in the current study. The COMBIN14 element was used to model the translational and rotational springs. This element can model either one longitudinal spring or one rotational spring damper at a time.

Mathematical Algorithm

The proposed mathematical algorithm is based on the Imbsen model (Imbsen et al., 1985) that was proposed for concrete bridges. Nevertheless, the proposed algorithm accounts for differences that result from the HCB's unique configuration. The temperature at points of equal depth is not constant as a result of the concrete arch's parabolic profile and the girder's hybrid nature. In general, the temperature in either a single or a double-web HCB varies with respect to the three main axes (x , y , and z). The parabolic profile also makes the HCB sections non-prismatic along the beam's length. Finally, the HCB incorporates different materials, each of which has its own mechanical and thermal properties. The proposed algorithm is based on the following one-dimensional beam assumptions:

1. All the constituting materials are homogeneous and isotropic.
2. The mechanical and thermal properties of the constituting materials are independent of temperature.
3. Materials have linear stress-strain and temperature-strain relationships. Consequently, the stresses that result from other loading conditions can be superimposed with the thermal stresses.
4. Plane sections before bending remain plane after bending.

5. The longitudinal and transverse thermal stresses are independent of each other, and hence their effects can be superimposed.
6. There is a perfect bond between the HCB constituents.

The design method is begun by dividing the girder into m number of elements to account for the beam's nonprismatic nature. The beam's moment of inertia is calculated at $(m+1)$ sections using the transformed area technique as follows:

$$n_i = \frac{E_i}{E_w} \quad (5)$$

$$A_{ij} = n_i A_{ij} \quad (6)$$

$$\bar{y}_j = \frac{\sum_{i=1}^k A_{ij} \bar{y}_{ij}}{\sum_{i=1}^k A_{ij}} \quad (7)$$

$$I_{j(z)} = \sum_{i=1}^k \left(I_{ij(z)} + A_{ij} \left(\bar{y}_{ij} - \bar{y}_j \right)^2 \right) \quad (8)$$

where n_i is the transformation factor (modular ratio) of component (material) i , E_w is the modulus of elasticity of the FRP web, E_i is the modulus of elasticity of component i , A_{ij} is the cross-sectional area of component i at section j , A_{ij} is the transformed area of component i at section j , \bar{y}_{ij} is the distance from the center of gravity (CG) of component i to the extreme lower fiber of the beam at section j , \bar{y}_j is the distance from the elastic neutral axis (ENA) of the composite section to the extreme lower fiber of the beam at section j , $I_{ij(z)}$ is the transformed moment of inertia of component i with respect to its CG about z-axis at section j , $I_{j(z)}$ is the moment of inertia of the composite section about z-axis at section j , k is the total number of HCB components and $j = 1, 2, \dots, m+1$.

The beam is assumed to be fully restrained at each end. The thermal stress ($\dagger_{Thij}(y, z)$) that induces in component i , at point (y, z) , at section j , is then calculated as

$$\dagger_{Thij}(y, z) = -E_i \Gamma_i \Delta T_{ij}(y, z) \quad (9)$$

$$\Delta T_{ij}(y, z) = T_{ij}(y, z) - T_{Ri} \quad (10)$$

where Γ_i is the coefficient of thermal expansion (CTE) of component i , $T_{ij}(y, z)$ is the temperature of component i at point (y, z) at section j , y and z are the distances from the point (y, z) to the CG of the composite section in the y and z -directions, respectively, and T_{Ri} is the reference temperature of the component i (the temperature at which the material is stress free). In bridge applications the reference temperature is taken the site temperature at the construction time.

Both the restraining axial force and the bending moment that are required to maintain full restraint are then calculated as

$$N_{RSj} = \sum_{i=1}^k \int \int \dagger_{Thij}(y, z) dz dy \quad (11)$$

$$M_{RSj(z)} = \sum_{i=1}^k \int \int \dagger_{Thij}(y, z) y dz dy \quad (12)$$

$$N_{RS} = \left(\sum_{i=2}^{m-1} N_{RSj} + \frac{1}{2} (N_{RS1} + N_{RSm}) \right) / m \quad (13)$$

$$M_{RS(z)} = \left(\sum_{i=2}^{m-1} M_{RSj(z)} + \frac{1}{2} (M_{RS1(z)} + M_{RSm(z)}) \right) / m \quad (14)$$

where N_{RSj} is the restraining axial force at section j , $M_{RSj(z)}$ is the restraining moment about z-axis at section j , N_{RS} is the average restraining axial force induced through the beam length, and M_{RS} is the average restraining moment about z-axis.

A bridge, however, undergoes deformations in a practical application. Thus, the stress given by equation (9) can be divided into two parts: a stress released from the structure due to its deformations; and an internal stress induced in the structure to maintain the inter-fiber compatibility. The latter, known as self-equilibrating stress, is the actual stress induced in a structure under temperature fluctuations.

The average force and moment calculated by equations (13) and (14), respectively, are applied at the HCB's ends. Both, the induced axial force and moment in the beam, under the applied force and moment at the beam's end, are related to the beam's deformations (released stresses). In this study, these forces and moments are referred to as released axial force (N_{RL}) and released moment ($M_{RL(z)}$), respectively. The self-equilibrium stress ($\dagger_{SEij}(y, z)$) is calculated as

$$\dagger_{SEij}(y, z) = \dagger_{Thij}(y, z) - \frac{N_{RLj}}{A_j} n_i - \frac{M_{RLj(z)} y}{I_{j(z)}} n_i \quad (15)$$

The stress obtained by equation (15) is the self-equilibrating stress produced by a vertical thermal gradient throughout the superstructure's depth. Nevertheless, if a transverse thermal gradient exists throughout the HCB's width, based on the fifth assumption, the transverse stresses can be included as follows:

$$M_{RSj(y)} = \sum_{i=1}^k \int \int \dagger_{Thij}(y, z) z dz dy \quad (16)$$

$$M_{RS(y)} = \left(\sum_{i=2}^{m-1} M_{RSj(y)} + \frac{1}{2} (M_{RS1(y)} + M_{RSm(y)}) \right) / m \quad (17)$$

$$\dagger_{SEij}(y, z) = \dagger_{Thij}(y, z) - \frac{N_{RLj}}{A_j} n_i - \frac{M_{RLj(z)}y}{I_{j(z)}} n_i - \frac{M_{RL(y)}z}{I_{j(y)}} n_i \quad (18)$$

where $M_{(y)}$ and $I_{(y)}$ are the bending moment and the moment of inertia about the y-axis, respectively.

If the HCB is assumed to be determinate during the design, both the released forces and moments at each section, in this case, are the restraining forces and moments calculated by equations (13), (14), and (17). The HCB examined here was assumed to be partially restrained at each end because of the restrained forces and moments at the beam-pad interface. Consequently, translational and rotational springs were applied, in conjunction with a roller support, at each end. The stiffnesses of these springs were obtained by the equations proposed by Yazdani et al. (2000). The average restraining axial force and moment were applied at each end and the released force and moment were obtained through structural analysis via *SAP2000 V14*.

The strain that is related to the self-equilibrating stress is the strain that the structure does not undergo. In this study, this strain is referred to as the self-equilibrating strain $v_{SEij}(y, z)$ and can be obtained as

$$v_{SEij}(y, z) = \dagger_{SEij}(y, z) / E_i \quad (19)$$

The actual strain $v_{ij}(y, z)$ that the structure experiences is

$$v_{ij}(y, z) = -\frac{N_{RLj}}{A_j E_w} - \frac{M_{RLj(z)}y}{I_{j(z)} E_w} - \frac{M_{RLj(y)}z}{I_{j(y)}} = v_{SEij}(y, z) + v_{Thij}(y, z) \quad (20)$$

where $v_{Thij}(y, z)$ is the thermal strain that is equal to

$$v_{Thij}(y, z) = r_i \Delta T_{ij}(y, z) \quad (21)$$

A *MATLAB R2012a* code was written to calculate the thermal stresses and strains in the instrumented HCB. The HCB in this code was divided into twenty elements; the foam was neglected during all of the calculations.

Correction of Measured Strains

Ideally, a strain gage would measure the stress-related strain. If the structure is subjected to thermal effects only, stress-related strain is the self-equilibrating strain that is given by either equation (15) or equation (18). However, due to the effect of the temperature change on the instrumented material and the gage itself, the measurements recorded by a strain gage are somewhat less than perfect. The temperature-dependant errors can be controlled and minimized by performing adequate compensations. The correction procedure for a resistive strain gage differs than that of a VWSG. The correction method for each type is briefly presented in the following sections.

Correction of VWSG Measurements

If a VWSG sensing elements are compromised of concrete, the gage will suffer the same thermal strain the concrete experiences. Thus, the gage measures, in this case, only the self-equilibrating strain. Since the gage elements are compromised of steel, a VWSG measures the self-equilibrating strain plus a thermal strain that is produced by the difference between the concrete's CTE and the steel's CTE. The concrete is also known to suffer shrinkage and creep phenomena. Consequently, a measured strain includes also the strains that are produced by these phenomena. To isolate the self-equilibrating strain the following correction is made (Johnson, 2005):

$$V_{SEV} = V_{MV} + (\Gamma_w - \Gamma_c) \Delta T - V_{cr} - V_{sh} \quad (22)$$

where V_{SEV} is the corrected self-equilibrating strain, V_{MV} is the strain measured by a VWSG, V_{cr} is the creep strain, V_{sh} is the shrinkage strain, Γ_c is the concrete's CTE and Γ_w is the gage wire's CTE (which was taken $11.5 \mu\text{m}/\text{m}/^\circ\text{C}$ ($6.4 \mu\text{in}/\text{in}/^\circ\text{F}$) (Roctest Ltd., Saint-Lambert, Quebec). The strains induced by the concrete's creep and shrinkage were

neglected in this study. The experimental measurements collected during this study were taken after approximately 22 months the SCC of the concrete arches was poured. Moreover, these concrete arches were isolated from the ambient conditions (i.e., relative humidity and temperature). Subsequently, they were expected either to suffer no or minimal shrinkage during this testing regime. Myers et al. (2014) found that the strains induced in the HCB2 concrete arches under the self weight of the concrete deck were significantly small. This indicated that the concrete creep effects could be neglected (Johnson, 2005). Consequently, the strains induced by the concrete's creep and shrinkage were neglected in this study.

Correction of Resistive Strain Gage Measurements

The electrical resistance of a resistive strain gage varies not only with the induced strain but also with the test temperature as well. This temperature-induced resistance change is known as thermal output of the gage. Two concurrent effects produce the thermal output. First, the electrical resistivity of the grid conductor is to some extent temperature dependant. The second participation to the thermal output is the difference between the thermal expansion of the material that is used to calibrate the gage and the material of the tested element. The thermal output strain ($v_{T/0}$) can be estimated as follows (Vishay Precision Group, Inc., Wendell, North Carolina):

$$v_{T/0} = (A_0 + A_1T + A_2T^2 + A_3T^3 + A_4T^4) + (\Gamma_i - \Gamma_G)\Delta T \quad (23)$$

where the coefficients (A_i) of the polynomial equation are given on the gage package, and Γ_G is the CTE of the gage grid. In the current study, Γ_G was taken $12.1\mu\text{m}/\text{m}/^\circ\text{C}$ ($6.7\mu\text{in}/\text{in}/^\circ\text{F}$) (Vishay Precision Group, Inc., Wendell, North Carolina). The corrected strain is obtained by subtracting the thermal output strain from the measured strain.

Material Properties

The thermal properties of the B0410 constituents were described by thermal conductivity and CTE. The mechanical properties were presented by the elastic modulus, the shear

modulus, and Poisson's ratio. These thermal and mechanical properties are temperature-dependant. In General, both the stiffness and the thermal conductivity of concrete, steel, and GFRP decrease as the temperature increases. In contrast, the CTEs of concrete and steel increase as the temperature increases. Fluctuations in a bridge service-temperature are typically small. They produce insignificant changes in the mechanical and thermal properties of a bridge's materials. Thus, all of the materials in this study were modeled using their room temperature (24°C, 75°F) properties. As such, both the mathematical algorithm and the FE analysis were simplified.

Concrete

Two types of concrete were used in the B0410 superstructure. Normally vibrated concrete (NVC) was used to form the bridge deck. Whereas, SCC was utilized to shape the HCBs' concrete arches. The NVC's CTE was estimated to be 8.1 $\mu\text{m}/\text{m}/^\circ\text{C}$ (4.51 $\mu\text{in.}/\text{in.}/^\circ\text{F}$) at room temperature. This value was calculated as follows (Rafi et al., 2008):

$$\alpha_c = \left(0.7871e^{(0.00147T)}\right) \times 10^{-5} \quad 0 \leq T \leq 1200^\circ\text{C} \quad (24)$$

SCC contains more cement and mineral filler, and fine aggregate and materials that incorporate quartz-based natural sand than NVC to achieve high fluidity and cohesiveness (Okamura and Ouchi, 2003). This altered mix design makes the CTE of SCC higher than that of NVC (Uyguno lu and Topçu, 2009). BIBM and ERMCO (2005) recommended that the CTE of SCC be assumed to be between 10 and 13 $\mu\text{m}/\text{m}/^\circ\text{C}$ (5.6-7.2 $\mu\text{in.}/\text{in.}/^\circ\text{F}$). CTE of SCC in this study was assumed to be 10 $\mu\text{m}/\text{m}/^\circ\text{C}$ (5.6 $\mu\text{in.}/\text{in.}/^\circ\text{F}$).

A material's thermal conductivity, the measure of its ability to conduct heat, is dependent on the material's composition (Neville et al., 1995). The thermal conductivity (k) of both normal strength concrete (NSC) and high strength concrete (HSC) is between 2.3 and 2.8 $\text{W}/\text{m.}^\circ\text{C}$ (15.9-19.4 $\text{BTU.in.}/\text{hr.ft}^2.^\circ\text{F}$) (Bazant and Kaplan, 1996). Here, k_c is assumed to be 2.7 $\text{W}/\text{m.}^\circ\text{C}$ (18.7 $\text{BTU.in.}/\text{hr.ft}^2.^\circ\text{F}$) (Hawileh et al., 2009). The SCC, typically has a higher thermal conductivity than either NSC or HSC. This difference can be attributed to the high ratio of paste content and admixtures in SCC (Topçu and

Uyguno lu, 2010). Khaliq and Kodur (2011) proposed a formula that can be used to estimate the thermal conductivity of SCC (k_{scc}). This formula is as follows:

$$k_{scc} = 3.12 - 0.0045T \quad 0 \leq T \leq 400^\circ\text{C} \quad (25)$$

Based on equation (25), k_{scc} was estimated to be 3 W/m. $^\circ\text{C}$ (1.73 Btu/hr.ft. $^\circ\text{F}$).

The Poisson's ratio for both types of concrete (NVC and SCC) was assumed to be 0.2. The Young's modulus was calculated using the following equation (ACI 318, 2011):

$$E_c = 57000\sqrt{f'_c} \quad (26)$$

where f'_c is the compressive strength of concrete. f'_c and E_c in equation (26) are in psi. The standard compressive strength tests performed on the SCC used in B0410 showed that the average compressive strength of the concrete arches was approximately 76 MPa (11 ksi).

Steel Reinforcement

Two types of reinforcement bars were used in the B0410 superstructure. Conventional prestressed concrete strands (1,860 MPa class; Grade 270) were used in the HCBs, and typical Grade 60 mild steel reinforcing bars were used to reinforce the bridge deck. The thermal conductivity of both reinforcing types was assumed to be 52 W/m. $^\circ\text{C}$ (361 BTU.in./hr.ft 2 . $^\circ\text{F}$) (Hawileh et al., 2009). The CTE of both types was estimated to be 12.4 $\mu\text{m}/\text{m}/^\circ\text{C}$ (6.9 $\mu\text{in.}/\text{in.}/^\circ\text{F}$) via the following equation (Rafi et al., 2008):

$$\alpha_s = (1.2286e^{(0.00037T)}) \times 10^{-5} \quad 0 \leq T \leq 1200^\circ\text{C} \quad (27)$$

The Young's modulus of the strands was assumed to be 196,500 MPa (28,500 ksi). The typical mild steel bars were assumed to have a Young's modulus that was equal to 199,948 MPa (29,000 ksi). Both steel types were assumed to have a Poisson's ratio of 0.3.

FRP Composites

The laminate composition of the FRP shell of B0410 is a woven glass reinforcing fabric with varying percentages of fibers. These fibers are oriented in the 0° , 90° , and $\pm 45^\circ$ directions relative to the longitudinal axis (x-axis). An RTM-80545 vinyl ester resin matrix was used to infuse the fibers. The shell was assumed to behave as transversely isotropic material. Snape and Lindyberg (2009) performed laboratory tests on a HCB before it was used in the Knickerboker bridge. The CTE of the GFRP shell was identified during these tests. Harbor Technologies Inc., fabricated the GFRP shell that was tested by Snape and Lindyberg (2009). The same manufacturer fabricated the composite shell of B0410 HCBs. Based on Snape and Lindyberg results, the CTE of the shell was assumed to be $10.4 \mu\text{m}/\text{m}/^\circ\text{C}$ ($6.3 \mu\text{in.}/\text{in.}/^\circ\text{F}$) in the longitudinal direction and $11.3 \mu\text{m}/\text{m}/^\circ\text{C}$ ($5.8 \mu\text{in.}/\text{in.}/^\circ\text{F}$) in the transverse directions. The shell thermal conductivity was assumed to be $2.4 \text{ W}/\text{m}\cdot^\circ\text{C}$ ($16.6 \text{ BTU}\cdot\text{in.}/\text{hr}\cdot\text{ft}^2\cdot^\circ\text{F}$) in all directions (Devendra and Rangaswamy, 2012).

The manufacturer provided the tensile and the compressive in-plane moduli of elasticity (E_x^+ , E_x^- , E_y^+ , E_y^-), the in-plane shear modulus (G_{xy}), the effective longitudinal compressive and tensile strengths (S_x^- , S_x^+ respectively), effective transverse compressive and tensile strengths (S_y^- , S_y^+ respectively), and the effective shear strength (S_{xy}) of B0410 shell. Poisson's ratio ϵ_{xy} was assumed to be 0.26 and ϵ_{yz} was assumed to be 0.30 (Kachlakev et al., 2001). A summary of the material properties that were used to model the FRP shell is listed in Table 2.

Table 2. Material Properties Used for Modeling the FRP Shell

Property	Strength	Stiffness	Shear Modulus
	MPa (ksi)	GPa (Msi)	GPa (ksi)
Tensile properties	$S_x^+ = 423(61.4)$	$E_x^+ = 25.8(3.8)$	$G_{xy} = 7.8(1130)$
	$S_y^+ = 138(20)$	$E_y^+ = 18.3(2.7)$	$G_{xz} = 7.8(1130)$
	$S_{xy} = 26.2(3.8)$	$E_z^+ = 18.3(2.7)$	$G_{yz} = 3.6(520)$
Compressive properties	$S_x^- = 157(22.8)$	$E_x^- = 13.7(2)$	$G_{xy} = 7.8(1130)$
	$S_y^- = 152(19.1)$	$E_y^- = 9.3(1.4)$	$G_{xz} = 7.8(1130)$
	$S_{xy} = 26.2(3.8)$	$E_z^- = 9.3(1.4)$	$G_{yz} = 3.6(520)$

Polyisocyanurate Foam

Polyiso foam is a light weight, rigid, closed cell foam. The elastic moduli and shear moduli in the longitudinal and perpendicular directions, as well as the thermal conductivity were provided by the manufacturer (Elliott Company of Indianapolis, Indianapolis, Indiana). The polyiso foam's thermal conductivity is 0.024 W/m.°C (0.165 BTU.in./hr.ft².°F). The polyiso foam's CTE was assumed to be 63 $\mu\text{m}/\text{m}^\circ\text{C}$ (35 $\mu\text{in.}/\text{in.}^\circ\text{F}$) which is the CTE of the STYROFOAM. This assumption was made because both types of foam have very similar mechanical properties and thermal resistance.

The polyiso foam was assumed to behave as transversely isotropic material (with respect to the mechanical properties). Poisson's ratio ($\epsilon_{.xy}$ and $\epsilon_{.xz}$) were assumed to be 0.33 (Friis et al. 1988). A summary of the material properties used for modeling the polyiso foam is listed in Table 3.

Table 3. Material Properties Used for Modeling the Polyisocyanurate Foam

Elastic Modulus kPa (psi)	Poisson's ratio	Shear Modulus kPa (psi)
$E_x^+ = 8440(1225)$	$\nu_{xy} = 0.33$	$G_{xy} = 1516(220)$
$E_y^+ = 3190(463)$	$\nu_{xz} = 0.33$	$G_{xz} = 1516(220)$
$E_z^+ = 3190(463)$	$\nu_{yz} = 0.308$	$G_{yz} = 1219(177)$

Results Discussion

A sample of the measured and calculated strains under the thermal load cases listed in Table 1 are illustrated in Figures 4 and 5. These figures present differential strains obtained by subtracting the strains measured at certain time from the strain measured at another time. The strains that were induced under temperature changes within the same day (diurnal cycles) are illustrated in Figure 4. In these cases, a positive temperature gradient occurred throughout the deck. The temperature of the concrete arch remained almost constant. The exterior FRP shell experienced a uniform temperature increase, and slight temperature change occurred in both the interior shell and the strands. The strains that were induced because of temperature changes within different periods (seasonal cycles) are illustrated in Figure 5. In these cases, a significant uniform temperature increase took place in all of the HCB's elements together, with a positive temperature gradient throughout the deck. In general, the results demonstrate that the strains calculated by the FE analysis and the proposed mathematical algorithm are in good agreement with the measured strains.

The difference between the measured and the estimated strains can be attributed mainly to the assumed material properties, in particular the CTEs, and the factor that presented the effects of aging and cold temperatures on the elastomer stiffness (C in equations 1 and 2). Moreover, the change in the temperature throughout the deck depth is not expected to follow ideal linear pattern, as was assumed in this study. A steep temperature change may have occurred within the deck's first 10 cm (4 in.) as suggested by AASHTO's (2012) thermal gradients. This effect is, however, was expected to be

minimized because the studied strains were differential strains. The temperature gun's accuracy is another factor that may have contributed to the difference between the measured and the calculated strains. Nevertheless, a significantly large number of measurements were taken by the gun for each point. These measurements were then averaged to minimize this error.

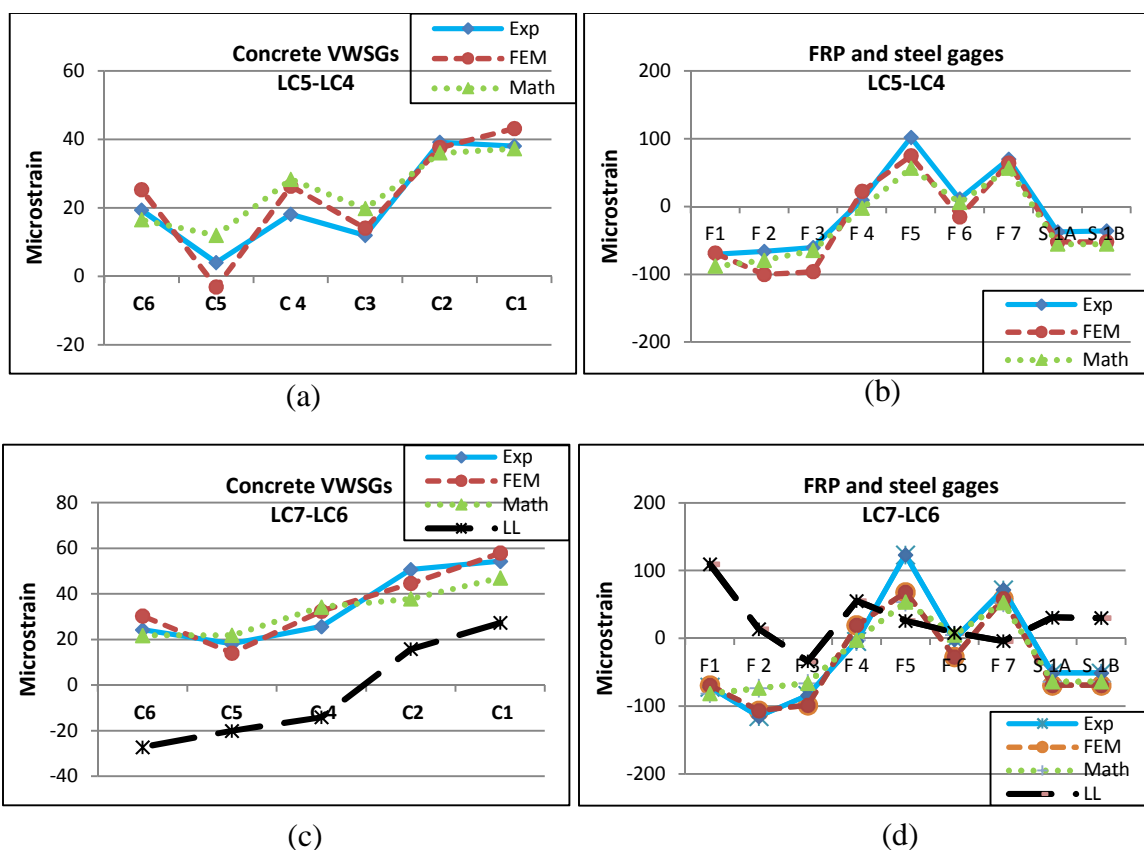


Fig. 4. Measured and self-equilibrating estimated strains in HCB2 produced by temperature fluctuations at the same day

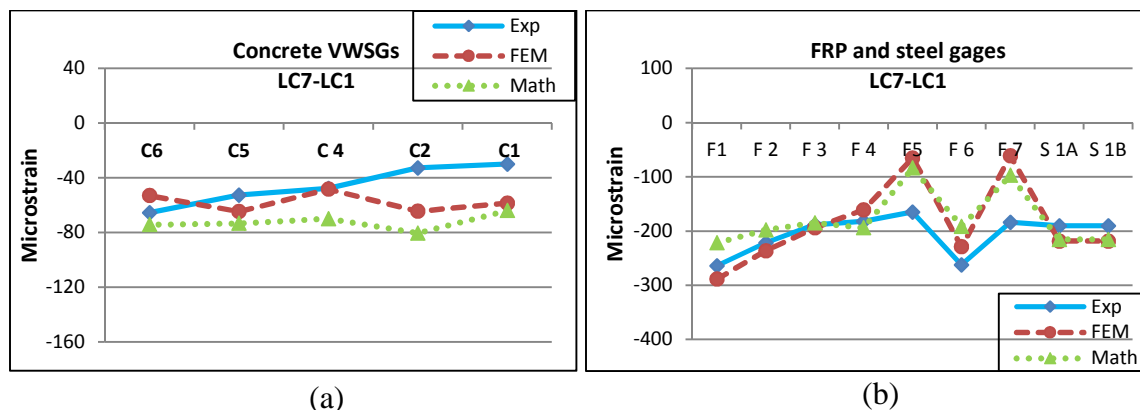


Fig. 5. Measured and self-equilibrating estimated strains in HCB2 produced by temperature fluctuations at different days

The estimated strains under seasonal temperature changes (Figure 5) were found to achieve a relatively poor correlation with the measured strains. Concrete volumetric changes may have contributed to this less accurate correlation between the measured and estimated strains. In some instances, an old concrete that has a particular combination of alkaline cement and aggregates may expand with time as it experiences chemical changes and recrystallization (Geokon Inc., Lebanon, New Hampshire). The concrete may also have suffered slight creep strains under the sustained load. Autogenous expansion is analogous to the creep. This expansion, however, occurs in the opposite direction (Geokon Inc., Lebanon, New Hampshire). Subsequently these two competing phenomena could have affected the concrete arch's strains. The effect of this autogenous growth can neither be easily predicted nor accounted for during strain estimations. The concrete arch is tied with prestressing tendons and encapsulated within a composite GFRP laminate. Thus, these volumetric changes might have also affected the strands and the shell's strains. The effect of the temperature fluctuation on the elastomer's stiffness is another factor that could have affected the correlation between the measured and estimated strains under seasonal cycles. Different values of C need to be used at different temperatures because the elastomer stiffness is temperature-time dependant. The stiffness, however, was assumed constant in this study because no criterion is available, to-date, which relates either the temperature or the pad's aging to the elastomer's stiffness. Gage C3 was found to provide unstable readings

for the data collected on August 21st (Load cases 6 and 7). Consequently, the strains provided by this VWSG were excluded from LC 6 and 7 results. Figure 6 illustrate the strains recorded by C3 on August 21st.

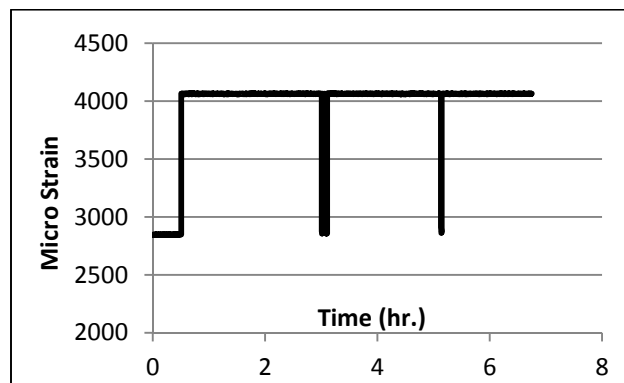


Fig. 6. Strains measured by C3 on Aug. 21st (LC6 and 7)

A comparison between the measured strains produced by positive thermal gradient in August and the measured strains under two trucks' loads (designated as LL) are illustrated in Figures 4c and 4d. These two trucks had a total load of 305 kN (113.5 kips). They performed three stops simulating different static load cases (Myers et al., 2014). The strains presented here are the maximum strains produced by these three stops. The results demonstrate that the maximum tensile strain induced in the concrete arch under the thermal gradient was approximately twice the maximum tensile strain induced in the arch under the trucks' loads. The maximum compressive stress induced in the composite shell under the thermal gradient was slightly higher than the maximum tensile stress induced in the shell under the live load. These results are in agreement with Radolli and Green's (1976) conclusion that the stresses induced by diurnal cycles throughout a bridge's superstructure can, in some instances, exceed live loading. The results also clarify that if a full-scale bridge testing is performed on a sunny day, a strain correction should be performed to account for the thermal effects.

The positive and negative thermal gradients provided by AASHTO (2012) were used to estimate the self-equilibrating stresses and strains that may induce under these thermal loads (Figures 7 and 8, respectively). The D1 in Figure 7 refers to the deck's stress at section (A-A). Estimating these stresses and strains aimed to further evaluate the efficiency of the proposed algorithm and to achieve a better understanding of the thermal effects on HCB bridge superstructures. Both the stresses and the strains estimated by the FE analysis, as well as the proposed algorithm are in good agreement ensuring that the proposed model can predict the stresses under thermal gradients with acceptable accuracy. The self-equilibrating strain profile of an HCB bridge superstructure under positive and negative thermal gradients are similar to those of a concrete bridge superstructure. In both bridge types, the most critical strains induce in the deck under a negative thermal gradient. The maximum tensile stress expected to take place in the B0410 deck, under the negative thermal gradient, was estimated to be approximately 1379 kPa (200 psi). This result indicates that B0410 superstructure's serviceability will not be affected by the expected temperature changes. The B0410 slab is significantly thick (38 cm, 15 in.). Thus, this result also suggests that the thermal effects on an HCB bridge superstructure are not critical and can be excluded from the design. Further investigations need to be executed to validate this conclusion.

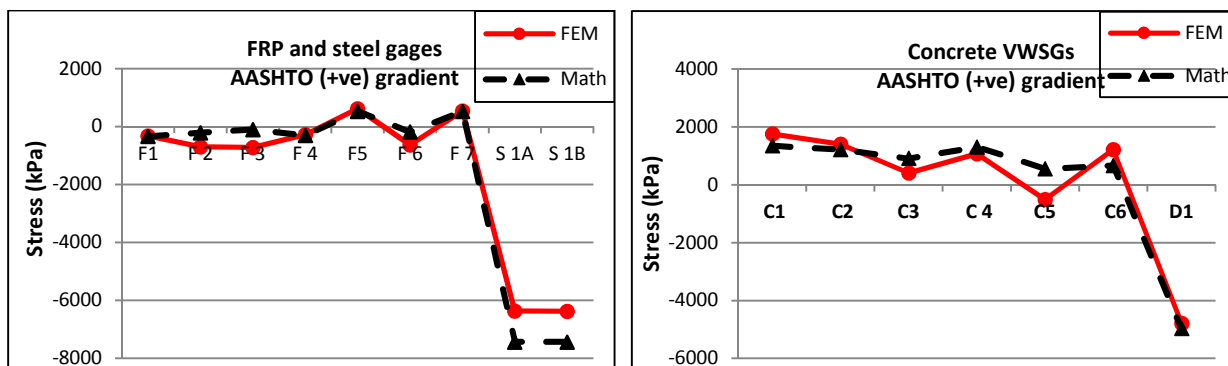


Fig. 7. Estimated self-equilibrating stresses in HCB2 due to AASHTO positive thermal gradient

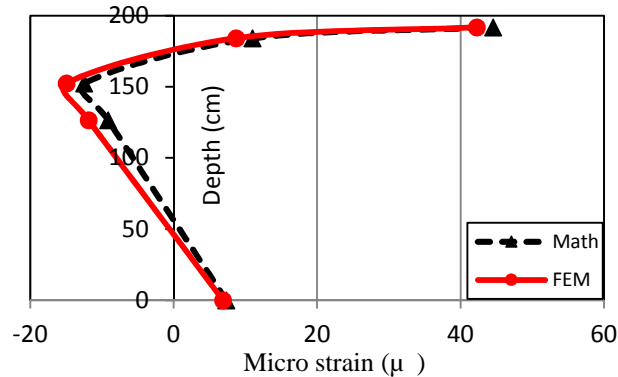


Fig. 8. Estimated self-equilibrating strains in HCB2 at sec. (A-A) due to AASHTO negative thermal gradient

The interior and exterior FRP webs were separated from the concrete arch by 2 cm (0.75 in.) of foam (see Figure 2). Moreover, the interior top and bottom flanges consisted of two FRP laminates that were separated by 10 cm (4 in.) and 5 cm (2 in.) of foam, respectively. This foam acts as thermal insulator because of its very low thermal conductivity, allowing the FRP webs to have temperatures that are different from those in the arch. It also allows the interior bottom and top flanges to have temperatures that are different than those in the exterior flanges. This foam's effect along with the collected temperatures during this study, indicate that the thermal gradients proposed by AASHTO (2012) for concrete bridges need to be slightly modified to well suit HCB bridges. The following modifications to the positive and negative thermal gradients provided by AASHTO (2012) are recommended for an HCB bridge:

- The thermal gradient proposed by AASHTO (2012) for concrete bridges should be applied to the deck, the top FRP flange, and the concrete arch and web.
- Temperature changes in both the exterior FRP shell and the strands can be assumed constant and equal to the temperature at the bottom of the deck.
- For double web HCBs with similar configuration to the HCB investigated herein, the temperature change in the interior shell (interior top and bottom flanges, and webs) can be assumed 0°C (0°F).

A parametric study was conducted to suggest design techniques that can reduce the thermal stresses in an HCB bridge deck (in case that these stresses are found critical during the design). In this study, B0410 slab's thickness was changed. At the same time, the deflection at the mid-span of HCB2 under the notional truck loads (HL-93) provided by AASHTO (2012) was kept constant. This was achieved by increasing either the arch thickness or the number of the strands. This study was based on maintaining constant deflection under the fictitious live load because the design of an HCB is up-to-date driven by its stiffness. The original depth of HCB2 concrete arch is 25.4cm (10 in.) (Figure 2). The two arches are tied by eighty-eight 13-mm (1/2 in.) diameter steel tendons. The results of this study are illustrated in Figure 9. In this figure, the decks were designated based on their depths in centimeter. For example, Deck22 refers to a deck that is 22 cm (8.5 in.) deep. The study demonstrates that as the deck depth decreases as the thermal stresses induced in the deck decreases, as it is expected. The study also clarifies that an increase in the number of the strands (to maintain the same deflection) leads to less thermal stresses in the deck than induced by increasing the arch depth. This study concluded that whenever the thermal stress in an HCB bridge's deck is critical, increasing the deck thickness needs to be avoided. At this case, increasing the stiffness of the composite section is recommended to be achieved by increasing the tension reinforcement.

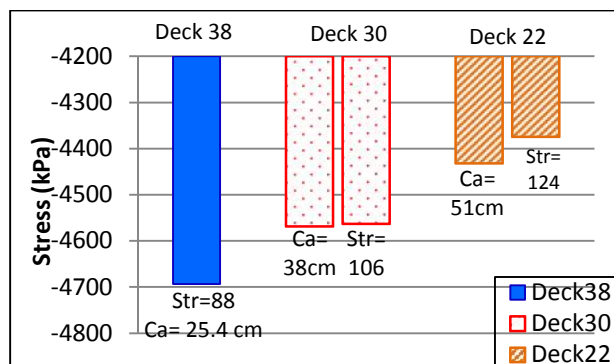


Fig. 9. Self-equilibrating stresses at the deck's top using different deck and arch depths, and tension reinforcement

Summary and Conclusions

Three bridges were recently constructed in Missouri. These bridges incorporated a new type of HCBs with traditional cast in place RC decks. This study sought to take the first step toward gaining an experience about the thermal behavior of this new type of bridges along with developing a mathematical algorithm for its design under thermal gradients. The proposed algorithm was shown to be effective and of practical applicability in predicting the stress and strain levels produced by temperature fluctuations. This study concluded that the increase of an HCB bridge superstructure stiffness can be best achieved (from the thermal point of view) by increasing the tension reinforcement rather than increasing the arch or deck thicknesses. The study also presented recommendations for modifying the thermal gradients recommended by AASHTO (2012) to suit the HCB bridges. This first investigation for the thermal behavior of an HCB bridge suggests that thermal stresses in the bridge superstructure are not critical and can be excluded from the design process. Further studies are needed to assure the conclusions and recommendations provided herein.

Acknowledgements

The authors would like to acknowledge the Missouri Department of Transportation (MoDOT) and the National University Transportation Center (NUTC) at Missouri SandT for sponsoring this research study. The staff support from the Dept. of Civil, Architectural and Environmental Engineering, and Center for Infrastructure Engineering Studies (CIES) at Missouri SandT are also greatly appreciated.

REFERENCES

- AASHTO (1996). *Standard specifications for highway bridges*, American Association of State Highway and Transportation Officials Washington, DC.
- AASHTO (1998). *Guide specifications for thermal effects in concrete bridge superstructures*, American Association of State Highway and Transportation Officials Washington, DC.
- AASHTO, LRFD (2012). *AASHTO LRFD bridge design specifications*, American Association of State Highway and Transportation Officials, Washington, DC.
- Aboelseoud, M. A. and Myers, J. J. (2014). "Finite-element modeling of hybrid composite beam bridges in Missouri." *Journal of Bridge Engineering*, ISSN (print) 1084-0702.
- Ahsan, S. (2012). "Evaluation of Hybrid-Composite Beam for Use in Tide Mill Bridge." M. S. thesis, Virginia Polytechnic Institute and State University, Blacksburg, VA.
- Bakht, B. (1988). "Observed behaviour of a new medium span slab-on beam bridge." Ministry of Transportation, Ontario, Canada.
- Bakht, B. and Jaeger, L. G. (1988). "Bearing restraint in slab-on-girder bridges." *Journal of Structural Engineering*, Vol. 114, No. 12, pp. 2724-2740.
- Bazant, Z. P. and Kaplan, M. F. (1996). *Concrete at high temperatures: Material properties and mathematical models*, Longman Group Limited, London.
- BIBM, CEMBUREAU and ERMCO, EFCA (2005). "Efnarc." The European guidelines for self-compacting concrete, specification, production and use (Available on Internet).
- Cai, C. S. and Shahawy, M. (2003). "Predicted and measured performance of prestressed concrete bridges." *Journal of Bridge Engineering*, Vol. 9, No. 1, pp. 4-13.
- Devendra, K. and Rangaswamy, T. (2012). "Evaluation of thermal properties of e-glass/epoxy composites filled by different filler materials." *International Journal of Computational Engineering Research*, Vol. 2, No. 5, pp. 1708-1714.
- Earley, C. R., AboelSeoud, M. A. and Myers, J. J. (2013). "Early-age behavior and construction sequencing of hybrid composite beam (HCB) bridges in missouri, USA." FRPRCS-11 – 11th International Symposium on Fiber Reinforced Polymer for Reinforced Concrete Structures, Guimarães, Portugal (CD-ROM).
- El Badry, M. M. and Ghali, A. (1983). "Temperature variations in concrete bridges." *J. Struct. Eng.*, ASCE, Vol. 109, No. 10, pp. 2355-2374.

- Gross, S. P. (1999). "Field performance of prestressed high performance concrete highway bridges in texas dissertation" PhD, University of Texas at Austin, University of Texas at Austin, Texas.
- Hawileh, R. A., Naser, M., Zaidan, W. and Rasheed, H. A. (2009). "Modeling of insulated CFRP-strengthened reinforced concrete t-beam exposed to fire." *Engineering Structures*, Vol. 31, No. 12, pp. 3072-3079.
- Hillman, J. R. (2003). "Investigation of a hybrid-composite beam system." High Speed Rail IDEA Program, HSR Project Rep. 23, Transportation Research Board of National Academies Chicago.
- Hillman, J. R. (2008). "Product application of a hybrid-composite beam system." IDEA Program Final Rep. HSR-43, Transportation Research Board of National Academies, Chicago.
- Hillman, J.R. (2012). *Hybrid-composite beam (hcb®) design and maintenance manual*, The Missouri Department of Transportation, Jefferson City, Mo.
- Imbsen, R. A., Vandershaf, D. E., Schamber, R. A. and Nutt, R. V. (1985). "Thermal effects in concrete bridge superstructures, NCHRP report 276." Transportation Research Board, Washington, DC.
- Johnson, J. (2005). "Concrete bridge deck behavior under thermal loads." M.S. thesis, Montana State University-Bozeman, College of Engineering, Bozeman, Montana.
- Kachlakev, D., Miller, T., Yim, S., Chansawat, K. and Potisuk, T. (2001). "Finite element modeling of concrete structures strengthened with FRP laminates." Final Rep. SPR 316, Oregon DOT, ResearchGroup, Salem, OR.
- Khaliq, W. and Kodur, V. (2011). "Thermal and mechanical properties of fiber reinforced high performance self-consolidating concrete at elevated temperatures." *Cement and Concrete Research*, Vol. 41, No. 11, pp. 1112-1122.
- Mahama, Farouk, Walter, David C, Currier, Nathan, Hamilton, HR and Consolazio, Gary R. (2009). "Validation of stresses caused by thermal gradients in segmental concrete construction."
- Mascaro, M. G. and Moen, C. D. (2012). "Out-of-plane web deformation and relative arch movement of hybrid-composite beams based on photogrammetry." Virginia Polytechnic Institute and State University, Blacksburg, VA.
- Mirambell, E. and Aguado, A. (1990). "Temperature and stress distributions in concrete box girder bridges." *Journal of structural engineering*, Vol. 116, No. 9, pp. 2388-2409.

- Myers, J. J., Holdener, D. J., Merkle, W. and Hernandez, E. (2008). "Preservation of missouri transportation infrastructures: Validation of FRP composite technology through field testing–in-situ load testing of bridges p-962, t-530, x-495, x-596 and y-298." Missouri Department of Transportation, Jefferson City, MO.
- Myers, J. J., Aboelseoud, M. A., Earley, C. R. and Washer, G. (2014). "Field evaluation of hybrid-composite girder bridges in missouri." Missouri Department of Transportation, Jefferson City, MO.
- Neville, A. M., and Neville, A. M. (1995). *Properties of concrete*, Longman, London.
- Nosdall, S. V. (2013). "Experiments on a hybrid composite beam for bridge applications". Master of Science, faculty of the Virginia Polytechnic Institute and State University, Blacksburg, VA.
- Okamura, H. and Ouchi, M. (2003). "Self-compacting concrete." *Adv Concr Technol*, Vol. 38, No. 2, pp. 103-116.
- Priestley, M. and Buckle, I. (1980). "Ambient thermal response of concrete bridges." RRU Bulletin 42, National Roads Board, New Zealand.
- Radolli, M. and Green, R. (1976). "Thermal stresses in concrete bridge superstructures under summer conditions." *Transportation Research Record 547*, Transportation Research Board, Washington, DC.
- Rafi, M. M., Nadjai, A. and Ali, F. (2008). "Finite element modeling of carbon fiber-reinforced polymer reinforced concrete beams under elevated temperatures." *ACI Structural Journal*, Vol. 105, No. 6, pp. 701-710.
- Ramachandran, U. (1994). "Restraint effect of bearings". M.S. thesis, University of South Florida Tampa, FL.
- Snape, T. and Lindyberg, R. (2009). "Test results: HC beam for the knickerbocker bridge." *Advanced Structures & Composites Center conducts*, University of Maine, Maine.
- Topçu, . B. and Uyguno lu, T. (2010). "Effect of aggregate type on properties of hardened self-consolidating lightweight concrete (SCLC)." *Construction and Building Materials*, Vol. 24, No. 7, pp. 1286-1295.
- Uyguno lu, T. and Topçu, . B. (2009). "Thermal expansion of self-consolidating normal and lightweight aggregate concrete at elevated temperature." *Construction and Building Materials*, Vol. 23, No. 9, pp. 3063-3069.
- Yazdani, N., Eddy, S. and Cai, C. S., (2000). "Effect of bearing pads on precast prestressed concrete bridges." *Journal of Bridge Engineering*, Vol. 5, No. 3, pp. 224-232.

SECTION

2. CONCLUSIONS AND RECOMMENDATIONS

2.1 SUMMARY

A new type of the HCBs was recently used to construct three bridges (B0439, B0410, and B0478) in Missouri. The HCB was conceived by Hillman in 1996 (Hillman, 2012). This new structural member incorporates GFRP composites with traditional construction materials (i.e concrete and steel) in a new configuration. This hybridization aims to optimize the beam's structural performance, weight, and durability.

A typical HCB consists of a compression reinforcement, a tension reinforcement, and a composite shell. The compression reinforcement is a SCC that is poured into a classical arch shape. The tension reinforcement is high-strength galvanized steel tendons. These tendons tie the concrete arch through two concrete end blocks (chimneys). The steel and concrete are encased inside a GFRP box. The voids within the composite shell are filled with lightweight, rigid Polyisocyanurate (polyiso) foam. Due to this unique configuration, the fiberglass box protects the steel and concrete from environmental effects. It also serves as a formwork during the concrete arch pour. The strength and stiffness, however, are provided by an efficient use of the steel in purely axial tension, and the concrete in purely axial compression. This configuration also produces a lightweight member that can be transported easily and erected rapidly making this technology well suited to accelerated bridge construction (ABC).

The HCB is relatively new. The previous studies clarified that its structural behavior is not completely understood. Many analysis and design aspects have not been comprehensively studied. The current study consisted of four main phases. The first FE analysis of an HCB bridge superstructure was performed during the first phase. A load test was conducted on B0439 (the first HCB bridge constructed in Missouri), simulating different load cases. The deflections along the HCBs' lengths under these load cases were measured using a Leica total station. Two FE models were constructed for the bridge superstructure via *SAP2000 14.2* and *ANSYS 13.0*. The accuracy of the method implemented for computer modeling of the HCB was verified. The existing method that

estimates the HCB's deflection was evaluated. The areas that need more investigation were highlighted.

The first phase pointed out that the flexural analysis method may need refinements. This phase recommended conducting further experimental investigation for the HCB's flexural behavior. Subsequently, the second phase aimed to analyze the flexural behavior of the HCB, evaluate the existing flexural analysis method, and propose new analysis methods to achieve better estimations for the HCB's strains. Elements of a double-web HCB in B0410 (the second bridge constructed in Missouri) were instrumented by various strain gages. The FRP shell and the strands' strains were recorded while the concrete arches and webs were poured. A series of load tests were conducted on B0410. The induced strains under these load tests were experimentally measured. A FE model for B0410 superstructure was constructed using *ANSYS 14.0*. Analysis methods were proposed for both simply supported HCBs and HCBs supported on bearing pads.

The third stage examined the durability of GFRP laminate used to encase the HCB elements in B0439. This E-glass/vinylester laminate was subjected to five aging regimes. The conditioning regimes simulated an alkaline attack, a salt attack, salt attack preceded by UV-irradiation exposure, and sustained stresses accompanied by controlled thermal cycles and natural weathering. A microstructural analysis was performed on unconditioned and conditioned specimens via optical microscopy (OM), scanning electron microscopy (SEM), energy-dispersive X-ray (EDX) analysis, and Fourier transform infrared (FTIR) spectroscopy. This stage provided information about the stress corrosion mechanism of the composite shell under different environmental aging regimes. Finally, recommendations were proposed to enhance the shell's durability, thus, the overall HCB's durability.

The last stage initiated the first step toward gaining an experience about the structural behavior of an HCB bridge under temperature fluctuations. The constituting elements' temperatures and the corresponding induced strains of the instrumented HCB in B0410 were recorded over six months. A mathematical algorithm based primarily on the Imbsen (Imbsen et al., 1985) model was proposed and tested to estimate the strains produced by thermal gradients. A two-step thermo-structural FE analysis was performed to further evaluate the proposed algorithm's performance.

2.2 CONCLUSIONS AND RECOMMENDATIONS

The following conclusions were drawn from the experimental investigations as well as the numerical and mathematical analyses' results gathered during this research project:

- HCB owns abundant nominal bending and shear strength to withstand the expected loads during its lifetime. This can be attributed to the fact that the design of the HCB is controlled by its deflection.
- The unique configuration of the HCB optimizes the load carrying behavior and maintains the gross section properties under the service loads.
- The shell webs are the most critical elements in the shell structure. Attentiveness needs to be paid to their elastic buckling and shear stresses during the design process.
- The polyisocyanurate foam and the cross-ties contribute to the lateral stability of the FRP webs. However, the shell webs of B0410 HCBs suffered outward deformation during the arch pour. This indicates that the cross-ties might be overstressed similar to what was observed by Snape and Lindyberg (2009).
- The linear FE analysis is accurate in predicting the static behavior of HCB under service level loading.
- The HCB neither exhibits a perfect beam behavior nor behaves like a tied arch.
- The polyiso foam works as a flexible shear connection. In doing so, this foam achieves partial composite action between the different HCB elements, allowing them to suffer differential deformations. Subsequently, the different components, at the same level, have different strains.
- The chimney at the beam's end provides partial fixity. This effect, however, is localized in the concrete components and thus doesn't affect the beam's overall behavior. The effect of the chimney should be accounted for when estimating the flexural strains of simply, supported HCBs.
- The existing flexural analysis method exhibits a poor performance in predicting the strains along the length of the concrete arch in both the non-composite and composite HCBs that either supported on bearing pads or are simply supported.

- The method is also significantly conservative when calculating the strains in the FRP shell and the strands for the HCBs rested on bearing pads and for the composite, simply supported HCB. However, it is fairly accurate when estimating the FRP shell and strands' strains in non-composite, simply-supported HCBs.
- The proposed flexural analysis method predicts the non-composite HCB's behavior with acceptable accuracy. However, after the deck being poured the proposed methods provide less accurate estimations for the HCBs strains.
- The stress corrosion mechanism under chemical attacks was dominated by diffusion rate of the aggressive ions, active SiO_2 network dissolution, and interface debonding.
- The stress corrosion mechanism of the conditioned specimens under sustained stresses was dominated by fiber-matrix interface debonding, matrix cracking, and fiber damage.
- The most common alkaline solution that simulated the concrete pore solution during FRP durability tests consisted of 11.8% $Ca(OH)_2$ and 0.09% KOH mixed in deionized water (Benmokrane and Rahman, 1998; Benmokrane et al., 2002). The findings of the current study confirm that the $NaOH$ can, in some cases, diffuse alone into the FRP composite when either the $Ca(OH)_2$ or KOH cannot. Therefore, a concrete pore simulated solution should contain $NaOH$.
- The vinyl ester resin used to infuse the HCB shell was intrinsically resistant not only to chemical attacks but also thermal cycling effects. None of these environmental effects caused significant matrix hydrolysis. Vinyl ester resins, however, are moisture sensitive. This resulted in a significant number of voids in the examined shell during the fabrication. These voids made the glass fibers as well as the interphase regions prone to the chemical and moisture attacks.
- It is suggested that the mold and all of the shell's layers be heated to 150°C prior to the lay up, to reduce the percentage of voids. It is also advisable that the vinyl ester be degased before vacuum infusion, such that the entrapped air bubbles be removed (Mohamed et al., 2014).

- Polyurethane resins have better mechanical properties, and chemical and impact resistance than vinyl ester resins (Connolly et al., 2006, Tuwair et al., 2014). Therefore, using polyurethane resins in the HCB applications is recommended.
- The post-applied gel layer that was applied to the exterior surfaces of panels 2 and 4 protected the resin from the UV-irradiation and prevented the formation of micro-cracks at the laminate surface. Applying this layer to the fascia HCBs is recommended. However, in the current study, the effect of this layer on the residual strength was absent because of large number of voids existed in the composite shell.
- Though the alkali attack resulted in relatively substantial reduction in the tensile strength of the shell, this is expected not to affect significantly the durability of the HCBs constructed to date. The GFRP webs are protected from the exposure to the concrete pore solution via a thin layer of polyiso foam, as it is shown in Figure 1. Only the GFRP top flange is subjected to concrete pore solution during the concrete arch and the deck pour. However, from both the mechanical and environmental points of view, this is the less critical element in the GFRP shell. As soon as the deck is poured, this element no longer contributes to the environmental protection of the HCB elements. It also becomes close to the neutral axis of the composite section and, thus, be subjected to low stresses. It is recommended that the FRP webs be always separated from the concrete arch by a layer of foam. If such protection is not achieved, AR glass fibers should be used in the shell's webs.
- The GFRP composite shell's contribution to the HCB's strength and stiffness is small. The main function of the shell is to protect the strands from the environmental attack. The chemicals and the moisture were not able to diffuse into the second lamina after exposure regimes extended up to eight months. Thus, it is expected that the GFRP polymer will protect the strands from the moisture attack. Subjecting a complete HCB to different synergistic environmental effects including harsh moisture attack is recommended, to assure the ability of the shell in protecting the strands from corrosion.
- The effect of the service veil layer used in the examined GFRP shell on the moisture uptake needs to be tested.

- The expected in-service stress levels in the shell maintain the ability for long-term durability of the shell, thereby, the HCB as a whole.
- The proposed thermal analysis method was shown to be effective and of practical applicability in predicting the stress and strain levels produced by temperature fluctuations.
- This study suggests that thermal stresses in an HCB bridge superstructure are not critical and can be excluded from the design process.
- Measured strains during a full-scale bridge testing should be corrected to account for the strains produced by thermal gradients.

2.3 RECOMMENDATIONS FOR FUTURE RESEARCH

This section highlights the issues that need to be addressed by future research to make the HCB commonly implemented technology. These issues can be summarized as follows:

- Nonlinear FE analysis for the HCB needs to be conducted. This analysis will enable understanding the beam behavior under ultimate loading. The experimental work that is needed to verify this FE analysis is unconventional. This test needs to be well designed to allow monitoring and specifying the cracks' formation in the concrete arch and web within the FRP shell.
- The efficiency of the proposed flexural analysis methods to estimate the nominal bending capacity of HCB needs to be experimentally verified.
- In future experimental studies, strain gages need to be placed throughout the composite HCB cross-section with gages in the concrete arch and web on the shell at the same locations. This is essential for a better evaluation to the partial composite action effects especially under the ultimate loads.
- Neither this work nor the literature examined the existing shear analysis method, though the existing method seems superficial in depth. Examining this method, and most probably developing more rigorous procedure, seems substantial.
- A sophisticated analysis method for the shell web-wrinkling needs to be developed.

- In a typical reinforced concrete beam, the reinforcement is protected by at least 30 mm (1.2-in.) of concrete cover. On the other hand, a GFRP laminate that is less than 5 mm (0.2-in.) protects the prestressing strands from the fire effects. The GFRP that is used to encase the HCB elements has a thermal conductivity that is similar to the concrete's conductivity. Thus, the ability of the HCB to achieve the endurance ratings of 2 hours [recommended by required by North American standards in typical building applications, (Hawileh et al., 2009)] during a fire exposure is a logical concern and an issue that needs to be addressed. The Polyiso foam that is used to fill the voids within the HCB's composite box has a tremendously low thermal conductivity. The most common application of this foam is for thermal insulation. Separating the tension reinforcement from the bottom flange with a thin layer of this foam seems to be a convenient solution that needs to be examined. An alternative solution is to isolate the GFRP shell with externally applied Gypsum products to protect all of the beam's elements from the direct fire exposure.
- The effect of a lateral impact, which may result from an over-height truck, on HCB bridge stability needs to be studied.
- Developing a technique that enables the long-term monitoring of corrosion damage for the tension reinforcement is recommended. Methods based on magnetic flux leakage (MFL) are good means for detecting this damage mode (Myers et al., 2014). However, this technology is experimental at this time, and generally not available for practical bridge inspections. Progress on the development of practical tools for conducting MFL should be monitored, and this tool should be considered.

APPENDIX A

FIGURES FOR THE HCB FABRICATION AND SCC MIX DESIGN

Fabrication of the HCB

The following pictures were provided by Harbor Technology Inc., Maine.



Fig. A-1. Layup of the GFRP shell



Fig. A-2. Placement and positioning of the strands



Fig. A-3. Cut and Preparation of the foam blocks



Fig. A-4. Placement of the lower foam blocks inside the box



Fig. A-5. Spacer's installation

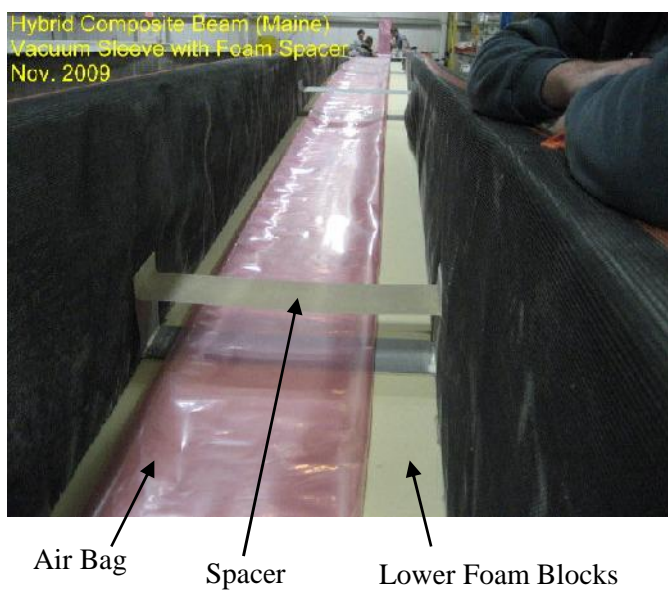


Fig. A-6. Placement of the air bag



Fig. A-7. Installation of the arch's reinforcement

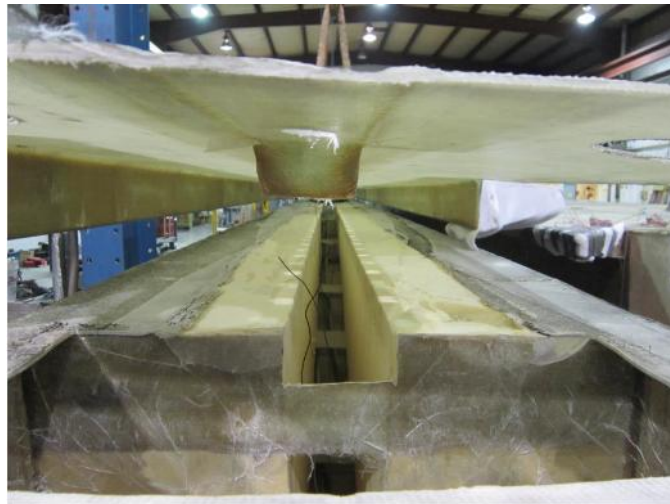


Fig. A-8. Placement of the FRP Lid onto the lower FRP shell (ref. from Nosedall, 2013)

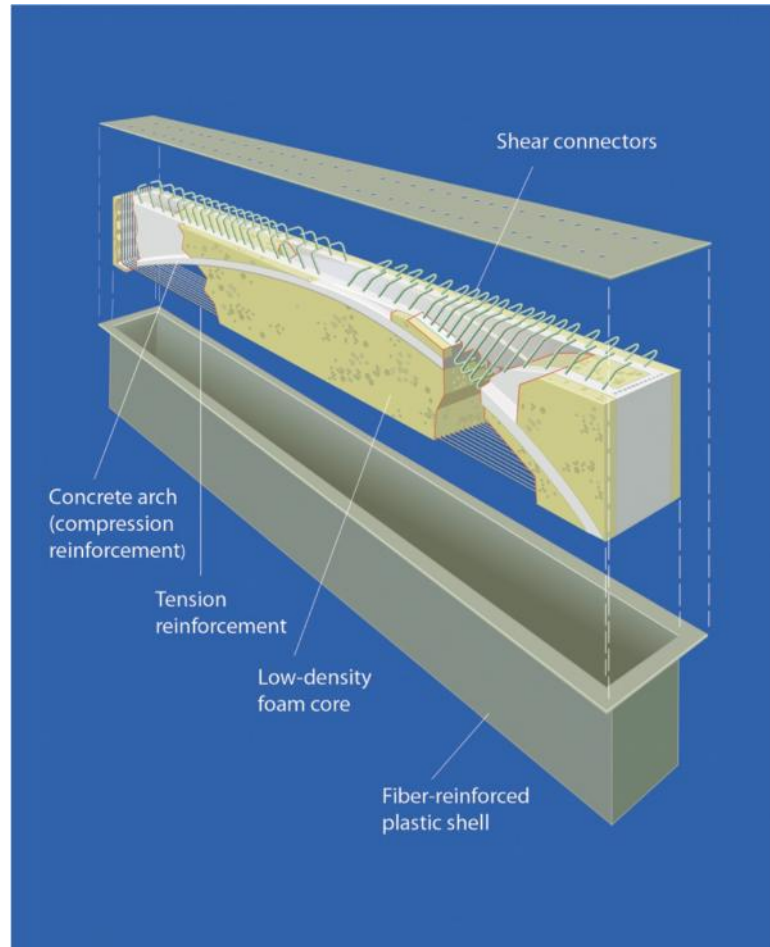


Fig. A-9. Fragmentary Perspective of a typical HCB (ref. from Hillman, 2012)

Self Consolidating Concrete (SCC) Mix Design

The mix design and proportioning of SCC is different from normal concrete. The design process is focused on balancing the fluidity, stability, and strength of the concrete. A typical mix design generally contains lower coarse aggregate volume and higher paste (cementitious, water, and fine aggregate material) volume to fulfill the required flowability. Lowering the coarse aggregate content in the design mix also reduces the risk of aggregate segregation. The stability of the SCC mix is directly related to the ability of the concrete to resist segregation. For typical SCC mix design, the coarse aggregate to total aggregate ratio (by volume) ranges between 50% and 55%. If the ratio is higher than 55%, Viscosity Modifying Admixtures (VMA) may be needed to stabilize the mix.

The SCC mix design utilizes a high-range water reducing (HRWR) admixture, to achieve the increased flow compared to normal concrete. The HRWR is a polycarbonate super-plasticizer chemical admixture. The addition of the HRWR to the concrete mix aims to increase the flow and workability of the concrete without increasing the water/cement (W/C) ratio. The advancements in HRWR's over the last several years have allowed for SCC to be produced and maintain the flow and stability needed to achieve the benefits of SCC.

The water content in the SCC mix is also of great importance, sine it affects the consistency and properties of the paste and the effectiveness of the HRWR. A typical SCC will have W/C ratio less than 45%. Since, small changes in water content can be the difference in the concrete not having the ability to properly flow to severe aggregate segregation, attentiveness should be paid to control the aggregate moisture during the mix design and production of SCC. The next two tables illustrate the mix design of the SCC used in B0439 and B0478, respectively. The mix design of the SCC used in B0410 is not available.

Table (A-1) Mix Design of SCC of B0439 (By Peterson Gravel and Ready Mix Inc.)

Product	Content	Yield	Comment
Type I Cement	600 (lbs)	3.05 (ft ³)	
Type C Fly Ash.	200 (lbs)	1.22 (ft ³)	
3/8" Gravel	1770 (lbs)	9.61 (ft ³)	
Sand	1200 (lbs)	7.34 (ft ³)	
Water	280 lbs (33.6 gal)	5.4 (ft ³)	
PolyHeed N	3 oz/cwt	N/A	Mid-Range Water Reducer
Glenium 7500	8 oz/cwt	N/A	Mid-Range and High-Range Water Reducer
Delvo	3 oz/cwt	N/A	Retarder and Water Reducer / Retarder
Rheomac VMA 362	2 oz/cwt	N/A	Viscosity Modifying Admixture
Total Yield		27.28 (ft ³)	
Water / cement ratio		0.35 lbs/lb	
Fly Ash / cementious		0.25 lbs/lb	

Conversion Units: add conversions for SAE to SI for the units above

Table (A-2) Mix Design of SCC of B0478 (By Plottie Ready-Mix, LLC)

Product	Content	Yield	Comment
Type I Cement	600 (lbs)	3.05 (ft ³)	
Type C Fly Ash.	200 (lbs)	1.22 (ft ³)	
3/8" Pea Gravel	1570 (lbs)	10.02 (ft ³)	
Big River Sand	1325 (lbs)	8.43 (ft ³)	
Water	280 lbs (33.6 gal)	4.5 (ft ³)	
Grace-Adva 140M	3-5 oz/cwt	24-40 oz/yd ³	High-Range Water Reducer
Grace-Adva Cast 575	7-10 oz/cwt	56-80 oz/yd ³	Mid-Range and High-Range Water Reducer
Grace-Recover	4-6 oz/cwt	32-48 oz/yd ³	Hydration Stabilizer
Grace-V MAR 3	1-2 oz/cwt	8-16 oz/yd ³	Concrete rheology-modifying admixture (Viscosity Modifying Admixture)
Total Yield		27.21 (ft ³)	
Water / cement ratio		0.35 lbs/lb	
Fly Ash / cementious		0.25 lbs/lb	

Conversion Units:

1lbs = 0.454 Kgf

1 ft = 304.8 mm

1 ozf = 0.028 Kgf

1 oz (mass) = 0.00063 cwt (hundredweights short US)

1 yd = 3 ft = 914.4 mm

APPENDIX B
MEASURED AND ESTIMATED DEFLECTIONS ALONG B0439 HCBS' LENGTHS

Stop 1 Results

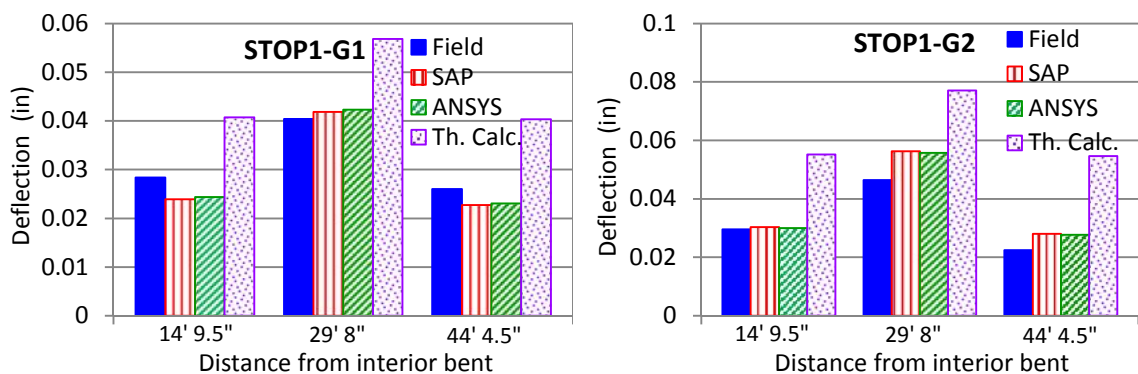
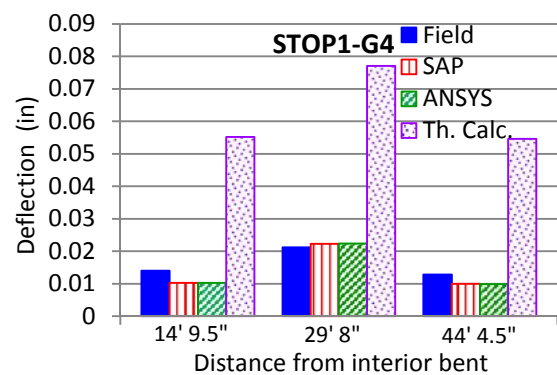
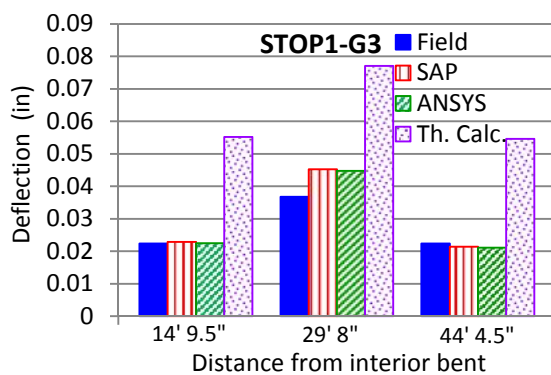


Table (B-1) Deflection along G1 length under stop 1 loads

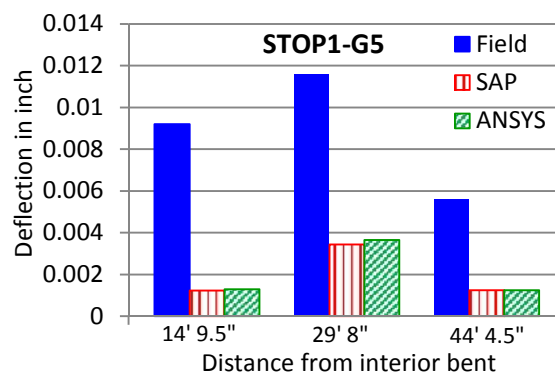
Stop 1 (G1)				
Dist. From Interior bent	Experimental (in)	Ansys (in)	Sap2000 (in)	Math. Calc. (in)
14' 9.5"	-0.0284	-0.02435	-0.02394	-0.0407
29' 8"	-0.0404	-0.04228	-0.04186	-0.0568
44 4.5"	-0.026	-0.02309	-0.02273	-0.04032

Stop 1 (G2)				
Dist. From Interior bent	Experimental (in)	Ansys (in)	Sap2000 (in)	Math. Calc. (in)
14' 9.5"	-0.0296	-0.03	-0.03036	-0.05517
29' 8"	-0.0464	-0.0557	-0.0563	-0.07703
44 4.5"	-0.0224	-0.0277	-0.02803	-0.05462



Stop 1 (G3)				
Dist. From Interior bent	Experimental (in)	Ansysis (in)	Sap2000 (in)	Math. Calc. (in)
14' 9.5"	-0.0224	-0.02252	-0.02283	-0.05517
29' 8"	-0.0368	-0.0447	-0.0452	-0.07703
44 4.5"	-0.0224	-0.0211	-0.02139	-0.05462

Stop 1 (G4)				
Dist. From Interior bent	Experimental (in)	Ansysis (in)	Sap2000 (in)	Math. Calc. (in)
14' 9.5"	-0.014	-0.010238	-0.01025	-0.05517
29' 8"	-0.0212	-0.02238	-0.02232	-0.07703
44' 4.5"	-0.0128	-0.00986	-0.01	-0.05462

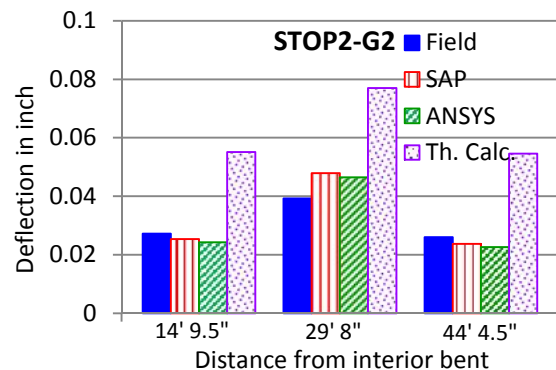
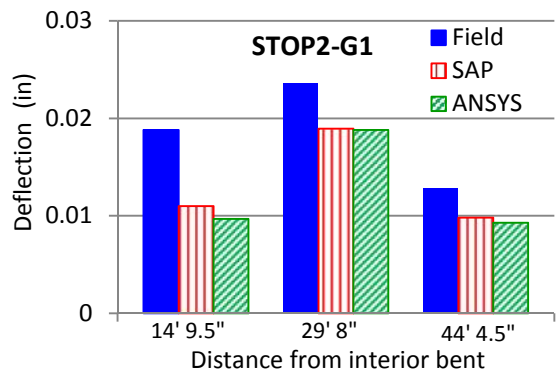


Stop 1 (G5)				
Dist. From Interior bent (inch)	Experimental (in)	Ansysis (in)	Sap2000 (in)	Math. Calc. (in)
14' 9.5"	-0.0092	-0.001291	-0.00123	0
29' 8"	-0.0116	-0.00365	-0.00344	0
44' 4.5"	-0.0056	-0.001244	-0.00125	0

FE models underestimated significantly the deflections through G5 in Stop 1 in comparison to the measured ones. It is clear from Figure 2 (in the second paper) that the truck loads transferred to G5 in Stop 1 tend to be zero. Consequently, this would result in very small deflections beyond the accuracy of the total station. The deflections through G5 span ranged from 0.0016 in. (0.004 cm) to 0.0044 in. (0.011 cm) according to ANSYS results, while the tolerance of the total station as observed by Myers et al. (2008) is ± 0.005 -in. (0.013 cm). This means that the total station measurements are not reliable in this case and FE models can predict the deflections more accurately. The significant difference between the deflections measured at G5 at distances 14 ft 9.5 in and 44 ft 4.5 in assures the inaccuracy of the experimental measurements in this case. These locations were expected

to suffer very close displacements similar to the deflections measured at (G1-G4) under the stop.

Stop 2 Results

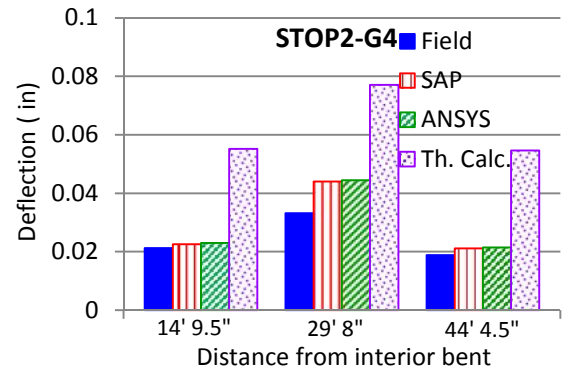
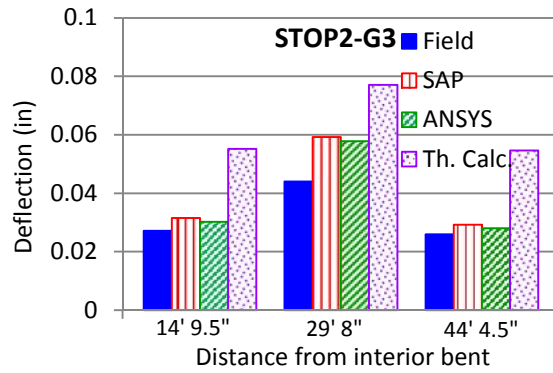


Stop 2 (G1)

Dist. From Interior bent (inch)	Experimental (in)	Anslys (in)	Sap2000 (in)	Math. Calc. (in)
14' 9.5"	-0.0188	-0.0097	-0.0110	0
29' 8"	-0.0236	-0.0188	-0.0189	0
44' 4.5"	-0.0128	-0.0093	-0.0098	0

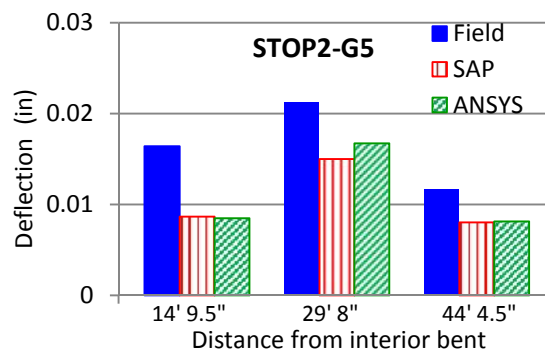
Stop 2 (G2)

Dist. From Interior bent (inch)	Experimental (in)	Anslys (in)	Sap2000 (in)	Math. Calc. (in)
14' 9.5"	-0.0272	-0.0242	-0.0254	-0.0552
29' 8"	-0.0392	-0.0464	-0.0479	-0.0770
44' 4.5"	-0.0260	-0.0226	-0.0237	-0.0546



Stop 2 (G3)				
Dist. From Interior bent	Experimental (in)	Ansysis (in)	Sap2000 (in)	Math. Calc. (in)
14' 9.5"	-0.0272	-0.0302	-0.0315	-0.0552
29' 8"	-0.0440	-0.0578	-0.0592	-0.0770
44 4.5"	-0.0260	-0.0280	-0.0292	-0.0546

Stop 2 (G4)				
Dist. From Interior bent	Experimental (in)	Ansysis (in)	Sap2000 (in)	Math. Calc. (in)
14' 9.5"	-0.0212	-0.0230	-0.0226	-0.0552
29' 8"	-0.0332	-0.0444	-0.0441	-0.0770
44 4.5"	-0.0188	-0.0214	-0.0212	-0.0546



Stop 2 (G5)				
Dist. From Interior bent	Experimental (in)	Anslys (in)	Sap2000 (in)	Math. Calc. (in)
14' 9.5"	-0.0164	-0.0085	-0.0086	0
29' 8"	-0.0212	-0.0167	-0.0150	0
44' 4.5"	-0.0116	-0.0081	-0.0080	0

Stop 3 Results

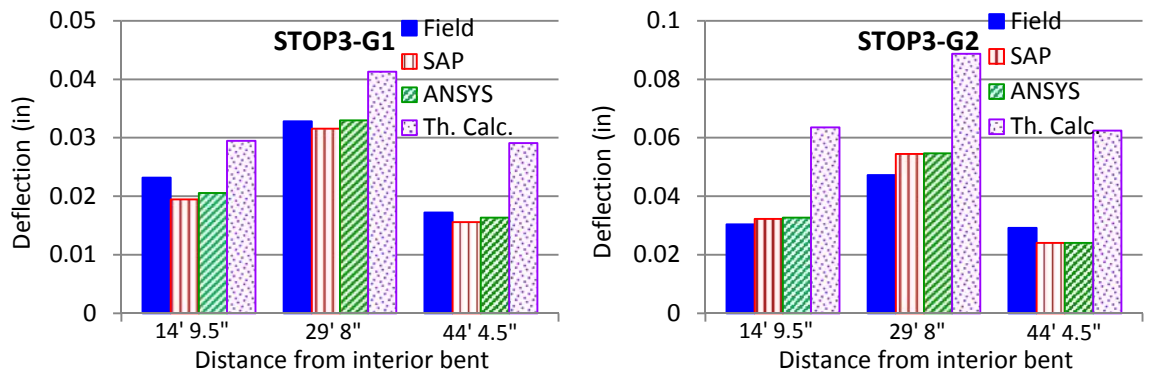


Fig. B-7 Deflection along G1 and G2 lengths under stop 3 loads

Stop 3 (G1)				
Dist. From Interior bent	Experimental (in)	Ansys (in)	Sap2000 (in)	Math. Calc. (in)
14' 9.5"	-0.0232	-0.0206	-0.0195	-0.0295
29' 8"	-0.0328	-0.0330	-0.0315	-0.0413
44' 4.5"	-0.0172	-0.0164	-0.0156	-0.0291

Stop 3 (G2)				
Dist. From Interior bent	Experimental (in)	Ansys (in)	Sap2000 (in)	Math. Calc. (in)
14' 9.5"	-0.0304	-0.0327	-0.0323	-0.0636
29' 8"	-0.0472	-0.0546	-0.0545	-0.0887
44' 4.5"	-0.0292	-0.0240	-0.0240	-0.0625

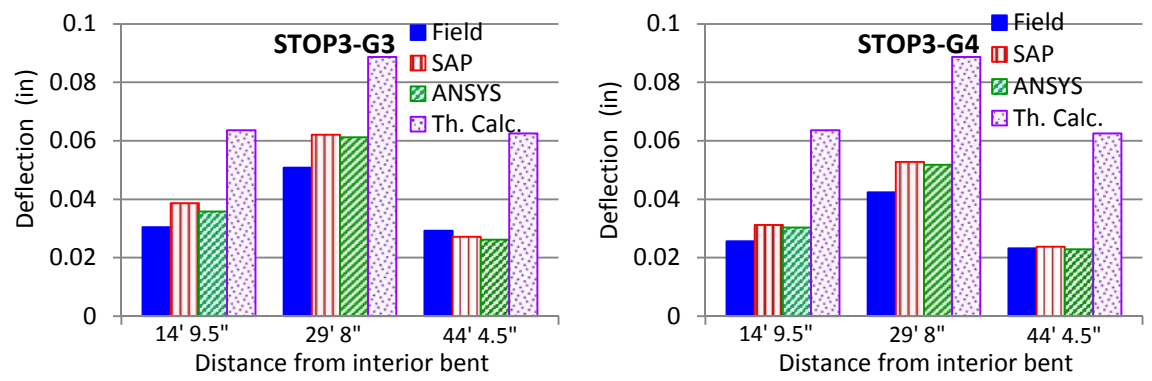


Fig. B-8 Deflection along G3 and G4 lengths under stop 3 loads

Stop 3 (G3)				
Dist. From Interior bent	Experimental (in)	Ansys (in)	Sap2000 (in)	Math. Calc. (in)
14' 9.5"	-0.0304	-0.0358	-0.0386	-0.0636
29' 8"	-0.0508	-0.0612	-0.0621	-0.0887
44' 4.5"	-0.0292	-0.0262	-0.0272	-0.0625

Stop 3 (G4)				
Dist. From Interior bent	Experimental (in)	Ansys (in)	Sap2000 (in)	Math. Calc. (in)
14' 9.5"	-0.0256	-0.0303	-0.0312	-0.0636
29' 8"	-0.0424	-0.0518	-0.0528	-0.0887
44' 4.5"	-0.0232	-0.0229	-0.0237	-0.0625

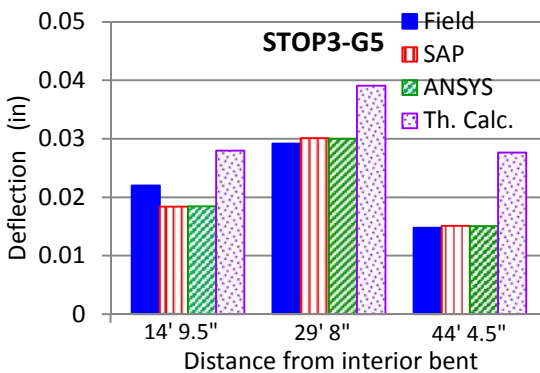


Fig. B-9 Deflection along G5 length under stop 3 loads

Table B-15 Deflection along G5 length under stop 3 loads

Stop 3 (G5)				
Dist. From Interior bent	Experimental (in)	Ansysis (in)	Sap2000 (in)	Math. Calc. (in)
14' 9.5"	-0.0220	-0.0184	-0.0184	-0.0280
29' 8"	-0.0292	-0.0300	-0.0301	-0.0391
44' 4.5"	-0.0148	-0.0150	-0.0151	-0.0277

APPENDIX C.

DERIVATION OF SLOPE-MOMENT EQUATIONS FOR NON-PRISMATIC BEAM

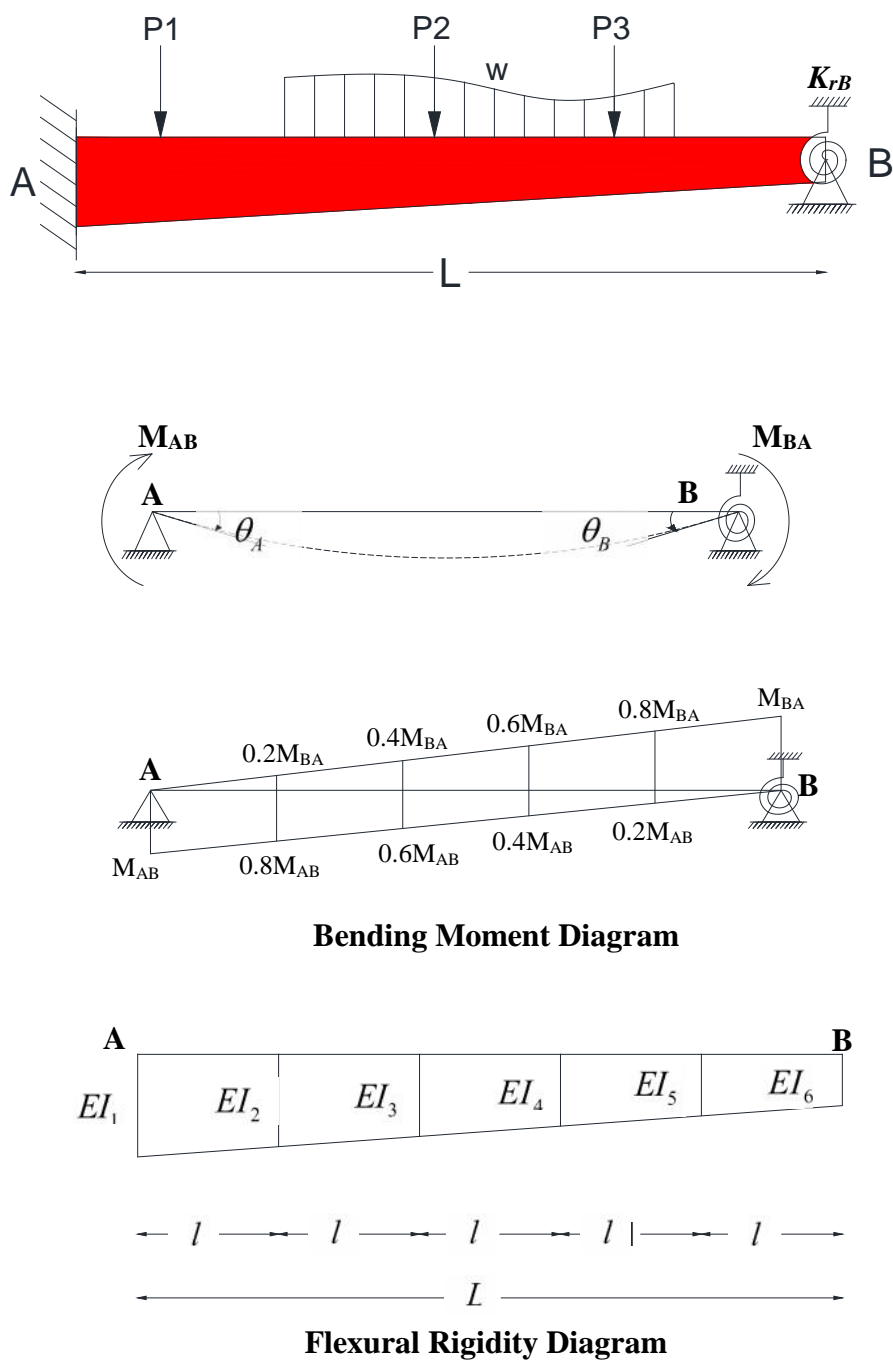


Fig. C-1. Moment and flexural rigidity of non-prismatic five-element beam

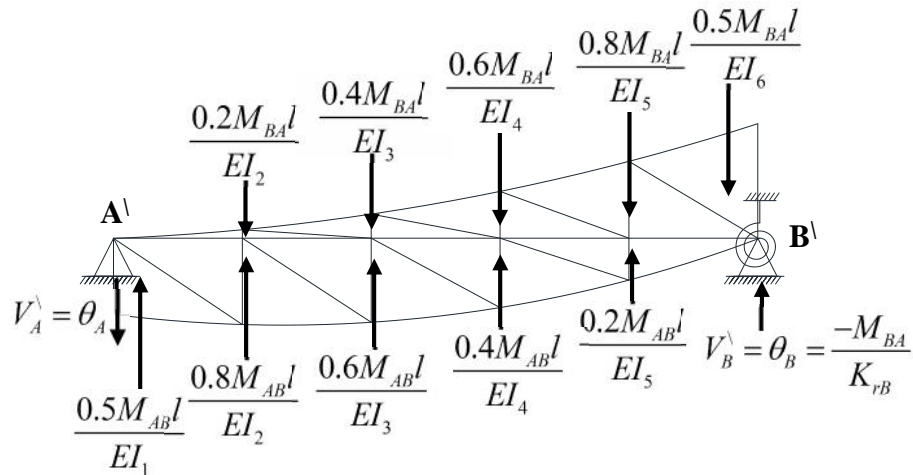


Fig. C-2. Loads on Conjugate Beam

$$\sum M @ A' = 0$$

$$\frac{M_{AB}l^2}{E} \left[\frac{1}{6I_1} + \frac{0.8}{I_2} + \frac{1.2}{I_3} + \frac{1.2}{I_4} + \frac{0.8}{I_5} \right] - \frac{M_{BA}l^2}{E} \left[\frac{0.2}{I_2} + \frac{0.8}{I_3} + \frac{1.8}{I_4} + \frac{3.2}{I_5} + \frac{7}{3I_6} + \frac{5E}{k_{rB}l} \right] = 0$$

$$\sum M @ B' = 0$$

$$\frac{M_{AB}l^2}{E} \left[\frac{0.2}{I_5} + \frac{0.8}{I_4} + \frac{1.8}{I_3} + \frac{3.2}{I_2} + \frac{7}{3I_1} \right] - \frac{M_{BA}l^2}{E} \left[\frac{1}{6I_6} + \frac{0.8}{I_5} + \frac{1.2}{I_4} + \frac{1.2}{I_3} + \frac{0.8}{I_2} \right] = 5_{rA}l$$

$$a = 0.2/I_5 + 0.8/I_4 + 1.8/I_3 + 3.2/I_2 + 7/3I_1$$

$$b = 0.2/I_2 + 0.8/I_3 + 1.8/I_4 + 3.2/I_5 + 7/3I_6$$

$$c = 1/6I_1 + 0.8/I_2 + 1.2/I_3 + 1.2/I_4 + 0.8/I_5$$

$$d = 1/6I_6 + 0.8/I_5 + 1.2/I_4 + 1.2/I_3 + 0.8/I_2$$

$$e = b + 25E/K_{rB}L$$

$$L = 5l$$

$$\frac{M_{BA}l}{E} \left(\frac{ae}{c} - d \right) = 5_{rA}$$

$$M_{BA} = \frac{25E}{L} \left(\frac{c}{ae - cd} \right) \quad (1)$$

$$\frac{M_{AB}l}{E} a - \frac{5_A cd}{(ae - cd)}$$

$$M_{AB} = \frac{25E}{L} \left(\frac{e}{ae - cd} \right) \quad (2)$$

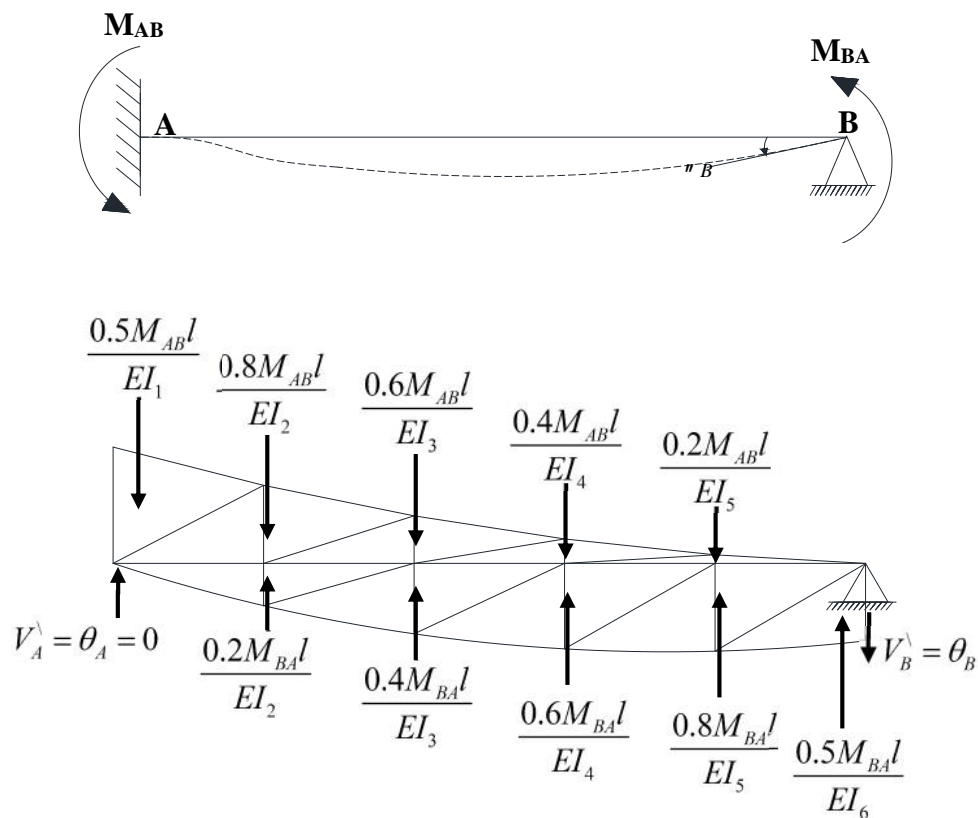


Fig. C-3. Loads on Conjugate Beam

$$\sum M @ B = 0$$

$$\frac{M_{BA} l^2}{E} d - \frac{M_{AB} l^2}{E} a = 0$$

$$\frac{M_{BA} l^2}{E} b - \frac{M_{AB} l^2}{E} c = 5 \theta_B$$

$$M_{AB} = \frac{25E}{L} \left(\frac{d}{ab - cd} \right) \theta_B \quad (3)$$

$$\frac{M_{BA} l}{E} e - \left(\frac{cd}{ab - cd} \right) \theta_B = 0$$

$$M_{BA} = \frac{25E}{L} \left(\frac{a}{ab - cd} \right) \theta_B \quad (4)$$

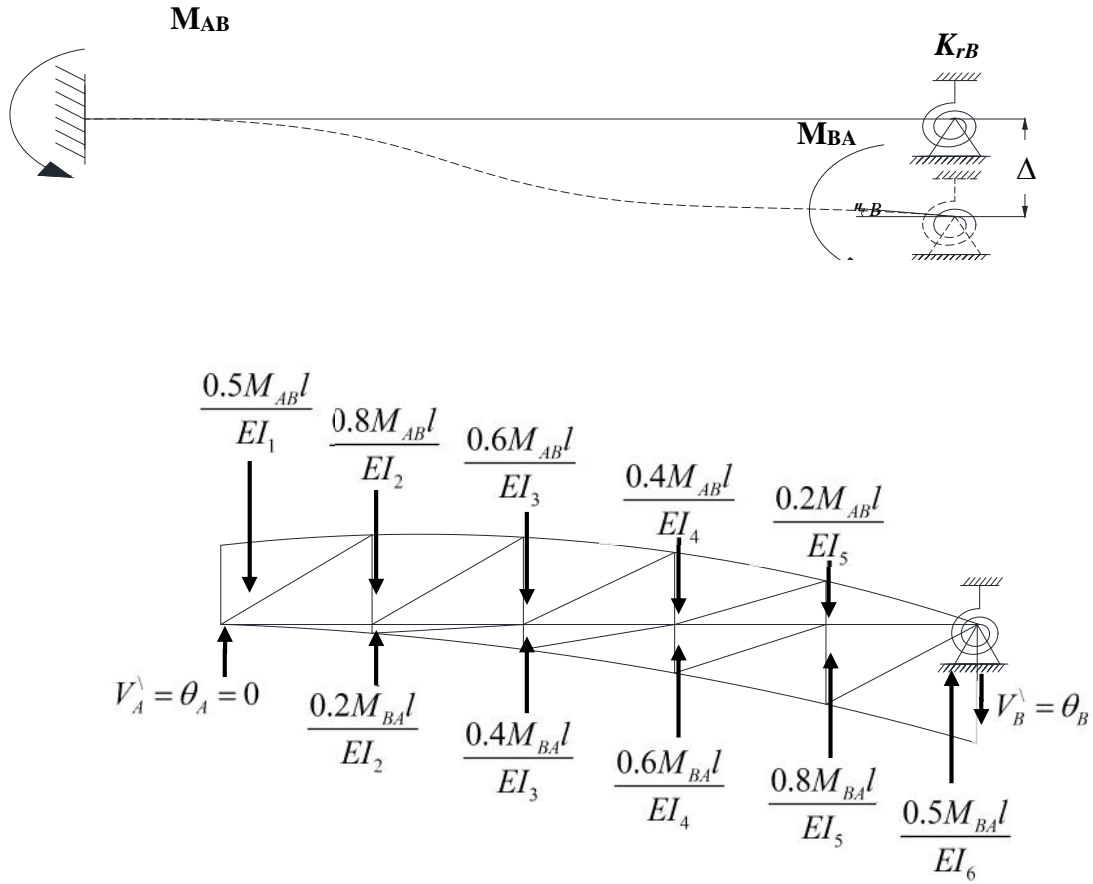


Fig. C-4. Loads on Conjugate Beam

$$\sum M @ B^{\vee} = 0$$

$$\frac{M_{BA}l^2}{E}d - \frac{M_{AB}l^2}{E}a = 0$$

$$\sum M @ A^{\vee} = \Delta$$

$$\frac{M_{AB}l^2}{E}c - \frac{M_{BA}l^2}{E}b = \Delta$$

$$M_{BA} = \frac{25E}{L^2} \left(\frac{a}{cd - ab} \right) \Delta \quad (5)$$

$$M_{AB} = \frac{25E}{L^2} \left(\frac{d}{cd - ab} \right) \Delta \quad (6)$$

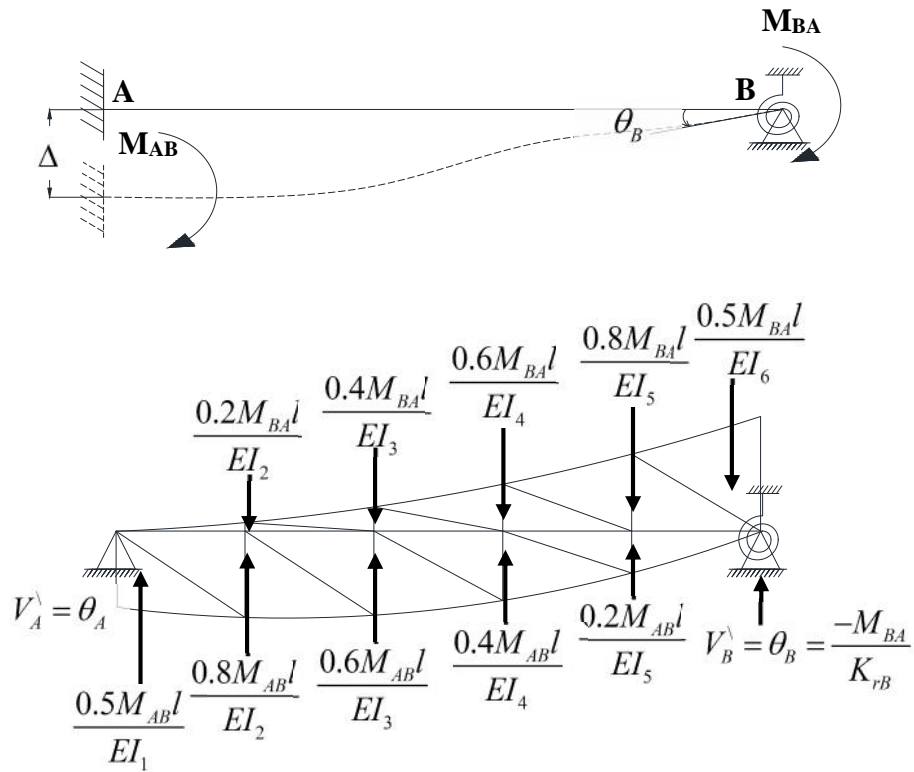


Fig. C-4. Loads on Conjugate Beam

$$\sum M @ B^{\vee} = \Delta$$

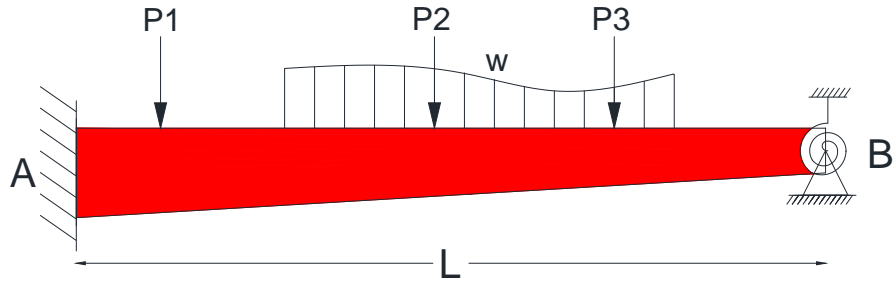
$$\frac{M_{BA} l^2}{E} d - \frac{M_{AB} l^2}{E} a = \Delta$$

$$\sum M @ A^{\vee} = 0$$

$$\frac{M_{AB} l^2}{E} c - \frac{M_{BA} l^2}{E} e = 0$$

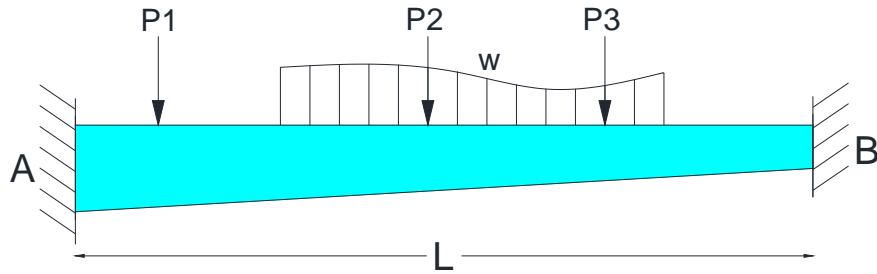
$$M_{BA} = \frac{25E}{L^2} \left(\frac{c}{cd - ae} \right) \Delta \quad (7)$$

$$M_{AB} = \frac{25E}{L^2} \left(\frac{e}{cd - ae} \right) \Delta \quad (8)$$



$$M_{AB} = \frac{25E}{L} \left(\frac{e}{ae - cd} \right) \theta_A + \frac{25E}{L} \left(\frac{d}{ab - cd} \right) \theta_B + \frac{25E}{L^2} \left(\frac{d + e}{cd - ae} \right) \Delta_{AB} + FEM_{AB} \quad (9)$$

$$M_{BA} = \frac{25E}{L} \left(\frac{a}{ab - cd} \right) \theta_B + \frac{25E}{L} \left(\frac{c}{ae - cd} \right) \theta_A + \frac{25E}{L^2} \left(\frac{a + c}{cd - ae} \right) \Delta_{AB} + FEM_{BA} \quad (10)$$



$$M_{AB} = \frac{25E}{L} \left(\frac{b}{ab - cd} \right) \theta_A + \frac{25E}{L} \left(\frac{d}{ab - cd} \right) \theta_B + \frac{25E}{L^2} \left(\frac{d + b}{cd - ab} \right) \Delta_{AB} + FEM_{AB} \quad (11)$$

$$M_{BA} = \frac{25E}{L} \left(\frac{a}{ab - cd} \right) \theta_B + \frac{25E}{L} \left(\frac{c}{ab - cd} \right) \theta_A + \frac{25E}{L^2} \left(\frac{a + c}{cd - ab} \right) \Delta_{AB} + FEM_{BA} \quad (12)$$

Equations from (9) to 12 can be expressed as follows:

$$M_{AB} = A_{AB} \theta_A + B_{AB} \theta_B + C_{AB} \Delta_{AB} + FEM_{AB} \quad (13)$$

$$M_{BA} = A_{BA} \theta_B + B_{BA} \theta_A + C_{BA} \Delta_{AB} + FEM_{BA} \quad (14)$$

where

$$a = 0.2/I_5 + 0.8/I_4 + 1.8/I_3 + 3.2/I_2 + 7/3I_1$$

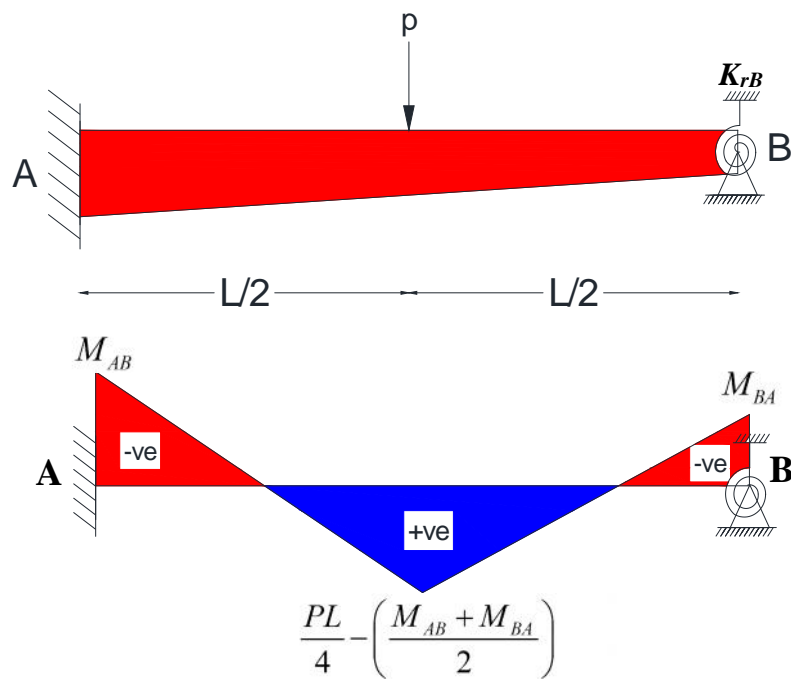
$$b = 0.2/I_2 + 0.8/I_3 + 1.8/I_4 + 3.2/I_5 + 7/3I_6$$

$$c = 1/6I_1 + 0.8/I_2 + 1.2/I_3 + 1.2/I_4 + 0.8/I_5$$

$$d = 1/6I_6 + 0.8/I_5 + 1.2/I_4 + 1.2/I_3 + 0.8/I_2$$

$$e = b + 25E/K_{rB}L$$

Fixed End Moment for point load at the mid span



Bending Moment Diagram

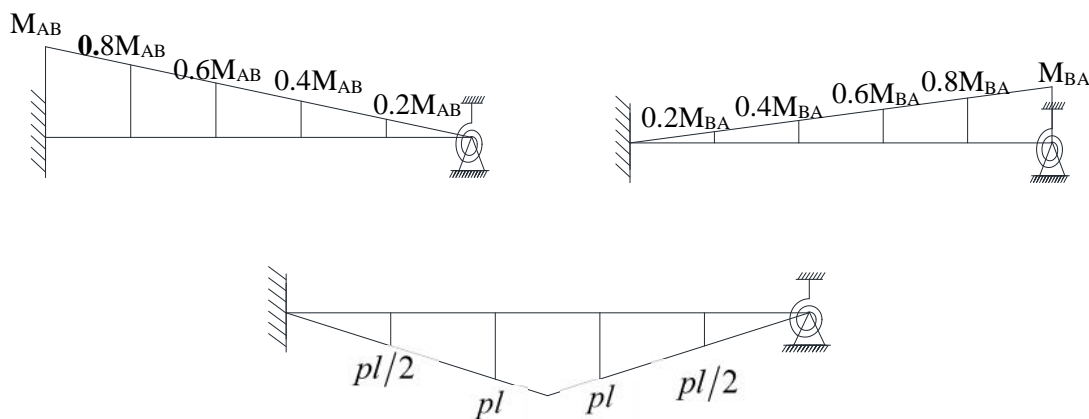


Fig. C-6. Bending Moment Diagram under point load at the midspan

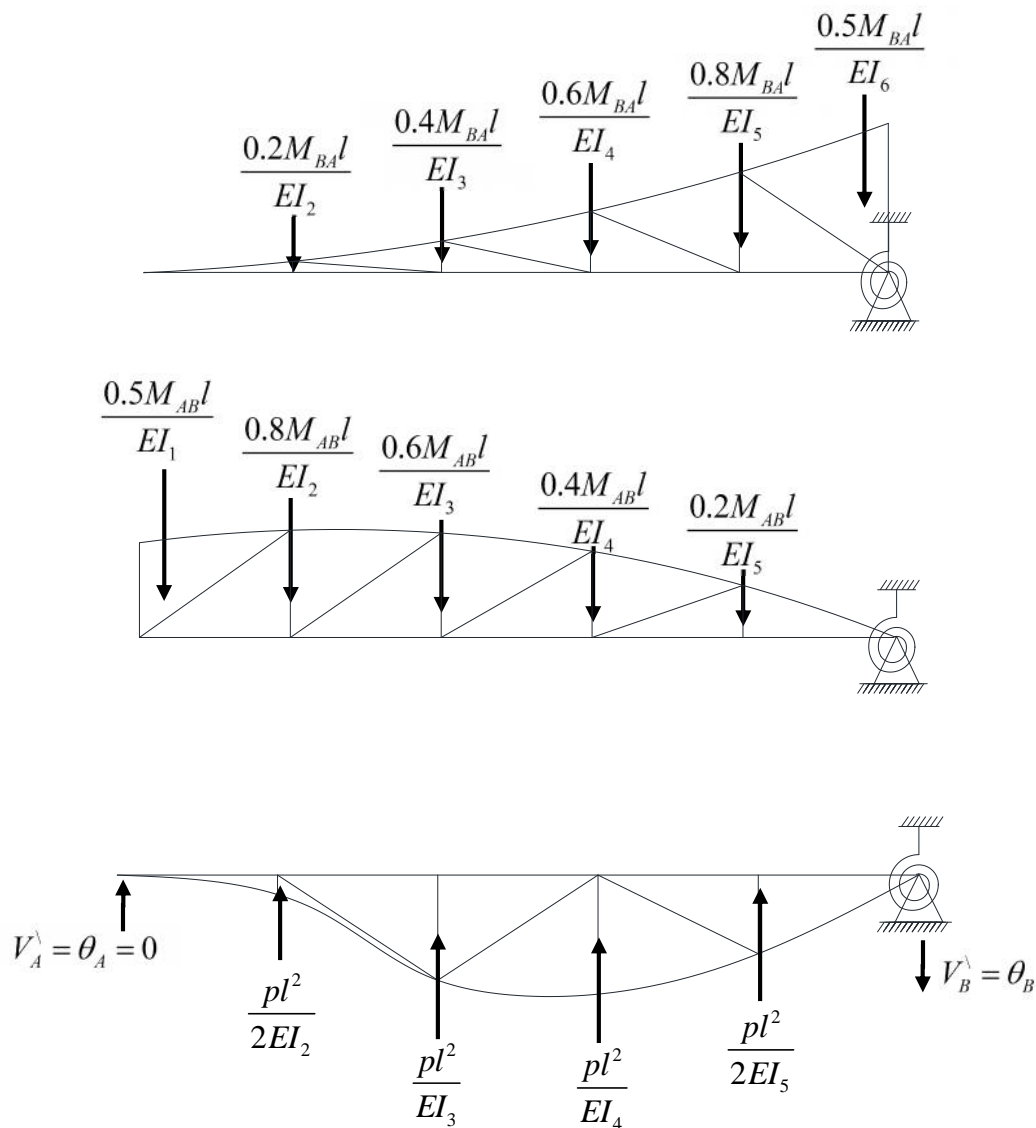


Fig. C-7. Loads on Conjugate Beam

$$\sum M @ A^{\lambda} = 0$$

$$\frac{M_{AB}l^2}{E}c + \frac{M_{BA}l^2}{E}e = \frac{pl^3}{E} \left(\frac{1}{2I_2} + \frac{2}{I_3} + \frac{3}{I_4} + \frac{2}{I_5} \right)$$

$$M_{AB}c + M_{BA}e = pl(p_1) = \frac{pL}{5}(p_1)$$

$$\sum M @ B^{\lambda} = 0$$

$$\frac{M_{AB}l^2}{E}a + \frac{M_{BA}l^2}{E}d = \frac{pl^3}{E} \left(\frac{1}{2I_5} + \frac{2}{I_4} + \frac{3}{I_3} + \frac{2}{I_2} \right)$$

$$M_{AB}a + M_{BA}d = pl(p_2) = \frac{pL}{5}(p_2)$$

$$M_{BA} \left(d - \frac{ae}{c} \right) = \frac{PL}{5} \left(p_2 - \frac{ap_1}{c} \right)$$

$$FEM_{BA} = \frac{pL}{5} \left(\frac{ap_1 - cp_2}{ae - cd} \right) \quad (15)$$

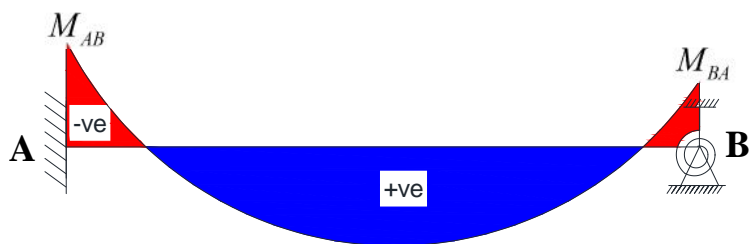
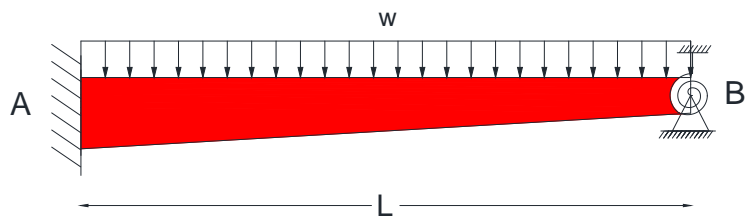
$$FEM_{AB} = \frac{pL}{5} \left(\frac{bp_2 - dp_1}{ae - cd} \right) \quad (16)$$

where

$$p_1 = 1/2I_2 + 2/I_3 + 3/I_4 + 2/I_5$$

$$p_2 = 1/2I_5 + 2/I_4 + 3/I_3 + 2/I_2$$

Fixed End Moment for uniform distributed load



$$\frac{wL^2}{8} - \left(\frac{M_{AB} + M_{BA}}{2} \right)$$

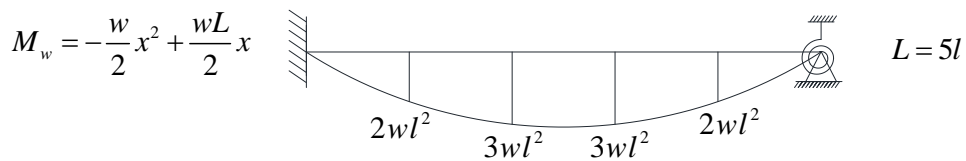
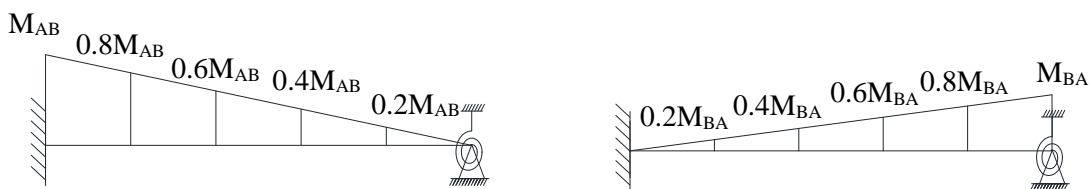


Fig. C-8. Bending moment under distributed load

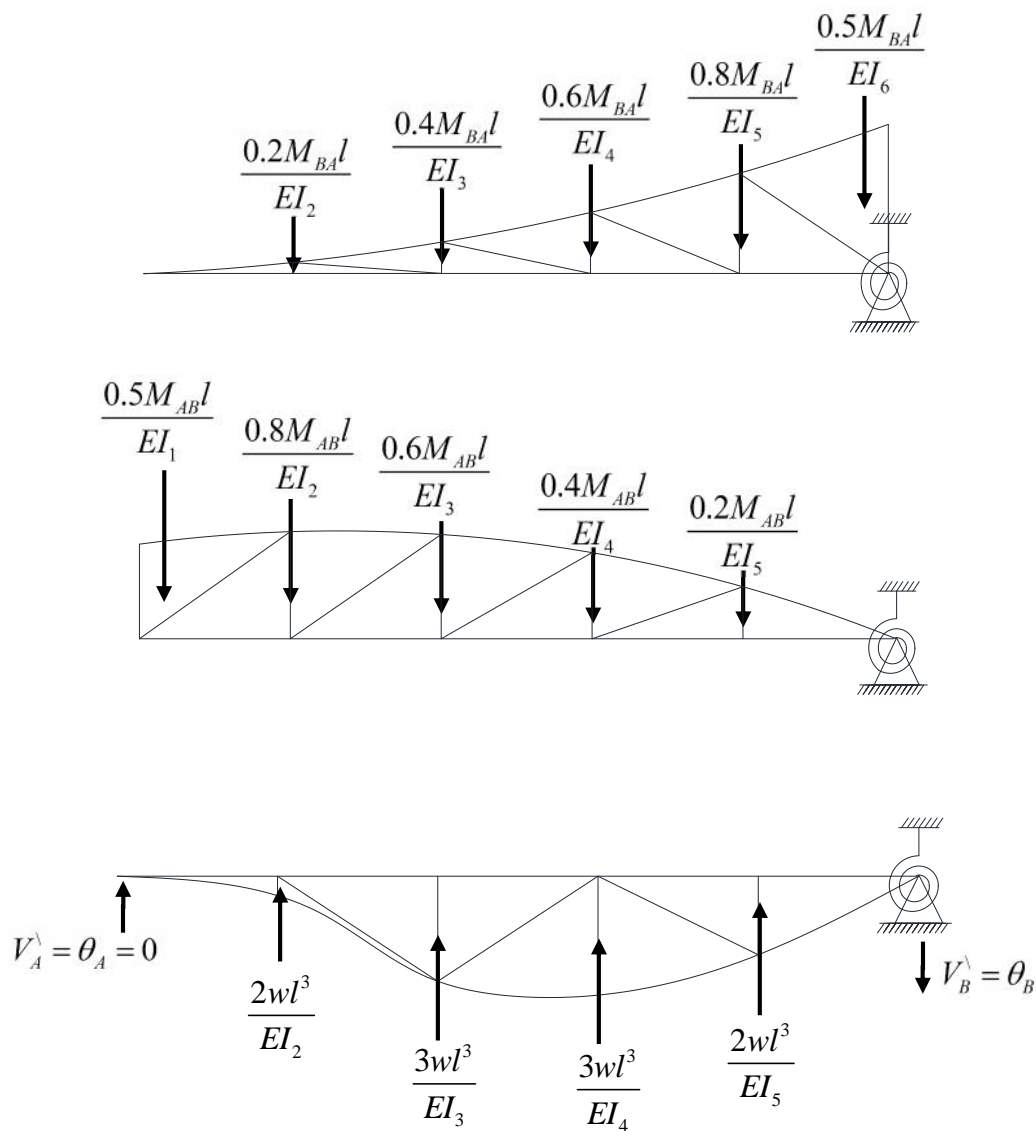


Fig. C-9. Loads on Conjugate Beam under distributed load

$$\sum M @ A^{\lambda} = 0$$

$$\sum M @ A^{\lambda} = 0$$

$$\frac{M_{AB}l^2}{E}c + \frac{M_{BA}l^2}{E}e = \frac{wl^4}{E} \left(\frac{2}{I_2} + \frac{6}{I_3} + \frac{9}{I_4} + \frac{8}{I_5} \right)$$

$$M_{AB}c + M_{BA}e = \frac{wL^2}{25}(w_1)$$

$$\sum M @ B^1 = 0$$

$$\frac{M_{AB}l^2}{E}a + \frac{M_{BA}l^2}{E}d = \frac{wl^4}{E} \left(\frac{2}{I_5} + \frac{6}{I_4} + \frac{9}{I_3} + \frac{8}{I_2} \right)$$

$$M_{AB}a + M_{BA}d = \frac{wL^2}{25}(w_2)$$

$$M_{BA} \left(d - \frac{ae}{c} \right) = \frac{wL^2}{25} \left(w_2 - \frac{aw_1}{c} \right)$$

$$FEM_{BA} = \frac{wL^2}{25} \left(\frac{aw_1 - cw_2}{ae - cd} \right) \quad (17)$$

$$FEM_{AB} = \frac{wL^2}{25} \left(\frac{bw_2 - dw_1}{ae - cd} \right) \quad (18)$$

where

$$w_1 = 2/I_2 + 6/I_3 + 9/I_4 + 8/I_5$$

$$w_2 = 2/I_5 + 6/I_4 + 9/I_3 + 8/I_2$$

APPENDIX D.

ESTIMATION OF THE STIFFNESSES PROVIDED BY THE CHIMNEY FOR TIDE

MILL BRIDGE HCB

(1) BASICS OF MECHANICS EQUATIONS

(2) MATLAB CODE

(1) Basics of mechanics equations

Point load at the mid span of Tide Mill bridge's HCB

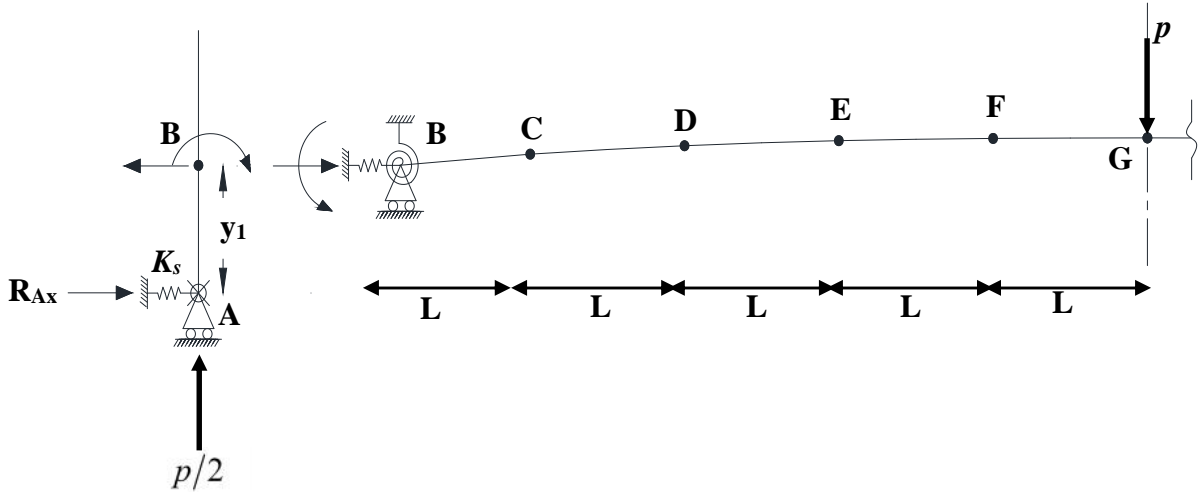


Fig. D-1. Midspan Point Load at the Tide Mill simulated HCB

$$\frac{R_{Ax}}{K_s} + \Delta_{AB} - \frac{\Delta_{BC} y_2}{L_{BC}} - \frac{\Delta_{CD} y_3}{L_{CD}} - \frac{\Delta_{DE} y_4}{L_{DE}} - \frac{\Delta_{EF} y_5}{L_{EF}} - \frac{\Delta_{EF} y_6}{L_{EF}} = 0 \quad (1)$$

$$-R_{Ax} y_1 + M_{AB} + M_{BA} = 0 \quad (2)$$

$$-R_{Ax} (y_1 + y_2) + M_{AB} + M_{CB} = -pL/2 \quad (3)$$

$$-R_{Ax} (y_1 + y_2 + y_3) + M_{AB} + M_{DC} = -pL \quad (4)$$

$$-R_{Ax} (y_1 + y_2 + y_3 + y_4) + M_{AB} + M_{ED} = -3pL/2 \quad (5)$$

$$-R_{Ax} (y_1 + y_2 + y_3 + y_4 + y_5) + M_{AB} + M_{FE} = -2pL \quad (6)$$

$$-R_{Ax} (y_1 + y_2 + y_3 + y_4 + y_5 + y_6) + M_{AB} + M_{GF} = -5pL/2 \quad (7)$$

$$M_{AB} - \frac{2(EI)_{AB}}{y_1} \theta_B + \frac{6(EI)_{AB}}{y_1^2} \Delta_{AB} = 0 \quad (8)$$

$$M_{BA} - \frac{4(EI)_{AB}}{y_1} \theta_B + \frac{6(EI)_{AB}}{y_1^2} \Delta_{AB} = 0 \quad (9)$$

$$-M_{BA} - A_{BC} \theta_B - B_{BC} \theta_C - C_{BC} \Delta_{BC} = 0 \quad (10)$$

$$(11)$$

$$M_{BC} - A_{CB}{}_{C} - B_{CB}{}_{B} - C_{CB}\Delta_{BC} = 0$$

$$-M_{CB} - A_{CD}{}_{C} - B_{CD}{}_{D} - C_{CD}\Delta_{CD} = 0 \quad (12)$$

$$M_{DC} - A_{DC}{}_{D} - B_{DC}{}_{c} - C_{DC}\Delta_{CD} = 0 \quad (13)$$

$$-M_{DC} - A_{DE}{}_{D} - B_{DE}{}_{E} - C_{DE}\Delta_{DE} = 0 \quad (14)$$

$$M_{ED} - A_{ED}{}_{D} - B_{ED}{}_{D} - C_{ED}\Delta_{DE} = 0 \quad (15)$$

$$-M_{ED} - A_{EF}{}_{E} - B_{EF}{}_{F} - C_{FE}\Delta_{EF} = 0 \quad (16)$$

$$M_{FE} - A_{FE}{}_{F} - B_{FE}{}_{F} - C_{FE}\Delta_{EF} = 0 \quad (17)$$

$$-M_{FE} - A_{FG}{}_{F} - C_{FG}\Delta_{FG} = 0 \quad (18)$$

$$M_{GF} - B_{GF}{}_{F} - C_{GF}\Delta_{FG} = 0 \quad (19)$$

Note

${}_{G} = 0$ (because of the symmetry)

$$K_{Rch} = \frac{M_{BA}}{{}_{B}}$$

$$K_{Xch} = \frac{-R_{Ax}}{(R_{Ax}/K_s - \Delta_{AB})}$$

$$y_2 = y_C - y_B$$

$$y_3 = y_D - y_C$$

$$y_4 = y_E - y_D$$

$$y_5 = y_F - y_E$$

$$y_6 = y_G - y_E$$

Two quarter point loads on the Tide Mill bridge's HCB

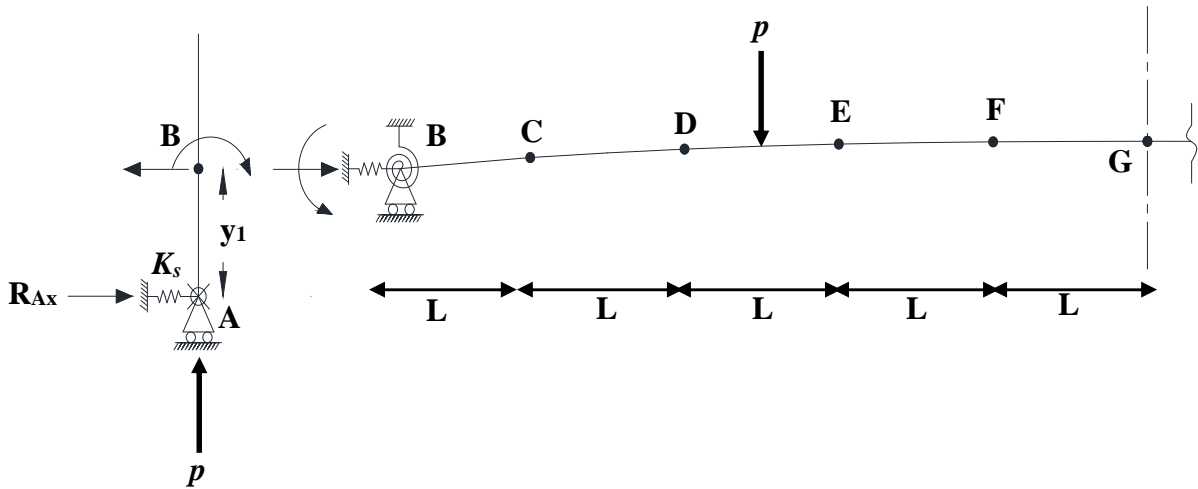


Fig. D-2. Two Point Loads at quarter Points at the Tide Mill simulated HCB

$$\frac{R_{Ax}}{K_s} + \Delta_{AB} - \frac{\Delta_{BC}y_2}{L_{BC}} - \frac{\Delta_{CD}y_3}{L_{CD}} - \frac{\Delta_{DE}y_4}{L_{DE}} - \frac{\Delta_{EF}y_5}{L_{EF}} - \frac{\Delta_{EF}y_6}{L_{EF}} = 0 \quad (1)$$

$$-R_{Ax}y_1 + M_{AB} + M_{BA} = 0 \quad (2)$$

$$-R_{Ax}(y_1 + y_2) + M_{AB} + M_{CB} = -pL \quad (3)$$

$$-R_{Ax}(y_1 + y_2 + y_3) + M_{AB} + M_{DC} = -2pL \quad (4)$$

$$-R_{Ax}(y_1 + y_2 + y_3 + y_4) + M_{AB} + M_{ED} = -5pL/2 \quad (5)$$

$$-R_{Ax}(y_1 + y_2 + y_3 + y_4 + y_5) + M_{AB} + M_{FE} = -5pL/2 \quad (6)$$

$$-R_{Ax}(y_1 + y_2 + y_3 + y_4 + y_5 + y_6) + M_{AB} + M_{GF} = -5pL/2 \quad (7)$$

$$M_{AB} - \frac{2(EI)_{AB}}{y_1} \theta_B + \frac{6(EI)_{AB}}{y_1^2} \Delta_{AB} = 0 \quad (8)$$

$$M_{BA} - \frac{4(EI)_{AB}}{y_1} \theta_B + \frac{6(EI)_{AB}}{y_1^2} \Delta_{AB} = 0 \quad (9)$$

$$-M_{BA} - A_{BC} \theta_B - B_{BC} \theta_C - C_{BC} \Delta_{BC} = 0 \quad (10)$$

$$M_{BC} - A_{CB} \theta_C - B_{CB} \theta_B - C_{CB} \Delta_{BC} = 0 \quad (11)$$

$$(12)$$

$$-M_{CB} - A_{CD''C} - B_{CD''D} - C_{CD}\Delta_{CD} = 0$$

$$M_{DC} - A_{DC''D} - B_{DC''c} - C_{DC}\Delta_{CD} = 0 \quad (13)$$

$$-M_{DC} - A_{DE''D} - B_{DE''E} - C_{DE}\Delta_{DE} = -FEM_{DE} \quad (14)$$

$$M_{ED} - A_{ED''D} - B_{ED''D} - C_{ED}\Delta_{DE} = FEM_{DE} \quad (15)$$

$$-M_{ED} - A_{EF''E} - B_{EF''F} - C_{FE}\Delta_{EF} = 0 \quad (16)$$

$$M_{FE} - A_{FE''F} - B_{FE''F} - C_{FE}\Delta_{EF} = 0 \quad (17)$$

$$-M_{FE} - A_{FG''F} - C_{FG}\Delta_{FG} = 0 \quad (18)$$

$$M_{GF} - B_{GF''F} - C_{GF}\Delta_{FG} = 0 \quad (19)$$

Uniform distributed load on the Tide Mill bridge's HCB

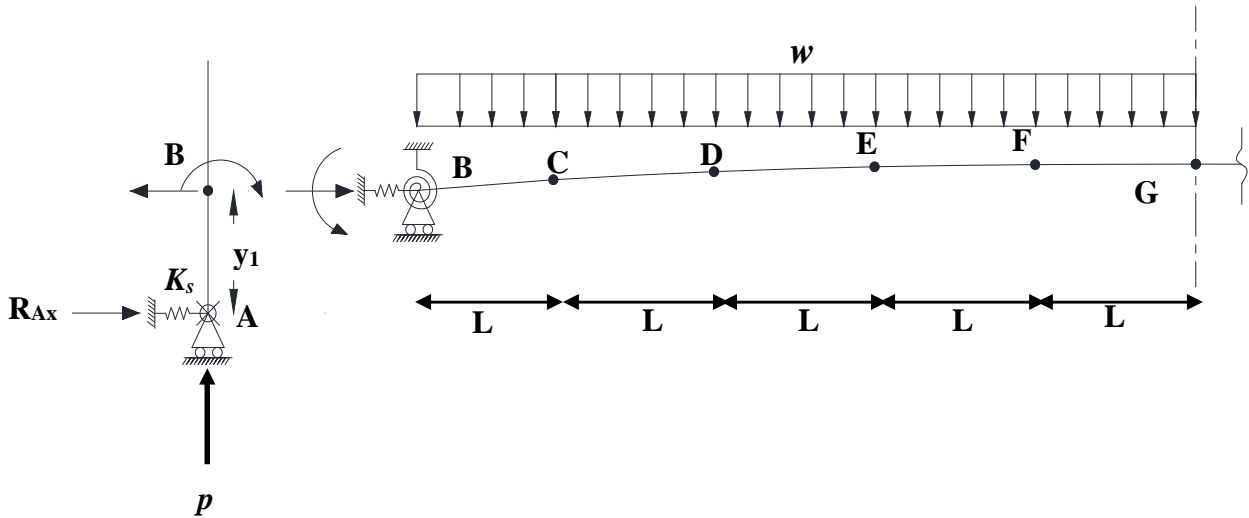


Fig. D-3. Uniform distributed load on the Tide Mill simulated HCB

$$\frac{R_{Ax}}{K_s} + \Delta_{AB} - \frac{\Delta_{BC} y_2}{L_{BC}} - \frac{\Delta_{CD} y_3}{L_{CD}} - \frac{\Delta_{DE} y_4}{L_{DE}} - \frac{\Delta_{EF} y_5}{L_{EF}} - \frac{\Delta_{FG} y_6}{L_{FG}} = 0 \quad (1)$$

$$-R_{Ax} y_1 + M_{AB} + M_{BA} = 0 \quad (2)$$

$$-R_{Ax} (y_1 + y_2) + M_{AB} + M_{CB} = -9wL^2/2 \quad (3)$$

$$-R_{Ax} (y_1 + y_2 + y_3) + M_{AB} + M_{DC} = -8wL^2 \quad (4)$$

$$-R_{Ax} (y_1 + y_2 + y_3 + y_4) + M_{AB} + M_{ED} = -23wL^2/2 \quad (5)$$

$$-R_{Ax} (y_1 + y_2 + y_3 + y_4 + y_5) + M_{AB} + M_{FE} = -12wL^2 \quad (6)$$

$$-R_{Ax} (y_1 + y_2 + y_3 + y_4 + y_5 + y_6) + M_{AB} + M_{GF} = -25wL^2/2 \quad (7)$$

$$M_{AB} - \frac{2(EI)_{AB}}{y_1} \Delta_{AB} + \frac{6(EI)_{AB}}{y_1^2} \Delta_{AB} = 0 \quad (8)$$

$$M_{BA} - \frac{4(EI)_{AB}}{y_1} \Delta_{AB} + \frac{6(EI)_{AB}}{y_1^2} \Delta_{AB} = 0 \quad (9)$$

$$-M_{BA} - A_{BC} \Delta_{BC} - B_{BC} \Delta_{BC} - C_{BC} \Delta_{BC} = -FEM_{BC} \quad (10)$$

$$(11)$$

$$M_{BC} - A_{CB''C} - B_{CB''B} - C_{CB}\Delta_{BC} = FEM_{CB}$$

$$-M_{CB} - A_{CD''C} - B_{CD''D} - C_{CD}\Delta_{CD} = -FEM_{CD} \quad (12)$$

$$M_{DC} - A_{DC''D} - B_{DC''c} - C_{DC}\Delta_{CD} = FEM_{DC} \quad (13)$$

$$-M_{DC} - A_{DE''D} - B_{DE''E} - C_{DE}\Delta_{DE} = -FEM_{DE} \quad (14)$$

$$M_{ED} - A_{ED''D} - B_{ED''D} - C_{ED}\Delta_{DE} = FEM_{ED} \quad (15)$$

$$-M_{ED} - A_{EF''E} - B_{EF''F} - C_{FE}\Delta_{EF} = -FEM_{FE} \quad (16)$$

$$M_{FE} - A_{FE''F} - B_{FE''F} - C_{FE}\Delta_{EF} = FEM_{FE} \quad (17)$$

$$-M_{FE} - A_{FG''F} - C_{FG}\Delta_{FG} = -FEM_{CD} \quad (18)$$

$$M_{GF} - B_{GF''F} - C_{GF}\Delta_{FG} = FEM_{GF} \quad (19)$$

(2) MATLAB code for estimating the stiffnesses provided by the Tide Mill bridge's chimney

```

%%%%%%%%%%%%%%%%%%%%%%%%%%%%%%%%%%%%%%%%%%%%%%%%%%%%%%%%%%%%%%%%%%%%%%%%%%
%%%%%%%%%          1- Material Properties          %%%%%%%%%%
%%%%%%%%%%%%%%%%%%%%%%%%%%%%%%%%%%%%%%%%%%%%%%%%%%%%%%%%%%%%%%%%%%%%%%%%%%

%%%%%%%%%%%%%%%%%%%%%%%%%%%%%%%%%%%%%%%%%%%%%%%%%%%%%%%%%%%%%%%%%%%%%%%%%% Concrete Properties %%%%%%%%%%%
%%% Arch
Fca = 6;          %%% compressive strength of concrete arch in
Ksi
Dca = 0.15;      %%% Denisty of concrete arch in Kip/cubic feet

%%% Deck
Fcd = 0;          %%% compressive strength of concrete deck in
Ksi
Dcd = 0.15;      %%% Denisty of concrete deck in Kip/cubic feet

%%%%%%%%%%%%%%%%%%%%%%%%%%%%%%%%%%%%%%%%%%%%%%%%%%%%%%%%%%%%%%%%%%%%%%%%%% Steel Properties %%%%%%%%%%%
%%% Strands
Astr = 0.153;     %%% Area of one prestressing strand in inch square
dstr = 0.5;       %%% Diameter of one strand in inch
Fpu = 270;        %%% Tensile strength of prestressing strand in Ksi
Ep = 27500;       %%% Modulus of elasticity of prestressing steel in
Ksi

%%%%%%%%%%%%%%%%%%%%%%%%%%%%%%%%%%%%%%%%%%%%%%%%%%%%%%%%%%%%%%%%%%%%%%%%%% FRP Properties %%%%%%%%%%%
%%% Webs
Ew11 = 3100;      %%% Modulus of elasticity in dir. 1-1 of GFRP of
web in Ksi
Ew22 = 2300;      %%% Modulus of elasticity in dir. 2-2 of GFRP of
web in Ksi
Gw12 = 1010;      %%% Shear Modulus in plane 1-2 of GFRP of web in
Ksi
Pw12 = 0.30;      %%% Poisson's ratio in plane 1-2 of GFRP of web
Shw = 19;         %%% Shear strength in plane 1-2 of GFRP of web in
Ksi

%%% Top flange
Etf11 = 3100;     %%% Modulus of elasticity in dir. 1-1 of GFRP of
top flange in Ksi
Etf22 = 2300;     %%% Modulus of elasticity in dir. 2-2 of GFRP of
top flange in Ksi
Gtf12 = 1010;     %%% Shear Modulus in plane 1-2 of GFRP of top
flange in Ksi
Ptf12 = 0.30;     %%% Major Poisson's ratio in plane 1-2 of GFRP of
top flange
Ptf21 = 0.26;     %%% Minor Poisson's ratio in plane 1-2 of GFRP of
top flange

%%% Bottom flange
Ebf11 = 3100;     %%% Modulus of elasticity in dir. 1-1 of GFRP of
bot. flange in Ksi
Ebf22 = 2300;     %%% Modulus of elasticity in dir. 2-2 of GFRP of
bot. flange in Ksi

```

```
Gbf12 = 1010;      %% Shear Modulus in plane 1-2 of GFRP of bot.
flange in Ksi
Pbf12 = 0.30;     %% Major Poisson's ratio in plane 1-2 of GFRP of
bot. flange
Pbf21 = 0.26;     %% Minor Poisson's ratio in plane 1-2 of GFRP of
bot. flange
```

```
%%%%%%%%%%%%%%%%%%%%%%%%%%%%%%%%%%%%%%%%%%%%%%%%%%%%%%%%%%%%%%%%%%%%%%%%
%%                               2- Geometry                               %%
%%%%%%%%%%%%%%%%%%%%%%%%%%%%%%%%%%%%%%%%%%%%%%%%%%%%%%%%%%%%%%%%%%%%%%%%
```

```
%%% Beam
```

```
h   = 21;          %% Height of HCB in inch
b   = 24;          %% Width of HCB in inch
bca = 22;          %% Width of HCB in inch
tw  = 0.156;       %% Thickness of FRP web in inch
ttf = 0.156;       %% Thickness of FRP top flange in inch
tbf = 0.156;       %% Thickness of FRP bot. flange in inch
tca = 4;           %% Thickness of concrete arch in inch
tcw = 3.5;         %% Thickness of concrete web(fin)in inch
WP  = 2;           %% Working point at thrut line (That is used to
determine the arch profile)
Nstr= 22;          %% no. of strands of the tensile reinforcement
Lovr= 44*12;       %% Overall length of the HCB in inch
LT  = 43*12;       %% Design span of the HCB in inch
```

```
%%% Bridge
```

```
SG  = 4;           %% spacing between the girders (HCBs)in feet
NG  = 3;           %% No. of girders
Wovr= 12;          %% Overall width of the bridge in feet
Wctc= 13.5;        %% curb to curb width of the bridge in feet
NEM = 50;          %% No. of elements that represent one HCB
```

```
X = zeros (1+NEM, 1);
```

```
%% vector of points at which the calculations of Moment, shear and
inertia are calculated in ft
```

```
L = 5*LT/NEM ; %% Lengths of each segment between two points in ft
```

```
for i= 1:NEM+1
    X(i,:) = L/5*(i-1);
end
aa = -4*(h-ttf-tca)/LT^2;
bb = 4*(h-ttf-tca)/LT;
cc = tca/2;
```

```
Yca = zeros (1+NEM, 1);
```

```
for i =1:NEM+1
    Yca(i,1) = aa*(X(i))^2+ bb*X(i) + cc;
end
```

```

%%%%%%%%%%%%%%%%%%%%%%%%%%%%%%%%%%%%%%%%%%%%%%%%%%%%%%%%%%%%%%%%%%%%%%%%
%%%%%%%% 4- Calculation of N.A. and Moment of inertia          %%%%%%%%%
%%%%%%%%%%%%%%%%%%%%%%%%%%%%%%%%%%%%%%%%%%%%%%%%%%%%%%%%%%%%%%%%%%%%%%%%

%%% 1- Identifying the Inertia of each component wrt its CG
%%% Tension RFT (strands)
Astr = Nstr*Astr;      %%%% Area of strands in inch square
Ys   = tbf+ 0.5*dstr;  %%%% CG of strands from the bottom of the HCB
nstr = Ep/Ew11;       %%%% modular ratio of the strands relative to
the FRP web
As   = Astr*nstr;     %%%% transformed area of strands in inch square
Is   = 0;             %%%% neglecting the moment of inertia of strands
%%% FRP Top flange
ntf  = Etf11/Ew11;
Ytf  = h-ttf/2;
Atf  = ttf*b*ntf;     %%%% transformed area of top flange in inch
square
Itf  = b*ttf^3/12*ntf; %%%% transformed Moment of inertia of top flange
in in^4
%%% FRP Bottom flange
nbf  = Ebf11/Ew11;
Ybf  = tbf/2;
Abf  = tbf*b*nbf;     %%%% transformed area of top flange in inch
square
Ibf  = b*tbf^3/12*nbf; %%%% transformed Moment of inertia of top flange
in in^4
%%% FRP Webs
Yw   = h/2;
Aw   = 2*tw*h;        %%%% area of two FRP webs in inch square
Iw   = 2*tw*h^3/12;   %%%% Moment of inertia of two webs in in^4
%%% Concrete Arch
Eca  = 57*sqrt(Fca*1000); %%%% Elastic modulus of concret in Ksi
nca  = Eca/Ew11;       %%%% modular ratio of the conc. Arch
relative to the FRP web
Aca  = tca*bca*nca;   %%%% transformed area of conc arch in
square inch
Ica  = bca*tca^3*nca/12; %%%% transformed Moment of inertia of conc
arch in in^4

%%% Concrete Web (fin)
Ecw  = 57*sqrt(Fca*1000); %%%% Elastic modulus of concrete in Ksi
ncw  = Ecw/Ew11;       %%%% modular ratio of the deck relative
to the FRP web
hcw  = zeros(NEM+1,1);
Ycw  = zeros(NEM+1,1);
Acw  = zeros(NEM+1,1);
Icw  = zeros(NEM+1,1);

for i=1:NEM+1          %%%% Calculating the height and the area
of the concrete web
    hcw(i,1)= h-(Yca(i,:)+tca/2+ttf);
    Ycw(i,1)= h-(hcw(i,+)/2+ttf);
    Acw(i,1)= hcw(i,1)*tcw*ncw;
    Icw(i,1)= tcw*(hcw(i,1))^3*ncw/12;
end

```



```

%%%% 1- Identifying the N.A. and moment of inertia of HCB

Ybar = zeros(NEM+1,1); %%%% N.A of HCB at each point
I     = zeros(NEM+1,1); %%%% moment of inertia of HCB in in^4
A     = zeros(NEM+1,1);

%%%% Area of HCB in in^2
for i= 1:NEM+1
    A(i,:) = As+Atf+Abf+Aw+Aca+Acw(i,:);
    Ybar(i,:)=
    (As*Ys+Atf*Ytf+Abf*Ybf+Aw*Yw+Aca*Yca(i,:)+Acw(i,:)*Ycw(i,:))/A(i,:);
    I (i,:) = Is+As*(Ys-Ybar(i,:))^2+Itf+Atf*(Ytf-
    Ybar(i,:))^2+Ibf+Abf*(Ybf-Ybar(i,:))^2+Iw+Aw*(Yw-
    Ybar(i,:))^2+Ica+Aca*(Yca(i,:)-
    Ybar(i,:))^2+Icw(i,:)+Acw(i,:)*(Ycw(i,:)-Ybar(i,:))^2;
end

Arch = zeros(NEM+1,1); %%%% Geometry of the curved beam based on
the ENAs

for i =1:NEM+1
    Arch(i,1) = Ybar(i,1)-Ybar(1,1);
end

%%%% Chimney
ach = 12; %%% the depth of the chimney in inch (the dimension
in the longitudinal direction of the beam (x))
bch = 22; %%% the width of the chimney in inch (the dimension
in the transverse direction (Z in ansys and y in sap))
Ich = bch*ach^3/12;
Ech = Eca;
P = 15; %%% POINT LOAD AT THE MIDSPAN IN KIP
PQ = 12.5; %%%% two Point loads at quarter points in Kip

y1 = Ybar(1,1);
y2 = Arch(6,1)-Arch(1,1);
y3 = Arch(11,1)-Arch(6,1);
y4 = Arch(16,1)-Arch(11,1);
y5 = Arch(21,1)-Arch(16,1);
y6 = Arch(26,1)-Arch(21,1);
LAB = y1;
LBC = sqrt (L^2+y2^2);
LCD = sqrt (L^2+y3^2);
LDE = sqrt (L^2+y4^2);
LEF = sqrt (L^2+y5^2);
LFG = sqrt (L^2+y6^2);

Ks = 2*Ep*Astr/LT;

```

```

aBC      =
(0.2/I(5,1)+0.8/I(4,1)+1.8/I(3,1)+3.2/I(2,1)+7/3/I(1,1));
bBC      =
(0.2/I(2,1)+0.8/I(3,1)+1.8/I(4,1)+3.2/I(5,1)+7/3/I(6,1));
cBC      =
(1/6/I(1,1)+0.8/I(2,1)+1.2/I(3,1)+1.2/I(4,1)+0.8/I(5,1));
dBC      =
(1/6/I(6,1)+0.8/I(5,1)+1.2/I(4,1)+1.2/I(3,1)+0.8/I(2,1));

ABC      =      (25*Ew11/LBC)*(bBC/(aBC*bBC-cBC*dBC));
BBC      =      (25*Ew11/LBC)*(dBC/(aBC*bBC-cBC*dBC));
CBC      =      (25*Ew11/LBC^2)*(bBC+dBC)/(cBC*dBC-aBC*bBC);
ACB      =      (25*Ew11/LBC)*(aBC/(aBC*bBC-cBC*dBC));
BCB      =      (25*Ew11/LBC)*(cBC/(aBC*bBC-cBC*dBC));
CCB      =      (25*Ew11/LBC^2)*(aBC+cBC)/(cBC*dBC-aBC*bBC);

aCD      =      (0.2/I(10,1)+0.8/I(9,1)+1.8/I(8,1)+3.2/I(7,1)+7/3/I(6,1));
bCD      =      (0.2/I(7,1)+0.8/I(8,1)+1.8/I(9,1)+3.2/I(10,1)+7/3/I(11,1));
cCD      =      (1/6/I(6,1)+0.8/I(7,1)+1.2/I(8,1)+1.2/I(9,1)+0.8/I(10,1));
dCD      =      (1/6/I(11,1)+0.8/I(10,1)+1.2/I(9,1)+1.2/I(8,1)+0.8/I(7,1));

ACD      =      (25*Ew11/LCD)*(bCD/(aCD*bCD-cCD*dCD));
BCD      =      (25*Ew11/LCD)*(dCD/(aCD*bCD-cCD*dCD));
CCD      =      (25*Ew11/LCD^2)*(bCD+dCD)/(cCD*dCD-aCD*bCD);
ADC      =      (25*Ew11/LCD)*(aCD/(aCD*bCD-cCD*dCD));
BDC      =      (25*Ew11/LCD)*(cCD/(aCD*bCD-cCD*dCD));
CDC      =      (25*Ew11/LCD^2)*(aCD+cCD)/(cCD*dCD-aCD*bCD);

aDE      =      (0.2/I(15,1)+0.8/I(14,1)+1.8/I(13,1)+3.2/I(12,1)+7/3/I(11,1));
bDE      =      (0.2/I(12,1)+0.8/I(13,1)+1.8/I(14,1)+3.2/I(15,1)+7/3/I(16,1));
cDE      =      (1/6/I(11,1)+0.8/I(12,1)+1.2/I(13,1)+1.2/I(14,1)+0.8/I(15,1));
dDE      =      (1/6/I(16,1)+0.8/I(15,1)+1.2/I(14,1)+1.2/I(13,1)+0.8/I(12,1));
P1DE     =      (1/2/I(12,1)+2/I(13,1)+3/I(14,1)+2/I(15,1));
P2DE     =      (1/2/I(15,1)+2/I(14,1)+3/I(13,1)+2/I(12,1));

ADE      =      (25*Ew11/LDE)*(bDE/(aDE*bDE-cDE*dDE));
BDE      =      (25*Ew11/LDE)*(dDE/(aDE*bDE-cDE*dDE));
CDE      =      (25*Ew11/LDE^2)*(bDE+dDE)/(cDE*dDE-aDE*bDE);
AED      =      (25*Ew11/LDE)*(aDE/(aDE*bDE-cDE*dDE));
BED      =      (25*Ew11/LDE)*(cDE/(aDE*bDE-cDE*dDE));
CED      =      (25*Ew11/LDE^2)*(aDE+cDE)/(cDE*dDE-aDE*bDE);
FEMDEQ   =      PQ*LDE/5*(bDE*P2DE-dDE*P1DE)/(aDE*bDE-cDE*dDE);
FEMEDQ   =      PQ*LDE/5*(aDE*P1DE-cDE*P2DE)/(aDE*bDE-cDE*dDE);

aEF      =      (0.2/I(20,1)+0.8/I(19,1)+1.8/I(18,1)+3.2/I(17,1)+7/3/I(16,1));
bEF      =      (0.2/I(17,1)+0.8/I(18,1)+1.8/I(19,1)+3.2/I(20,1)+7/3/I(21,1));
cEF      =      (1/6/I(16,1)+0.8/I(17,1)+1.2/I(18,1)+1.2/I(19,1)+0.8/I(20,1));
dEF      =      (1/6/I(21,1)+0.8/I(20,1)+1.2/I(19,1)+1.2/I(18,1)+0.8/I(17,1));

AEF      =      (25*Ew11/LEF)*(bEF/(aEF*bEF-cEF*dEF));
BEF      =      (25*Ew11/LEF)*(dEF/(aEF*bEF-cEF*dEF));

```

```

CEF      =      (25*Ew11/LEF^2)*(bEF+dEF)/(cEF*dEF-aEF*bEF);
AFE      =      (25*Ew11/LEF)*(aEF/(aEF*bEF-cEF*dEF));
BFE      =      (25*Ew11/LEF)*(cEF/(aEF*bEF-cEF*dEF));
CFE      =      (25*Ew11/LEF^2)*(aEF+cEF)/(cEF*dEF-aEF*bEF);

aFG =      (0.2/I(25,1)+0.8/I(24,1)+1.8/I(23,1)+3.2/I(22,1)+7/3/I(21,1));
bFG =      (0.2/I(22,1)+0.8/I(23,1)+1.8/I(24,1)+3.2/I(25,1)+7/3/I(26,1));
cFG =      (1/6/I(21,1)+0.8/I(22,1)+1.2/I(23,1)+1.2/I(24,1)+0.8/I(25,1));
dFG =      (1/6/I(26,1)+0.8/I(25,1)+1.2/I(24,1)+1.2/I(23,1)+0.8/I(22,1));

AFG      =      (25*Ew11/LFG)*(bFG/(aFG*bFG-cFG*dFG));
BFG      =      (25*Ew11/LFG)*(dFG/(aFG*bFG-cFG*dFG));
CFG      =      (25*Ew11/LFG^2)*(bFG+dFG)/(cFG*dFG-aFG*bFG);
AGF      =      (25*Ew11/LFG)*(aFG/(aFG*bFG-cFG*dFG));
BGF      =      (25*Ew11/LFG)*(cFG/(aFG*bFG-cFG*dFG));
CGF      =      (25*Ew11/LFG^2)*(aFG+cFG)/(cFG*dFG-aFG*bFG);

COF      =      zeros (19,19);          %%%% coefficient for slope
deflection
F         =      zeros (19,1);          %%%% force vector

F (13,1) =      5/2*P*L;
F (14,1) =      2*P*L;
F (15,1) =      3/2*P*L;
F (16,1) =      P*L;
F (17,1) =      1/2*P*L;

COF (1,1) =      1;
COF (13,1) =     -1;

COF (2,2) =     -1;
COF (3,2) =      1;
COF (14,2) =     -1;

COF (4,3) =     -1;
COF (5,3) =      1;
COF (15,3) =     -1;

COF (6,4) =     -1;
COF (7,4) =      1;
COF (16,4) =     -1;

COF (8,5) =     -1;
COF (9,5) =      1;
COF (17,5) =     -1;

COF (1,6) =     -CGF;
COF (2,6) =     -CFG;
COF (19,6) =     -y6/LFG;

COF (3,7) =     -CFE;
COF (4,7) =     -CEF;

```

COF (19,7) = $-y5/LEF;$

 COF (5,8) = $-CED;$
 COF (6,8) = $-CDE;$
 COF (19,8) = $-y4/LDE;$

 COF (7,9) = $-CDC;$
 COF (8,9) = $-CCD;$
 COF (19,9) = $-y3/LCD;$

 COF (9,10) = $-CCB;$
 COF (10,10) = $-CBC;$
 COF (19,10) = $-y2/LBC;$

 COF (1,11) = $-BGF;$
 COF (2,11) = $-AFG;$
 COF (3,11) = $-AFE;$
 COF (4,11) = $-BEF;$

 COF (3,12) = $-BFE;$
 COF (4,12) = $-AEF;$
 COF (5,12) = $-AED;$
 COF (6,12) = $-BDE;$

 COF (5,13) = $-BED;$
 COF (6,13) = $-ADE;$
 COF (7,13) = $-ADC;$
 COF (8,13) = $-BCD;$

 COF (7,14) = $-BDC;$
 COF (8,14) = $-ACD;$
 COF (9,14) = $-ACB;$
 COF (10,14) = $-BBC;$

 COF (12,15) = $1;$
 COF (13,15) = $-1;$
 COF (14,15) = $-1;$
 COF (15,15) = $-1;$
 COF (16,15) = $-1;$
 COF (17,15) = $-1;$
 COF (18,15) = $-1;$

 COF (11,16) = $6*Ech*Ich/y1^2;$
 COF (12,16) = $6*Ech*Ich/y1^2;$
 COF (19,16) = $1;$

 COF (13,17) = $y1+y2+y3+y4+y5+y6;$
 COF (14,17) = $y1+y2+y3+y4+y5;$
 COF (15,17) = $y1+y2+y3+y4;$
 COF (16,17) = $y1+y2+y3;$
 COF (17,17) = $y1+y2;$
 COF (18,17) = $y1;$
 COF (19,17) = $1/Ks;$

```
COF (9,18) = -BCB;
COF (10,18) = -ABC;
COF (11,18) = -4*Ech*Ich/y1;
COF (12,18) = -2*Ech*Ich/y1;
```

```
COF (10,19) = -1;
COF (11,19) = 1;
COF (18,19) = -1;
```

```
UN = COF\F;
KR = UN(19)/UN(18);
KX = -UN(17)/(UN(16)-UN(17)/Ks);
```

```
%%%%%%%%%%%%%%%%%%%%%%%%%%%%%%%%%%%%%%%%%%%%%%%%%%%%%%%%%%%%%%%%%%%%%%%% two quarter Point Loads
%%%%%%%%%%%%%%%%%%%%%%%%%%%%%%%%%%%%%%%%%%%%%%%%%%%%%%%%%%%%%%%%%%%%%%%%
FQ = zeros (19,1); %%%% force vector For
uniform load
%%%%%%%%%%%%%%%%%%%%%%%%%%%%%%%%%%%%%%%%%%%%%%%%%%%%%%%%%%%%%%%%%%%%%%%%
%%%%%%%%%%%%%%%%%%%%%%%%%%%%%%%%%%%%%%%%%%%%%%%%%%%%%%%%%%%%%%%%%%%%%%%%
```

```
PQ = 12.5; %%%% two Point loads at
quarter points in Kip
```

```
FQ (5,1) = FEMEDQ;
FQ (6,1) = -FEMDEQ;
FQ (13,1) = 5/2*PQ*L;
FQ (14,1) = 5/2*PQ*L;
FQ (15,1) = 5/2*PQ*L;
FQ (16,1) = 2*PQ*L;
FQ (17,1) = PQ*L;
```

```
UNQ = COF\FQ;
KRQ = UNQ(19)/UNQ(18);
KXQ = -UNQ(17)/(-UNQ(16)+UNQ(17)/Ks);
```

APPENDIX E.
MATLAB CODES FOR ESTIMATING THE STRAINS IN HCBS AND HCBS
SUPPORTED ON BEARING PADS

(1) MATLAB code for estimating the strains in non-composite HCB supported on bearing pads

```

%%%%%%%%%%%%%%%%%%%%%%%%%%%%%%%%%%%%%%%%%%%%%%%%%%%%%%%%%%%%%%%%%%%%%%%%
%%%%%%%%%%%%%%%%%%%%%%%%%%%%%%%%%%%%%%%%%%%%%%%%%%%%%%%%%%%%%%%%%%%%%%%%
%%% This Matlab Code calculates the deflections, strains and stresses %
%%% of the multi-celled HCB of bridge B0410 at certain locations %%%
%%%%%%%%%%%%%%%%%%%%%%%%%%%%%%%%%%%%%%%%%%%%%%%%%%%%%%%%%%%%%%%%%%%%%%%% using transformed area Method %%%%%%%%%
%%%%%%%%%%%%%%%%%%%%%%%%%%%%%%%%%%%%%%%%%%%%%%%%%%%%%%%%%%%%%%%%%%%%%%%%
%%%%%%%%%%%%%%%%%%%%%%%%%%%%%%%%%%%%%%%%%%%%%%%%%%%%%%%%%%%%%%%%%%%%%%%%

%%%%%%%%%%%%%%%%%%%%%%%%%%%%%%%%%%%%%%%%%%%%%%%%%%%%%%%%%%%%%%%%%%%%%%%%
%%%%%%%%%%%%%%%%%%%%%%%%%%%%%%%%%%%%%%%%%%%%%%%%%%%%%%%%%%%%%%%%%%%%%%%%
%%%%%%%%%%%%%%%%%%%%%%%%%%%%%%%%%%%%%%%%%%%%%%%%%%%%%%%%%%%%%%%%%%%%%%%% 1- Material Properties %%%%%%%%%
%%%%%%%%%%%%%%%%%%%%%%%%%%%%%%%%%%%%%%%%%%%%%%%%%%%%%%%%%%%%%%%%%%%%%%%%

%%%%%%%%%%%%%%%%%%%%%%%%%%%%%%%%%%%%%%%%%%%%%%%%%%%%%%%%%%%%%%%%%%%%%%%% Concrete Properties %%%%%%%%%
%%% Arch
Sca = 11;           %% compressive strength of concrete arch in Ksi
Dca = 0.14;        %% Denisty of concrete arch in Kip/cubic feet
%% Cg of concrete arch in inch
Yca = [5; 6.367; 14.48; 22.96; 27.539; 30.44; 36.93; 42.42; 42.744;
46.91; 50.4; 51.725; 52.89; 54.39; 54.89; 54.39; 52.89; 50.4; 46.91;
42.42; 36.93; 30.44; 22.96; 14.48; 5];
X = [0; 9; 53.4; 115.8; 154; 178.2; 240.6; 303; 307.5; 365.4; 427.8;
461; 490.2; 552.6; 615; 677.4; 739.8; 802.2; 864.6; 927; 989.4; 1051.8;
1114.2; 1176.6; 1230]; %% vector of points at which the calculations
of Moment, shear and inertia are calculated in inch

%%% Deck
%Sd = 6.0;           %% compressive strength of concrete deck in Ksi
%Dd = 0.15;         %% Denisty of concrete arch in Kip/cubic feet

%%%%%%%%%%%%%%%%%%%%%%%%%%%%%%%%%%%%%%%%%%%%%%%%%%%%%%%%%%%%%%%%%%%%%%%% FRP Properties %%%%%%%%%
%%%%%%%%%%%%%%%%%%%%%%%%%%%%%%%%%%%%%%%%%%%%%%%%%%%%%%%%%%%%%%%%%%%%%%%%
%%%%%%%%%%%%%%%%%%%%%%%%%%%%%%%%%%%%%%%%%%%%%%%%%%%%%%%%%%%%%%%%%%%%%%%% Webs
Ew11 = 3100;        %% Modulus of elasticity in dir. 1-1 of GFRP of
web in Ksi (1378 psi from tests)
Ew22 = 1378;        %% Modulus of elasticity in dir. 2-2 of GFRP of
web in Ksi
Gw12 = 919;        %% Shear Modulus in plane 1-2 of GFRP of web in
Ksi
Pw12 = 0.26;       %% Poisson's ratio in plane 1-2 of GFRP of web
%Shw = 19;         %% Shear strength in plane 1-2 of GFRP of web in
Ksi
%%%%%%%%%%%%%%%%%%%%%%%%%%%%%%%%%%%%%%%%%%%%%%%%%%%%%%%%%%%%%%%%%%%%%%%% Top flange
Etf11 = 3100;      %% Modulus of elasticity in dir. 1-1 of GFRP of
top flange in Ksi
Etf22 = 1378;      %% Modulus of elasticity in dir. 2-2 of GFRP of
top flange in Ksi
Gtf12 = 919;      %% Shear Modulus in plane 1-2 of GFRP of top
flange in Ksi
Ptf12 = 0.26;     %% Major Poisson's ratio in plane 1-2 of GFRP of
top flange

```

```

%Ptf21 = 0.26;      %% Minor Poisson's ratio in plane 1-2 of GFRP of
top flange
%% %% Bottom flange
Ebf11 = 4000;      %% Modulus of elasticity in dir. 1-1 of GFRP of
bot. flange in Ksi
Ebf22 = 2277;      %% Modulus of elasticity in dir. 2-2 of GFRP of
bot. flange in Ksi
Gbf12 = 919;       %% Shear Modulus in plane 1-2 of GFRP of bot.
flange in Ksi
Pbf12 = 0.26;      %% Major Poisson's ratio in plane 1-2 of GFRP of
bot. flange
%Pbf21 = 0.26;      %% Minor Poisson's ratio in plane 1-2 of GFRP of
bot. flange

%%%%%%%%%%%%%%%%%%%%%%%%%%%%%%%%%%%%%%%%%%%%%%%%%%%%%%%%%%%%%%%%%%%%%%%%
%% %% 2- Geometry  %% %%
%%%%%%%%%%%%%%%%%%%%%%%%%%%%%%%%%%%%%%%%%%%%%%%%%%%%%%%%%%%%%%%%%%%%%%%%

%% %% Beam
h = 60.16;          %% Height of HCB in inch
b = 72;             %% Width of beam in inch
btf = 27.5;         %% Width of Top flange in inch (upper layer of
FRP Lid above two concrete arch)
btf2 = 44.5;        %% Width of Top flange2 in inch (The upper
layer of FRP Lid between the two concret arches)
btf3 = 44.3;        %% Width of Top flange3 in inch (Lower layer
of FRP Lid between the two concret arches)
bsw = 48;           %% Width of FRP sandwich between the girders
and under the deck
bbf = 66;           %% Width of Lower flange in inch
bbf2 = 38.4;        %% Width of Lower flange in inch (upper layert
of Lower flange between the two beams)
tw = 0.18;          %% Thickness of FRP web in inch
ttf = 0.37;         %% Thickness of FRP top flange in inch
tsw = 0.2;          %% Thickness of FRP sandwich
tbf = 0.08;         %% Thickness of FRP bot. flange in inch
tbf2 = 0.08;        %% Thickness of FRP bot. flange in inch
tca = 10;           %% Thickness of concrete arch in inch
bca = 10.5;         %% breadth of concrete arch in inch
tcw = 5;            %% Thickness of concrete web(fin)in inch
%WP = 2;            %% Working point at thrut line (That is used
to determine the arch profile)
Nstr = 88;          %% no. of strands of the tensile reinforcement
Nub = 30;           %% no. of uper deck bars
Nlb = 19;           %% no. of lower deck bars
Lovr = 1267;        %% Overall length of the HCB in inch
L = 1230;           %% Design span of the HCB in inch

%% %% Bridge
SG = 120;           %% spacing between the girders (HCBs)in inch
NG = 3;             %% No. of girders
%Wovr= 28;          %% Overall width of the bridge in feet
%Wctc= 30.667;      %% curb to curb width of the bridge in feet
NEM = 24;           %% No. of elements that represent one HCB

```



```

%%% Slab
%ts = 15.0;          %%% thickness of cast in place slab in inch
%bs = min( min (SG, 12*ts+b), L/4); %%% width of the CIP slab in
inch

Lseg = zeros (NEM,1); %%% Lengths of each segment between two points
in ft

for i= 1:NEM
    Lseg(i,:) = X (i+1,:)- X (i,:);
end

%%%%%%%%%%%%%%%%%%%%%%%%%%%%%%%%%%%%%%%%%%%%%%%%%%%%%%%%%%%%%%%%%%%%%%%%
%% 3- Loads
%%%%%%%%%%%%%%%%%%%%%%%%%%%%%%%%%%%%%%%%%%%%%%%%%%%%%%%%%%%%%%%%%%%%%%%%

%%% 1-applied Live load
LL1 = 10.02;          %%% The load of the rear tire  of Truck#1995M
in kips
XLL1 = 525;           %%% Location of the rear tire load of
Truck#1995M (X=0 is at left support) in inch
LL2 = 12.2;           %%% The load of the rear tire  of Truck#2406M
in kips
XLL2 = 529.9;         %%% Location of the rear tire  of Truck#2406M
(X=0 is at left support)in inch
LL3 = 10.26;          %%% The load of the middle tire of Truck#1995M
in kips
XLL3 = 580;           %%% Location of the the middle tire load of
Truck#1995M (X=0 is at left support)in inch
LL4 = 7.79;           %%% The load of the middle tire of Truck#2406M
in kips
XLL4 = 583.4;         %%% Location of the middle tire of Truck#2406M
(X=0 is at left support) in inch
LL5 = 8.34;           %%% The load of the front tire of Truck#1995M
in kips
XLL5 = 770;           %%% Location of the the front tire of
Truck#1995M (X=0 is at left support)in inch
LL6 = 8.16;           %%% The load of the Front tire of Truck#2406M
in kips
XLL6 = 773;           %%% Location of the Front tire load (X=0 is at
left support)in inch

%%% 2- Moment and Normal force due to Live load

%%% These Moments and forces were calculated using SAP2000 by
simulating the non-composite beam as curved beam %%%
M = zeros (25,1);
N = zeros (25,1);

M (2,1) = -7900;
N (2,1) = -30;

```

```

M (5,1) = -1396;
N (5,1) = -28;
M (9,1) = 3280.4;
N (9,1) = -26.9;
M (12,1) = 6117.5;
N (12,1) = -26.5;
M (15,1) = 7080;
N (15,1) = -26;

```

```

%%%%%%%%%%%%%%%%%%%%%%%%%%%%%%%%%%%%%%%%%%%%%%%%%%%%%%%%%%%%%%%%%%%%%%%%
%%%%%% 4- Calculation of ENA and Moment of inertia %%%%%%%%%
%%%%%%%%%%%%%%%%%%%%%%%%%%%%%%%%%%%%%%%%%%%%%%%%%%%%%%%%%%%%%%%%%%%%%%%%

```

```

%%%% 1- Identifying the Inertia of each component w.r.t its CG
%%%% Tension RFT (strands)
Astr = Nstr*Astrand; %%% Area of strands in inch square
Ys = tbf+ dstr; %%% CG of two layers of strands from the bottom
of the HCB
nstr = Ep/Ew11; %%% modular ratio of the strands relative to
the FRP web
As = Astr*nstr; %%% transformed area of strands in inch square
Is = Nstr*pi*dstr^4*nstr/64+As*(dstr/2)^2; %%% moment of inertia
of strands around their CG
%%%% FRP Top flanges
ntf = Etf11/Ew11;
Ytf = h-ttf/2;
Atf = ttf*btf*ntf; %%% transformed area of top flange in
inch square
Itf = btf*ttf^3/12*ntf; %%% transformed Moment of inertia of top
flange in in^4
Ytf2 = h-ttf2/2;
Atf2 = ttf2*btf2*ntf; %%% transformed area of top flange2 in
inch square
Itf2 = btf2*ttf2^3/12*ntf; %%% transformed Moment of inertia of top
flange2 in in^4
Ytf3 = h-ttf2-2-ttf3/2;
Atf3 = ttf3*btf3*ntf; %%% transformed area of top flange3 in
inch square
Itf3 = btf3*ttf3^3/12*ntf; %%% transformed Moment of inertia of top
flange3 in in^4
%%%% FRP Bottom flanges
nbf = Ebf11/Ew11;
Ybf = tbf/2;
Abf = tbf*bbf*nbf; %%% transformed area of top flange in
inch square
Ibf = bbf*tbf^3/12*nbf; %%% transformed Moment of inertia of top
flange in in^4
Ybf2 = tbf2/2+tbf+2;
Abf2 = tbf2*bbf2*nbf; %%% transformed area of top flange in
inch square
Ibf2 = bbf2*tbf^3/12*nbf; %%% transformed Moment of inertia of top
flange in in^4
%%%% FRP Webs
Yw = h/2;
Aw = 4*tw*h; %%% area of four FRP webs in inch square

```



```

PNA      = zeros (NEM+1,1);
strssbf  = zeros (NEM+1,1);
strnbf   = zeros (NEM+1,1);
Fbf      = zeros (NEM+1,1);
strssbf2 = zeros (NEM+1,1);
strnbf2  = zeros (NEM+1,1);
Fbf2     = zeros (NEM+1,1);
strsstf  = zeros (NEM+1,1);
Ftf      = zeros (NEM+1,1);
strsstf2 = zeros (NEM+1,1);
Ftf2     = zeros (NEM+1,1);
strsstf3 = zeros (NEM+1,1);
strntf3  = zeros (NEM+1,1);
Ftf3     = zeros (NEM+1,1);
strssstr = zeros (NEM+1,1);
strnstr  = zeros (NEM+1,1);
Fstr     = zeros (NEM+1,1);
strsslw  = zeros (NEM+1,1);
strssuw  = zeros (NEM+1,1);
Fw       = zeros (NEM+1,1);
strsssw  = zeros (NEM+1,1);
Fsw      = zeros (NEM+1,1);
strssub  = zeros (NEM+1,1);
strnub   = zeros (NEM+1,1);
Fub      = zeros (NEM+1,1);
Flb      = zeros (NEM+1,1);
strsslca = zeros (NEM+1,1);
strnlca  = zeros (NEM+1,1);
strssuca = zeros (NEM+1,1);
strnuca  = zeros (NEM+1,1);
Fca      = zeros (NEM+1,1);
Fd       = zeros (NEM+1,1);
strnlcw  = zeros (NEM+1,1);
strnucw  = zeros (NEM+1,1);
Fcw      = zeros (NEM+1,1);
Comp     = zeros (NEM+1,1);
Ten      = zeros (NEM+1,1);
Dif      = zeros (NEM+1,1);

for i = 1:NEM+1
    PNA(i,1) = Ybar(i,1);
end

syms y Epsca Epscd Epscw
Epsndca = 0.0021;          %%% Epsilon node of concret arch and
web(The strain at which maximum compressive stress takes place)
Epsndcd = 0.0021;          %%% Epsilon node of concret deck
Epsu    = 0.003;          %%% Ultimate Concrete strain beyond it the
concrete assumed to be crashed

for i= 1:NEM

    %%% Force in FRP Bottom flanges

```

```

        strssbf (i,1) = (M(i,1)*(PNA(i,1)-Ybf)/I(i,:)*nbf)+
N(i,1)*nbf/A(i,:);
        strnbf(i,1) = M(i,1)*(PNA(i,1)-Ybf)/I(i,+)/Ew11 +
N(i,1)/A(i,+)/Ew11 ;
        if strssbf (i,1)>54 || strssbf (i,1)<-20 %%% In this case we
need to reduce the A and I by subtracting the contribution of the
flange to the A & I and the same for the other components
            Fbf(i,1)=0;
        else
            Fbf(i,1) = strssbf (i,1)*Abf/nbf;
        end
        if Fbf(i,1)>0
            Ten (i,1) = Ten (i,1)+ Fbf(i,1);
        else
            Comp (i,1) = Comp (i,1)+ Fbf(i,1);
        end

        strssbf2 (i,1) = (M(i,1)*(PNA(i,1)-Ybf2)/I(i,:)*nbf)+
N(i,1)*nbf/A(i,:);
        strnbf2 (i,1) = M(i,1)*(PNA(i,1)-Ybf2)/I(i,+)/Ew11 +
N(i,1)/A(i,+)/Ew11 ;
        if strssbf2 (i,1)>54 || strssbf2 (i,1)<-20
            Fbf2(i,1)=0;
        else
            Fbf2(i,1) = strssbf2 (i,1)*Abf2/nbf;
        end
        if Fbf2(i,1)>0
            Ten (i,1) = Ten (i,1)+ Fbf2(i,1);
        else
            Comp (i,1) = Comp (i,1)+ Fbf2(i,1);
        end

        %%% Force in FRP top flanges
        strsstf (i,1) = (M(i,1)*(PNA(i,1)-Ytf)/I(i,:)*ntf)+
N(i,1)*ntf/A(i,:);
        if strsstf (i,1) > 54 || strsstf (i,1) < -20
            Ftf(i,1)=0;
        else
            Ftf(i,1) = strsstf (i,1)*Atf/ntf;
        end
        if Ftf(i,1)>0
            Ten (i,1) = Ten (i,1)+ Ftf(i,1);
        else
            Comp (i,1) = Comp (i,1)+ Ftf(i,1);
        end

        strsstf2 (i,1) = (M(i,1)*(PNA(i,1)-Ytf2)/I(i,:)*ntf)+
N(i,1)*ntf/A(i,:);
        if strsstf2 (i,1) > 54 || strsstf2 (i,1) < -20
            Ftf2(i,1)=0;
        else
            Ftf2(i,1) = strsstf2 (i,1)*Atf2/ntf;
        end
        if Ftf2(i,1)>0
            Ten (i,1) = Ten (i,1)+ Ftf2(i,1);
        else

```

```

        Comp (i,1) = Comp (i,1)+ Ftf2(i,1);
    end

    strsstf3 (i,1) = (M(i,1)*(PNA(i,1)-Ytf3)/I(i, :)*ntf)+
N(i,1)*ntf/A(i, :);
    strntf3 (i,1) = M(i,1)*(PNA(i,1)-Ytf3)/I(i, :)/Ew11+
N(i,1)/A(i, :)/Ew11 ;
    if strsstf3 (i,1)>54 || strsstf3 (i,1)<-20
        Ftf3(i,1)=0;
    else
        Ftf3(i,1) = strsstf3 (i,1)*Atf3/ntf;
    end
    if Ftf3(i,1)>0
        Ten (i,1) = Ten (i,1)+ Ftf3(i,1);
    else
        Comp (i,1) = Comp (i,1)+ Ftf3(i,1);
    end

    %%% Force in (strands)
    Epsstr = M(i,1)*(PNA(i,1)-Ys)/I(i, :)/Ew11 + N(i,1)/A(i, :)/Ew11
;
    strnstr (i,1)= M(i,1)*(PNA(i,1)-Ys)/I(i, :)/Ew11 +
N(i,1)/A(i, :)/Ew11 ;
    strssstr (i,1)= M(i,1)*(PNA(i,1)-Ys)/I(i, :)+
N(i,1)*nstr/A(i, :);
    if Epsstr > 0.0076
        Fstr(i,1) = (250 - (0.04/(Epsstr-0.0064)))*Astr;
    end
    if Epsstr < -0.0076
        Fstr(i,1) = -Astr*(250 - (0.04/(-1*Epsstr-0.0064)));
    end
    if Epsstr<= 0.0076 && Epsstr>= -0.0076
        Fstr(i,1) = Ep*Epsstr*Astr;
    end

    if Fstr(i,1)>0
        Ten (i,1) = Ten (i,1)+ Fstr(i,1);
    else
        Comp (i,1) = Comp (i,1)+ Fstr(i,1);
    end

    %%% Force in FRP Webs
    strsslw (i,1) = M(i,1)* PNA(i,1)/I(i, :)+ N(i,1)/A(i, :);
    strssuw (i,1) = M(i,1)* (PNA(i,1)-h)/I(i, :)+ N(i,1)/A(i, :);
    Fw (i,1) = (strsslw (i,1) + strssuw (i,1))*h*2*tw;
    if strsslw (i,1)> 54 && strssuw (i,1)> 54
        Fw (i,1) = 0;
    end
    if strsslw (i,1)< -20 && strssuw (i,1)< -20
        Fw (i,1) = 0;
    end

    if Fw(i,1)>0
        Ten (i,1) = Ten (i,1)+ Fw(i,1);
    end

```

```

else
    Comp (i,1) = Comp (i,1)+ Fw(i,1);
end

%%%% Force in Conc Arch

y1 = Yca (i,1)- (tca/2);
y2 = Yca (i,1)+ (tca/2);
Epsca1 = M(i,1)*(PNA(i,1)-y1)/I(i,+)/Ew11 + N(i,1)/A(i,+)/Ew11;
Epsca2 = M(i,1)*(PNA(i,1)-y2)/I(i,+)/Ew11 + N(i,1)/A(i,+)/Ew11;
strnlca (i,1) = M(i,1)*(PNA(i,1)-y1)/I(i,+)/Ew11 +
N(i,1)/A(i,+)/Ew11;
strnuca (i,1) = M(i,1)*(PNA(i,1)-y2)/I(i,+)/Ew11 +
N(i,1)/A(i,+)/Ew11;
strssl1 = M(i,1)*(PNA(i,1)-y1)/I(i,+) *nca + N(i,1)*nca/A(i,);
strssl2 = M(i,1)*(PNA(i,1)-y2)/I(i,+) *nca + N(i,1)*nca/A(i,);
%strsslca (i,1) = M(i,1)*(PNA(i,1)-y1)/I(i,+) *nca;
%strssuca (i,1) = M(i,1)*(PNA(i,1)-y2)/I(i,+) *nca;
Epsca = (M(i,1)*(PNA(i,1)-y)/I(i,+)/Ew11 +
N(i,1)/A(i,+)/Ew11)/Epsndca;

Fca(i,1) = (strssl1+strssl2)*tca*bca;

if Fca(i,1)>0
    Ten (i,1) = Ten (i,1)+ Fca(i,1);
else
    Comp (i,1) = Comp (i,1)+ Fca(i,1);
end

%%%% Force in Conc Web

y1 = Ycw (i,1)- (hcw(i,1)/2);
y2 = Ycw (i,1)+ (hcw(i,1)/2);
Epscwl = M(i,1)*(PNA(i,1)-y1)/I(i,+)/Ew11+ N(i,1)/A(i,+)/Ew11;
strnlcw (i,1) = M(i,1)*(PNA(i,1)-y1)/I(i,+)/Ew11 +
N(i,1)/A(i,+)/Ew11;
Epscw2 = M(i,1)*(PNA(i,1)-y2)/I(i,+)/Ew11+ N(i,1)/A(i,+)/Ew11;
strnucw (i,1) = M(i,1)*(PNA(i,1)-y2)/I(i,+)/Ew11 +
N(i,1)/A(i,+)/Ew11;
strsscwl = M(i,1)*(PNA(i,1)-y1)/I(i,+) *nca + N(i,1)*nca/A(i,);
strsscw2 = M(i,1)*(PNA(i,1)-y2)/I(i,+) *nca + N(i,1)*nca/A(i,);
Epscw = (M(i,1)*(PNA(i,1)-y)/I(i,+)/Ew11 +
N(i,1)/A(i,+)/Ew11)/Epsndca ;

Fcw(i,1) = tcw*hcw (i,1)*(strsscwl+strsscw2);

if Fcw(i,1)>0
    Ten (i,1) = Ten (i,1)+ Fcw(i,1);
else
    Comp (i,1) = Comp (i,1)+ Fcw(i,1);
end

Dif (i,:) = abs((N(i,1)-(Ten(i,1)+Comp(i,1)))/N(i,1))*100;

end

```

(2) MATLAB code for estimating the strains in simply supported hcb via beam-model

```

%%%%%%%%%%%%%%%%%%%%%%%%%%%%%%%%%%%%%%%%%%%%%%%%%%%%%%%%%%%%%%%%%%%%%%%%
%%%%%%%%%%%%%%%%%%%%%%%%%%%%%%%%%%%%%%%%%%%%%%%%%%%%%%%%%%%%%%%%%%%%%%%%
%%%%%%%% This Matlab Code calculates the strains and stresses          %%%%%%%%%
%%%%%%%% of the multi-celled non-composite, simply supported HCB      %%%%%%%%%
%%%%%%%% of bridge B0410 using the beam-model                          %%%%%%%%%
%%%%%%%%%%%%%%%%%%%%%%%%%%%%%%%%%%%%%%%%%%%%%%%%%%%%%%%%%%%%%%%%%%%%%%%%
%%%%%%%%%%%%%%%%%%%%%%%%%%%%%%%%%%%%%%%%%%%%%%%%%%%%%%%%%%%%%%%%%%%%%%%%

%%%%%%%% 1- Material Properties                                       %%%%%%%%%
%%%%%%%%%%%%%%%%%%%%%%%%%%%%%%%%%%%%%%%%%%%%%%%%%%%%%%%%%%%%%%%%%%%%%%%%

%%%%%%%% Concrete Properties%%%%%%%%%%%%%%%%%%%%%%%%%%%%%%%%%%%%%%%%

%%% Arch
Sca = 11;                %%% compressive strength of concrete arch in Ksi
Dca = 0.14;              %%% Denisty of concrete arch in Kip/cubic feet
%%% Cg of concrete arch in inch
%Yca = [5; 14.48; 22.96; 30.44; 36.93; 42.42; 46.91; 50.4; 52.89;
54.39; 54.89; 54.39; 52.89; 50.4; 46.91; 42.42; 36.93; 30.44; 22.96;
14.48; 5];
Yca = [5; 6.44; 8.7639; 22.96; 27.539; 30.44; 36.93; 42.42; 42.744;
46.91; 50.4; 51.725; 52.89; 54.39; 54.89; 54.39; 52.89; 50.4; 46.91;
42.42; 36.93; 30.44; 22.96; 14.48; 5];
%X = [0; 53.4; 115.8; 178.2; 240.6; 303; 365.4; 427.8; 490.2; 552.6;
615; 677.4; 739.8; 802.2; 864.6; 927; 989.4; 1051.8; 1114.2; 1176.6;
1230]; %%% vector of points at which the calculations of Moment, shear
and inertia are calculated in inch
X = [0; 9; 23.8; 115.8; 154; 178.2; 240.6; 303; 307.5; 365.4; 427.8;
461; 490.2; 552.6; 615; 677.4; 739.8; 802.2; 864.6; 927; 989.4; 1051.8;
1114.2; 1176.6; 1230]; %%% vector of points at which the calculations
of Moment, shear and inertia are calculated in inch

%%% Deck
Sd = 6.5;                %%% compressive strength of concrete deck in Ksi
Dd = 0.14;               %%% Denisty of concrete arch in Kip/cubic feet

%%%%%%%%%%%%%%%%%%%%%%%%%%%%%%%%%%%%%%%%%%%%%%%%%%%%%%%%%%%%%%%%%%%%%%%%
%%%%%%%%%%%%%%%%%%%%%%%%%%%%%%%%%%%%%%%%%%%%%%%%%%%%%%%%%%%%%%%%%%%%%%%%
%%%%%%%% FRP Properties%%%%%%%%%%%%%%%%%%%%%%%%%%%%%%%%%%%%%%%%
%%%%%%%%%%%%%%%%%%%%%%%%%%%%%%%%%%%%%%%%%%%%%%%%%%%%%%%%%%%%%%%%%%%%%%%%
%%%%%%%% Webs%%%%%%%%%%%%%%%%%%%%%%%%%%%%%%%%%%%%%%%%
Ew11 = 2000;             %%% Modulus of elasticity in dir. 1-1 of GFRP of
web in Ksi (1378 psi from tests)
Ew22 = 1400;             %%% Modulus of elasticity in dir. 2-2 of GFRP of
web in Ksi
Gw12 = 1130;            %%% Shear Modulus in plane 1-2 of GFRP of web in
Ksi
Pw12 = 0.26;            %%% Poisson's ratio in plane 1-2 of GFRP of web

```



```

%Shw = 19;          %%% Shear strength in plane 1-2 of GFRP of web in
Ksi
%%% Top flange
Etf11 = 2000;      %%% Modulus of elasticity in dir. 1-1 of GFRP of
top flange in Ksi
Etf22 = 1400;      %%% Modulus of elasticity in dir. 2-2 of GFRP of
top flange in Ksi
Gtf12 = 1130;      %%% Shear Modulus in plane 1-2 of GFRP of top
flange in Ksi
Ptf12 = 0.26;      %%% Major Poisson's ratio in plane 1-2 of GFRP of
top flange
%Ptf21 = 0.26;     %%% Minor Poisson's ratio in plane 1-2 of GFRP of
top flange
%%% Bottom flange
Ebf11 = 3800;      %%% Modulus of elasticity in dir. 1-1 of GFRP of
bot. flange in Ksi
Ebf22 = 1130;      %%% Modulus of elasticity in dir. 2-2 of GFRP of
bot. flange in Ksi
Gbf12 = 1130;      %%% Shear Modulus in plane 1-2 of GFRP of bot.
flange in Ksi
Pbf12 = 0.26;      %%% Major Poisson's ratio in plane 1-2 of GFRP of
bot. flange
%Pbf21 = 0.26;     %%% Minor Poisson's ratio in plane 1-2 of GFRP of
bot. flange

```

```

%%%%%%%%%%%%%%%%%%%%%%%%%%%%%%%%%%%%%%%%%%%%%%%%%%%%%%%%%%%%%%%%%%%%%%%%
%%% 2- Geometry %%%
%%%%%%%%%%%%%%%%%%%%%%%%%%%%%%%%%%%%%%%%%%%%%%%%%%%%%%%%%%%%%%%%%%%%%%%%

```

```

%%% Beam
h = 60.16;          %%% Height of HCB in inch
b = 72;             %%% Width of beam in inch
btf = 27.5;         %%% Width of Top flange in inch (upper layer of
FRP Lid above two concrete arch)
btf2 = 44.5;        %%% Width of Top flange2 in inch (The upper
layer of FRP Lid between the two concret arches)
btf3 = 44.3;        %%% Width of Top flange3 in inch (Lower layer
of FRP Lid between the two concret arches)
bsw = 48;           %%% Width of FRP sandwich between the girders
and under the deck
bbf = 66;           %%% Width of Lower flange in inch
bbf2 = 38.4;        %%% Width of Lower flange in inch (upper layert
of Lower flange between the two beams)
tw = 0.19;          %%% Thickness of FRP web in inch
ttf = 0.43;         %%% Thickness of FRP top flange in inch
tsw = 0.2;          %%% Thickness of FRP sandwich
tbf = 0.08;         %%% Thickness of FRP bot. flange in inch
tbf2 = 0.08;        %%% Thickness of FRP bot. flange in inch
%tsr = 0.03;        %%% Thickness of FRP side return portion in
inch
%hsr = 6;           %%% Height of FRP side return portion in inch
tca = 10;           %%% Thickness of concrete arch in inch
bca = 10.5;         %%% breadth of concrete arch in inch
tcw = 5;            %%% Thickness of concrete web(fin)in inch

```

```

%WP = 2;          %% Working point at thrut line (That is used
to determine the arch profile)
Nstr = 88;       %% no. of strands of the tensile reinforcement
Nub = 30;       %% no. of uper deck bars
Nlb = 19;       %% no. of lower deck bars
Lovr = 1267;    %% Overall length of the HCB in inch
L = 1230;      %% Design span of the HCB in inch

%%%% Bridge
SG = 120;      %% spacing between the girders (HCBs)in inch
NG = 3;       %% No. of girders
%Wovr= 28;    %% Overall width of the bridge in feet
%Wctc= 30.667; %% curb to curb width of the bridge in feet
NEM = 24;     %% No. of elements that represent one HCB
%%%% Slab
%ts = 15.5;   %% thicness of cast in place slab in inch
%bs = min( min (SG, 12*ts+b), L/4); %% width of the CIP slab in
inch

Lseg = zeros (NEM,1); %% Lengths of each segment between two points
in ft

for i= 1:NEM
    Lseg(i,:) = X (i+1,:)- X (i,:);
end

%%%%%%%%%%%%%%%%%%%%%%%%%%%%%%%%%%%%%%%%%%%%%%%%%%%%%%%%%%%%%%%%%%%%%%%%
%%%%%%%% 3- Loads %%%%%%%%%
%%%%%%%%%%%%%%%%%%%%%%%%%%%%%%%%%%%%%%%%%%%%%%%%%%%%%%%%%%%%%%%%%%%%%%%%

%%%% 1-applied Live load
LL1 = 10.02;    %% The load of the rear tire of Truck#1995M
in kips
XLL1 = 525;    %% Location of the rear tire load of
Truck#1995M (X=0 is at left support) in inch
LL2 = 12.2;    %% The load of the rear tire of Truck#2406M
in kips
XLL2 = 529.9;  %% Location of the rear tire of Truck#2406M
(X=0 is at left support)in inch
LL3 = 10.26;   %% The load of the middle tire of Truck#1995M
in kips
XLL3 = 580;    %% Location of the the middle tire load of
Truck#1995M (X=0 is at left support)in inch
LL4 = 7.79;    %% The load of the middle tire of Truck#2406M
in kips
XLL4 = 583.4;  %% Location of the middle tire of Truck#2406M
(X=0 is at left support) in inch
LL5 = 8.34;    %% The load of the front tire of Truck#1995M
in kips
XLL5 = 770;    %% Location of the the front tire of
Truck#1995M (X=0 is at left support)in inch
LL6 = 8.16;    %% The load of the Front tire of Truck#2406M
in kips

```

```
XLL6 = 773;          %%% Location of the Front tire load (X=0 is at
left support)in inch
```

```
%%%%%%%%%%%%%%%%%%%%%%%%%%%%%%%%%%%%%%%%%%%%%%%%%%%%%%%%%%%%%%%%%%%%%%%%
%% 4- Calculation of ENA and Moment of inertia          %%%
%%%%%%%%%%%%%%%%%%%%%%%%%%%%%%%%%%%%%%%%%%%%%%%%%%%%%%%%%%%%%%%%%%%%%%%%
```

```
%% 1- Identifying the Inertia of each component w.r.t its CG
%% Tension RFT (strands)
Astr = Nstr*Astrand; %%% Area of strands in inch square
Ys   = tbf+ dstr;    %%% CG of two layers of strands from the bottom
of the HCB
nstr = Ep/Ew11;     %%% modular ratio of the strands relative to
the FRP web
As   = Astr*nstr;   %%% transformed area of strands in inch square
Is   = Nstr*pi*dstr^4*nstr/64+As*(dstr/2)^2; %%% moment of inertia
of strands around their CG
%% FRP Top flanges
ntf  = Etf11/Ew11;
Ytf  = h-ttf/2;
Atf  = ttf*btf*ntf; %%% transformed area of top flange in
inch square
Itf  = btf*ttf^3/12*ntf; %%% transformed Moment of inertia of top
flange in in^4
Ytf2 = h-ttf2/2;
Atf2 = ttf2*btf2*ntf; %%% transformed area of top flange2 in
inch square
Itf2 = btf2*ttf2^3/12*ntf; %%% transformed Moment of inertia of top
flange2 in in^4
Ytf3 = h-ttf2-2-ttf3/2;
Atf3 = ttf3*btf3*ntf; %%% transformed area of top flange3 in
inch square
Itf3 = btf3*ttf3^3/12*ntf; %%% transformed Moment of inertia of top
flange3 in in^4
%% FRP Bottom flanges
nbf  = Ebf11/Ew11;
Ybf  = tbf/2;
Abf  = tbf*bbf*nbf; %%% transformed area of top flange in
inch square
Ibf  = bbf*tbf^3/12*nbf; %%% transformed Moment of inertia of top
flange in in^4
Ybf2 = tbf2/2+tbf+2;
Abf2 = tbf2*bbf2*nbf; %%% transformed area of top flange in
inch square
Ibf2 = bbf2*tbf^3/12*nbf; %%% transformed Moment of inertia of top
flange in in^4
%% FRP Webs
Yw   = h/2;
Aw   = 4*tw*h;      %%% area of four FRP webs in inch square
Iw   = 4*tw*h^3/12; %%% Moment of inertia of two webs in
in^4
```

```

%%%% Concrete Arch
frca = 7.5/1000*sqrt(Sca*1000); %%%% modulus of rupture of concret
arch in Ksi
Eca = 57*sqrt(Sca*1000); %%%% Elastic modulus of concret arch in
Ksi
nca = Eca/Ew11; %%%% modular ratio of the conc. Arch
relative to the FRP web
Aca = 2*tca*bca*nca; %%%% transformed area of two conc arches
in square inch
Ica = 2*bca*tca^3*nca/12; %%%% transformed Moment of inertia of two
conc arches in in^4

%%%% Concrete Web (fin)
Ecw = 57*sqrt(Sca*1000); %%%% Elastic modulus of concrete in Ksi
ncw = Ecw/Ew11; %%%% modular ratio of the deck relative
to the FRP web
hcw = zeros(NEM+1,1);
Ycw = zeros(NEM+1,1);
Acw = zeros(NEM+1,1);
Icw = zeros(NEM+1,1);
for i=1:NEM+1 %%%% Calculating the height and the area
of the concrete web
    hcw(i,1)= h-(Yca(i,)+tca/2+ttf);
    Ycw(i,1)= h-(hcw(i,)/2+ttf);
    Acw(i,1)= 2*hcw(i,1)*tcw*ncw;
    Icw(i,1)= 2*tw* (hcw(i,1))^3*ncw/12;
end
hcw(15,1)= 0;
Acw(15,1)= 0;
Icw(15,1)= 0;

%%%% 1- Identifying the N.A. and moment of inertia of HCB
Ybar = zeros(NEM+1,1); %%%% N.A of HCB at each
point
I = zeros(NEM+1,1); %%%% moment of inertia of
HCB in in^4
A = zeros(NEM+1,1); %%%% Area of HCB in in^2

for i= 1:NEM+1
    A (i,:) = As+Atf+Atf2+Atf3+Abf+Abf2+Aw+Aca+Acw(i,:);
    Ybar(i,:) =
    (As*Ys+Atf*Ytf+Atf2*Ytf2+Atf3*Ytf3+Abf*Ybf+Abf2*Ybf2+Aw*Yw+Aca*Yca(i,:)+
    Acw(i,)*Ycw(i,))/A(i,:);
    I (i,:) = Is+As*(Ys-Ybar(i,:))^2+Itf+Atf*(Ytf-
    Ybar(i,:))^2+Itf2+Atf2*(Ytf2-Ybar(i,:))^2+Itf3+Atf3*(Ytf3-
    Ybar(i,:))^2+Ibf+Abf*(Ybf-Ybar(i,:))^2+Ibf2+Abf2*(Ybf2-
    Ybar(i,:))^2+Iw+Aw*(Yw-Ybar(i,:))^2+Ica+Aca*(Yca(i,:)-
    Ybar(i,:))^2+Icw(i,)+Acw(i,)*(Ycw(i,)-Ybar(i,:))^2;
end

%%%% Decoupling the beam
Ifrpc = zeros(NEM+1,1);
Itiec = zeros(NEM+1,1);

```

```

Atie      = zeros(NEM+1,1);
Ytie      = zeros(NEM+1,1);
Itie      = zeros(NEM+1,1);
Afrp      = Atf+Atf2+Atf3+Abf+Abf2+Aw;
Yfrp      = (Atf*Ytf+Atf2*Ytf2+Atf3*Ytf3+Abf*Ybf+Abf2*Ybf2+Aw*Yw)/Afrp;
Ifrp      = Itf+Atf*(Ytf-Yfrp)^2+Itf2+Atf2*(Ytf2-
Yfrp)^2+Itf3+Atf3*(Ytf3-Yfrp)^2+Ibf+Abf*(Ybf-Yfrp)^2+Ibf2+Abf2*(Ybf2-
Yfrp)^2+Iw+Aw*(Yw-Yfrp)^2;

```

```

for i= 1:NEM+1
    Atie (i,1) = Aca + Acw(i,1)+As;
    Ytie (i,1) = (Aca*Yca(i,1) + Acw(i,1)*Ycw(i,1)+As*Ys)/Atie(i,1);
    Itie (i,1) = Ica+Aca*(Yca(i,:)-
Ytie(i,:))^2+Icw(i,:)+Acw(i,:)*(Ycw(i,:)-Ytie(i,:))^2+Is+(Ys -
Ytie(i,:))^2;
    Ifrpc(i,1) = Itf+Atf*(Ytf-Ybar(i,1))^2+Itf2+Atf2*(Ytf2-
Ybar(i,1))^2+Itf3+Atf3*(Ytf3-Ybar(i,1))^2+Ibf+Abf*(Ybf-
Ybar(i,1))^2+Ibf2+Abf2*(Ybf2-Ybar(i,1))^2+Iw+Aw*(Yw-Ybar(i,1))^2;
    Itiec(i,1) = Ica+Aca*(Yca(i,:)-
Ybar(i,:))^2+Icw(i,:)+Acw(i,:)*(Ycw(i,:)-Ybar(i,:))^2+Is+As*(Ys -
Ybar(i,:))^2;
end

```

```

%%%%%%%%%%%%%%%%%%%%%%%%%%%%%%%%%%%%%%%%%%%%%%%%%%%%%%%%%%%%%%%%%%%%%%%%
%%%%%%%% 5- Calculation of stresses and strains %%%%%%%%%
%%%%%%%%%%%%%%%%%%%%%%%%%%%%%%%%%%%%%%%%%%%%%%%%%%%%%%%%%%%%%%%%%%%%%%%%

```

```

strssbf   = zeros (NEM+1,1);
strnbf    = zeros (NEM+1,1);
Fbf       = zeros (NEM+1,1);
strssbf2  = zeros (NEM+1,1);
strnbf2   = zeros (NEM+1,1);
Fbf2      = zeros (NEM+1,1);
strsstf   = zeros (NEM+1,1);
strntf    = zeros (NEM+1,1);
Ftf       = zeros (NEM+1,1);
strsstf2  = zeros (NEM+1,1);
Ftf2      = zeros (NEM+1,1);
strsstf3  = zeros (NEM+1,1);
strntf3   = zeros (NEM+1,1);
Ftf3      = zeros (NEM+1,1);
strssstr  = zeros (NEM+1,1);
strnstr   = zeros (NEM+1,1);
Fstr      = zeros (NEM+1,1);
strsslw   = zeros (NEM+1,1);
strssuw   = zeros (NEM+1,1);
strnuw    = zeros (NEM+1,1);
strnlw    = zeros (NEM+1,1);
Fw        = zeros (NEM+1,1);
%FWT      = zeros (NEM+1,1);
%strsslsr = zeros (NEM+1,1);
%strssusr = zeros (NEM+1,1);

```

```

%FsrC      = zeros (NEM+1,1);
%FsrT      = zeros (NEM+1,1);
strsssw    = zeros (NEM+1,1);
Fsw        = zeros (NEM+1,1);
strssub    = zeros (NEM+1,1);
strnub     = zeros (NEM+1,1);
Fub        = zeros (NEM+1,1);
Flb        = zeros (NEM+1,1);
strsslca   = zeros (NEM+1,1);
strnlca    = zeros (NEM+1,1);
strssuca   = zeros (NEM+1,1);
strnuca    = zeros (NEM+1,1);
Fca        = zeros (NEM+1,1);
Fd         = zeros (NEM+1,1);
strnlcw    = zeros (NEM+1,1);
strnucw    = zeros (NEM+1,1);
Fcw        = zeros (NEM+1,1);
Comp       = zeros (NEM+1,1);
Ten        = zeros (NEM+1,1);
Dif        = zeros (NEM+1,1);
Mbf        = zeros (NEM+1,1);
Mbf2       = zeros (NEM+1,1);
Mtf        = zeros (NEM+1,1);
Mtf2       = zeros (NEM+1,1);
Mtf3       = zeros (NEM+1,1);
Flw        = zeros (NEM+1,1);
Fuw        = zeros (NEM+1,1);
Mlw        = zeros (NEM+1,1);
Muw        = zeros (NEM+1,1);
Mstr       = zeros (NEM+1,1);
Flca       = zeros (NEM+1,1);
Fuca       = zeros (NEM+1,1);
Muca       = zeros (NEM+1,1);
Mlca       = zeros (NEM+1,1);
Flcw       = zeros (NEM+1,1);
Fucw       = zeros (NEM+1,1);
Mucw       = zeros (NEM+1,1);
Mlcw       = zeros (NEM+1,1);
MFRP       = zeros (NEM+1,1);
MC         = zeros (NEM+1,1);
MT         = zeros (NEM+1,1);
FFRP       = zeros (NEM+1,1);
FC         = zeros (NEM+1,1);
FT         = zeros (NEM+1,1);
Mcw        = zeros (NEM+1,1);
M          = zeros (NEM+1,1);
N          = zeros (NEM+1,1);
MF         = zeros (NEM+1,1);
NF         = zeros (NEM+1,1);
Mfrp       = zeros (NEM+1,1);
Nfrp       = zeros (NEM+1,1);
Mtie       = zeros (NEM+1,1);
Ntie       = zeros (NEM+1,1);
Comptie    = zeros (NEM+1,1);
Tentie     = zeros (NEM+1,1);

```

```

MF (1,1) = -4413;
NF (1,1) = -18;
MF (2,1) = -4142;
NF (2,1) = -17.9;
MF (3,1) = -3696;
NF (3,1) = -17.8;
MF (5,1) = 282;
NF (5,1) = -17;
MF (9,1) = 5025;
NF (9,1) = -16.1;
MF (12,1) = 8679;
NF (12,1) = -15.6;
MF (15,1) = 10211;
NF (15,1) = -15.5;

```

```

M (2,1) = 287;
M (3,1) = 759;
M (5,1) = 4911;
M (9,1) = 9802;
M (12,1) = 13557;
M (15,1) = 15169;

```

```

for i= 1:NEM+1
    Mfrp (i,1)      = Ifrp /I(i,1)*M(i,1);
    Mtie  (i,1)     = Itie (i,1)/I(i,1)*MF(i,1);
    Ntie(i,1)      = Atie(i,1)/A(i,1)*NF(i,1);
end

```

```

for i= 1:NEM

```

```

    %%% FRP Bottom flanges

```

```

    strssbf(i,1) = Mfrp(i,1)*(Yfrp -Ybf)/Ifrp*nbf;
    strnbf(i,1)  = Mfrp(i,1)*(Yfrp -Ybf)/Ifrp/Ew11;
    Fbf(i,1)     = strssbf (i,1)*Abf/nbf;
    if Fbf(i,1)>0
        Ten (i,1) = Ten (i,1)+ Fbf(i,1);
    else
        Comp (i,1) = Comp (i,1)+ Fbf(i,1);
    end

```

```

    strssbf2(i,1) = Mfrp(i,1)*(Yfrp-Ybf2)/Ifrp*nbf;
    strnbf2(i,1)  = Mfrp(i,1)*(Yfrp-Ybf2)/Ifrp/Ew11;
    Fbf2(i,1)     = strssbf2 (i,1)*Abf2/nbf;
    if Fbf2(i,1)>0
        Ten (i,1) = Ten (i,1)+ Fbf2(i,1);
    else
        Comp (i,1) = Comp (i,1)+ Fbf2(i,1);
    end

```

```

##### FRP Top flanges
strsstf(i,1) = Mfrp(i,1)*(Yfrp -Ytf)/Ifrp*ntf;
strntf(i,1) = Mfrp(i,1)*(Yfrp -Ytf)/Ifrp/Ew11;
Ftf(i,1) = strsstf (i,1)*Atf/ntf;
if Ftf(i,1)>0
    Ten (i,1) = Ten (i,1)+ Ftf(i,1);
else
    Comp (i,1) = Comp (i,1)+ Ftf(i,1);
end

strsstf2(i,1) = Mfrp(i,1)*(Yfrp-Ytf2)/Ifrp*ntf;
Ftf2(i,1)      = strsstf2 (i,1)*Atf2/ntf;
if Ftf2(i,1)>0
    Ten (i,1) = Ten (i,1)+ Ftf2(i,1);
else
    Comp (i,1) = Comp (i,1)+ Ftf2(i,1);
end

strsstf3(i,1) = Mfrp(i,1)*(Yfrp-Ytf3)/Ifrp*ntf;
strntf3(i,1)  = Mfrp(i,1)*(Yfrp-Ytf3)/Ifrp/Ew11;
Ftf3(i,1)     = strsstf3 (i,1)*Atf3/ntf;
if Ftf3(i,1)>0
    Ten (i,1) = Ten (i,1)+ Ftf3(i,1);
else
    Comp (i,1) = Comp (i,1)+ Ftf3(i,1);
end

##### Force in FRP Webs
strsslw (i,1) = Mfrp(i,1)*Yfrp/Ifrp;
strssuw (i,1) = Mfrp(i,1)*(Yfrp-h)/Ifrp;
Fw (i,1) = (strsslw (i,1) + strssuw (i,1))*h*2*tw;

if Fw(i,1)>0
    Ten (i,1) = Ten (i,1)+ Fw(i,1);
else
    Comp (i,1) = Comp (i,1)+ Fw(i,1);
end

##### Force in (strands)
strnstr (i,1)= Mtie(i,1)*(Ytie(i,1)-Ys)/Itie(i,+)/Ew11 +
Ntie(i,1)/Atie(i,+)/Ew11 ;
strsstr (i,1)= Mtie(i,1)*(Ytie(i,1)-Ys)/Itie(i,+) *nstr+
N(i,1)*nstr/A(i,);
Fstr(i,1) = strsstr (i,1)*Astr;
Mstr (i,1) = Fstr(i,1)* (Ytie(i,1)-Ys);

if Fstr(i,1)>0
    Tentie (i,1) = Tentie (i,1)+ Fstr(i,1);
else
    Comptie (i,1) = Comptie (i,1)+ Fstr(i,1);
end

```



```

      %%%% Force in Conc Arch
      y1 = Yca (i,1)- (tca/2);
      y2 = Yca (i,1)+ (tca/2);
      strnlca (i,1) = Mtie(i,1)*(Ytie(i,1)-y1)/Itie(i,+)/Ewll +
      Ntie(i,1)/Atie(i,+)/Ewll;
      strnuca (i,1) = Mtie(i,1)*(Ytie(i,1)-y2)/Itie(i,+)/Ewll +
      Ntie(i,1)/Atie(i,+)/Ewll;
      strssl = Mtie(i,1)*(Ytie(i,1)-y1)/Itie(i,+) * nca +
      Ntie(i,1) * nca / Atie(i,);
      strss2 = Mtie(i,1)*(Ytie(i,1)-y2)/Itie(i,+) * nca +
      Ntie(i,1) * nca / Atie(i,);
      Fca(i,1) = (strssl+strss2)*tca*bca;

      if Fca(i,1)>0
          Tentie (i,1) = Tentie (i,1)+ Fca(i,1);
      else
          Comptie (i,1) = Comptie (i,1)+ Fca(i,1);
      end
      Flca (i,1) = strssl *tca*bca;
      Fuca (i,1) = strss2 *tca*bca;
      Mlca (i,1) = Flca (i,1) * (Ytie(i,1)-(y1+tca/3));
      Muca (i,1) = Fuca (i,1) * (Ytie(i,1)-(y1+2*tca/3));

      %%%% Force in Conc Web
      ycw1 = Ycw (i,1)- (hcw(i,1)/2);
      ycw2 = Ycw (i,1)+ (hcw(i,1)/2);
      strnlcw (i,1) = Mtie(i,1)*(Ytie(i,1)-ycw1)/Itie(i,+)/Ewll +
      N(i,1)/A(i,+)/Ewll;
      strnucw (i,1) = Mtie(i,1)*(Ytie(i,1)-ycw2)/Itie(i,+)/Ewll +
      N(i,1)/A(i,+)/Ewll;
      strsscwl = Mtie(i,1)*(Ytie(i,1)-ycw1)/Itie(i,+) * nca +
      N(i,1) * nca / A(i,);
      strsscw2 = Mtie(i,1)*(Ytie(i,1)-ycw2)/Itie(i,+) * nca +
      N(i,1) * nca / A(i,);

      Fcw(i,1) = tcw*hcw (i,1)*(strsscwl+strsscw2);

      if Fcw(i,1)>0
          Tentie (i,1) = Tentie (i,1)+ Fcw(i,1);
      else
          Comptie (i,1) = Comptie (i,1)+ Fcw(i,1);
      end

      Flcw (i,1) = strsscwl *tcw*hcw (i,1);
      Fucw (i,1) = strsscw2 *tcw*hcw (i,1);
      Mcw (i,1) = strsscwl *2*tcw*hcw (i,1)* (Ytie(i,1)-Ycw(i,1))+
      (strsscw2-strsscwl)*tcw*hcw (i,1)* (Ytie(i,1)-(ycw1+2*hcw (i,1)/3));
      Mlcw (i,1) = Flcw (i,1) * (Ytie(i,1)-(ycw1+hcw (i,1)/3));
      Mucw (i,1) = Fucw (i,1) * (Ytie(i,1)-(ycw1+2*hcw (i,1)/3));

```

```
Dif (i,:) = abs((N(i,1)-(Ten(i,1)+Comp(i,1)))/N(i,1))*100;  
  
MC (i,1) = Mlca(i,1)+Muca(i,1)+Mlcw(i,1)+Mucw(i,1);  
MFRP (i,1) =  
Mbf(i,1)+Mbf2(i,1)+Mtf(i,1)+Mtf2(i,1)+Mtf3(i,1)+Mlw(i,1)+Muw(i,1);  
FC (i,1) = Flca(i,1)+Fuca(i,1)+Flcw(i,1)+Fucw(i,1);  
FFRP (i,1) =  
Fbf(i,1)+Fbf2(i,1)+Ftf(i,1)+Ftf2(i,1)+Ftf3(i,1)+Flw(i,1)+Fuw(i,1);  
  
end
```

(3) *MATLAB* code for estimating the strains in non-composite simply supported HCB using the tie-model

```

%%%%%%%%%%%%%%%%%%%%%%%%%%%%%%%%%%%%%%%%%%%%%%%%%%%%%%%%%%%%%%%%%%%%%%%%
%%%%%%%%%%%%%%%%%%%%%%%%%%%%%%%%%%%%%%%%%%%%%%%%%%%%%%%%%%%%%%%%%%%%%%%%
%%%%%%%% This Matlab Code calculates the strains and stresses          %%%%%%%%%
%%%%%%%% of the multi-celled simply supported HCB of bridge B0410    %%%%%%%%%
%%%%%%%% using the tie model                                          %%%%%%%%%
%%%%%%%%%%%%%%%%%%%%%%%%%%%%%%%%%%%%%%%%%%%%%%%%%%%%%%%%%%%%%%%%%%%%%%%%
%%%%%%%%%%%%%%%%%%%%%%%%%%%%%%%%%%%%%%%%%%%%%%%%%%%%%%%%%%%%%%%%%%%%%%%%

%%%%%%%% 1- Material Properties                                     %%%%%%%%%
%%%%%%%%%%%%%%%%%%%%%%%%%%%%%%%%%%%%%%%%%%%%%%%%%%%%%%%%%%%%%%%%%%%%%%%%
%%%%%%%% Concrete Properties %%%%%%%%%
%%%%%%%% Arch
Sca = 11;                %% compressive strength of concrete arch in Ksi
Dca = 0.14;              %% Denisty of concrete arch in Kip/cubic feet
%%%%%%%% Cg of concrete arch in inch
%Yca = [5; 14.48; 22.96; 30.44; 36.93; 42.42; 46.91; 50.4; 52.89;
54.39; 54.89; 54.39; 52.89; 50.4; 46.91; 42.42; 36.93; 30.44; 22.96;
14.48; 5];
Yca = [5; 6.44; 8.7639; 22.96; 27.539; 30.44; 36.93; 42.42; 42.744;
46.91; 50.4; 51.725; 52.89; 54.39; 54.89; 54.39; 52.89; 50.4; 46.91;
42.42; 36.93; 30.44; 22.96; 14.48; 5];
%X = [0; 53.4; 115.8; 178.2; 240.6; 303; 365.4; 427.8; 490.2; 552.6;
615; 677.4; 739.8; 802.2; 864.6; 927; 989.4; 1051.8; 1114.2; 1176.6;
1230]; %% vector of points at which the calculations of Moment, shear
and inertia are calculated in inch
X = [0; 9; 23.8; 115.8; 154; 178.2; 240.6; 303; 307.5; 365.4; 427.8;
461; 490.2; 552.6; 615; 677.4; 739.8; 802.2; 864.6; 927; 989.4; 1051.8;
1114.2; 1176.6; 1230]; %% vector of points at which the calculations
of Moment, shear and inertia are calculated in inch

%%%%%%%% Deck
Sd = 6.5;                %% compressive strength of concrete deck in Ksi
Dd = 0.14;              %% Denisty of concrete arch in Kip/cubic feet

%%%%%%%%%%%%%%%%%%%%%%%%%%%%%%%%%%%%%%%%%%%%%%%%%%%%%%%%%%%%%%%%%%%%%%%% FRP Properties%%%%%%%%%%%%%%%%%%%%%%%%%%%%%%%%%%%%%%%%%%%%%%%%%%%%%%%%%%%%%%%%%%%%%%%%
%%%%%%%% Webs
Ew11 = 2000;            %% Modulus of elasticity in dir. 1-1 of GFRP of
web in Ksi (1378 psi from tests)
Ew22 = 1400;            %% Modulus of elasticity in dir. 2-2 of GFRP of
web in Ksi
Gw12 = 1130;           %% Shear Modulus in plane 1-2 of GFRP of web in
Ksi
Pw12 = 0.26;           %% Poisson's ratio in plane 1-2 of GFRP of web
%Shw = 19;             %% Shear strength in plane 1-2 of GFRP of web in
Ksi
%%%%%%%% Top flange

```

```

Etf11 = 2000;      %% Modulus of elasticity in dir. 1-1 of GFRP of
top flange in Ksi
Etf22 = 1400;      %% Modulus of elasticity in dir. 2-2 of GFRP of
top flange in Ksi
Gtf12 = 1130;      %% Shear Modulus in plane 1-2 of GFRP of top
flange in Ksi
Ptf12 = 0.26;      %% Major Poisson's ratio in plane 1-2 of GFRP of
top flange
%Ptf21 = 0.26;     %% Minor Poisson's ratio in plane 1-2 of GFRP of
top flange
%%% Bottom flange
Ebf11 = 3800;      %% Modulus of elasticity in dir. 1-1 of GFRP of
bot. flange in Ksi
Ebf22 = 1130;      %% Modulus of elasticity in dir. 2-2 of GFRP of
bot. flange in Ksi
Gbf12 = 1130;      %% Shear Modulus in plane 1-2 of GFRP of bot.
flange in Ksi
Pbf12 = 0.26;      %% Major Poisson's ratio in plane 1-2 of GFRP of
bot. flange
%Pbf21 = 0.26;     %% Minor Poisson's ratio in plane 1-2 of GFRP of
bot. flange

%%%%%%%%%%%%%%%%%%%%%%%%%%%%%%%%%%%%%%%%%%%%%%%%%%%%%%%%%%%%%%%%%%%%%%%%
%% 2- Geometry
%%%%%%%%%%%%%%%%%%%%%%%%%%%%%%%%%%%%%%%%%%%%%%%%%%%%%%%%%%%%%%%%%%%%%%%%
%% Beam
h      = 60.16;      %% Height of HCB in inch
b      = 72;         %% Width of beam in inch
btf    = 27.5;       %% Width of Top flange in inch (upper layer of
FRP Lid above two concrete arch)
btf2   = 44.5;       %% Width of Top flange2 in inch (The upper
layer of FRP Lid between the two concret arches)
btf3   = 44.3;       %% Width of Top flange3 in inch (Lower layer
of FRP Lid between the two concret arches)
bsw    = 48;         %% Width of FRP sandwich between the girders
and under the deck
bbf    = 66;         %% Width of Lower flange in inch
bbf2   = 38.4;       %% Width of Lower flange in inch (upper layer
of Lower flange between the two beams)
tw     = 0.19;       %% Thickness of FRP web in inch
ttf    = 0.43;       %% Thickness of FRP top flange in inch
tsw    = 0.2;        %% Thickness of FRP sandwich
tbf    = 0.08;       %% Thickness of FRP bot. flange in inch
tbf2   = 0.08;       %% Thickness of FRP bot. flange in inch
%tsr   = 0.03;       %% Thickness of FRP side return portion in
inch
%hsr   = 6;          %% Height of FRP side return portion in inch
tca    = 10;         %% Thickness of concrete arch in inch
bca    = 10.5;       %% breadth of concrete arch in inch
tcw    = 5;          %% Thickness of concrete web(fin)in inch
%WP    = 2;          %% Working point at thrut line (That is used
to determine the arch profile)
Nstr   = 88;         %% no. of strands of the tensile reinforcement
Nub    = 30;         %% no. of uper deck bars
Nlb    = 19;         %% no. of lower deck bars

```

```

Lovr = 1267;          %%% Overall length of the HCB in inch
L     = 1230;        %%% Design span of the HCB in inch

%%%% Bridge
SG = 120;           %%% spacing between the girders (HCBs)in inch
NG = 3;            %%% No. of girders
%Wovr= 28;         %%% Overall width of the bridge in feet
%Wctc= 30.667;     %%% curb to curb width of the bridge in feet
NEM = 24;          %%% No. of elements that represent one HCB
%%%% Slab
%ts = 15.5;        %%% thickness of cast in place slab in inch
%bs = min( min (SG, 12*ts+b), L/4); %%% width of the CIP slab in
inch

Lseg = zeros (NEM,1); %%% Lengths of each segment between two points
in ft

for i= 1:NEM
    Lseg(i,:) = X (i+1,:)- X (i,:);
end

%%%%%%%%%%%%%%%%%%%%%%%%%%%%%%%%%%%%%%%%%%%%%%%%%%%%%%%%%%%%%%%%%%%%%%%%
%%%% 3- Loads %%%
%%%%%%%%%%%%%%%%%%%%%%%%%%%%%%%%%%%%%%%%%%%%%%%%%%%%%%%%%%%%%%%%%%%%%%%%

%%%% 1-applied Live load
LL1 = 10.02;       %%% The load of the rear tire of Truck#1995M
in kips
XLL1 = 525;        %%% Location of the rear tire load of
Truck#1995M (X=0 is at left support) in inch
LL2 = 12.2;        %%% The load of the rear tire of Truck#2406M
in kips
XLL2 = 529.9;     %%% Location of the rear tire of Truck#2406M
(X=0 is at left support)in inch
LL3 = 10.26;      %%% The load of the middle tire of Truck#1995M
in kips
XLL3 = 580;       %%% Location of the the middle tire load of
Truck#1995M (X=0 is at left support)in inch
LL4 = 7.79;       %%% The load of the middle tire of Truck#2406M
in kips
XLL4 = 583.4;    %%% Location of the middle tire of Truck#2406M
(X=0 is at left support) in inch
LL5 = 8.34;       %%% The load of the front tire of Truck#1995M
in kips
XLL5 = 770;      %%% Location of the the front tire of
Truck#1995M (X=0 is at left support)in inch
LL6 = 8.16;      %%% The load of the Front tire of Truck#2406M
in kips
XLL6 = 773;     %%% Location of the Front tire load (X=0 is at
left support)in inch

%%%% 2- Moment & Normal force due to Live load

```

```

##### First trial (Moment and axial force due to Pin pin curved beam
#####
%M = [0; 225.83; 1340.95; 2968.77; 3982.36; 4624.88; 6305.71; 8007.64;
8131.65; 9727.30; 11461.63; 12390.73; 13207.91; 14410.59; 14184.06;
13444.99; 12714.66; 11487.4; 9749.31; 8025.9; 6320.2; 4635.61; 2975.75;
1344.16; 0];
%N= [-83.48; -83.48; -83.18; -83.03; -83.03; -82.90; -82.79; -82.7; -
82.7; -82.62; -82.55; -82.55; -82.5; -82.44; -82.44; -82.46; -82.56; -
82.56; -82.62; -82.70; - 82.79; -82.91; -83.03; -83.18; -83.48];

#####
##### 4- Calculation of ENA and Moment of inertia #####
#####

%%% 1- Identifying the Inertia of each component w.r.t its CG
%%% Tension RFT (strands)
Astr = Nstr*Astrand;   %%% Area of strands in inch square
Ys   = tbf+ dstr;      %%% CG of two layers of strands from the bottom
of the HCB
nstr  = Ep/Ew11;       %%% modular ratio of the strands relative to
the FRP web
As    = Astr*nstr;     %%% transformed area of strands in inch square
Is    = Nstr*pi*dstr^4*nstr/64+As*(dstr/2)^2; %%% moment of inertia
of strands around their CG
%%% FRP Top flanges
ntf   = Etf11/Ew11;
Ytf   = h-ttf/2;
Atf   = ttf*btf*ntf;   %%% transformed area of top flange in
inch square
Itf   = btf*ttf^3/12*ntf; %%% transformed Moment of inertia of top
flange in in^4
Ytf2  = h-ttf2/2;
Atf2  = ttf2*btf2*ntf; %%% transformed area of top flange2 in
inch square
Itf2  = btf2*ttf2^3/12*ntf; %%% transformed Moment of inertia of top
flange2 in in^4
Ytf3  = h-ttf2-2-ttf3/2;
Atf3  = ttf3*btf3*ntf; %%% transformed area of top flange3 in
inch square
Itf3  = btf3*ttf3^3/12*ntf; %%% transformed Moment of inertia of top
flange3 in in^4
%%% FRP Bottom flanges
nbf   = Ebf11/Ew11;
Ybf   = tbf/2;
Abf   = tbf*bbf*nbf;   %%% transformed area of top flange in
inch square
Ibf   = bbf*tbf^3/12*nbf; %%% transformed Moment of inertia of top
flange in in^4
Ybf2  = tbf2/2+tbf+2;
Abf2  = tbf2*bbf2*nbf; %%% transformed area of top flange in
inch square
Ibf2  = bbf2*tbf^3/12*nbf; %%% transformed Moment of inertia of top
flange in in^4
%%% FRP Webs
Yw    = h/2;

```

```

Aw      = 4*tw*h;          %%%% area of four FRP webs in inch square
Iw      = 4*tw*h^3/12;    %%%% Moment of inertia of two webs in
in^4

%%%%% Concrete Arch
frca    = 7.5/1000*sqrt(Sca*1000); %%%% modulus of rupture of concret
arch in Ksi
Eca     = 57*sqrt(Sca*1000); %%%% Elastic modulus of concret arch in
Ksi
nca     = Eca/Ew11;       %%%% modular ratio of the conc. Arch
relative to the FRP web
Aca     = 2*tca*bca*nca;  %%%% transformed area of two conc arches
in square inch
Ica     = 2*bca*tca^3*nca/12; %%%% transformed Moment of inertia of two
conc arches in in^4

%%%%% Concrete Web (fin)
Ecw     = 57*sqrt(Sca*1000); %%%% Elastic modulus of concrete in Ksi
ncw     = Ecw/Ew11;       %%%% modular ratio of the deck relative
to the FRP web
hcw     = zeros(NEM+1,1);
Ycw     = zeros(NEM+1,1);
Acw     = zeros(NEM+1,1);
Icw     = zeros(NEM+1,1);
for i=1:NEM+1             %%%% Calculating the height and the area
of the concrete web
    hcw(i,1)= h-(Yca(i,:)+tca/2+ttf);
    Ycw(i,1)= h-(hcw(i,+)/2+ttf);
    Acw(i,1)= 2*hcw(i,1)*tcw*ncw;
    Icw(i,1)= 2*tw* (hcw(i,1))^3*ncw/12;
end

hcw(15,1) = 0;
Acw(15,1) = 0;
Icw(15,1) = 0;

%%%%% 1- Identifying the N.A. and moment of inertia of HCB
Ybar    = zeros(NEM+1,1); %%%% N.A of HCB at each
point
I       = zeros(NEM+1,1); %%%% moment of inertia of
HCB in in^4
A       = zeros(NEM+1,1); %%%% Area of HCB in
in^2
for i= 1:NEM+1
    A (i,:) = As+Atf+Atf2+Atf3+Abf+Abf2+Aw+Aca+Acw(i,:);
    Ybar(i,:) =
(As*Ys+Atf*Ytf+Atf2*Ytf2+Atf3*Ytf3+Abf*Ybf+Abf2*Ybf2+Aw*Yw+Aca*Yca(i,:)
+Acw(i,)*Ycw(i,))/A(i,);
    I (i,:) = Is+As*(Ys-Ybar(i,))^2+Itf+Atf*(Ytf-
Ybar(i,))^2+Itf2+Atf2*(Ytf2-Ybar(i,))^2+Itf3+Atf3*(Ytf3-
Ybar(i,))^2+Ibf+Abf*(Ybf-Ybar(i,))^2+Ibf2+Abf2*(Ybf2-
Ybar(i,))^2+Iw+Aw*(Yw-Ybar(i,))^2+Ica+Aca*(Yca(i,))-
Ybar(i,))^2+Icw(i,)+Acw(i,)*(Ycw(i,)-Ybar(i,))^2;
end

```

```

%%% Approach
Ifrpc = zeros(NEM+1,1);
Icctie = zeros(NEM+1,1);
Itiec = zeros(NEM+1,1);
Isc = zeros(NEM+1,1);
Ac      = zeros(NEM+1,1);
Yc      = zeros(NEM+1,1);
Ic      = zeros(NEM+1,1);
Atie    = zeros(NEM+1,1);
Ytie    = zeros(NEM+1,1);
Itie    = zeros(NEM+1,1);
Afrp    = Atf+Atf2+Atf3+Abf+Abf2+Aw;
Yfrp    = (Atf*Ytf+Atf2*Ytf2+Atf3*Ytf3+Abf*Ybf+Abf2*Ybf2+Aw*Yw)/Afrp;
Ifrp    = Itf+Atf*(Ytf-Yfrp)^2+Itf2+Atf2*(Ytf2-
Yfrp)^2+Itf3+Atf3*(Ytf3-Yfrp)^2+Ibf+Abf*(Ybf-Yfrp)^2+Ibf2+Abf2*(Ybf2-
Yfrp)^2+Iw+Aw*(Yw-Yfrp)^2;

for i= 1:NEM+1
    Ac(i,1) = Aca + Acw(i,1);
    Yc(i,1) = (Aca*Yca(i,1) + Acw(i,1)*Ycw(i,1))/Ac(i,1);
    Ic(i,1) = Ica+Aca*(Yca(i,:)-
Yc(i,:))^2+Icw(i,)+Acw(i,)*(Ycw(i,)-Yc(i,:))^2;
    Atie(i,1) = Aca + Acw(i,1)+As;
    Ytie(i,1) = (Aca*Yca(i,1) + Acw(i,1)*Ycw(i,1)+As*Ys)/Atie(i,1);
    Itie(i,1) = Ica+Aca*(Yca(i,:)-
Ytie(i,:))^2+Icw(i,)+Acw(i,)*(Ycw(i,)-Ytie(i,:))^2+Is+(Ys -
Ytie(i,:))^2;
    Ifrpc(i,1) = Itf+Atf*(Ytf-Ybar(i,1))^2+Itf2+Atf2*(Ytf2-
Ybar(i,1))^2+Itf3+Atf3*(Ytf3-Ybar(i,1))^2+Ibf+Abf*(Ybf-
Ybar(i,1))^2+Ibf2+Abf2*(Ybf2-Ybar(i,1))^2+Iw+Aw*(Yw-Ybar(i,1))^2;
    Icctie(i,1) = Ica+Aca*(Yca(i,:)-
Ytie(i,:))^2+Icw(i,)+Acw(i,)*(Ycw(i,)-Ytie(i,:))^2;
    Itiec(i,1) = Ica+Aca*(Yca(i,:)-
Ybar(i,:))^2+Icw(i,)+Acw(i,)*(Ycw(i,)-Ybar(i,:))^2+Is+As*(Ys -
Ybar(i,:))^2;
    Isc(i,1) = Is+As*(Ys -Ybar(i,:))^2;
end

%%%%%%%%%%%%%%%%%%%%%%%%%%%%%%%%%%%%%%%%%%%%%%%%%%%%%%%%%%%%%%%%%%%%%%%%%%
%%% 5- Calculation of stresses and strains %%%%%%%%%%%
%%%%%%%%%%%%%%%%%%%%%%%%%%%%%%%%%%%%%%%%%%%%%%%%%%%%%%%%%%%%%%%%%%%%%%%%%%

PNA      = zeros (NEM+1,1);
strssbf  = zeros (NEM+1,1);
strnbf   = zeros (NEM+1,1);
Fbf      = zeros (NEM+1,1);
strssbf2 = zeros (NEM+1,1);
strnbf2  = zeros (NEM+1,1);
Fbf2     = zeros (NEM+1,1);
strsstf  = zeros (NEM+1,1);

```



```

strntf  = zeros (NEM+1,1);
Ftf     = zeros (NEM+1,1);
strsstf2 = zeros (NEM+1,1);
Ftf2    = zeros (NEM+1,1);
strsstf3 = zeros (NEM+1,1);
strntf3  = zeros (NEM+1,1);
Ftf3    = zeros (NEM+1,1);
strsstr  = zeros (NEM+1,1);
strnstr  = zeros (NEM+1,1);
Fstr     = zeros (NEM+1,1);
strsslw  = zeros (NEM+1,1);
strssuw  = zeros (NEM+1,1);
Fw       = zeros (NEM+1,1);
%FwT     = zeros (NEM+1,1);
%strsslsr = zeros (NEM+1,1);
%strssusr = zeros (NEM+1,1);
%FsrC    = zeros (NEM+1,1);
%FsrT    = zeros (NEM+1,1);
strsssw  = zeros (NEM+1,1);
Fsw      = zeros (NEM+1,1);
strssub  = zeros (NEM+1,1);
strnub   = zeros (NEM+1,1);
Fub      = zeros (NEM+1,1);
Flb      = zeros (NEM+1,1);
strsslca = zeros (NEM+1,1);
strnlca  = zeros (NEM+1,1);
strssuca = zeros (NEM+1,1);
strnuca  = zeros (NEM+1,1);
Fca      = zeros (NEM+1,1);
Fd       = zeros (NEM+1,1);
strnlcw  = zeros (NEM+1,1);
strnucw  = zeros (NEM+1,1);
Fcw      = zeros (NEM+1,1);
Comp     = zeros (NEM+1,1);
Ten      = zeros (NEM+1,1);
Dif      = zeros (NEM+1,1);

```

```

for i = 1:NEM+1
    PNA(i,1) = Ybar(i,1);
end

```

```

M = zeros (NEM+1,1);
N = zeros (NEM+1,1);
MF = zeros (NEM+1,1);
NF = zeros (NEM+1,1);
Mfrp  = zeros (NEM+1,1);
Nfrp  = zeros (NEM+1,1);
Mc    = zeros (NEM+1,1);
Nc    = zeros (NEM+1,1);
March = zeros (NEM+1,1);
MarchT = zeros (NEM+1,1);
Narch = zeros (NEM+1,1);
strnca = zeros (NEM+1,1);
Fc     = zeros (NEM+1,1);
strnc  = zeros (NEM+1,1);

```

```

Mtie          = zeros (NEM+1,1);

MF (1,1) = -4413;
NF (1,1) = -18;
MF (2,1) = -4142;
NF (2,1) = -17.9;
MF (3,1) = -3696;
NF (3,1) = -17.8;
MF (5,1) = 282;
NF (5,1) = -17;
MF (9,1) = 5025;
NF (9,1) = -16.1;
MF (12,1) = 8679;
NF (12,1) = -15.6;
MF (15,1) = 10211;
NF (15,1) = -15.5;

M (2,1) = 287;
M (3,1) = 759;
M (5,1) = 4911;
M (9,1) = 9802;
M (12,1) = 13557;
M (15,1) = 15169;

for i= 1:NEM+1
    Mfrp(i,1) = Ifrp /I(i,1)*M(i,1);
    Mc(i,1) = Ic (i,1)/I (i,1)*MF(i,1);
    March (i,1) = Itiec (i,1)/I (i,1)*MF(i,1)-Mc(i,1);

end

for i= 1:NEM+1

    %%% FRP Bottom flanges
    strssbf(i,1) = Mfrp(i,1)*(Yfrp -Ybf)/Ifrp*nbf;
    strnbf(i,1) = Mfrp(i,1)*(Yfrp -Ybf)/Ifrp/Ew11;
    Fbf(i,1) = strssbf (i,1)*Abf/nbf;
    if Fbf(i,1)>0
        Ten (i,1) = Ten (i,1)+ Fbf(i,1);
    else
        Comp (i,1) = Comp (i,1)+ Fbf(i,1);
    end

    strssbf2(i,1) = Mfrp(i,1)*(Yfrp-Ybf2)/Ifrp*nbf;
    strnbf2(i,1) = Mfrp(i,1)*(Yfrp-Ybf2)/Ifrp/Ew11;
    Fbf2(i,1) = strssbf2 (i,1)*Abf2/nbf;
    if Fbf2(i,1)>0
        Ten (i,1) = Ten (i,1)+ Fbf2(i,1);
    else

```

```

        Comp (i,1) = Comp (i,1)+ Fbf2(i,1);
end

%%% FRP Top flanges
strsstf(i,1) = Mfrp(i,1)*(Yfrp -Ytf)/Ifrp*ntf;
strntf(i,1) = Mfrp(i,1)*(Yfrp -Ytf)/Ifrp/Ew11;
Ftf(i,1) = strsstf (i,1)*Atf/ntf;
if Ftf(i,1)>0
    Ten (i,1) = Ten (i,1)+ Ftf(i,1);
else
    Comp (i,1) = Comp (i,1)+ Ftf(i,1);
end

strsstf2(i,1) = Mfrp(i,1)*(Yfrp-Ytf2)/Ifrp*ntf;
Ftf2(i,1) = strsstf2 (i,1)*Atf2/ntf;
if Ftf2(i,1)>0
    Ten (i,1) = Ten (i,1)+ Ftf2(i,1);
else
    Comp (i,1) = Comp (i,1)+ Ftf2(i,1);
end

strsstf3(i,1) = Mfrp(i,1)*(Yfrp-Ytf3)/Ifrp*ntf;
strntf3(i,1) = Mfrp(i,1)*(Yfrp-Ytf3)/Ifrp/Ew11;
Ftf3(i,1) = strsstf3 (i,1)*Atf3/ntf;
if Ftf3(i,1)>0
    Ten (i,1) = Ten (i,1)+ Ftf3(i,1);
else
    Comp (i,1) = Comp (i,1)+ Ftf3(i,1);
end

%%% Force in FRP Webs
strsslw (i,1) = Mfrp(i,1)*Yfrp/Ifrp;
strssuw (i,1) = Mfrp(i,1)*(Yfrp-h)/Ifrp;
Fw (i,1) = (strsslw (i,1) + strssuw (i,1))*h*2*tw;

    if Fw(i,1)>0
        Ten (i,1) = Ten (i,1)+ Fw(i,1);
    else
        Comp (i,1) = Comp (i,1)+ Fw(i,1);
    end

%%% Strands
Fstr (i,1) = March(i,1)/(Yc(i,1)-Ys);
strnstr (i,1) = Fstr(i,1)/Ep/Astr;
if Fstr(i,1)>0
    Ten (i,1) = Ten (i,1)+ Fstr(i,1);
else
    Comp (i,1) = Comp (i,1)+ Fstr(i,1);
end

%%% Concrete Arch
Fc (i,1) = -March(i,1)/(Yc(i,1)-Ys);
strnc (i,1) = Fc(i,1)/(Ac(i,1)/nca)/Eca;
strnuca (i,1) = strnc (i,1)+(Mc(i,1)*(Yc(i,1)-Yca(i,1)-
tca/2)/Ic(i,:)/Ew11);

```

```

        strnlca (i,1)    = strnc (i,1)+(Mc(i,1)*(Yc(i,1)-
Yca(i,1)+tca/2)/Ic(i,:)/Ew11);
        strss1          = strnuca (i,1)*Eca;
        strss2          = strnlca (i,1)*Eca;
        Fca(i,1) = (strss1+strss2)*tca*bca;

        if Fca(i,1)>0
            Ten (i,1) = Ten (i,1)+ Fca(i,1);
        else
            Comp (i,1) = Comp (i,1)+ Fca(i,1);
        end

        %%% Concrete Web
        strnlcw (i,1) = strnc (i,1)+Mc(i,1)*(Yc(i,1)-
Ycw(i,1)+hcw(i,1))/Ic(i,1)/Ew11;
        strnucw (i,1) = strnc (i,1)+Mc(i,1)*(Yc(i,1)-Ycw(i,1)-
hcw(i,1))/Ic(i,1)/Ew11;
        strsscwl = strnucw (i,1)*Eca;
        strsscw2 = strnlcw (i,1)*Eca;

        Fcw(i,1) = tcw*hcw (i,1)*(strsscwl+strsscw2);

        if Fcw(i,1)>0
            Ten (i,1) = Ten (i,1)+ Fcw(i,1);
        else
            Comp (i,1) = Comp (i,1)+ Fcw(i,1);
        end
        Dif (i,:) = Ten(i,1)+Comp(i,1);

end

```

APPENDIX F.
MEASURED AND ESTIMATED STRAINS IN HCB2 OF B0410
AND TIDE MILL BRIDGE SIMULATED HCB

Stage 1 Loading

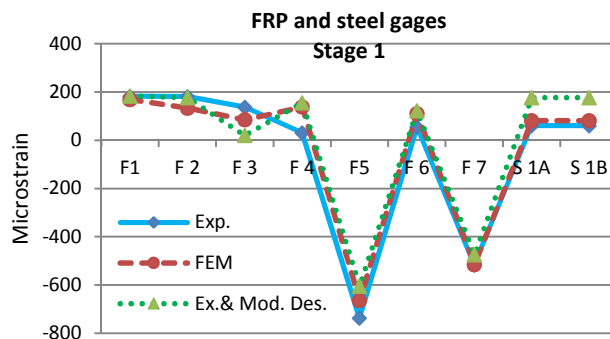


Fig. F-1. Measured and estimated strains under stage 1 loads

Table (F-1) Measured and estimated strains under stage 1 loads

Stage 1	Experimental (μ)	FE model (μ)	Existing and Mod. Des. (μ)
F1	183	169	184
F2	180	134	177
F3	137	86	20
F4	31	139	156
F5	-736	-663	-604
F6	56	111	123
F7	-515	-514	-473
S1A	60	82	177
S1B	60	82	177

Stage 2 Loading

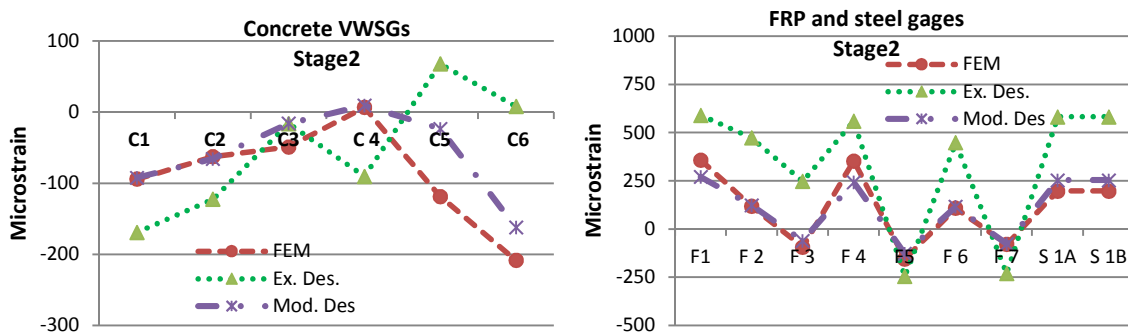


Fig. F-2. Measured and estimated strains under stage 2 loads

Table (F-2) Measured and estimated strains under stage 1 loads

Stage 2	FE model ($\mu\epsilon$)	Mod. Des. ($\mu\epsilon$)	Existing Des. ($\mu\epsilon$)
C1	-94	-92	-169
C2	-62	-65	-122
C3	-49	-16	-16
C4	7	10	-90
C5	-118	-23	68
C6	-208	-153	8
F1	358	271	591
F2	119	124	474
F3	-93	-60	248
F4	353	244	560
F5	-155	-127	-245
F6	109	116	448
F7	-78	-77	-230
S1A	197	254	583
S1B	197	254	583

Stage 3 Loading

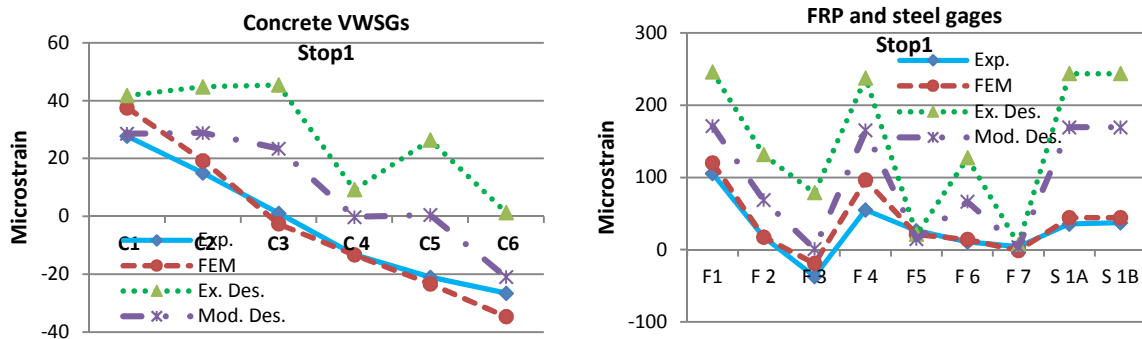


Fig. F-3. Measured and estimated strains under Stop 1 loads

Table (F-3) Measured and estimated strains under stop 1 loads

STOP 1	Experimental ($\mu\epsilon$)	FE model ($\mu\epsilon$)	Modified Des. ($\mu\epsilon$)	Existing Des. ($\mu\epsilon$)
C1	28	37	29	42
C2	15	19	29	45
C3	1	-3	24	46
C4	-13	-13	0	9
C5	-21	-23	1	26
C6	-27	-35	-21	1
F1	106	120	171	246
F2	17	18	69	132
F3	-37	-19	1	79
F4	55	97	165	238
F5	27	21	15	21
F6	11	14	66	127
F7	4	-1	4	8
S1A	36	44	170	244
S1B	37	45	170	244

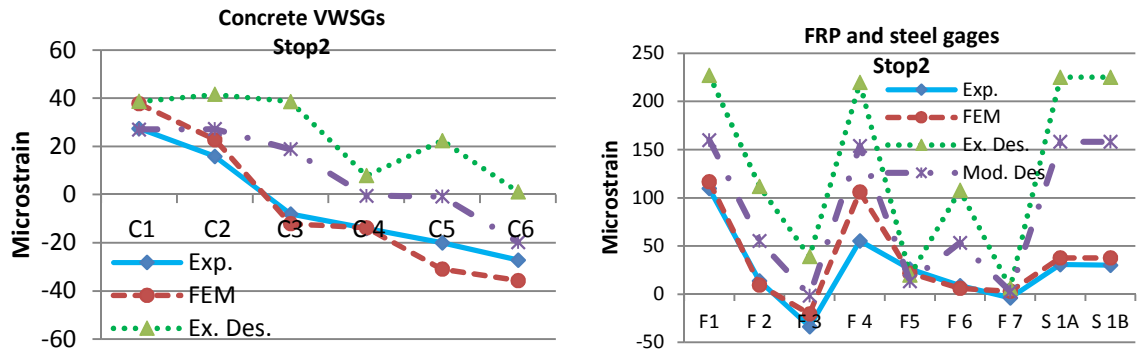


Fig. F-4. Measured and estimated strains under Stop 2 loads

Table (F-4) Measured and estimated strains under stop 2 loads

STOP 2	Experimental ($\mu\epsilon$)	FE model ($\mu\epsilon$)	Mod. Des. ($\mu\epsilon$)	Existing Des. ($\mu\epsilon$)
C1	27	38	27	39
C2	16	23	27	42
C3	-8	-12	19	39
C4	-14	-14	0	8
C5	-20	-31	-1	22
C6	-27	-36	-20	1
F1	110	117	160	227
F2	14	9	55	112
F3	-34	-20	-1	39
F4	55	106	154	220
F5	26	22	14	20
F6	9	6	53	108
F7	-4	3	3	7
S1A	31	38	158	225
S1B	30	38	158	225

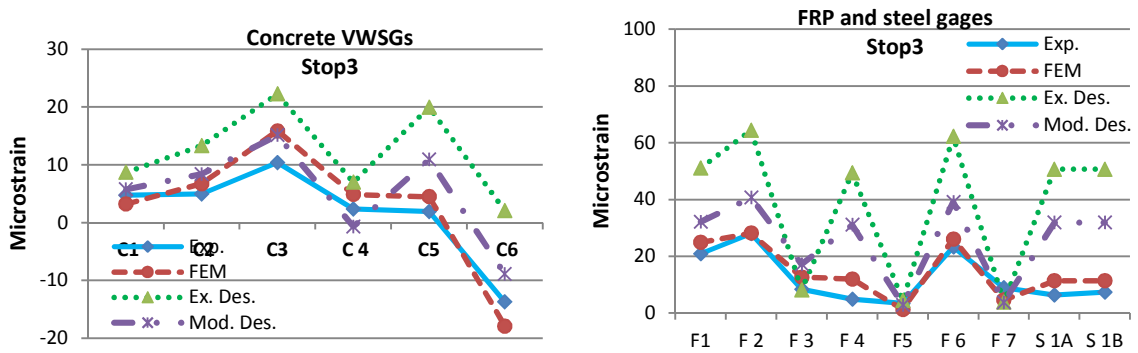


Fig. F-5. Measured and estimated strains under Stop 3 loads

Table (F-5) Measured and estimated strains under stop 3 loads

STOP 3	Experimental ($\mu\epsilon$)	FE model ($\mu\epsilon$)	Mod. Design ($\mu\epsilon$)	Existing Design ($\mu\epsilon$)
C1	5	3	6	9
C2	5	7	8	13
C3	10	16	15	22
C4	2	5	-1	7
C5	2	5	11	20
C6	-14	-19	-9	2
F1	21	25	32	51
F2	28	28	41	64
F3	8	13	17	8
F4	5	12	31	49
F5	3	1	3	4
F6	23	26	39	62
F7	9	5	4	4
S1A	6	11	32	51
S1B	7	11	32	51

Total Loads of the three stages

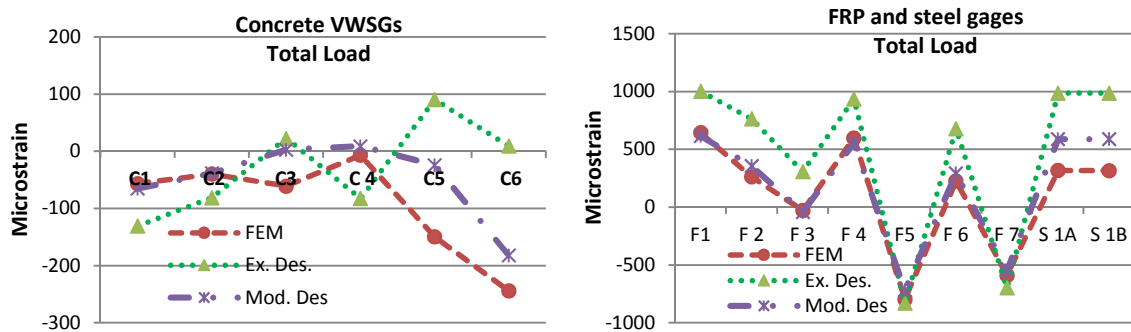


Fig. F-6. Measured and estimated strains under total loads of the three stages

Table (F-6) Measured and estimated strains under total loads of the three stages

Total Loads	FE model ($\mu\epsilon$)	Mod. Des. ($\mu\epsilon$)	Existing Des. ($\mu\epsilon$)
C1	-54	-65	-130
C2	-37	-38	-81
C3	-61	3	23
C 4	-7	9	-82
C5	-149	-24	91
C6	-241	-172	9
F1	644	616	1002
F 2	262	356	762
F 3	-28	-41	308
F 4	598	553	936
F5	-796	-718	-829
F 6	226	292	679
F 7	-589	-547	-697
S 1A	317	589	985
S 1B	317	589	985

Simply Supported HCB

Two mathematical models were proposed to estimate the strains in a simply supported HCB: a beam model, and a tied arch model. In both models, the HCB beam was decoupled into two structural components to apply different boundary conditions on the HCB's elements. The first structural component consisted of the FRP shell. The second component consisted of the concrete arch and web, and the strands (in addition to the deck in case of composite HCB).

Beam Model

This model decoupled the HCB into a straight, simply supported beam (represented the shell) and a curved beam (represented the strands and the concrete components). The chimney's effect was represented at the curved beam's end by translational and rotational springs. The load was divided between the two components (straight and curved beams) based on their contributions to the flexural rigidity of the overall system.

Tied-Arch Model

The tied arch model is similar to the model proposed by Nossall (2013). However, the model was modified to account for the chimney's effect and to include the concrete web and the deck into the calculations. The tied-arch model divided the HCB into a straight, simply supported beam (represented the shell) and a tied arch (represented the strands and the concrete components). The chimney's effect was represented at the tied arch's end by a rotational spring. The load was divided between the shell and the tied arch based on their contributions to the flexural rigidity of the overall system. The load that was given to the tied arch was divided into two parts: a load producing axial forces in the arch and the tie, and a load causing local bending in the arch. The second load was estimated based on the contribution of the arch's local flexural stiffness to the total flexural stiffness of the overall system. The tie model is depicted in Figure F-7.

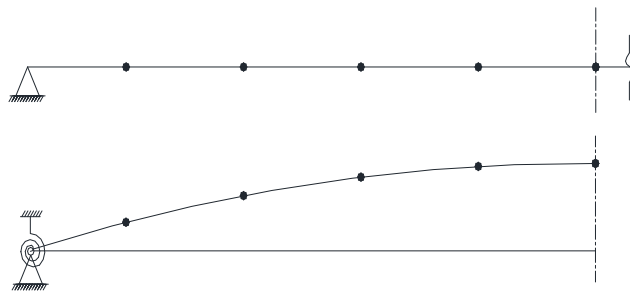


Fig. F-7. Decoupling of the simply supported HCB into tied arch and simply supported beam (tied arch model)

The strains estimated by the FE model, beam model (B-model), tie model (T-model), and the existing analysis method for B0410 HCB and Tide Mill Bridge simulated HCB are presented in the following sections.

1- B0410 HCB results

A- Uniform distributed load from the support to three quarter point.

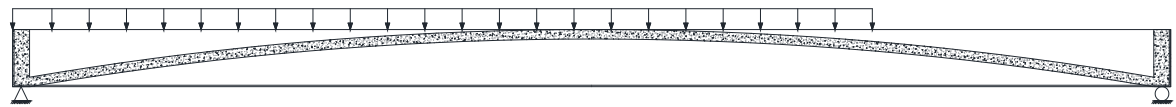


Fig. F-8. Possible load case during deck pour (stage 2)

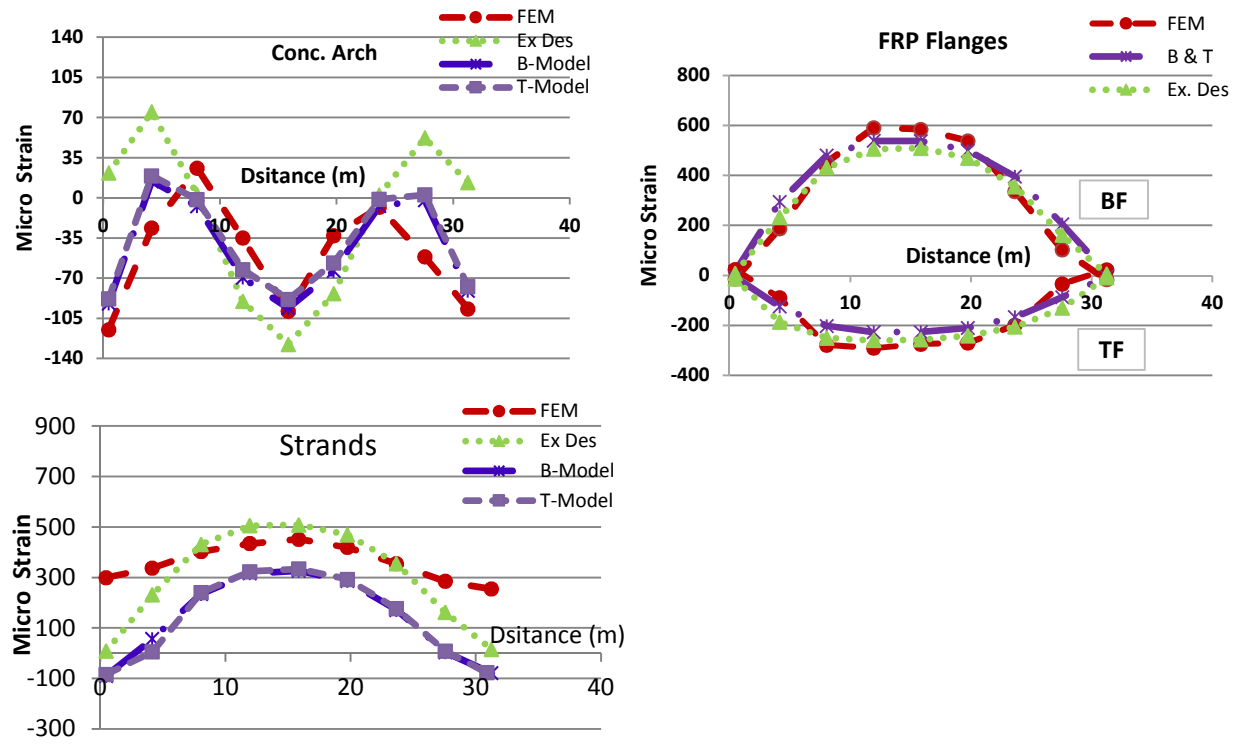


Fig. F-9. Strains in simply supported B0410 HCB under partial distributed load

Table (F-7) Strains in concrete arch of simply supported B0410 HCB under partial distributed load

Distance from support (m)	Concrete Arch Strains	FE model (μ)	Beam model (μ)	Tied-arch model (μ)	Ex. Design (μ)
0.46	CA1	-115	-92	-88	9
4.15	CA2	-26	15	19	75
8.05	CA3	26	-7	-1	3
11.95	CA4	-35	-69	-62	-90
15.85	CA5	-99	-96	-88	-128
19.75	CA6	-33	-64	-57	-83
23.65	CA7	-8	-7	-1	3
27.55	CA8	-51	-2	3	52
31.24	CA9	-97	-81	-77	5

Table (F-8) Strains in bottom flange of simply supported B0410 HCB under partial distributed load

Distance from support (m)	Bottom Flange Strains	FE model (μ)	Beam model (μ)	Tied-arch model (μ)	Ex. Design (μ)
0.46	BF1	-13	16	16	9
4.15	BF 2	188	295	295	232
8.05	BF 3	453	480	480	432
11.95	BF 4	591	539	539	506
15.85	BF 5	585	538	538	509
19.75	BF 6	539	501	501	470
23.65	BF 7	337	396	396	356
27.55	BF 8	103	206	206	162
31.24	BF 9	-16	9	9	6

Table (F-9) Strains in strands of simply supported B0410 HCB under partial distributed load

Distance from support (m)	Strands Strains	FE model (μ)	Beam model (μ)	Tied-arch model (μ)	Ex. Design (μ)
0.46	S1	300	-90	-84	9
4.15	S2	338	57	6	232
8.05	S3	403	235	241	432
11.95	S4	435	317	324	506
15.85	S5	452	327	335	509
19.75	S6	420	287	294	470
23.65	S7	355	172	178	356
27.55	S8	285	4	9	162
31.24	S9	255	-78	-76	6

B- Uniform distributed load on the overall beam length

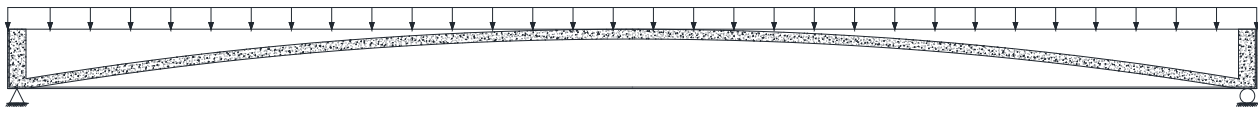


Fig. F-10. Simply supported non-composite B0410 HCB under full deck weight

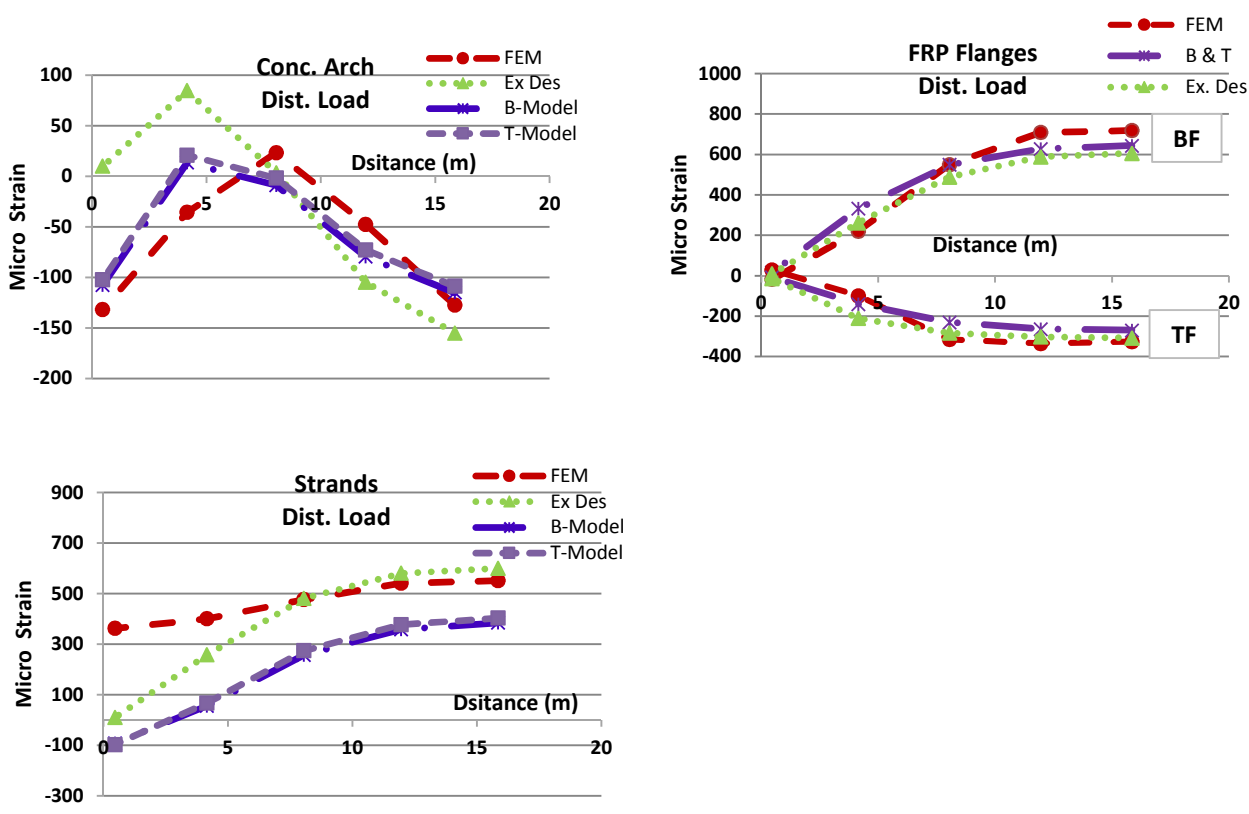


Fig. F-11. Strains in simply supported B0410 HCB under full distributed load

Table (F-10) Strains in concrete arch of simply supported B0410 HCB under full distributed load

Distance from support (m)	Concrete Arch Strains	FE model (μ)	Beam model (μ)	Tied-arch model (μ)	Ex. Design (μ)
15.85	CA1	-127	-115	-109	-155
11.95	CA2	-47	-79	-73	-105
8.05	CA3	24	-9	-2	4
4.15	CA4	-36	14	21	85
0.46	CA5	-132	-108	-102	10

Table (F-11) Strains in bottom flange of simply supported B0410 HCB under full distributed load

Distance from support (m)	Bottom flange Strains	FE model (μ)	Beam model (μ)	Tied-arch model (μ)	Ex. Design (μ)
15.85	BF1	720	644	644	606
11.95	BF2	710	628	628	589
8.05	BF3	551	550	550	489
4.15	BF4	221	333	333	262
0.46	BF5	-17	17	17	10

Table (F-12) Strains in strands of simply supported B0410 HCB under full distributed load

Distance from support (m)	Strands Strains	FE model (μ)	Beam model (μ)	Tied-arch model (μ)	Ex. Design (μ)
15.85	S1	552	385	404	601
11.95	S2	542	359	378	581
8.05	S3	477	258	275	481
4.15	S4	401	56	67	258
0.46	S5	363	-93	-97	10

2- Tide Mill Bridge simulated HCB results

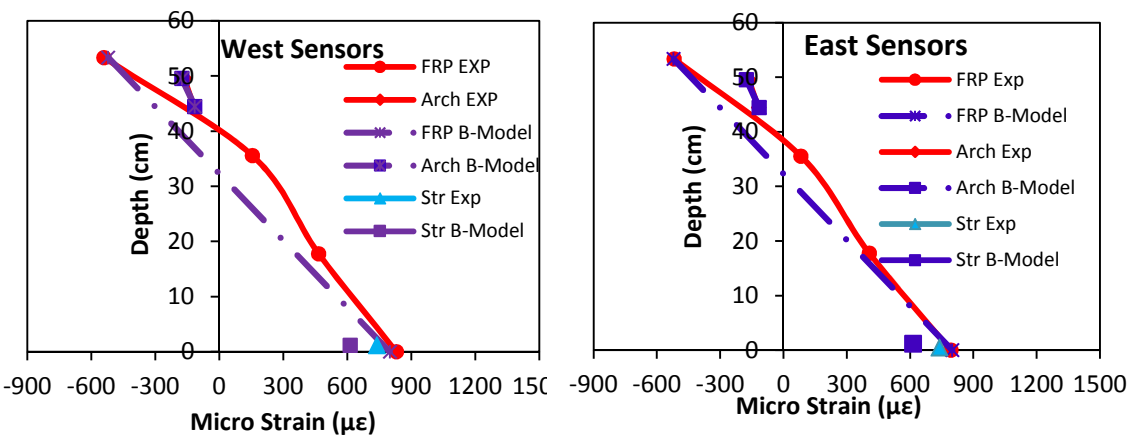


Fig. F-12. Strains at the midspan produced by one point-load at the midspan Measured data (Ahsan 2012, Nossdall 2013) and Beam-model estimations (west sensors left image & east sensors right image)

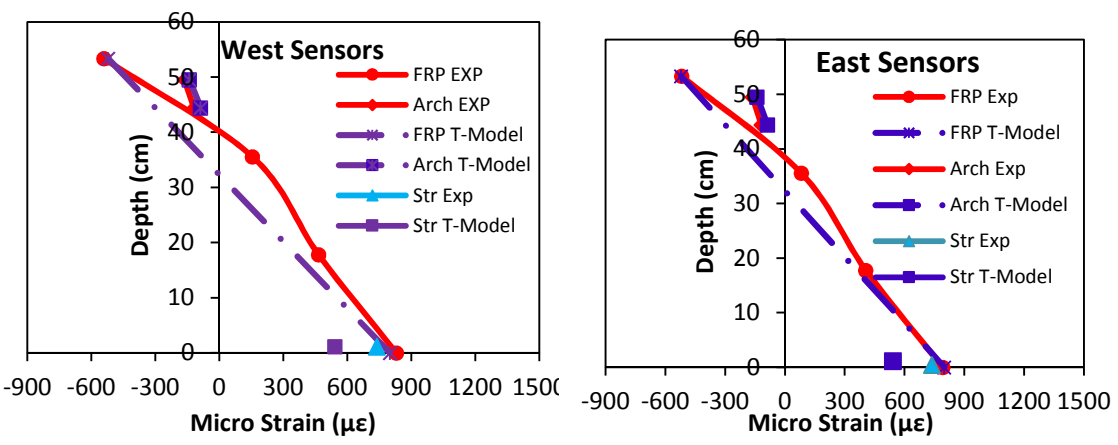


Fig. F-13. Strains at the midspan produced by one point-load at the midspan Measured data (Ahsan 2012, Nossdall 2013) and Tie-arch model estimations (west sensors left image & east sensors right image)

Table (F-13) Strains in strands of simply supported B0410 HCB under full distributed load

Element	Measured (μ)	Estimated by Ahsan (2012) (μ) (Existing Method)	Beam-Model (μ)	Tied- Arch Model (μ)
TF E	-518	-425	-521	-521
TF W	-541	-425	-521	-521
BF E	793	1222	800	800
BF W	830	1222	800	800
Strand	738	1191	614	542
Ca T	-164	-268	-175	-140
Ca B	-119	-180	-115	-88

Chimney Effect:

Two approaches were proposed to estimate the stiffnesses provided by the chimneys at the beam's end. Table (F-14) illustrates a comparison between the stiffnesses estimated by the two approaches as well as a FE model for the stiffnesses provided by the Tide Mill bridge simulated HCB's chimney.

Table (F-14) Estimated Rotational and Extensional Stiffnesses for Tide Mill Bridge
Simulated HCB's Chimney

Load case	Stiffness	1 st approach	Slope-def. approach	Diff. % (1 st App & slope def.)	FE model	Diff. % (1 st App and FE model)
Midspan Load	K_{rch} MN.in/rad (Kip.in/rad)	275 (2.44E+6)	281 (2.48E+6)	-1.9	280 (2.48E+6)	-1.8
	K_{xch} MN.in (kip/in)	63 (359)	67 (383)	-6.2	68 (383)	-6.3
2-Quar. Point Loads	K_{rch} MN.in/rad (Kip.in/rad)	275 (2.44E+6)	279 (2.47E+6)	-1.4	279 (2.47E+6)	-1.5
	K_{xch} MN.in (kip/in)	63 (359)	69 (392)	-8.4	68 (388)	-7.5
Dist. Load	K_{rch} MN.in/rad (Kip.in/rad)	275 (2.44E+6)	280 (2.47E+6)	-1.5	280 (2.48E+6)	-1.5
	K_{xch} MN.in(kip/in)	63 (359)	68 (389.5)	-7.8	68 (387)	-7.2

The stiffnesses provided by the chimney do not affect the FRP shell strains. The chimney's stiffnesses that were estimated by the two approaches were used to estimate the concrete arch and web, and the strands' strains at the midspan due to one point load. Table (F-15) illustrates a comparison between these strains.

Table (F-15) Strains at the midspan of Tide Mill bridge simulated HCB under point load

Element	Measured (μ)	Beam-Model (Stiffnesses by first approach) (μ)	Beam-Model (Stiffnesses by slope-def. approach) (μ)
Strand	738	613.7	612.4
Ca T	-164	-175.5	-175.4
Ca B	-119	-115.3	-115.3

Notes:

- 1- The strain profiles through the FRP shell didn't show linear pattern. A significant scatter was observed in the measured data. This scatter led to such nonlinearity throughout the beam's depth. Figures F-14 to F-17 illustrate the large spread in the measured strains in the FRP shell (Nosdall 2013). Nosdall (2013) attributed this scatter in the measured data to differences between the tested HCBs (these beams were supposed to be identical) and to inaccuracy in applying the loads.
- 2- The Tide Mill bridge simulated HCB suffered lateral displacement under the one-point and two-point loads testing. This behavior may have also contributed to the shell's strain nonlinearity. This lateral displacement was captured via close-range Photogrammetry (Mascaro and Moen, 2012).

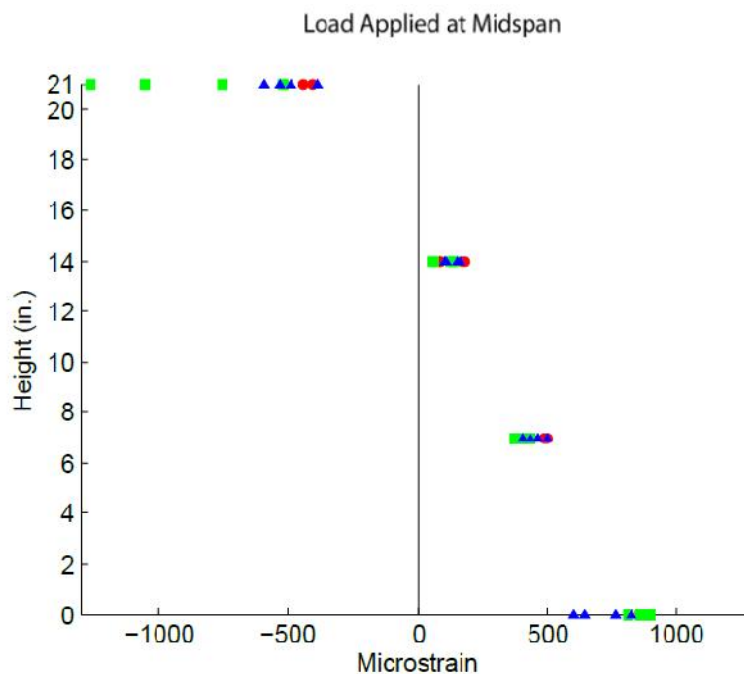


Fig. F-14. Mid span strains in the FRP shell of Tide Mill Bridge simulated HCB (copied from Nosedall 2013)

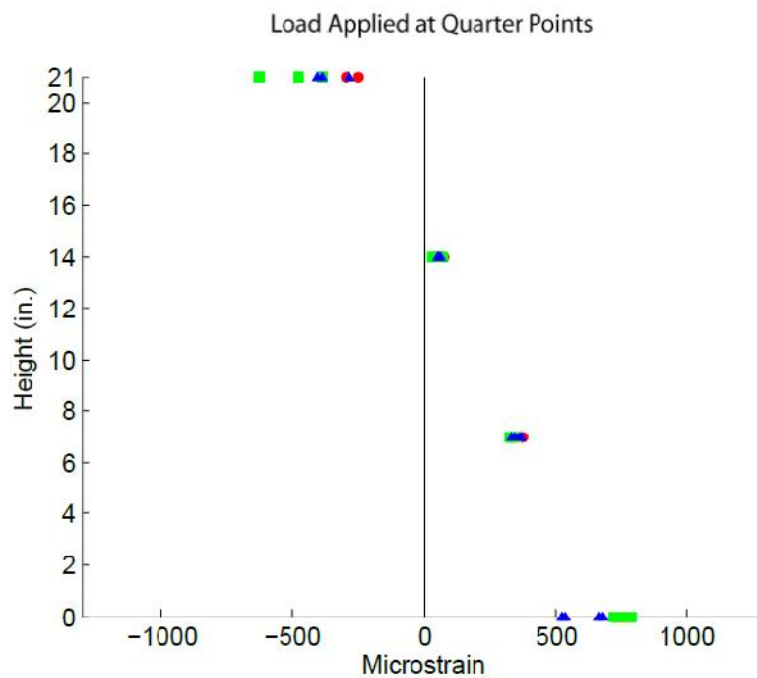


Fig. F-15. Mid span strains in the FRP shell of Tide Mill Bridge simulated HCB (copied from Nosedall 2013)

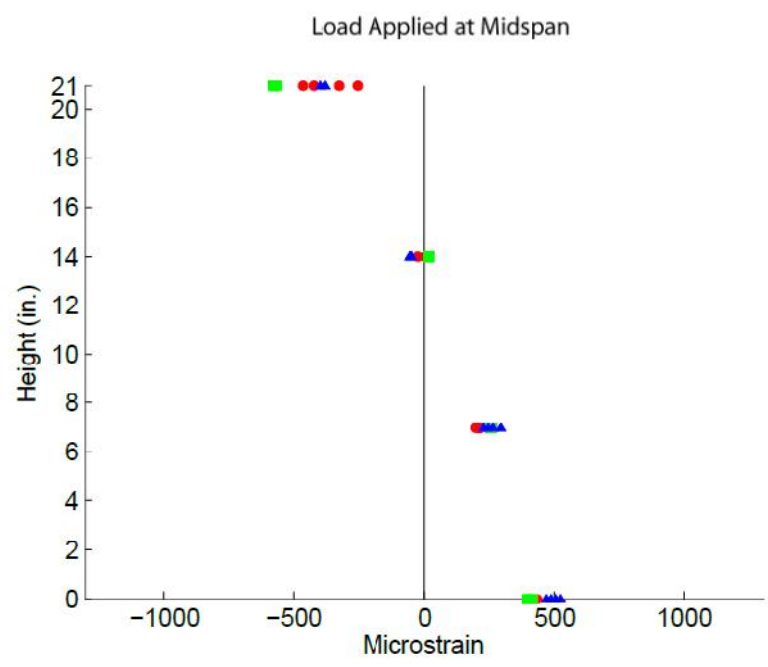


Fig. F-16. Strains at quarter points in the FRP shell of Tide Mill Bridge simulated HCB (copied from Nossdall 2013)

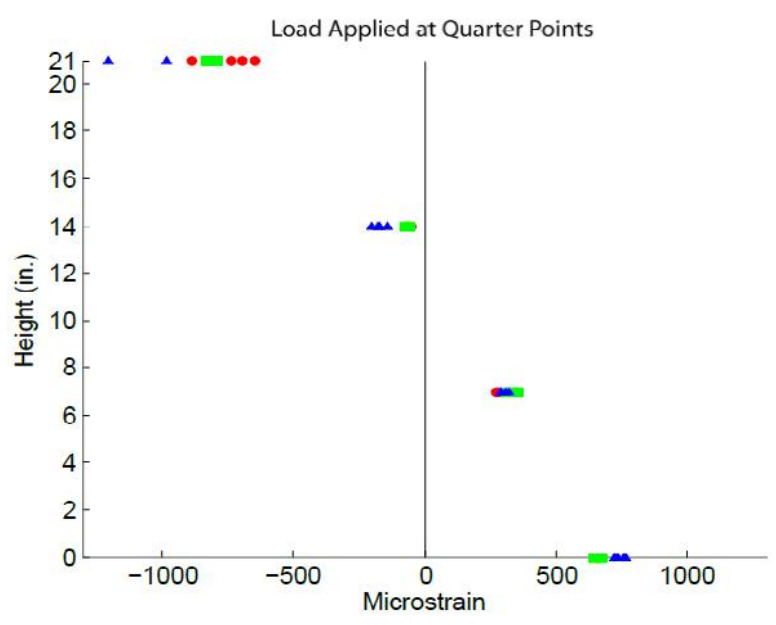


Fig. F-17. Strains at quarter points in the FRP shell of Tide Mill Bridge simulated HCB (copied from Nossdall 2013)

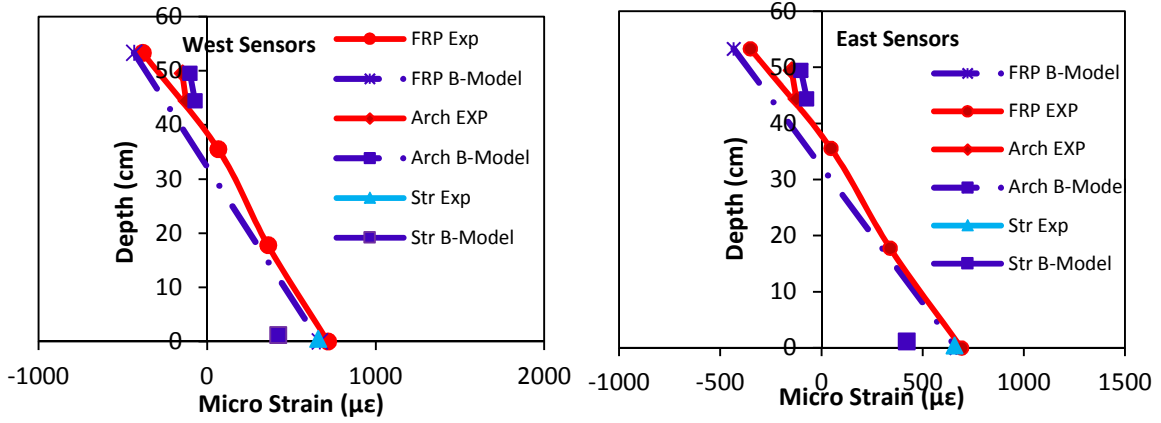


Fig. F-18. Measured strains (Ahsan 2012, Nosdall 2013) and estimated strains (beam model) at the midspan produced by two point-load at the quarter points (West sensors left image & east sensors right image)

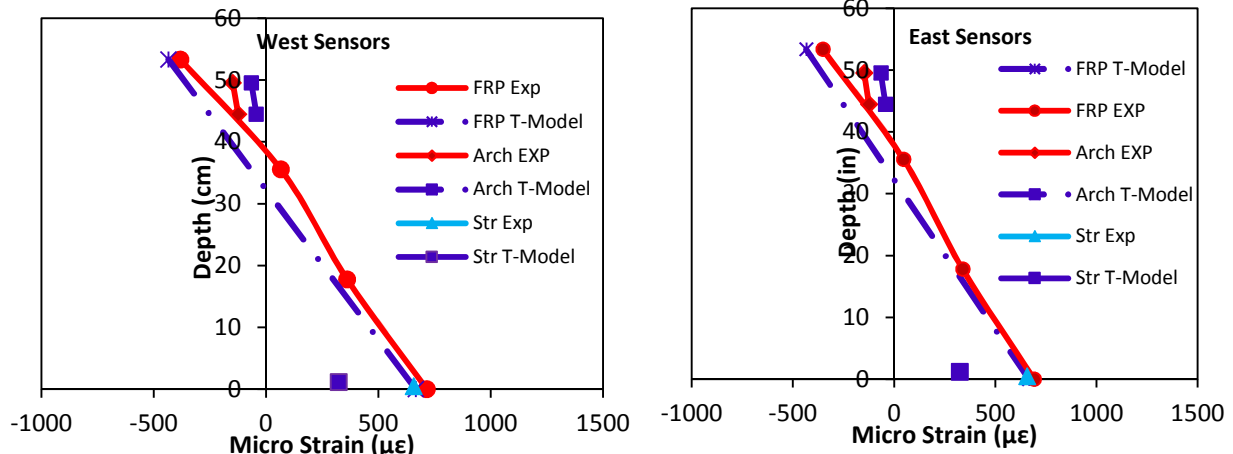


Fig. F-19. Measured strains (Ahsan 2012, Nosdall 2013) and estimated strains (beam model) at the midspan produced by two point-load at the quarter points (West sensors left image & east sensors right image)

Table (F-16) Strains in strands of simply supported B0410 HCB under full distributed load

Element	Measured (μ)	Estimated by Ahsan (Current Method) (μ)	Tie-Model (μ)	Beam-Model (μ)
TF E	-353	N/A	-434	-434
TF W	-382	N/A	-434	-434
BF E	692	N/A	666	666
BF W	716	N/A	666	666
Strand	657	N/A	323	420
Ca T	-148	N/A	-66	-103
Ca B	-124	N/A	-44	-73

Notes:

The arch was found to be susceptible to local buckling under point loads (Ahsan 2012, Nosdall 2013). However, the arch didn't suffer local buckling under the point load at the midspan because it was supported at the mid-span by FRP shell attached between the two webs (Ahsan 2012, Nosdall 2013). The shaded area in Figure F-20 illustrate the area in the concrete arch that was supported by FRP shell. Nosdall (2013) concluded that the FRP shell below the arch worked as flexible spring below the arch. This spring increased the arch stiffness and allowed it to carry higher loads than the normal (Nosdall 2013). This may explain why the proposed beam model underestimated the arch's strains at the mid-span.

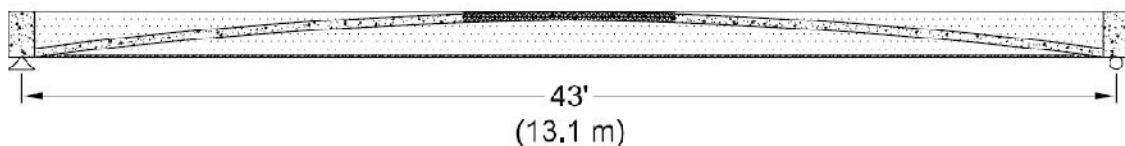


Fig. F-20. The location of the FRP shell below the concrete arch in the Tide Mill Bridge simulated HCB

Figure F-21 display the strains at the bottom of the concrete in non-composite simply supported HCB of B0410. As it is shown similar behavior to what was measured experimentally by Ahsan (2012) was predicted by the FE model.

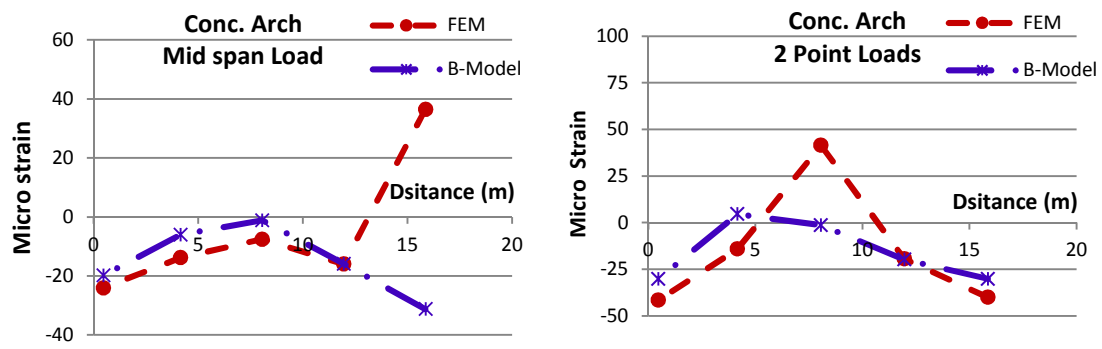


Fig. F-21. Concrete arch's strains under: midspan point load (left image) and two point loads (right image)

Solving the HCB supported on bearing pads by the beam model

The beam model that was proposed for estimating the strains in simply supported HCBs, was used to estimate strains in B0410 HCBs supported on bearing pads. The non-composite and composite HCBs were decoupled into two structural systems. These two systems had the same boundary conditions.

(A) Non-composite HCB (Stage 2)

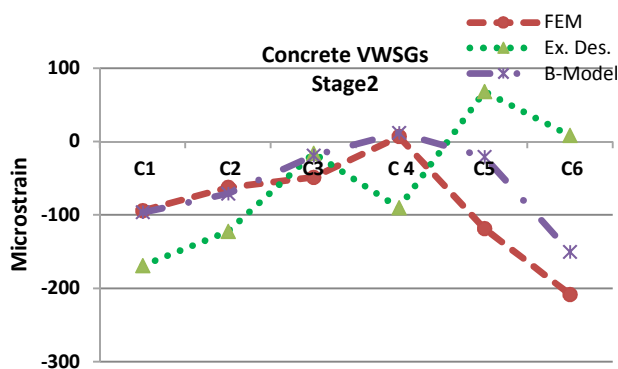


Fig. F-22. Concrete arch's stain under uniform distributed load

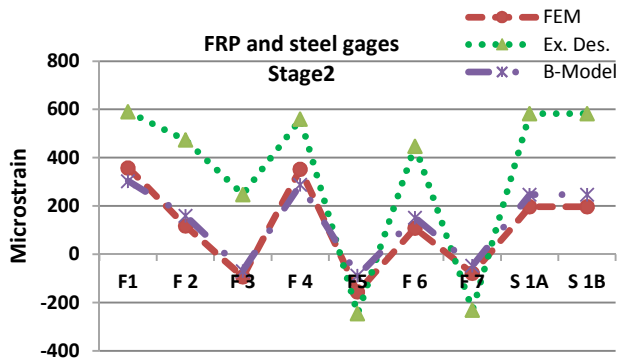


Fig. F-23. FRP shell's stain under uniform distributed load

Table (F-17) HCB2 strains under uniform distributed load

Stage 2	FE model	Mod. Des.	Beam Model
C1	-94	-92	-97
C2	-62	-65	-71
C3	-49	-16	-19
C 4	7	10	12
C5	-118	-23	-21
C6	-208	-153	-150
F1	358	271	304
F 2	119	124	161
F 3	-93	-60	-68
F 4	353	244	290
F5	-155	-127	-88
F 6	109	116	153
F 7	-78	-77	-46
S 1A	197	254	248
S 1B	197	254	248

(B) Composite HCB (Stage 3)

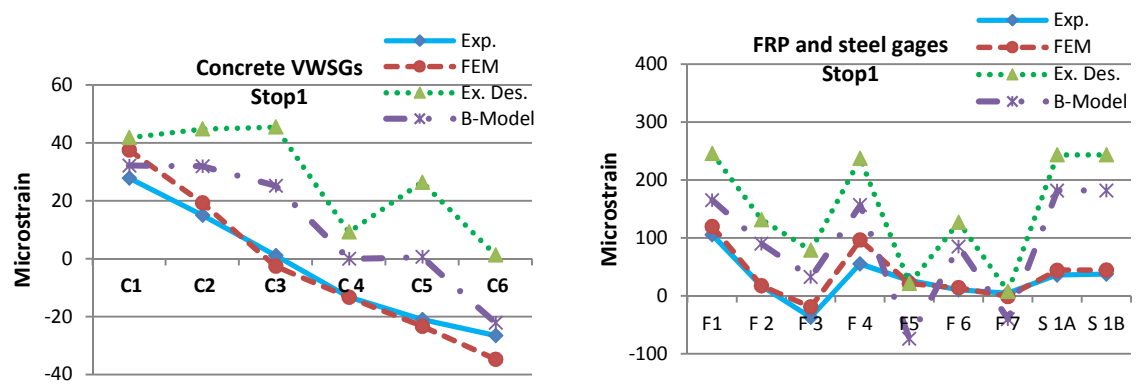


Fig. F-24. HCB2 strains under stop1 loads: Concrete arch (left image)
FRP shell and strands (right image)

Table (F-17) HCB2 strains under uniform distributed load

STOP 1	Experimental	FE model	Modified Des.	Beam Model
C1	28	37	29	32
C2	15	19	29	32
C3	1	-3	24	25
C 4	-13	-13	0	0
C5	-21	-23	1	1
C6	-27	-35	-21	-22
F1	106	120	171	165
F 2	17	18	69	90
F 3	-37	-19	1	32
F 4	55	97	165	157
F5	27	21	15	-74
F 6	11	14	66	85
F 7	4	-1	4	-40
S 1A	36	44	170	182
S 1B	37	45	170	182

APPENDIX G.
MECHANICAL TESTING AND MICROSTRUCTURAL ANALYSIS' RESULTS OF
ENVIROMENTAL EFFECTS ON THE GFRP SHELL

Mechanical Testing Results

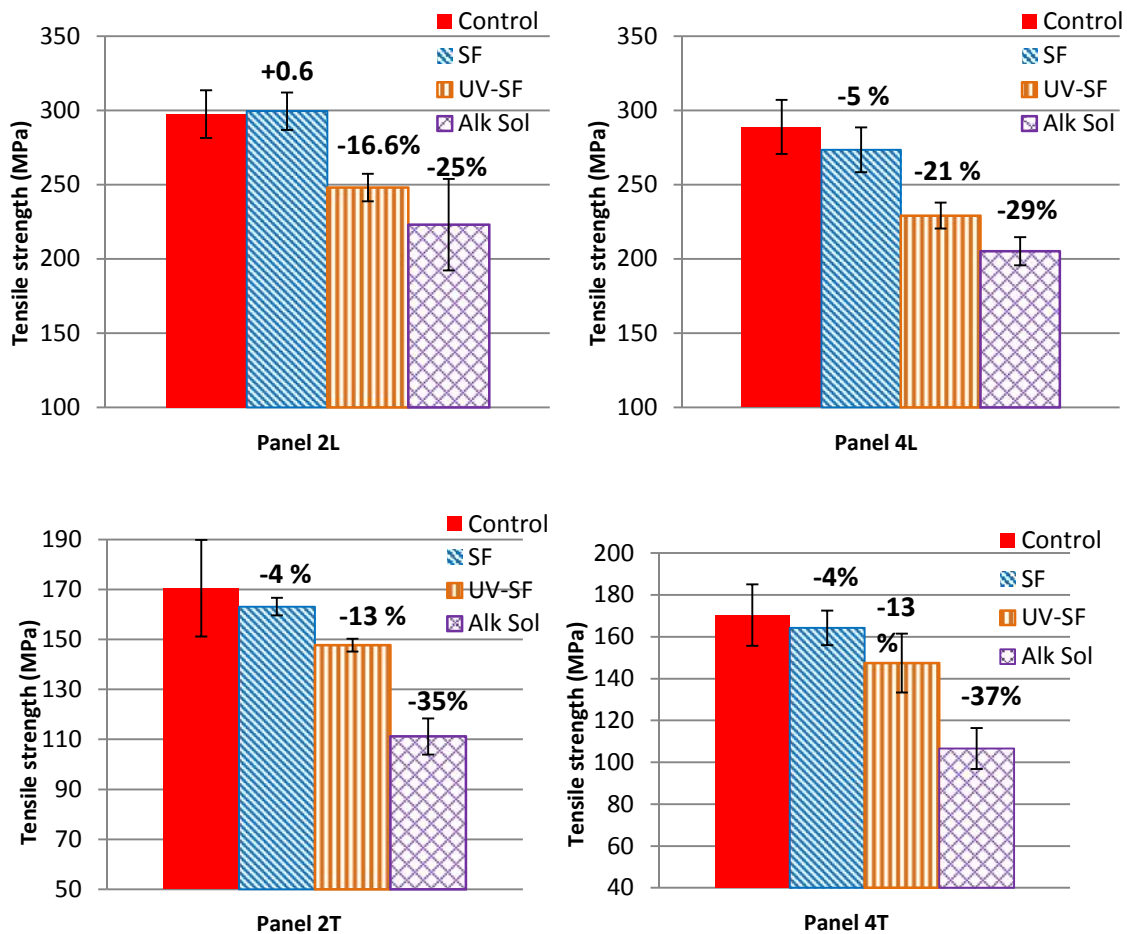


Fig. H-1. Tensile testing results for control and conditioned samples from panels 2 and 4 (written above each bar the percentage of the change in the strength with respect to the control specimens)

Table (H-1) Tensile testing results for (2L and 4L) specimens

Conditioning Regime	Longitudinal direction of Panel 2 (2L)			Longitudinal direction of Panel 4 (4L)		
	Strength (MPa)	Standard dev. (MPa)	COV %	Strength (MPa)	Standard dev.(MPa)	COV %
Unconditioned	298	16	5.4	289	18	6.3
Alk. Sol.	223	31	13.8	205	9	4.6
UV-Salt Fog	248	9	3.7	229	9	3.8
Salt Fog	299	13	4.2	273	15	5.5

Table (H-2) Tensile testing results for (2T and 4T) specimens

Conditioning Regime	Transverse direction of Panel 2 (2T)			Transverse direction of Panel 4 (4T)		
	Strength (MPa)	Standard dev. (Mpa)	COV %	Strength (MPa)	Standard dev.(MPa)	COV %
Unconditioned	171	19	11.3	170	15	8.6
Alk. Sol.	111	7	6.5	107	10	9.2
UV-Salt Fog	148	3	1.7	147	14	9.5
Salt Fog	163	4	2.2	164	8	5.0

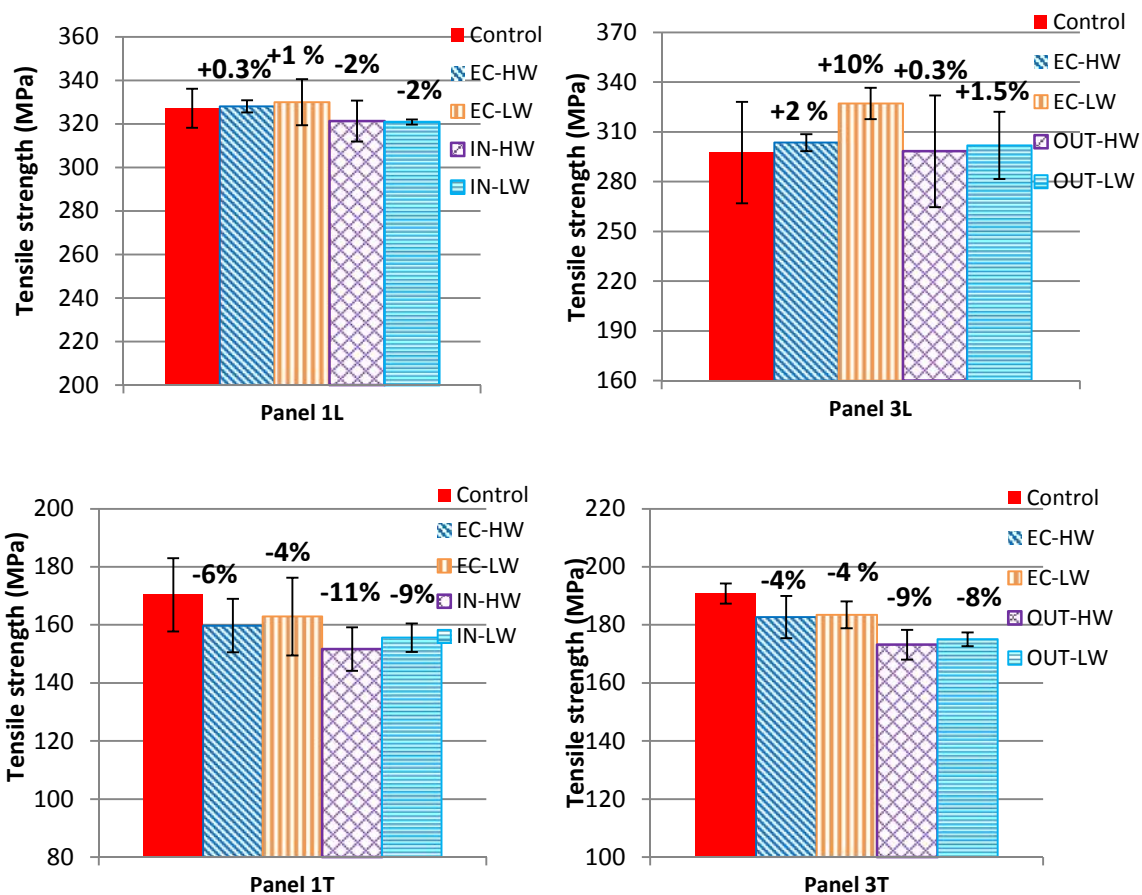


Fig. H-2. Tensile testing results for control and conditioned samples from panels 1 and 3 (written above each bar the percentage of the change in the strength with respect to the control specimens)

Table (H-3) Tensile testing results for (1L and 3L) specimens

Conditioning Regime	Longitudinal direction of Panel 1 (1L)			Longitudinal direction of Panel 3 (3L)		
	Strength (MPa)	Standard dev. (MPa)	COV %	Strength (MPa)	Standard dev.(MPa)	COV %
Unconditioned	327	9	2.7	298	31	10.3
In-HW	321	9	2.9	298	34	11.3
In-LW	321	1	0.4	302	20	6.7
EC-HW	328	3	0.9	304	5	1.7
EC-LW	330	11	3.2	327	10	2.9

Table (H-4) Tensile testing results for (1T and 3T) specimens

Conditioning Regime	Transvers direction of Panel 1 (1T)			Transvers direction of Panel 3 (3T)		
	Strength (MPa)	Standard dev. (MPa)	COV %	Strength (MPa)	Standard dev.(MPa)	COV %
Unconditioned	170	13	7.4	191	3	1.8
In-HW	152	7	4.9	173	5	3.0
In-LW	156	5	3.2	175	2	1.3
EC-HW	160	9	5.7	183	7	4.0
EC-LW	163	13	8.2	183	5	2.5

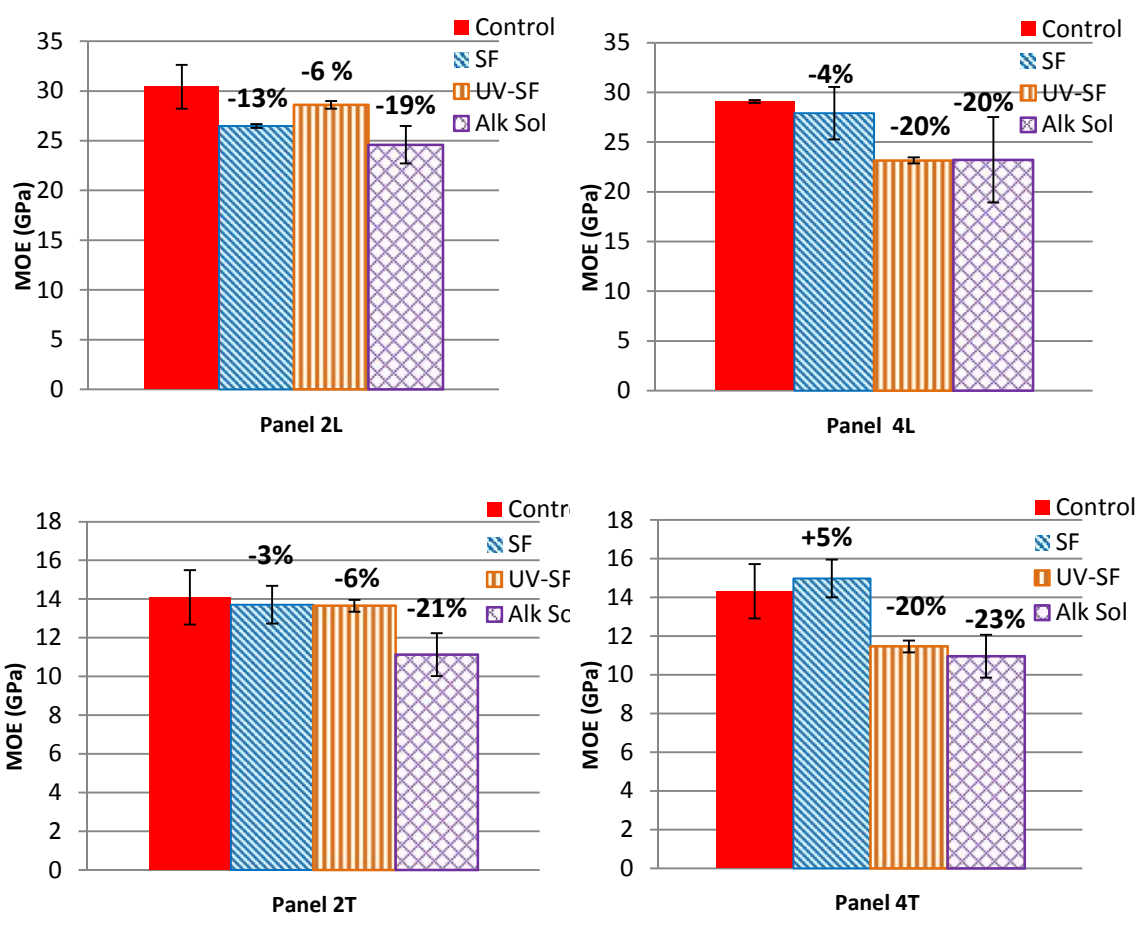


Fig. H-3. Modulus of elasticity (MOE) results for control and conditioned samples from panels 2 and 4 (written above each bar the percentage of the change in the MOE with respect to the control specimens)

Table (H-5) Modulus of elasticity results for (2L and 4L) specimens

Conditioning Regime	Longitudinal direction of Panel 2 (2L)			Longitudinal direction of Panel 4 (4L)		
	MOE (GPa)	Standard dev. (GPa)	COV %	MOE (GPa)	Standard dev. (GPa)	COV %
Unconditioned	30.4	2.2	7	29.1	0.1	0
Alk. Sol.	24.6	1.9	8	23.2	4.3	19
UV-Salt Fog	28.6	0.4	1	23.2	0.3	1
Salt Fog	26.5	0.2	1	27.9	2.6	9

Table (H-6) Modulus of elasticity results for (2T and 4T) specimens

Conditioning Regime	Transverse direction of Panel 2 (2T)			Transverse direction of Panel 4 (4T)		
	MOE (GPa)	Standard dev. (GPa)	COV %	MOE (GPa)	Standard dev. (GPa)	COV %
Unconditioned	14.1	1.4	10	14.3	0.8	5
Alk. Sol.	11.1	1.1	10	11.0	0.9	8
UV-Salt Fog	13.7	0.2	2	11.5	2.0	18
Salt Fog	13.7	1.0	7	15.0	1.8	12

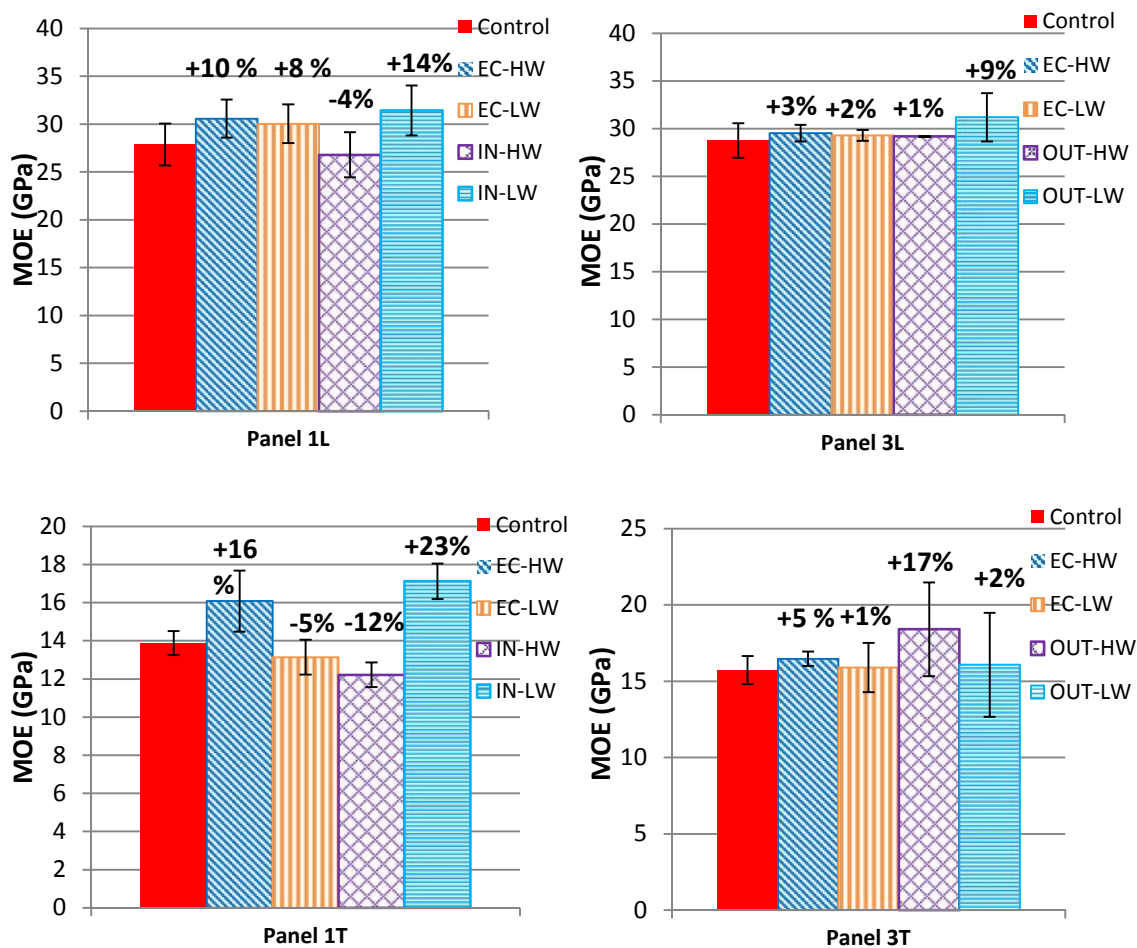


Fig. H-4. Modulus of elasticity (MOE) results for control and conditioned samples from panels 1 and 3 (written above each bar the percentage of the change in the MOE with respect to the control specimens)

Table (H-7) Modulus of elasticity results for (1L and 3L) specimens

Conditioning Regime	Longitudinal direction of Panel 1 (1L)			Longitudinal direction of Panel 3 (3L)		
	Strength (GPa)	Standard dev. (Gpa)	COV %	Strength (GPa)	Standard dev. (Gpa)	COV %
Unconditioned	28	2.2	7.9	29	1.8	6.3
In-HW	27	2.4	8.8	29	0.0	0.2
In-LW	31	2.6	8.3	31	2.5	8.1
EC-HW	31	2.0	6.5	30	0.9	2.9
EC-LW	30	2.0	6.8	29	0.6	2.0

Table (H-8) Modulus of elasticity results for (1T and 3T) specimens

Conditioning Regime	Transverse direction of Panel 1 (1T)			Transverse direction of Panel 3 (3T)		
	Strength (GPa)	Standard dev. (Gpa)	COV %	Strength (GPa)	Standard dev. (Gpa)	COV %
Unconditioned	14	0.6	4.6	16	0.9	5.9
In-HW	12	0.6	5.3	18	3.1	16.7
In-LW	17	0.9	5.5	16	3.4	21.2
EC-HW	16	1.6	10.0	16	0.5	2.9
EC-LW	13	0.9	7.0	16	1.6	10.1

Tensile Strength versus Modulus of Elasticity Changes

All of the exposure regimes but the alkali and the UV-SF aging regimes resulted in small reductions in the tensile strength. No correlation between the ultimate tensile strength and the MOE's changes was observed, during these conditioning regimes. Sometimes, when the tensile strength decreased, the MOE increased and vice versa. These regimes resulted in very localized and limited damages in the fibers and/or fiber-matrix interface. The matrix cracking was also rare. The MOE is less sensitive to these localized damages than the tensile strength.

The fiber and the interface deteriorations spread in the first lamina, during the alkali and the UV-SF exposure regimes, resulting in significant reductions in the ultimate tensile strength. This spread resulted in better agreement between the tensile strength and the MOE's changes. The MOE always decreased, during these two regimes, but to less extent than the tensile strength. This is attributed to the damage spread into the first ply it was

localized around the fibers making the MOE less sensitive to the damage. It is also known that the alkali attack leads to fibers embrittlement due to the nucleation of sodium hydroxide on the fibers' surfaces (Sonawala and Spontak, 1996; Benmokrane et al., 2002). This embrittlement may have contributed to the less MOE reduction in the case of the alkali attack.

Generally, the reduction in the strength under environmental effects results from deficiency in the stress transfer between the fiber and the matrix due to localized damages. Since, the MOE is less sensitive to this localized effects, it is not a good indicator to the deleterious effects of aging regimes. The change in the strength gives more clear insight to the environmental effects. When the aging regime causes damage mainly to the fiber and/or the interface, the change in the tensile strength may be a good indicator to the extent of the damage. When the environmental attack causes damage mainly to the resin, the change in the shear or torsion strengths may be good indicators to the extent of the damage. When the environmental attack causes damage to fiber, interface and the resin, studying the change in both the flexural and shear strengths may provide better insight to the deleterious effects of the aging regime.

Sample preparation for SEM

1. Conditioned and unconditioned specimens were cut into 0.5" X 0.5 " samples using a diamond saw.
2. The samples were mounted into plastic moulds with a mixed epoxy prepared by mixing two parts of VariDur powder to one part of VariDur liquid (Figure H-1).



Fig. H-5. Samples' mounting with Varidur epoxy

3. The samples were unmolded and then polished by 240, 400, 600, 800, 1200 grit sand papers with a mechanical polisher (Figure H-2).



Fig. H-6. Samples' polishing via mechanical polisher

4. The samples were polished by 3 and 1 micron monocrystalline diamond solution.



Fig. H-7. Polished samples by 1 micron monocrystalline diamond solution.

5. Finally, the samples were coated with Gold palladium via the sputter coater device illustrated in Figure (H-4).



Fig. H-8. Sputter Coater Device

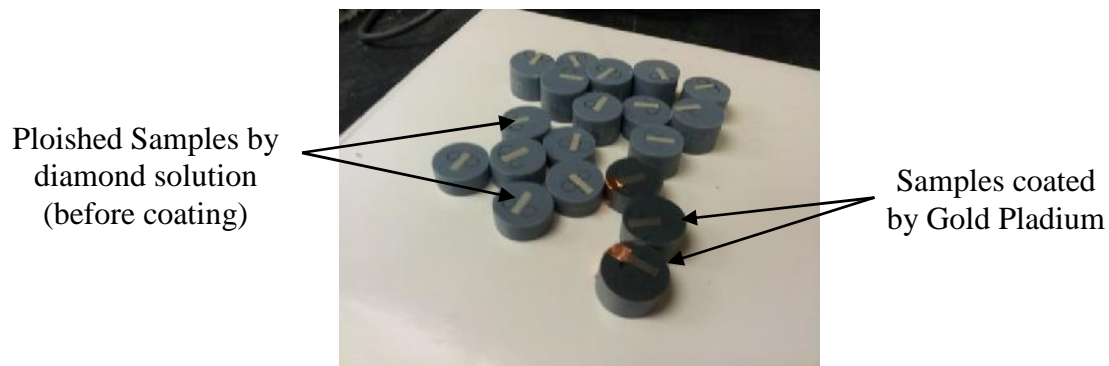


Fig. H-9. Coated Samples by Gold Pladium

SEM Results

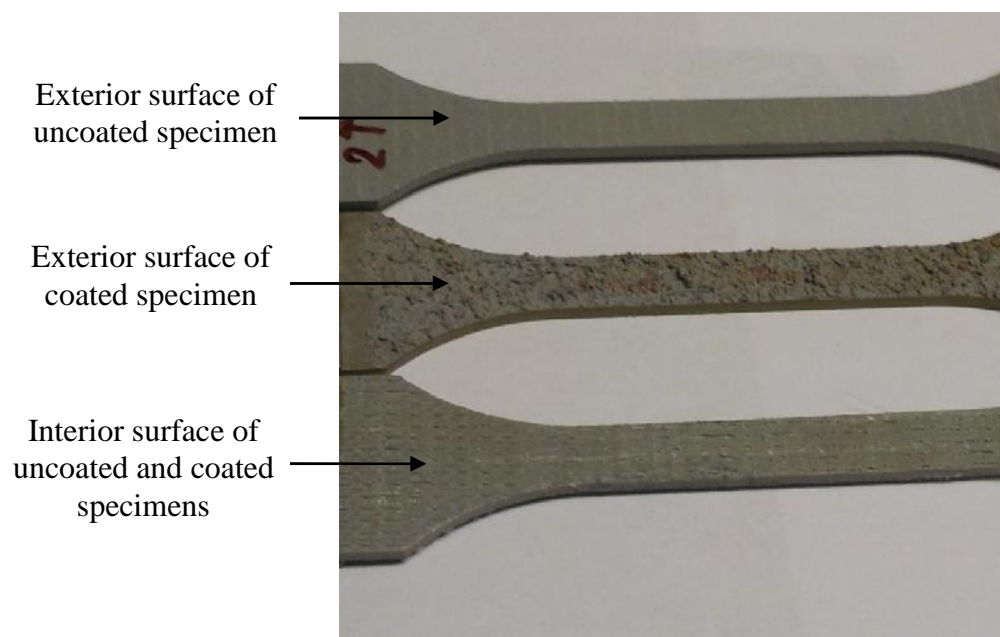


Fig. H-10. Coated an uncoated GFRP

Control specimens results

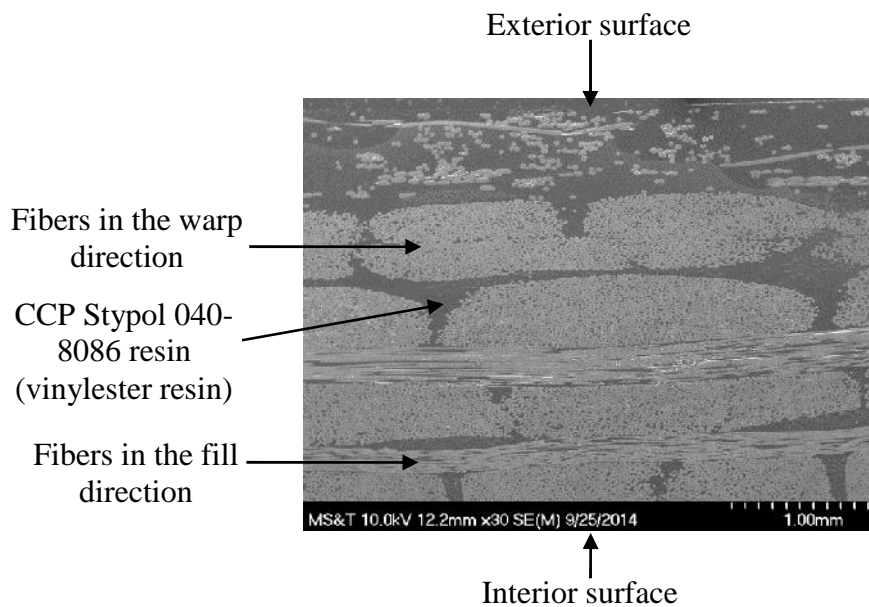


Fig. H-11. SEM micrograph in longitudinal specimen reveals the laminate composition (X30 = magnified 30 times)

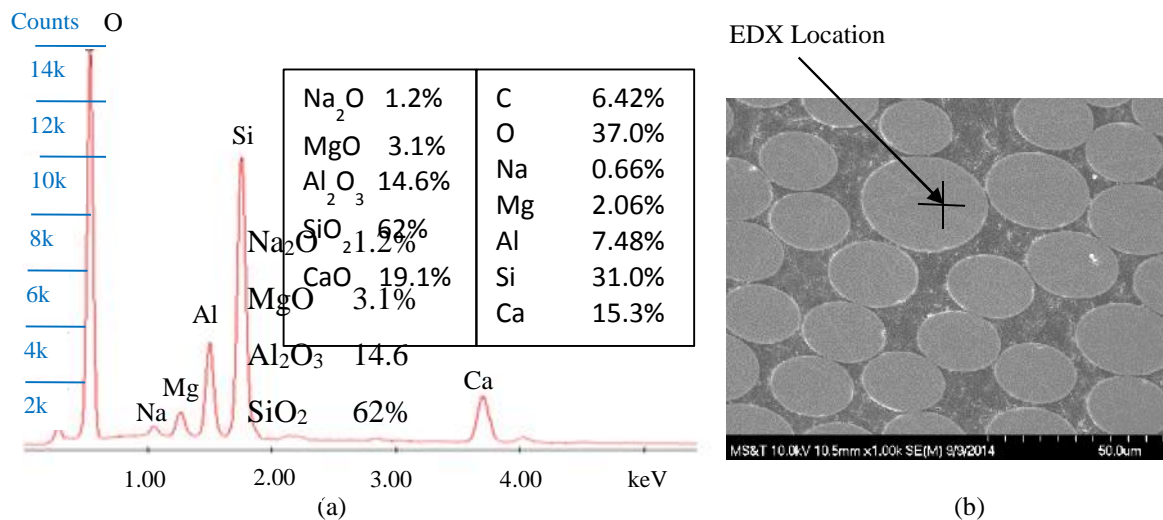


Fig. H-12. Control specimen in the transverse direction of panel 4 (4T-C) (a) Elemental analysis by EDX(b) Surface morphology by SEM (X1000 = magnified 1000 times)

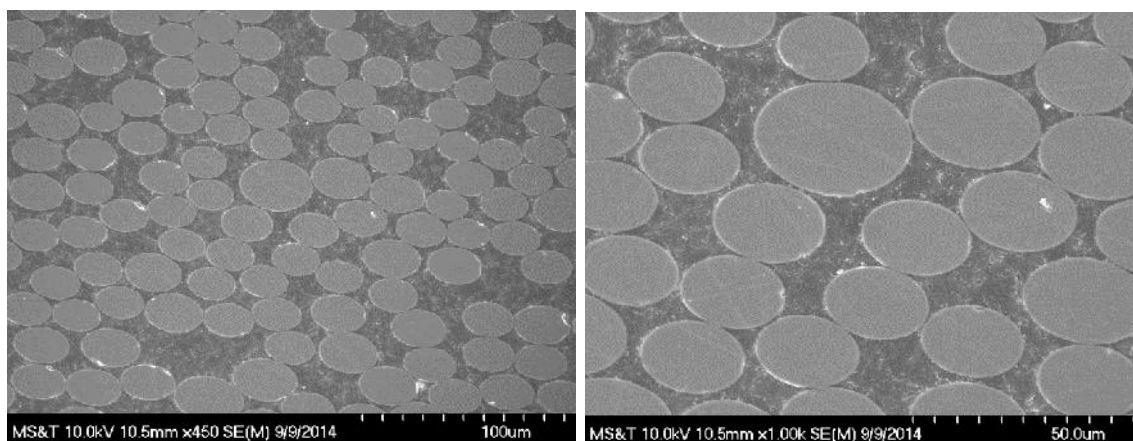


Fig. H-13. Images show unconditioned fibers (X450 left image, X1000 right image)

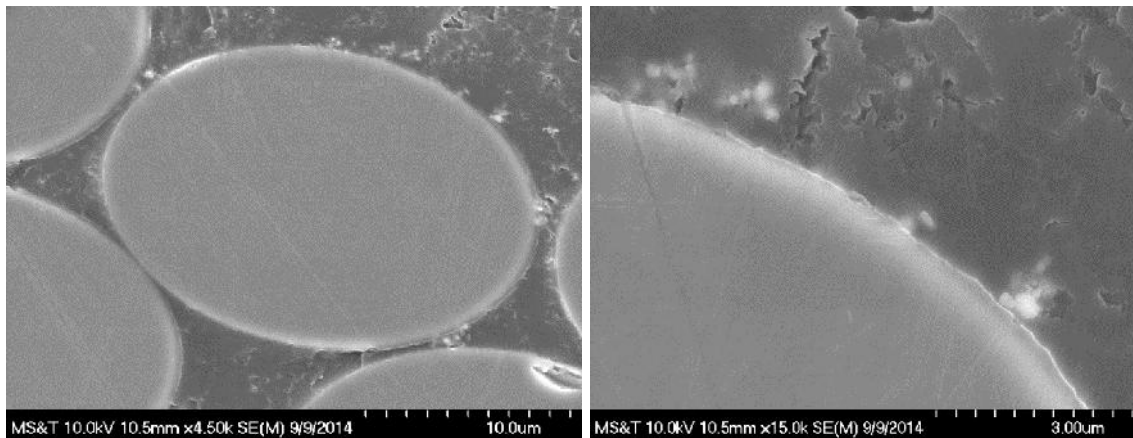


Fig. H-14. Images show undeteriorated fiber-matrix interphase (X4500 left image, X15000 right image)

Alkali (Alk) exposure Results



Fig. H-15. GFRP specimens immersed in Alkaline Solution with pH = 13.25

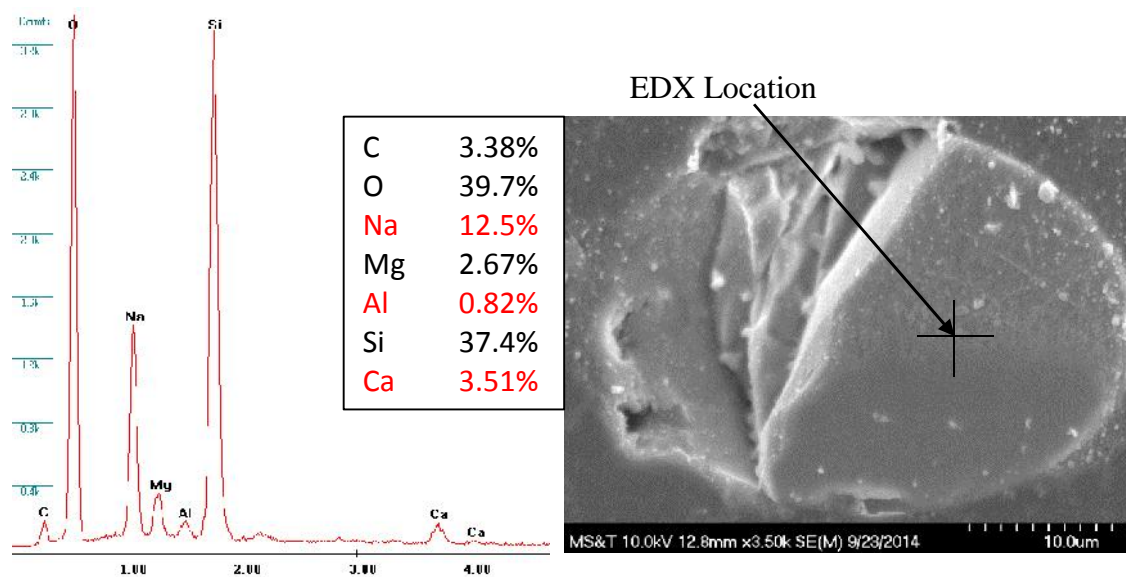


Fig. H-16. Fiber damage in 4L- Alk specimen (a) Elemental analysis by EDX (b) Surface morphology by SEM (X3500)

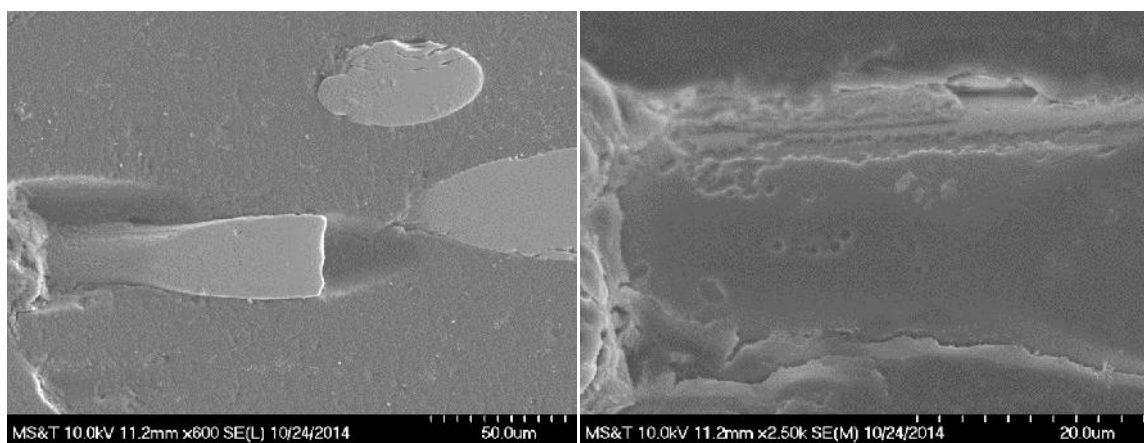


Fig. H-17. Images show fiber damage, interface deterioration, and fiber notching in 4T-Alk specimen (X600, left image and X2500, right image)

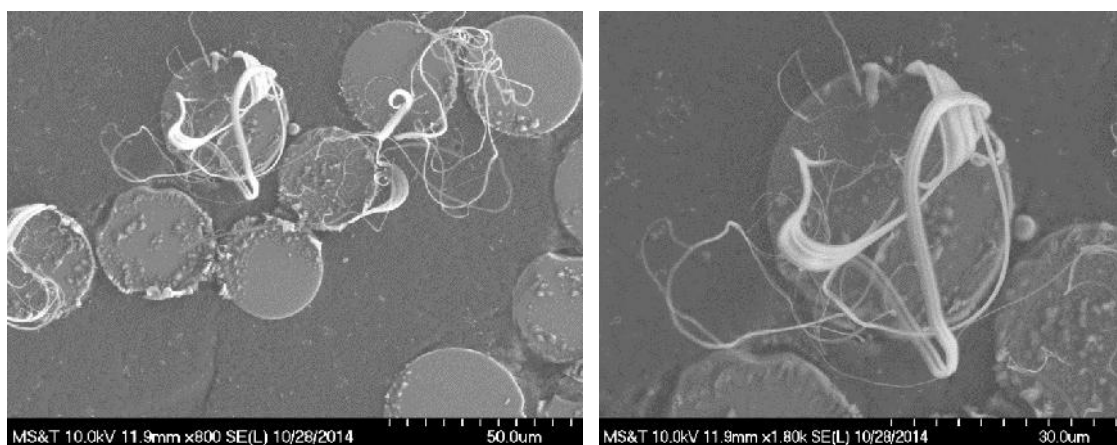


Fig. H-18. Images show: chemical reaction between the alkali solution and the coupling agent or formation of water glass (Na_2SiO_3) produced by the alkali attack

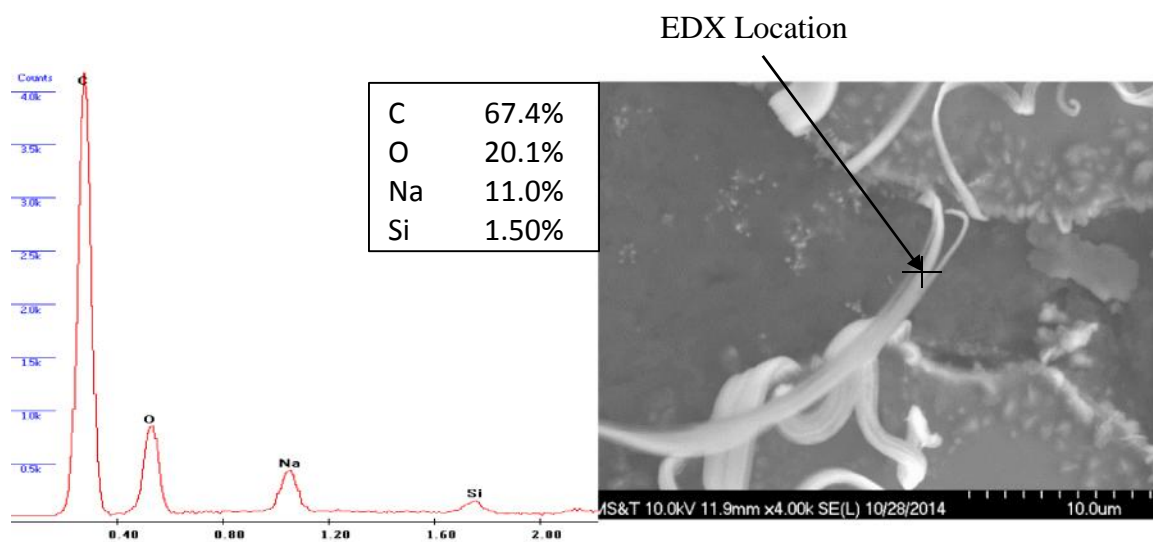


Fig. H-19. 4L-Alk specimen (a) Elemental analysis by EDX (b) Surface morphology by SEM (X4000)

Salt fog (SF) exposure images



Fig. H-20. Slat fog apparatus (Left image)
GFRP specimen exposed to salt fog (Right image)

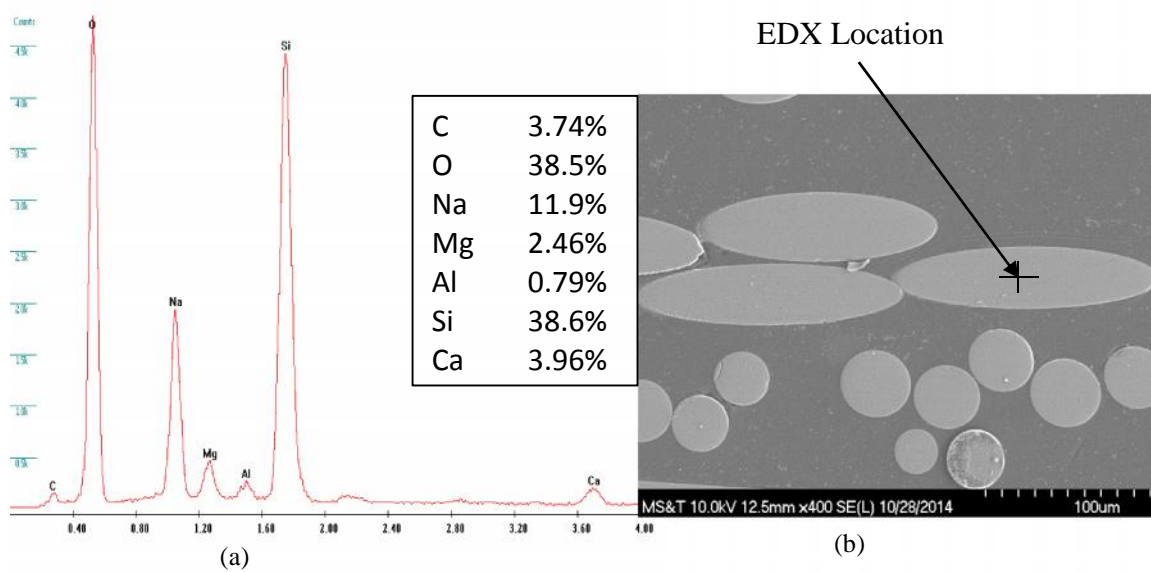


Fig. H-21. Attacked fibers 4L-SF (a) Elemental analysis by EDX (b) Surface morphology by SEM (X400)

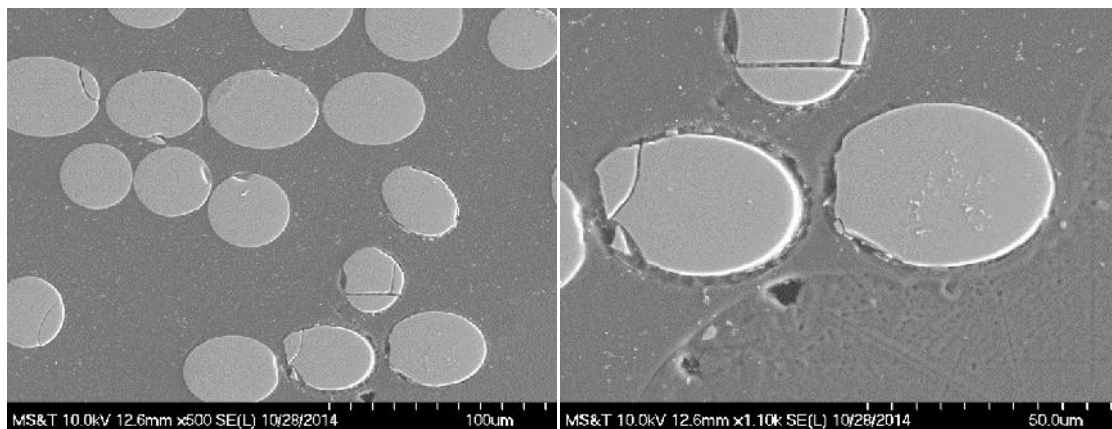


Fig. H-22. Fiber damage and interface debonding in 4L-SF (X500 left image, X1100 right image)

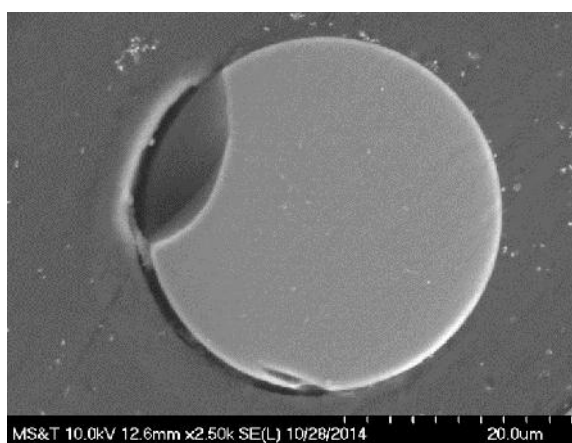


Fig. H-23. Interface debonding in 4L-SF

UV and salt fog (UV-SF) exposure images



Fig. H-24. UV-irradiation apparatus (Left image)
GFRP specimen exposed to UV-irradiation (Right image)

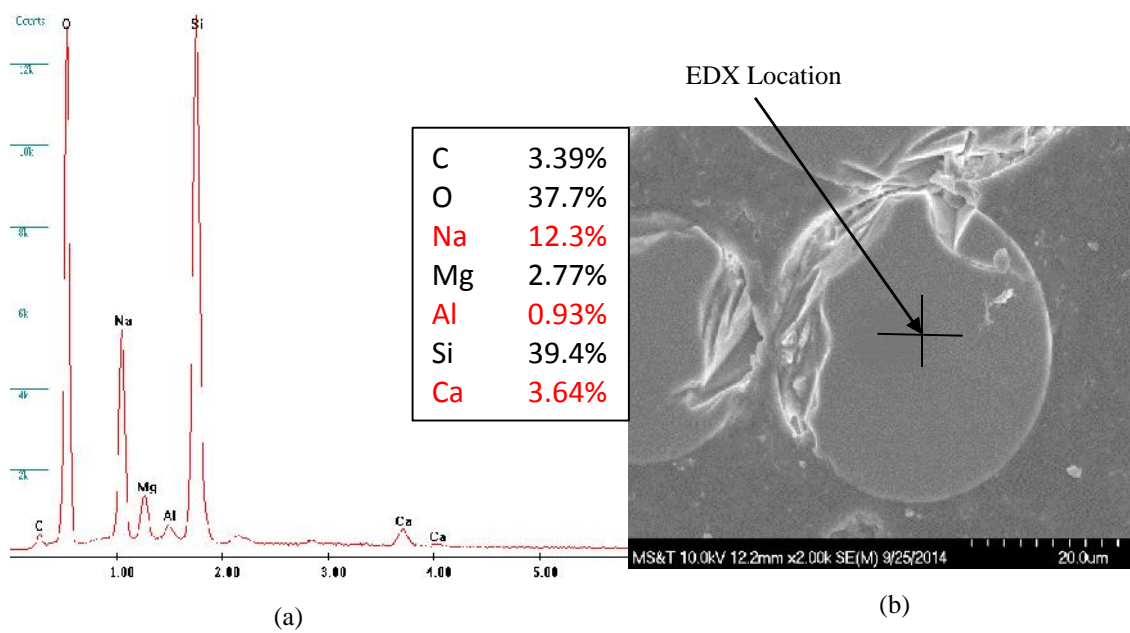


Fig. H-25. Deteriorated fibers 4L-UV-SF (a) Elemental analysis by EDX (b) Surface morphology by SEM (X1000 = magnified 1000 times)

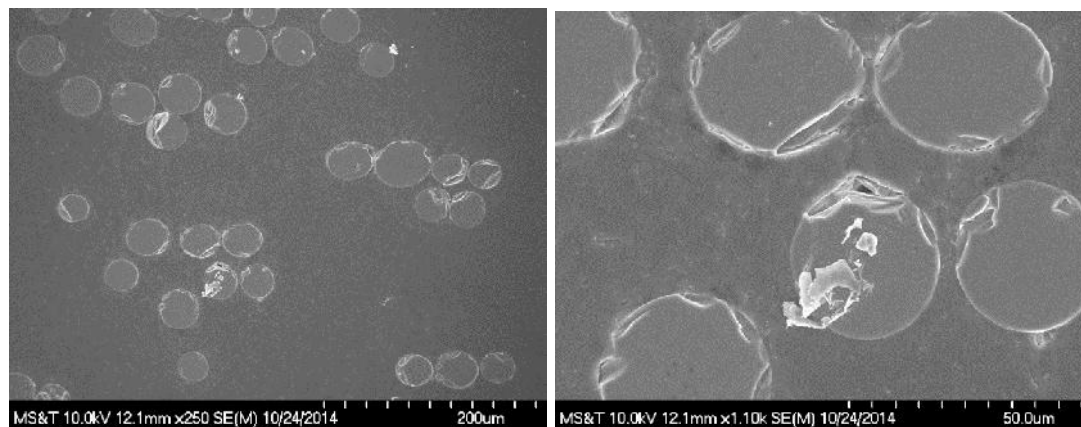


Fig. H-26. Deteriorated fibers 4L-UV-SF (X250 left image, X1100 right image)

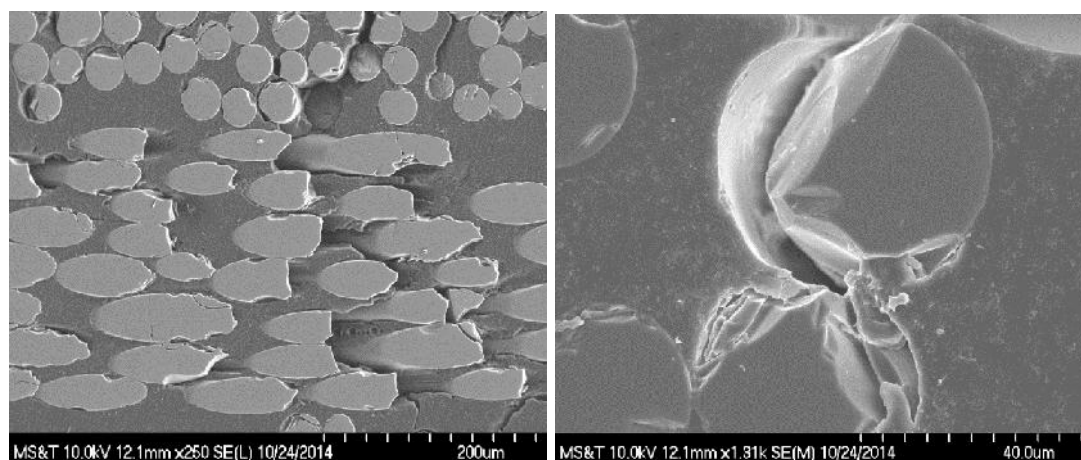


Fig. H-27. Deteriorated fibers and interphases 4L-UV-SF (X250 left image, X1300 right image)

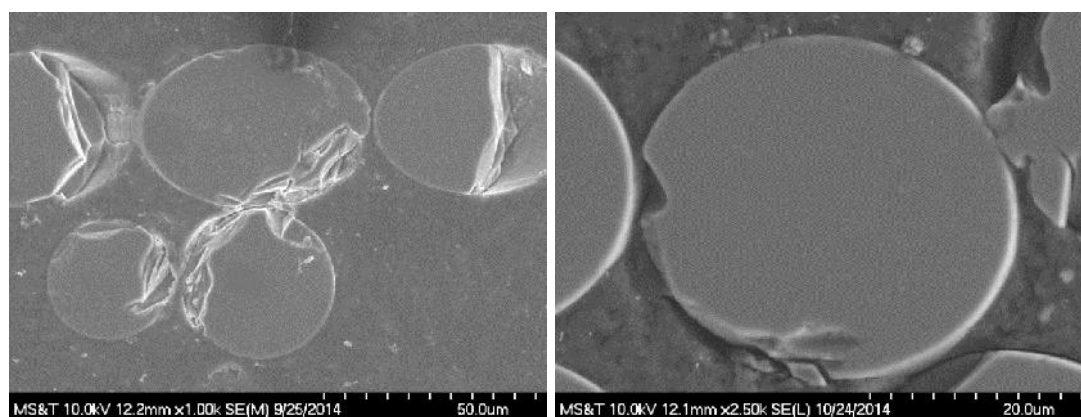


Fig. H-28. Deteriorated fibers and interphases 4L-UV-SF (X1000 left image, X2500 right image)

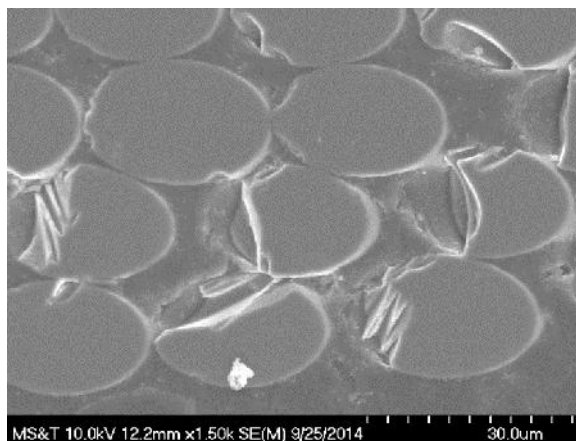


Fig. H-27. Undeteriorated fibers 4L-UV-SF, damage was produced by polishing as was clarified by the EDX analysis

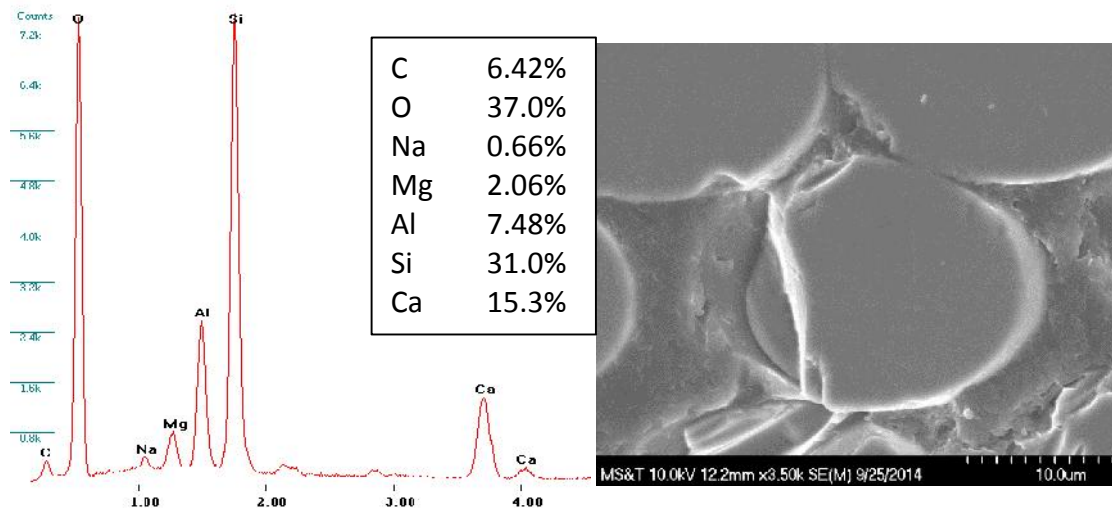


Fig. H-27. Undeteriorated fibers 4L-UV-SF, (EDX analysis, left image and SEM image, right image)

Sustained stresses exposure images



Fig. H-28. Sustained stresses together with natural thermal cycles (left image) and computer controlled thermal cycles (right image)



Fig. H-29. Sustained stresses in controlled room temperature

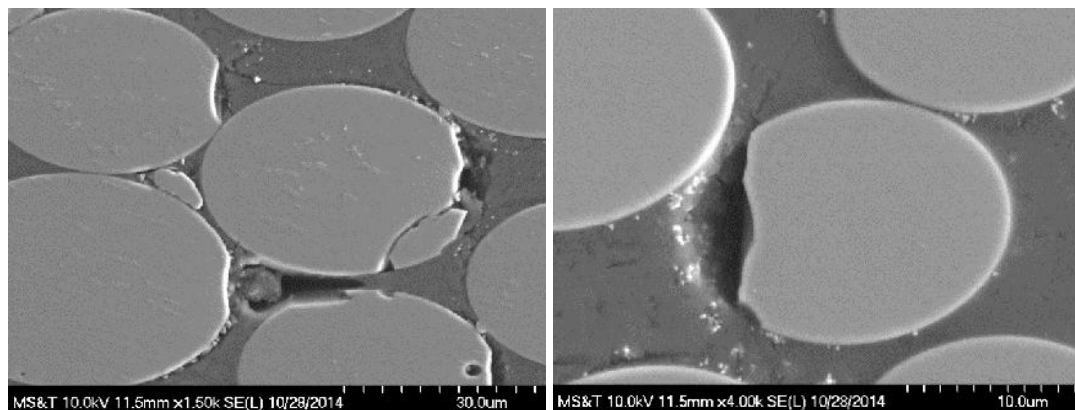


Fig. H-30. Fiber damage and interface debonding in specimens subjected to sustained stresses in control indoor weathering (1T-IN-HW) (X1500, left image and X4000, right image)

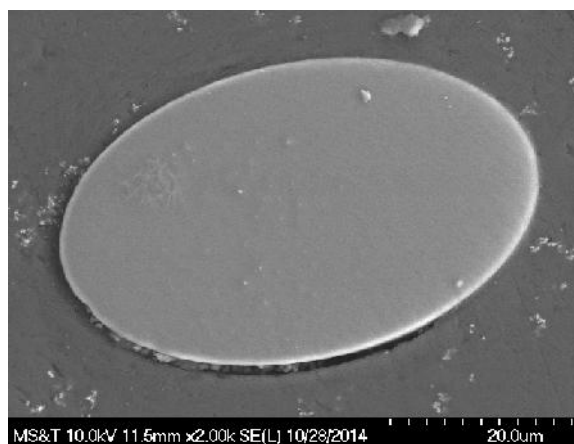


Fig. H-31. Interface debonding in specimens subjected to sustained stresses in control indoor (1T-IN-HW) (X1500)

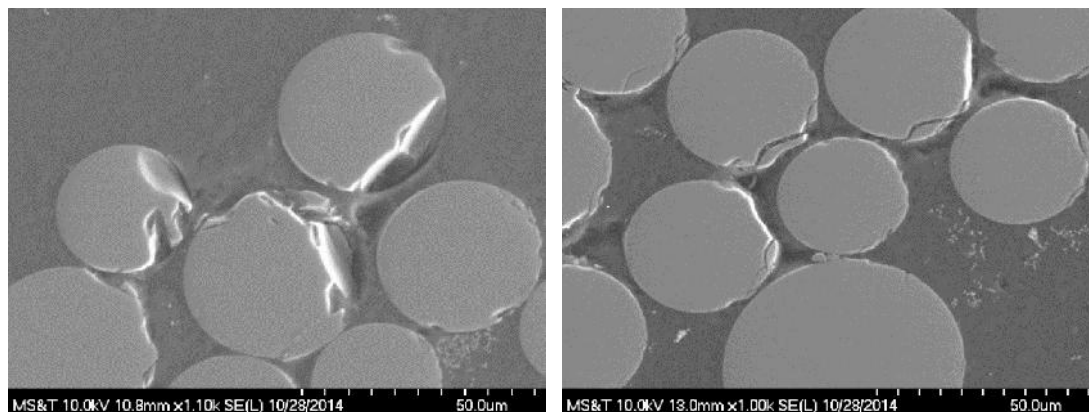


Fig. H-32. Fiber damage and interface debonding in specimens subjected to sustained stresses in outdoor weathering (3T-OUT-HW) (X1100, left image and X1000 right image)

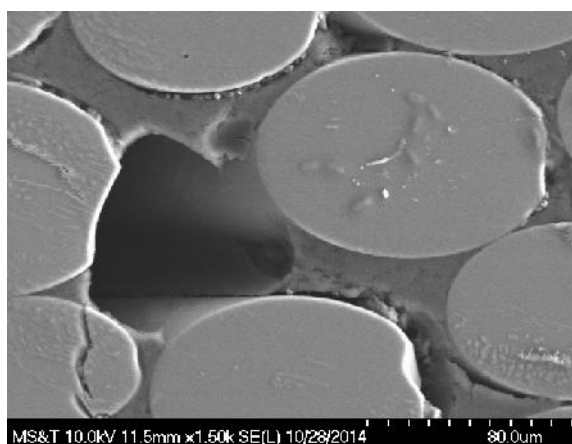


Fig. H-33. Interface debonding in specimens subjected to sustained stresses in outdoor weathering (3T-OUT-HW) (X1500)

Optical Microscope and Camera Images

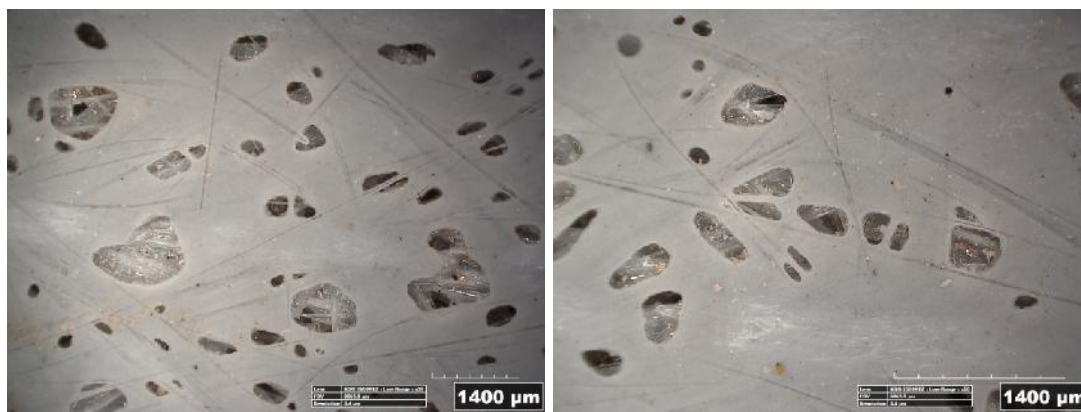


Fig. H-34. Existing voids in unconditioned specimens' exterior surface



Fig. H-35. Existing voids in unconditioned specimens' exterior surface



Fig. H-36. Existing voids in unconditioned specimens' interior surface

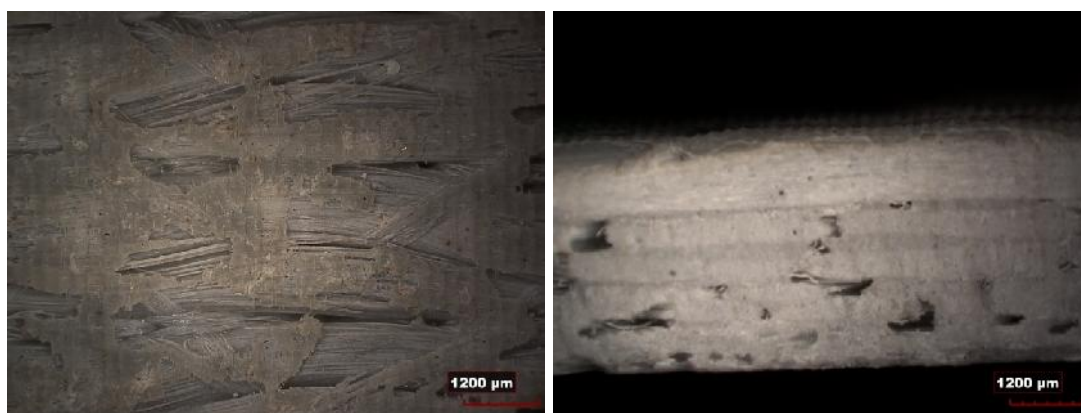


Fig. H-37. Existing voids in unconditioned specimens' interior surface (left image) and side surface (right image)



Fig. H-38. Camera image shows the voids on the exterior surface of 2L-Alk specimen

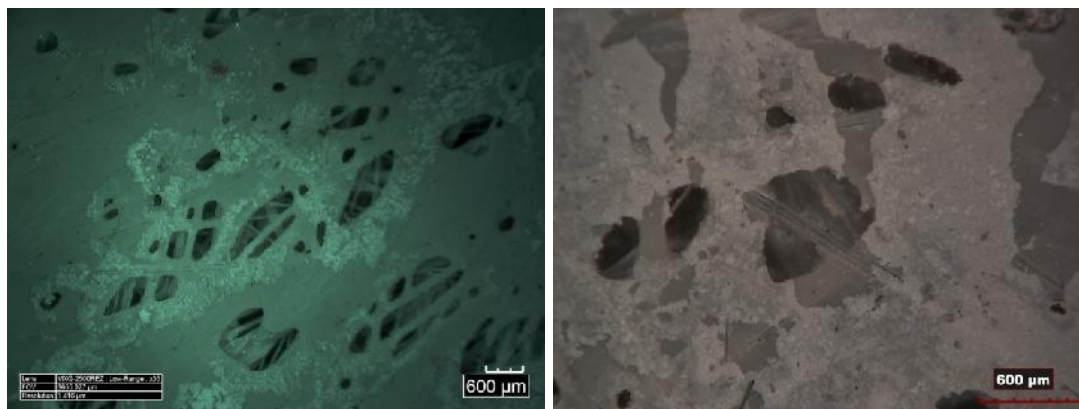


Fig. H-39. NaCl attacked 2T-SF specimen's fibers (left image) and NaoH attacked 2T-Alk specimen's fibers (right image) through the existing voids

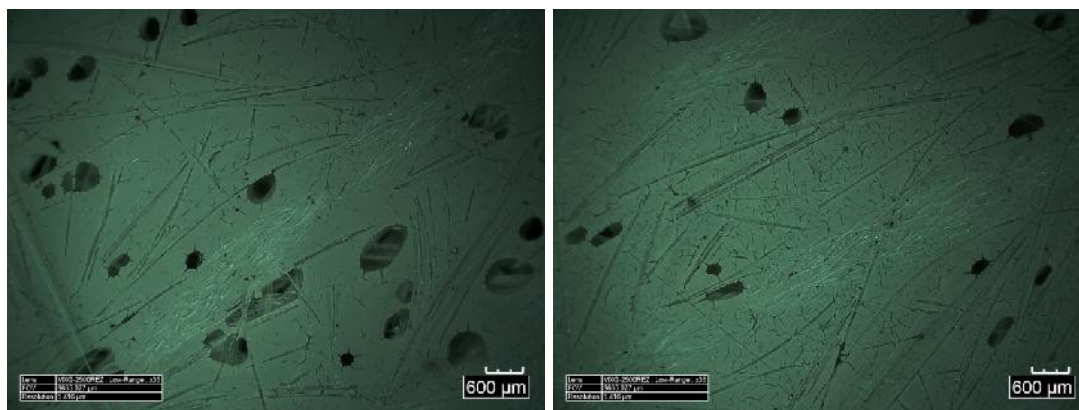


Fig. H-40. Formation of microcracks (2-UV) after 4 months of exposure to UV-irradiation

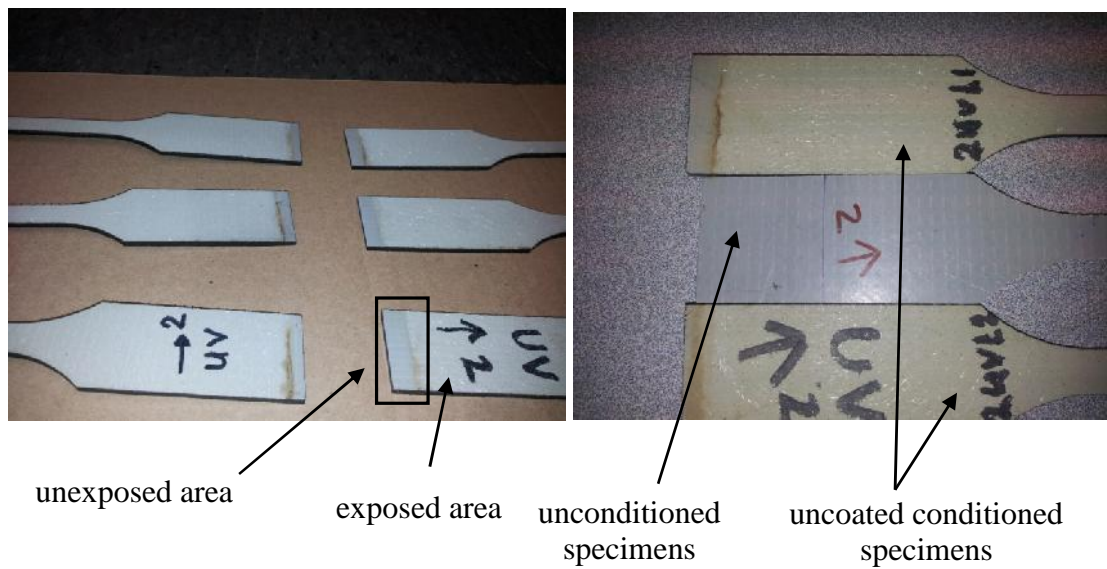


Fig. H-41. Discoloration of uncoated specimens (2-UV) after 2 months (left image) and 4 months (right image) of exposure to UV-irradiation

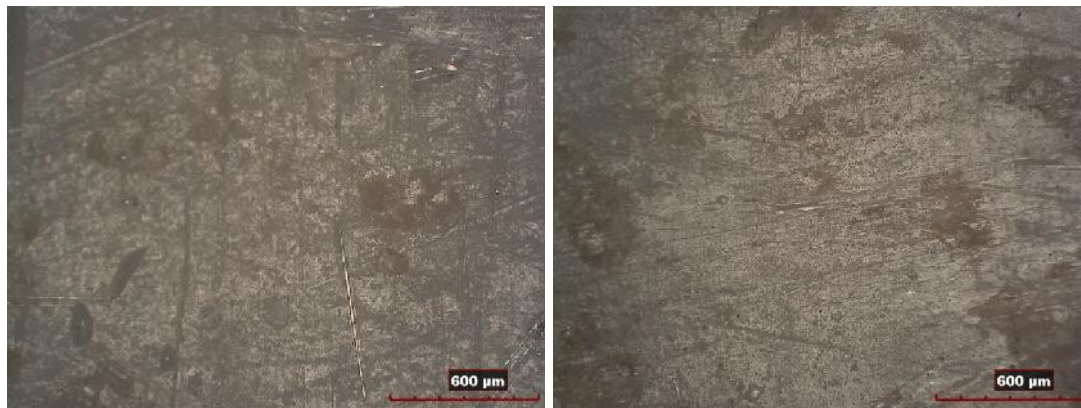


Fig. H-42. No cracks were formed in coated specimens (4-UV-SF) after 4 months exposure to UV-irradiation

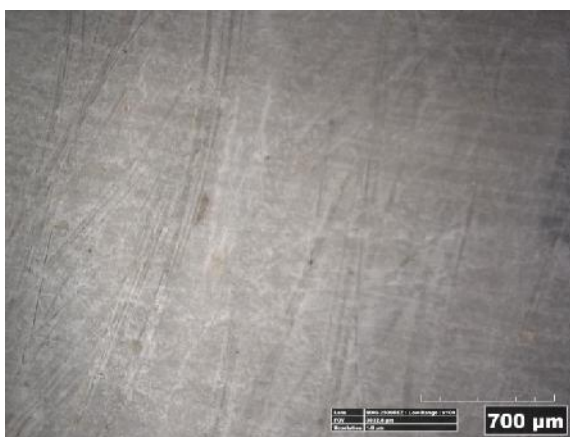


Fig. H-43. No cracks were formed in a specimen (1T-EC-LW) exposed to thermal cycles in the environmental chamber

Table (H-9) FTIR Test Results

Specimen		OH/CH	Average
1T-C	1T-C-1	0.77	0.79
	1T-C-2	0.83	
	1T-C-3	0.88	
	1T-C-4	0.69	
1T-IN-HW	1T-IN-HW-1	0.75	0.79
	1T-IN-HW-2	0.79	
	1T-IN-HW-3	0.82	
	1T-IN-HW-4	0.78	
3L-C	3L-C-1	0.76	0.77
	3L-C-2	0.87	
	3L-C-3	0.69	
3L-EC-LW	3L-EC-LW-1	0.79	0.77
	3L-EC-LW-2	0.76	
	3L-EC-LW-3	0.76	
	3L-EC-LW-4	0.75	
3T-OUT-HW	3T-OUT-HW-1	0.66	0.77
	3T-OUT-HW-2	0.87	
	3T-OUT-HW-3	0.77	

Continue Table (H-9) FTIR Test
Results

Specimen		OH/CH	Average
4L-C	4L-C-1	0.85	0.79
	4L-C-2	0.8	
	4L-C-3	0.72	
	4L-C-4	0.84	
	4L-C-5	0.72	
4L-Alk	4L-Alk-1	0.72	0.72
	4L-Alk-2	0.72	
4L-UVSF	4L-UVSF-1	0.83	0.82
	4L-UVSF-2	0.85	
	4L-UVSF-3	0.8	
	4L-UVSF-4	0.79	
4L-SF	4L-SF-1	0.77	0.78
	4L-SF-2	0.79	
	4L-SF-3	0.77	
2L-UVSF	2L-UVSF-1	0.88	0.86
	2L-UVSF-3	0.84	
	2L-UVSF-4	0.87	
4T-Alk	4T-Alk-1	0.78	0.78
	4T-Alk-2	0.77	
	4T-Alk-3	0.8	

Sample of the FTIR Test Curves

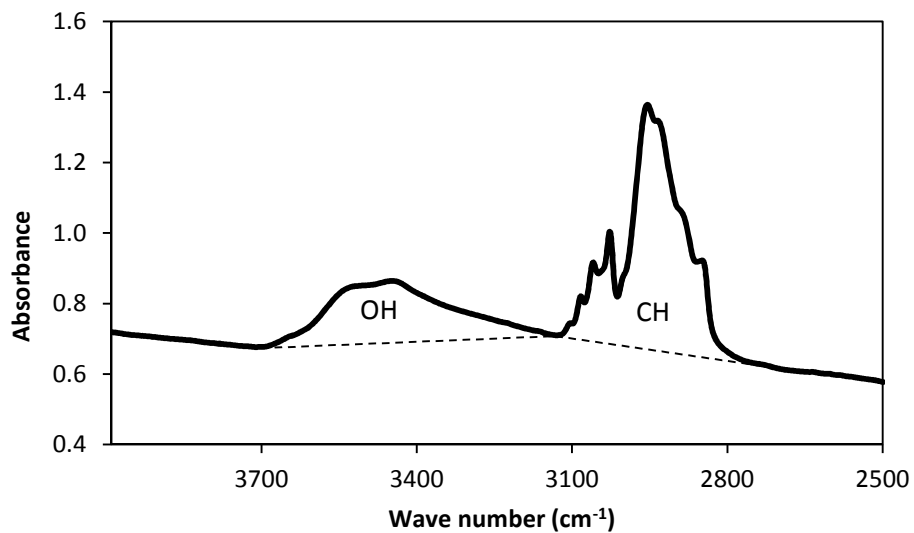


Fig. H-44. FTIR Spectra for 1T-C-1

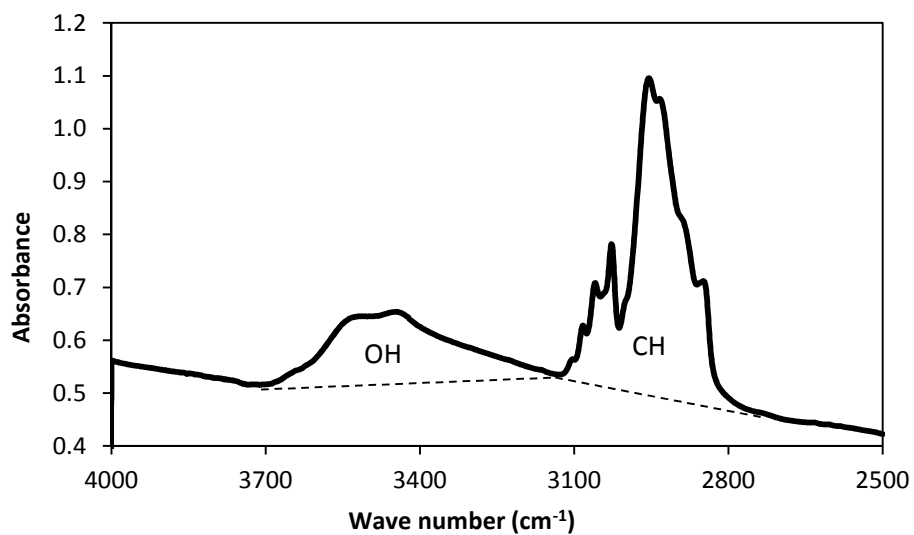


Fig. H-45. FTIR Spectra for 1T-IN-HW-1

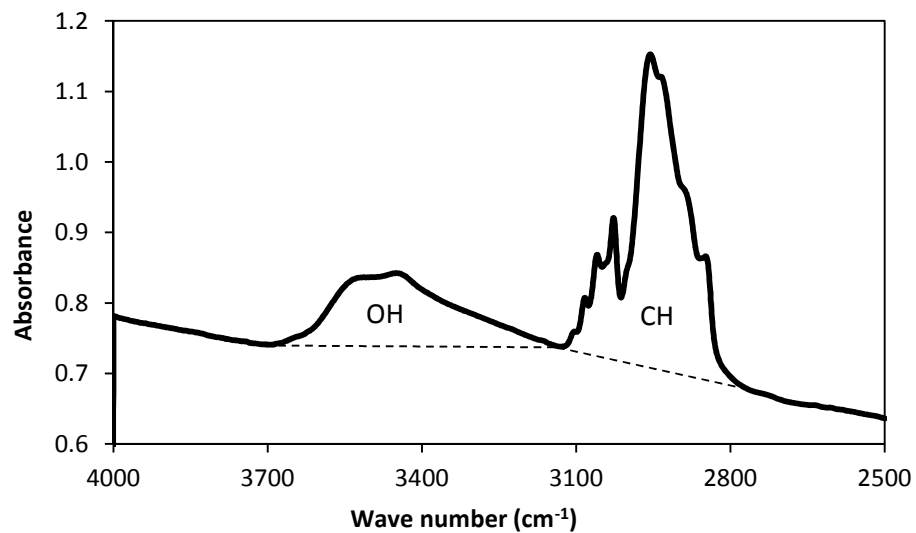


Fig. H-46. FTIR Spectra for 4L-C-1

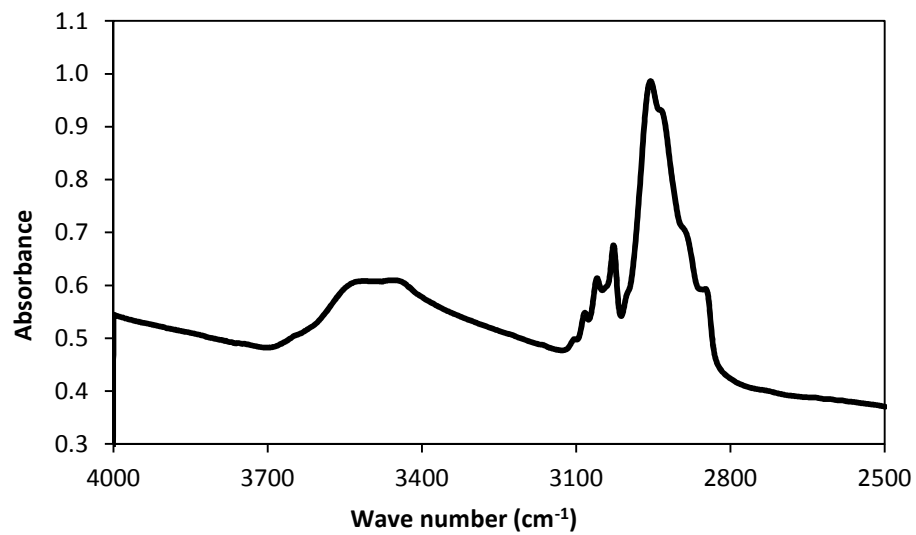


Fig. H-47. FTIR Spectra for 4L-UVSF-1

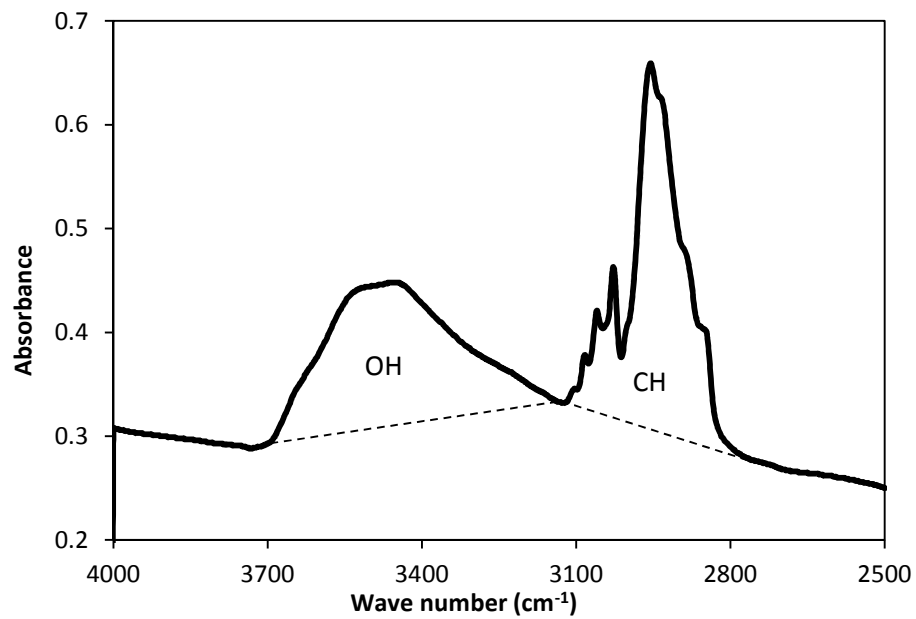


Fig. H-48. FTIR Spectra for 2L-UVSF-1

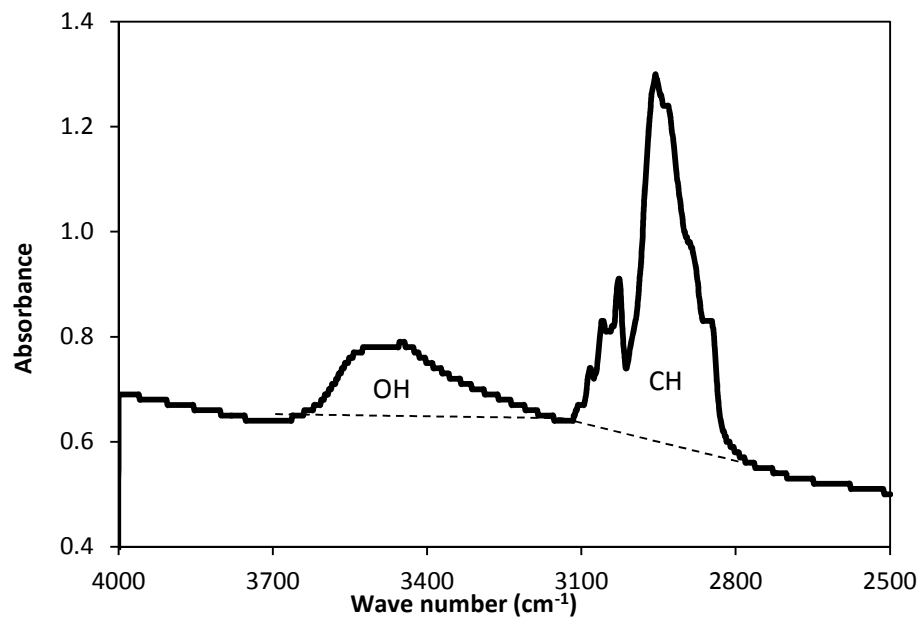


Fig. H-49. FTIR Spectra for 4L-SF-1

APPENDIX H.
MATLAB CODE FOR ESTIMATING THE THERMAL STRESSES AND STRAINS IN
B0410 SUPERSTRUCTURE


```

%%%%%%%%%%%%%%%%%%%%%%%%%%%%%%%%%%%%%%%%%%%%%%%%%%%%%%%%%%%%%%%%%%%%%%%%
%%%%%%%%%%%%%%%%%%%%%%%%%%%%%%%%%%%%%%%%%%%%%%%%%%%%%%%%%%%%%%%%%%%%%%%%
%%%%%%%% This Matlab Code calculates the Thermal strains and stresses %%%
%%%%%%%% of the multi-celled HCB of bridge B0410 at certain locations %
%%%%%%%% using transformed area Method and assuming linear stress-strain%
%%%%%%%%%%%%%%%%%%%%%%%%%%%%%%%%%%%%%%%%%%%%%%%%%%%%%%%%%%%%%%%%%%%%%%%%
%%%%%%%%%%%%%%%%%%%%%%%%%%%%%%%%%%%%%%%%%%%%%%%%%%%%%%%%%%%%%%%%%%%%%%%%

```

```

%%%%%%%%%%%%%%%%%%%%%%%%%%%%%%%%%%%%%%%%%%%%%%%%%%%%%%%%%%%%%%%%%%%%%%%%
%%%%%%%%%%%%%%%%%%%%%%%%%%%%%%%%%%%%%%%%%%%%%%%%%%%%%%%%%%%%%%%%%%%%%%%% 1- Material Properties %%%%%%%%%
%%%%%%%%%%%%%%%%%%%%%%%%%%%%%%%%%%%%%%%%%%%%%%%%%%%%%%%%%%%%%%%%%%%%%%%%

```

```

%%%%%%%%%%%%%%%%%%%%%%%%%%%%%%%%%%%%%%%%%%%%%%%%%%%%%%%%%%%%%%%%%%%%%%%% Concrete Properties %%%%%%%%%
%% Arch

```

```

Sca      = 11;          %% compressive strength of concrete arch in
Ksi
Dca      = 0.14;       %% Denisty of concrete arch in Kip/cubic feet
phaca    = 10e-6;      %% Coefficient of thermal expansion in mm/mm/C
%% C.g. of concrete arch in inch
%Yca     = [5; 14.48; 22.96; 30.44; 36.93; 42.42; 46.91; 50.4; 52.89;
54.39; 54.89; 54.39; 52.89; 50.4; 46.91; 42.42; 36.93; 30.44; 22.96;
14.48; 5];
Yca      = [5; 6.367; 14.48; 22.96; 27.539; 30.44; 36.93; 42.42; 42.744;
46.91; 50.4; 51.725; 52.89; 54.39; 54.89; 54.39; 52.89; 50.4; 46.91;
42.42; 36.93; 30.44; 22.96; 14.48; 5];
%X       = [0; 53.4; 115.8; 178.2; 240.6; 303; 365.4; 427.8; 490.2;
552.6; 615; 677.4; 739.8; 802.2; 864.6; 927; 989.4; 1051.8; 1114.2;
1176.6; 1230]; %% vector of points at which the calculations of
Moment, shear and inertia are calculated in inch
X        = [0; 9; 53.4; 115.8; 154; 178.2; 240.6; 303; 307.5; 365.4;
427.8; 461; 490.2; 552.6; 615; 677.4; 739.8; 802.2; 864.6; 927; 989.4;
1051.8; 1114.2; 1176.6; 1230]; %% vector of points at which the
calculations of Moment, shear and inertia are calculated in inch

```

```

%% Deck
Sd       = 6.0;        %% compressive strength of concrete deck in
Ksi
Dd       = 0.14;       %% Denisty of concrete arch in Kip/cubic feet
phacd    = 8.1e-6;     %% Coefficient of thermal expansion in mm/mm/C

```

```

%%%%%%%%%%%%%%%%%%%%%%%%%%%%%%%%%%%%%%%%%%%%%%%%%%%%%%%%%%%%%%%%%%%%%%%% Steel Properties %%%%%%%%%
%% Strands

```

```

Astrand  = 0.1964;     %% Area of one prestressing strand (Grade 250)
in inch square
dstr     = 0.5;        %% Diameter of one strand in inch
Fpu      = 250;        %% Tensile strength of prestressing strand in
Ksi
Ep       = 28500;      %% Modulus of elasticity of prestressing steel
in Ksi
phas     = 12.4e-6;    %% Coefficient of thermal expansion in mm/mm/C
%% Deck RFT bars (upper and lower)
Ab       = 0.442;      %% Area of one bar in inch square (uper and
lower RFT has the diameter)
db       = 0.75;       %% Diameter of one bar in inch

```

```

Fb      = 60;          %% Tensile strength of prestressing strand in
Ksi
Eb      = 29000;      %% Modulus of elasticity of deck rft in Ksi
phab    = 12.4e-6;    %% Coefficient of thermal expansion in mm/mm/C

```

```

%%%%%%%%%%%%%%%%%%%%%%%%%%%%%%%%%%%%%%%%%%%%%%%%%%%%%%%%%%%%%%%%%%%%%%%% FRP Properties %%%%%%%%%%%%%%%%%%%%%%%%%%%%%%%%%%%%%%%%%%%%%%%%%%%%%%%%%%%%%%%%%%%%%%%%%

```

```

%%% Webs

```

```

Ew11 = 2000;          %% Modulus of elasticity in dir. 1-1 of GFRP of
web in Ksi
Ew22 = 1400;          %% Modulus of elasticity in dir. 2-2 of GFRP of
web in Ksi
Gw12 = 919;           %% Shear Modulus in plane 1-2 of GFRP of web in
Ksi
Pw12 = 0.26;          %% Poisson's ratio in plane 1-2 of GFRP of web
%Shw = 19;            %% Shear strength in plane 1-2 of GFRP of web in
Ksi

```

```

%%% Top flange

```

```

Etf11 = 2000;          %% Modulus of elasticity in dir. 1-1 of GFRP of
top flange in Ksi
Etf22 = 1400;          %% Modulus of elasticity in dir. 2-2 of GFRP of
top flange in Ksi
Gtf12 = 919;           %% Shear Modulus in plane 1-2 of GFRP of top
flange in Ksi
Ptf12 = 0.26;          %% Major Poisson's ratio in plane 1-2 of GFRP of
top flange
%Ptf21 = 0.26;         %% Minor Poisson's ratio in plane 1-2 of GFRP of
top flange

```

```

%%% Bottom flange

```

```

Ebf11 = 2000;          %% Modulus of elasticity in dir. 1-1 of GFRP of
bot. flange in Ksi
Ebf22 = 1400;          %% Modulus of elasticity in dir. 2-2 of GFRP of
bot. flange in Ksi
Gbf12 = 919;           %% Shear Modulus in plane 1-2 of GFRP of bot.
flange in Ksi
Pbf12 = 0.26;          %% Major Poisson's ratio in plane 1-2 of GFRP of
bot. flange
%Pbf21 = 0.26;         %% Minor Poisson's ratio in plane 1-2 of GFRP of
bot. flange

```

```

phaf = 10.4e-6;        %% Coefficient of thermal expansion in mm/mm/C

```

```

%%%%%%%%%%%%%%%%%%%%%%%%%%%%%%%%%%%%%%%%%%%%%%%%%%%%%%%%%%%%%%%%%%%%%%%%
%%% 2- Geometry %%%%%%%%%%%%%%%%%%%%%%%%%%%%%%%%%%%%%%%%%%%%%%%%%%%%%%%%%%%%%%%%%%%%%%%%%
%%%%%%%%%%%%%%%%%%%%%%%%%%%%%%%%%%%%%%%%%%%%%%%%%%%%%%%%%%%%%%%%%%%%%%%%

```

```

%%% Beam

```

```

h      = 60.16;        %% Height of HCB in inch
b      = 72;           %% Width of beam in inch
btf    = 27.5;         %% Width of Top flange in inch (upper layer of
FRP Lid above two concrete arch)
btf2   = 44.5;         %% Width of Top flange2 in inch (The upper
layer of FRP Lid between the two concret arches)
btf3   = 44.3;         %% Width of Top flange3 in inch (Lower layer
of FRP Lid between the two concret arches)

```



```

%% 1- Identifying the Inertia of each component w.r.t its CG
%% Tension RFT (strands)
Astr = Nstr*Astrand; %% Area of strands in inch square
Ys   = tbf+ dstr;    %% CG of two layers of strands from the bottom
of the HCB
nstr = Ep/Ew11;     %% modular ratio of the strands relative to
the FRP web
As   = Astr*nstr;   %% transformed area of strands in inch square
Is   = Nstr*pi*dstr^4*nstr/64+As*(dstr/2)^2; %% moment of inertia
of strands around their CG
%% FRP Top flanges
ntf  = Etf11/Ew11;
Ytf  = h-ttf/2;
Atf  = ttf*btf*ntf; %% transformed area of top flange in
inch square
Itf  = btf*ttf^3/12*ntf; %% transformed Moment of inertia of top
flange in in^4
Ytf2 = h-ttf2/2;
Atf2 = ttf2*btf2*ntf; %% transformed area of top flange2 in
inch square
Itf2 = btf2*ttf2^3/12*ntf; %% transformed Moment of inertia of top
flange2 in in^4
Ytf3 = h-ttf2-2-ttf3/2;
Atf3 = ttf3*btf3*ntf; %% transformed area of top flange3 in
inch square
Itf3 = btf3*ttf3^3/12*ntf; %% transformed Moment of inertia of top
flange3 in in^4
%% FRP Bottom flanges
nbf  = Ebf11/Ew11;
Ybf  = tbf/2;
Abf  = tbf*bbf*nbf; %% transformed area of top flange in
inch square
Ibf  = bbf*tbf^3/12*nbf; %% transformed Moment of inertia of top
flange in in^4
Ybf2 = tbf2/2+tbf+2;
Abf2 = tbf2*bbf2*nbf; %% transformed area of top flange in
inch square
Ibf2 = bbf2*tbf^3/12*nbf; %% transformed Moment of inertia of top
flange in in^4
%% FRP Webs
Yw   = h/2;
Aw   = 4*tw*h; %% area of four FRP webs in inch square
Iw   = 4*tw*h^3/12; %% Moment of inertia of two webs in
in^4
%% FRP sandwich panel
Ysw  = h-tsw/2;
Asw  = bsw*tsw; %% area of four FRP side FRP sandwich
panel in inch square
Isw  = bsw*tsw^3/12; %% Moment of inertia of FRP sandwich
panel in in^4
%% Concrete Arch
frca = 7.5/1000*sqrt(Sca*1000); %% modulus of rupture of concret
arch in Ksi
Eca  = 57*sqrt(Sca*1000); %% Elastic modulus of concret arch in
Ksi

```

```

nca = Eca/Ew11;          %%%% modular ratio of the conc. Arch
relative to the FRP web
Aca = 2*tca*bca*nca;    %%%% transformed area of two conc arches
in square inch
Ica = 2*bca*tca^3*nca/12; %%%% transformed Moment of inertia of two
conc arches in in^4
%%%% Concrete Deck
frd = 7.5/1000*sqrt(Sd*1000); %%%% modulus of rupture of concret deck
in Ksi
Yd = h+ ts/2;
Ed = 57*sqrt(Sd*1000);  %%%% Elastic modulus of deck's concrete
in Ksi
nd = Ed/Ew11;          %%%% modular ratio of the deck relative
to the FRP web
Ad = ts*bs*nd;         %%%% transformed area of deck in square
inch
Id = bs*ts^3*nd/12;    %%%% transformed Moment of inertia of
deck in in^4

%%%% Concrete Web (fin)
Ecw = 57*sqrt(Sca*1000); %%%% Elastic modulus of concrete in Ksi
ncw = Ecw/Ew11;        %%%% modular ratio of the deck relative
to the FRP web
hcw = zeros(NEM+1,1);
Ycw = zeros(NEM+1,1);
Acw = zeros(NEM+1,1);
Icw = zeros(NEM+1,1);
for i=1:NEM+1          %%%% Calculating the height and the area
of the concrete web
    hcw(i,1)= h-(Yca(i,:)+tca/2+ttf);
    Ycw(i,1)= h-(hcw(i,+)/2+ttf);
    Acw(i,1)= 2*hcw(i,1)*tcw*ncw;
    Icw(i,1)= 2*tw* (hcw(i,1))^3*ncw/12;
end
hcw(15,1) = 0;
Acw(15,1) = 0;
Icw(15,1) = 0;

%%%% RFT of deck
nb = Eb/Ew11;          %%%% modular ratio of the
bars relative to the FRP web
Aub = Nub*Ab*nb;      %%%% transformed Area of
bars in inch square
Alb = Nlb*Ab*nb;      %%%% transformed Area of
bars in inch square
Yub = h+ts-(3);        %%%% CG of upper bars from
the bottom of the HCB
Ylb = h+2+1.5*db;     %%%% CG of upper bars from
the bottom of the HCB
Iub = Nub*pi*db^4*nb/64; %%%% transformed moment of
inertia of upper Rft
Ilb = Nlb*pi*db^4*nb/64; %%%% transformed moment of
inertia of lower Rft

```

```

%% 1- Identifying the N.A. and moment of inertia of HCB
Ybar = zeros(NEM+1,1);          %% N.A of HCB at each
point
I     = zeros(NEM+1,1);        %% moment of inertia of
HCB in in^4
A     = zeros(NEM+1,1);        %% Area of HCB in in^2

for i= 1:NEM+1
    A (i,:) =
As+Atf+Atf2+Atf3+Abf+Abf2+Aw+Asw+Aca+Ad+Acw(i,:)+Aub+Alb;
    Ybar(i,:) =
(As*Ys+Atf*Ytf+Atf2*Ytf2+Atf3*Ytf3+Abf*Ybf+Abf2*Ybf2+Aw*Yw+Asw*Ysw+Aca*
Yca(i,:)+Ad*Yd+Acw(i,:)*Ycw(i,:)+Aub*Yub+Alb*Ylb)/A(i,:);
    I (i,:) = Is+As*(Ys-Ybar(i,:))^2+Itf+Atf*(Ytf-
Ybar(i,:))^2+Itf2+Atf2*(Ytf2-Ybar(i,:))^2+Itf3+Atf3*(Ytf3-
Ybar(i,:))^2+Ibf+Abf*(Ybf-Ybar(i,:))^2+Ibf2+Abf2*(Ybf2-
Ybar(i,:))^2+Iw+Aw*(Yw-Ybar(i,:))^2+Isw+Asw*(Ysw-
Ybar(i,:))^2+Ica+Aca*(Yca(i,:)-Ybar(i,:))^2+Id+Ad*(Yd-
Ybar(i,:))^2+Icw(i,:)+Acw(i,:)*(Ycw(i,:)-Ybar(i,:))^2+Iub+Aub*(Yub-
Ybar(i,:))^2+Ilb+Alb*(Ylb-Ybar(i,:))^2;
end

%%%%%%%%%%%%%%%%%%%%%%%%%%%%%%%%%%%%%%%%%%%%%%%%%%%%%%%%%%%%%%%%%%%%%%%%
%% 5- Calculation of stresses and strains %%%%%%%%%
%%%%%%%%%%%%%%%%%%%%%%%%%%%%%%%%%%%%%%%%%%%%%%%%%%%%%%%%%%%%%%%%%%%%%%%%

%% stresses and strains due to temperature changes %%%%%%%%%

NEMTH      = 24;
strthbf    = zeros (NEMTH+1,1);
strthbf2   = zeros (NEMTH+1,1);
Nthbf      = zeros (NEMTH+1,1);
Mthbf      = zeros (NEMTH+1,1);
Nthbf2     = zeros (NEMTH+1,1);
Mthbf2     = zeros (NEMTH+1,1);
strthtf    = zeros (NEMTH+1,1);
strthtf2   = zeros (NEMTH+1,1);
strthtf3   = zeros (NEMTH+1,1);
Nthtf      = zeros (NEMTH+1,1);
Mthtf      = zeros (NEMTH+1,1);
Nthtf2     = zeros (NEMTH+1,1);
Mthtf2     = zeros (NEMTH+1,1);
Nthtf3     = zeros (NEMTH+1,1);
Mthtf3     = zeros (NEMTH+1,1);
strthsw    = zeros (NEMTH+1,1);
Nthsw      = zeros (NEMTH+1,1);
Mthsw      = zeros (NEMTH+1,1);
strthstr   = zeros (NEMTH+1,1);
Nthstr     = zeros (NEMTH+1,1);
Mthstr     = zeros (NEMTH+1,1);
%Ym2w      = zeros (NEMTH+1,1);
%Ymlw      = zeros (NEMTH+1,1);

```

```

strthw      = zeros (NEMTH+1,1);
%strthlw    = zeros (NEMTH+1,1);
%strthm2w   = zeros (NEMTH+1,1);
%strthmlw   = zeros (NEMTH+1,1);
Nthw        = zeros (NEMTH+1,1);
Mthw        = zeros (NEMTH+1,1);
strthlb1    = zeros (NEMTH+1,1);
strthlb2    = zeros (NEMTH+1,1);
strthlb3    = zeros (NEMTH+1,1);
strthub1    = zeros (NEMTH+1,1);
strthub2    = zeros (NEMTH+1,1);
strthub3    = zeros (NEMTH+1,1);
Nthlb       = zeros (NEMTH+1,1);
Mthlb       = zeros (NEMTH+1,1);
Nthub       = zeros (NEMTH+1,1);
Mthub       = zeros (NEMTH+1,1);
%Ymca       = zeros (NEMTH+1,1);
strthuca    = zeros (NEMTH+1,1);
%strthmca   = zeros (NEMTH+1,1);
strthlca    = zeros (NEMTH+1,1);
Nthca       = zeros (NEMTH+1,1);
Mthca       = zeros (NEMTH+1,1);
%Ymcw1      = zeros (NEMTH+1,1);
%Ymcw2      = zeros (NEMTH+1,1);
strthucw    = zeros (NEMTH+1,1);
%strthmlcw  = zeros (NEMTH+1,1);
%strthm2cw  = zeros (NEMTH+1,1);
strthlcw    = zeros (NEMTH+1,1);
Nthcw       = zeros (NEMTH+1,1);
Mthcw       = zeros (NEMTH+1,1);
%Ymcd       = zeros (NEMTH+1,1);
strthucd1   = zeros (NEMTH+1,1);
strthucd2   = zeros (NEMTH+1,1);
strthucd3   = zeros (NEMTH+1,1);
%strthmcd   = zeros (NEMTH+1,1);
strthlcd1   = zeros (NEMTH+1,1);
strthlcd2   = zeros (NEMTH+1,1);
strthlcd3   = zeros (NEMTH+1,1);
Nthcd       = zeros (NEMTH+1,1);
Mthcd       = zeros (NEMTH+1,1);
Nth         = zeros (NEMTH+1,1);
Mth         = zeros (NEMTH+1,1);
Tempca      = zeros (NEMTH+1,1);
Ntht        = 0;
Mtht        = 0;

```

```

%%%%%%%%%%%%%%%%%%%%%%%%%%%%%%%%%%%%%%%%%%%%%%%%%%%%%%%%%%%%%%%%%%%%%%%%
%%%%%%%%%%%%%%%%%%%%%%%%%%%%%%%%%%%%%%%%%%%%%%%%%%%%%%%%%%%%%%%%%%%%%%%%
%%% Define the temperature changes at the different elements %%%%
%%%%%%%%%%%%%%%%%%%%%%%%%%%%%%%%%%%%%%%%%%%%%%%%%%%%%%%%%%%%%%%%%%%%%%%%
%%%%%%%%%%%%%%%%%%%%%%%%%%%%%%%%%%%%%%%%%%%%%%%%%%%%%%%%%%%%%%%%%%%%%%%%

```

```

syms a b c d e f y

```

```

%%%%%%%% 1- The temperature differences between LC3 & LC1 %%%%

```

%%%%%%%%% where LC1 measured on March 5th at 10:00 am and LC3 measured on April 10th at 4:00 pm %%%%%%%%%

```

Tempxcd      = 13.1;           %%%% The temperature change at the
top of the deck
Tempbcd      = 5.1;           %%%% The temperature change at the
bottom of the deck
Tempsh       = 6.4;           %%%% The temperature change at the
FRP shell (bot. flange and web only)
Tempbx       = -1.6;          %%%% The temperature change inside
the FRP shell (between the two webs)
Tempstr      = 2.8;           %%%% The temperature change at the
strands
Tempca (2,1) = 0.1;           %%%% The temperature change at the
bot of the concrete arch at sec (E-E)
Tempca (5,1) = 0.4;           %%%% The temperature change at the
bot of the concrete arch at sec (D-D)
Tempca (9,1) = 0.4;           %%%% The temperature change at the
bot of the concrete arch at sec (C-C)
Tempca (12,1) = -0.5;         %%%% The temperature change at the
bot of the concrete arch at sec (B-B)
Tempca (15,1) = -0.3;         %%%% The temperature change at the
bot of the concrete arch at sec (A-A)
Results      = [2,5,9,12,15]; %%%% The vector results identify the
locations where the results need to be calculated

```

```

for j= 1:5
    i = Results (1,j);

    yxcd      = Yd + (ts/2);
    ybcd      = Yd - (ts/2);
    %ybc      = Yca (i,1)- (tca/2);
    [a1,b1] = solve (((yxcd-Ybar(i,1))*a+b)==Tempxcd, ((ybcd-
Ybar(i,1))*a+b)==Tempbcd);
    [c1,d1] = solve (((yxcd-Ybar(i,1))*c+d)==Tempxcd, ((h-
Ybar(i,1))*c+d)==Tempca(i,1));
    [e1,f1] = solve (((yxcd-Ybar(i,1))*e+f)==Tempxcd, ((Ytf3-
Ybar(i,1))*e+f)==Tempbx);

```

%%%%%%%% Thermal stresses in FRP Bottom flanges

```

strthbf (i,1) = -Ebf11*phaf*Tempsh;
Nthbf (i,1) = strthbf (i,1)*tbf*bbf;
Mthbf (i,1) = Nthbf (i,1)*(Ybf-Ybar(i,1));

```

```

strthbf2 (i,1) = -Ebf11*phaf*Tempbx;
Nthbf2 (i,1) = strthbf2 (i,1)*tbf2*bbf2;
Mthbf2 (i,1) = Nthbf2 (i,1)*(Ybf2-Ybar(i,1));

```

%%%%%%%% Thermal stresses in FRP top flanges

```

strthtf (i,1) = -Ebf11*phaf*(c1*(Ytf-Ybar(i,1))+d1);

```



```

Nthtf (i,1) = strthtf (i,1)*ttf*btf;
Mthtf (i,1) = Nthtf (i,1)*(Ytf-Ybar(i,1));

strthtf2(i,1) = -Ebfl1*phaf*(e1*(Ytf2-Ybar(i,1))+f1);
Nthtf2 (i,1) = strthtf2 (i,1)*ttf2*btf2;
Mthtf2 (i,1) = Nthtf2 (i,1)*(Ytf2-Ybar(i,1));

strthtf3(i,1) = -Ebfl1*phaf*Tempbx;
Nthtf3 (i,1) = strthtf3 (i,1)*ttf3*btf3;
Mthtf3 (i,1) = Nthtf3 (i,1)*(Ytf3-Ybar(i,1));

%%% Thermal stresses in FRP Webs

strthw (i,1) = -Ew11*phaf*(Tempsh+Tempbx)/2;
Nthw (i,1) = strthw (i,1)*Aw;
Mthw (i,1) = Nthw (i,1)*(Yw-Ybar(i,1));

%%% Thermal stresses in FRP sandwich panel

strthsw (i,1) = -Ew11*phaf*Tempbcd;
Nthsw (i,1) = strthsw (i,1)*tsw*bsw;
Mthsw (i,1) = Nthsw (i,1)*(Ysw-Ybar(i,1));

%%% Thermal stresses in (strands)

strthstr (i,1) = -Ep*phas*Tempstr;
Nthstr (i,1) = strthstr (i,1)*Astrand;
Mthstr (i,1) = Nthstr (i,1)*(Ys-Ybar(i,1));

%%% Thermal stresses in Deck Rft

strthlb1 (i,1) = -Eb*phab*(a1*(Ylb-Ybar(i,1))+b1);
strthlb2 (i,1) = -Eb*phab*(c1*(Ylb-Ybar(i,1))+d1);
strthlb3 (i,1) = -Eb*phab*(e1*(Ylb-Ybar(i,1))+f1);

strthub1 (i,1) = -Eb*phab*(a1*(Yub-Ybar(i,1))+b1);
strthub2 (i,1) = -Eb*phab*(c1*(Yub-Ybar(i,1))+d1);
strthub3 (i,1) = -Eb*phab*(e1*(Yub-Ybar(i,1))+f1);

Nthlb (i,1) = strthlb1 (i,1)*Nlb*Ab*(bs-btf-btf2)/bs+
strthlb2(i,1)*Nlb*Ab*btf/bs+ strthlb3 (i,1)*Nlb*Ab*btf2/bs;
Mthlb (i,1) = Nthlb (i,1)*(Ylb-Ybar(i,1));
Nthub (i,1) = strthub1 (i,1)*Nub*Ab*(bs-btf-btf2)/bs+
strthub2(i,1)*Nub*Ab*btf/bs+ strthub3 (i,1)*Nub*Ab*btf2/bs;
Mthub (i,1) = Nthub (i,1)*(Yub-Ybar(i,1));

%%% Thermal stresses in concrete arch

```

```

ybca          = Yca (i,1)- (tca/2);
ytca          = Yca (i,1)+ (tca/2);
strthuca (i,1) = -Eca*phaca*Tempca(i,1);
strthlca (i,1) = -Eca*phaca*Tempca(i,1);
Nthca (i,1)   = 2*-Eca*phaca*Tempca(i,1)*bca*tca;
Mthca (i,1)   = Nthca (i,1)*(Yca (i,1)-Ybar(i,1));

```

```

%%%% Thermal stresses in concrete web

```

```

ybcw          = Ycw (i,1)- (hcw (i,1)/2);
ytcw          = Ycw (i,1)+ (hcw (i,1)/2);
strthucw (i,1) = -Eca*phaca*Tempca(i,1);
strthlcw (i,1) = -Eca*phaca*Tempca(i,1);
Nthcw (i,1)   = 2*-Eca*phaca*Tempca(i,1)*tcw*hcw (i,1);
Mthcw (i,1)   = Nthcw (i,1)*(Ycw (i,1)-Ybar(i,1));

```

```

%%%% Thermal stresses in concrete deck

```

```

strthucd1 (i,1) = -Ed*phacd*(a1*(ytcd-Ybar(i,1))+b1);
strthucd2 (i,1) = -Ed*phacd*(c1*(ytcd-Ybar(i,1))+d1);
strthucd3 (i,1) = -Ed*phacd*(e1*(ytcd-Ybar(i,1))+f1);
strthlcd1 (i,1) = -Ed*phacd*(a1*(ybcd-Ybar(i,1))+b1);
strthlcd2 (i,1) = -Ed*phacd*(c1*(ybcd-Ybar(i,1))+d1);
strthlcd3 (i,1) = -Ed*phacd*(e1*(ybcd-Ybar(i,1))+f1);
Nthcd      (i,1) = int((bs-btf-btf2)*-Ed*phacd*(a1*(y-
Ybar(i,1))+b1),ybcd,ytcd)+int(btf*-Ed*phacd*(c1*(y-
Ybar(i,1))+d1),ybcd,ytcd)+int(btf2*-Ed*phacd*(e1*(y-
Ybar(i,1))+f1),ybcd,ytcd);
Mthcd      (i,1) = int((bs-btf-btf2)*-Ed*phacd*(a1*(y-
Ybar(i,1))+b1)*(y-Ybar(i,1)),ybcd,ytcd)+int(btf*-Ed*phacd*(c1*(y-
Ybar(i,1))+d1)*(y-Ybar(i,1)),ybcd,ytcd)+int(btf2*-Ed*phacd*(c1*(y-
Ybar(i,1))+d1)*(y-Ybar(i,1)),ybcd,ytcd);

```

```

Nth (i,1) =
Nthbf(i,1)+Nthbf2(i,1)+Nthtf(i,1)+Nthtf2(i,1)+Nthtf3(i,1)+Nthsw(i,1)+Nt
hstr(i,1)+Nthw(i,1)+Nthlb(i,1)+Nthub(i,1)+Nthca(i,1)+Nthcw(i,1)+Nthcd(i
,1);

```

```

Mth (i,1) =
Mthbf(i,1)+Mthbf2(i,1)+Mthtf(i,1)+Mthtf2(i,1)+Mthtf3(i,1)+Mthsw(i,1)+Mt
hstr(i,1)+Mthw(i,1)+Mthlb(i,1)+Mthub(i,1)+Mthca(i,1)+Mthcw(i,1)+Mthcd(i
,1);

```

```

if i==2
    Ntht = Ntht+ 0.5*Nth (i,1);
    Mtht = Mtht+ 0.5*Mth (i,1);
else
    Ntht = Ntht+ Nth (i,1);
    Mtht = Mtht+ Mth (i,1);
end
end

```

```

Nthav = Ntht/(4.5);

```

```
Mthav = Mtht/(4.5);
```

```
M = zeros (25,1);
N = zeros (25,1);
```

```
%%%%%%%%%%%%%%%%%%%%%%%%%%%%%%%%%%%%%%%%%%%%%%%%%%%%%%%%%%%%%%%%%%%%%%%%
%%%%%%%% These moments and forces are those which not resisted by %%%%%%%%%
%%%%%%%% (released from)the structure %%%%%%%%%
%%%%%%%% These Moments and forces were calculated via SAP2000 %%%%%%%%%
%%%%%%%%%%%%%%%%%%%%%%%%%%%%%%%%%%%%%%%%%%%%%%%%%%%%%%%%%%%%%%%%%%%%%%%%
```

```
%%%%%%%% Moment and normal force when HCB is modeled as straight beam %%%
%for i= 1:1+NEMTH
% M (i,1) = -2792;
% N (i,1) = 505.2;
%end
```

```
%%%%%%%% Moment and normal force when HCB is modeled as cureved beam %%%
N (2,1) = 502.3;
M (2,1) = -2799;
N (5,1) = 502.3;
M (5,1) = -2787.4;
N (9,1) = 502.7;
M (9,1) = -2781;
N (12,1) = 502.7;
M (12,1) = -2777.6;
N (15,1) = 502.7;
M (15,1) = -2777;
```

```
%%%%%%%%%%%%%%%%%%%%%%%%%%%%%%%%%%%%%%%%%%%%%%%%%%%%%%%%%%%%%%%%%%%%%%%%
%%%%%%%% 6- Calculation of streses and strains %%%%%%%%%
%%%%%%%%%%%%%%%%%%%%%%%%%%%%%%%%%%%%%%%%%%%%%%%%%%%%%%%%%%%%%%%%%%%%%%%%
```

```
PNA = zeros (NEM+1,1);
strssbf = zeros (NEM+1,1);
strssbfse = zeros (NEM+1,1);
strnbf = zeros (NEM+1,1);
strnbfse = zeros (NEM+1,1);
Fbf = zeros (NEM+1,1);
strssbf2 = zeros (NEM+1,1);
strssbf2se = zeros (NEM+1,1);
strnbf2 = zeros (NEM+1,1);
strnbf2se = zeros (NEM+1,1);
Fbf2 = zeros (NEM+1,1);
strsstf = zeros (NEM+1,1);
strsstfse = zeros (NEM+1,1);
Ftf = zeros (NEM+1,1);
strsstf2 = zeros (NEM+1,1);
strsstf2se = zeros (NEM+1,1);
Ftf2 = zeros (NEM+1,1);
strsstf3 = zeros (NEM+1,1);
strsstf3se = zeros (NEM+1,1);
strntf3 = zeros (NEM+1,1);
```

```

strntf3se = zeros (NEM+1,1);
Ftf3      = zeros (NEM+1,1);
strsstr   = zeros (NEM+1,1);
strsstrse= zeros (NEM+1,1);
strnstr   = zeros (NEM+1,1);
strnstrse = zeros(NEM+1,1);
Fstr      = zeros (NEM+1,1);
strsslw   = zeros (NEM+1,1);
strsslwse = zeros (NEM+1,1);
%strssmw  = zeros (NEM+1,1);
strssuw   = zeros (NEM+1,1);
strssuwse= zeros (NEM+1,1);
strnuw    = zeros (NEM+1,1);
Fw        = zeros (NEM+1,1);
FwC       = zeros (NEM+1,1);
FwT       = zeros (NEM+1,1);
%strsslslr = zeros (NEM+1,1);
%strssusr  = zeros (NEM+1,1);
%FsrC     = zeros (NEM+1,1);
%FsrT     = zeros (NEM+1,1);
strsssw   = zeros (NEM+1,1);
strssswse= zeros (NEM+1,1);
Fsw       = zeros (NEM+1,1);
strssub   = zeros (NEM+1,1);
strssubse= zeros (NEM+1,1);
strnub    = zeros (NEM+1,1);
Fub       = zeros (NEM+1,1);
Flb       = zeros (NEM+1,1);
strsslca  = zeros (NEM+1,1);
strsslcase = zeros (NEM+1,1);
strnlca   = zeros (NEM+1,1);
strnlcase = zeros (NEM+1,1);
ca        = zeros (NEM+1,1);
strssuca  = zeros (NEM+1,1);
strssucase = zeros (NEM+1,1);
strnuca   = zeros (NEM+1,1);
strnucase = zeros (NEM+1,1);
%strssmca = zeros (NEM+1,1);
Fca       = zeros (NEM+1,1);
Fd        = zeros (NEM+1,1);
strssucwse = zeros (NEM+1,1);
strssucw   = zeros (NEM+1,1);
%strssm2cw = zeros (NEM+1,1);
%strssmlcw = zeros (NEM+1,1);
strsslcw   = zeros (NEM+1,1);
strsslcwse = zeros (NEM+1,1);
strnlcw    = zeros (NEM+1,1);
strnlcwse  = zeros (NEM+1,1);
strnucw    = zeros (NEM+1,1);
cw         = zeros (NEM+1,1);
strnucwse  = zeros (NEM+1,1);
Fcw        = zeros (NEM+1,1);
Comp       = zeros (NEM+1,1);
Ten        = zeros (NEM+1,1);
Dif        = zeros (NEM+1,1);
strssucd   = zeros (NEM+1,1);

```

```

strssucdse = zeros (NEM+1,1);
strsslcd   = zeros (NEM+1,1);
strsslcdse = zeros (NEM+1,1);
%strssmcd  = zeros (NEM+1,1);
strnucd    = zeros (NEM+1,1);
%strnmcd   = zeros (NEM+1,1);
strnlcd    = zeros (NEM+1,1);
strnlcdse  = zeros (NEM+1,1);
%strnmcldse = zeros (NEM+1,1);
strnucdse  = zeros (NEM+1,1);

for i = 1:NEM+1
    PNA(i,1) = Ybar(i,1);
end

%syms y Epsca Epscd Epscw
%Epsndca = 0.0021;          %%% Epsilon node of concret arch and
web(The strain at which maximum compressive stress takes place)
%Epsndcd = 0.0021;          %%% Epsilon node of concret deck
%Epsu    = 0.003;           %%% Ultimate Concrete strain beyond it
the concrete assumed to be crashed

for j= 1:5
    i = Results (1,j);

        %%% Force in FRP Bottom flanges
        strssbf (i,1) = (M(i,1)*(PNA(i,1)-Ybf)/I(i,:)*nbf)+
N(i,1)*nbf/A(i,:);          %%% This is the
stress that doesn't induce in the structure if the structure is
determinate
        strssbfse(i,1) = strthbf(i,1)+(M(i,1)*(PNA(i,1)-
Ybf)/I(i,:)*nbf)+ N(i,1)*nbf/A(i,:);          %%% This is the
self-equilibrating stress (the real stress that the structure undergo)
        strnbf(i,1) = M(i,1)*(PNA(i,1)-Ybf)/I(i,:)/Ew11 +
N(i,1)/A(i,:)/Ew11 ;          %%% This is the
actual strain that the structure undergo
        strnbfse(i,1) = strthbf(i,1)/Eb11+M(i,1)*(PNA(i,1)-
Ybf)/I(i,:)/Ew11 + N(i,1)/A(i,:)/Ew11 ;          %%% This is the
strain corresponding to the self-equilibrating stress (the strain that
the structure doesn't undergo) (Mechanical strain in Ansys)
        if strssbf (i,1)>54 || strssbf (i,1)<-20 %%% In this case we
need to reduce the A and I by subtracting the contribution of the
flange to the A & I and the same for the other components
            Fbf(i,1)=0;
        else
            Fbf(i,1) = strssbf (i,1)*Abf/nbf;
        end

        if Fbf(i,1)>0
            Ten (i,1) = Ten (i,1)+ Fbf(i,1);
        else
            Comp (i,1) = Comp (i,1)+ Fbf(i,1);
        end
    end
end

```

```

        strssbf2 (i,1) = (M(i,1)*(PNA(i,1)-Ybf2)/I(i,:)*nbf)+
N(i,1)*nbf/A(i,:);          %%% This is the stress that doesn't
induce in the structure if the structure is determinate
        strssbf2se(i,1) = strthbf2(i,1)+(M(i,1)*(PNA(i,1)-
Ybf2)/I(i,:)*nbf)+ N(i,1)*nbf/A(i,:);          %%% This is the
self-equilibrating stress (the real stress that the structure undergo)
        strnbf2 (i,1) = M(i,1)*(PNA(i,1)-Ybf2)/I(i,+)/Ew11 +
N(i,1)/A(i,+)/Ew11 ;          %%% This is the actual
strain that the structure undergo
        strnbf2se (i,1) = strthbf2(i,1)/Ebf11+M(i,1)*(PNA(i,1)-
Ybf2)/I(i,+)/Ew11 + N(i,1)/A(i,+)/Ew11 ;          %%% This is the strain
corresponding to the self-equilibrating stress (the strain that the
structure doesn't undergo)
        if strssbf2 (i,1)>54 || strssbf2 (i,1)<-20
            Fbf2(i,1)=0;
        else
            Fbf2(i,1) = strssbf2 (i,1)*Abf2/nbf;
        end

        if Fbf2(i,1)>0
            Ten (i,1) = Ten (i,1)+ Fbf2(i,1);
        else
            Comp (i,1) = Comp (i,1)+ Fbf2(i,1);
        end

        %%% Force in FRP top flanges
        strsstf (i,1) = (M(i,1)*(PNA(i,1)-Ytf)/I(i,:)*ntf)+
N(i,1)*ntf/A(i,:);
        strsstfse (i,1) = strthtf(i,1)+(M(i,1)*(PNA(i,1)-
Ytf)/I(i,:)*ntf)+ N(i,1)*ntf/A(i,:);
        if strsstf (i,1) > 54 || strsstf (i,1) < -20
            Ftf(i,1)=0;
        else
            Ftf(i,1) = strsstf (i,1)*Atf/ntf;
        end

        if Ftf(i,1)>0
            Ten (i,1) = Ten (i,1)+ Ftf(i,1);
        else
            Comp (i,1) = Comp (i,1)+ Ftf(i,1);
        end

        strsstf2 (i,1) = (M(i,1)*(PNA(i,1)-Ytf2)/I(i,:)*ntf)+
N(i,1)*ntf/A(i,:);
        strsstf2se (i,1) = strthtf2(i,1)+(M(i,1)*(PNA(i,1)-
Ytf2)/I(i,:)*ntf)+ N(i,1)*ntf/A(i,:);
        if strsstf2 (i,1) > 54 || strsstf2 (i,1) < -20
            Ftf2(i,1)=0;
        else
            Ftf2(i,1) = strsstf2 (i,1)*Atf2/ntf;
        end
        if Ftf2(i,1)>0
            Ten (i,1) = Ten (i,1)+ Ftf2(i,1);
        else
            Comp (i,1) = Comp (i,1)+ Ftf2(i,1);
        end

```

```

end

strsstf3 (i,1) = (M(i,1)*(PNA(i,1)-Ytf3)/I(i,:)*ntf)+
N(i,1)*ntf/A(i,:);
strsstf3se (i,1) = strthtf3(i,1)+(M(i,1)*(PNA(i,1)-
Ytf3)/I(i,:)*ntf)+ N(i,1)*ntf/A(i,:);
strntf3 (i,1) = M(i,1)*(PNA(i,1)-Ytf3)/I(i,+)/Ew11+
N(i,1)/A(i,+)/Ew11 ;
strntf3se (i,1) = strthtf3(i,1)/Etf11+ M(i,1)*(PNA(i,1)-
Ytf3)/I(i,+)/Ew11+ N(i,1)/A(i,+)/Ew11 ;
if strsstf3 (i,1)>54 || strsstf3 (i,1)<-20
    Ftf3(i,1)=0;
else
    Ftf3(i,1) = strsstf3 (i,1)*Atf3/ntf;
end
if Ftf3(i,1)>0
    Ten (i,1) = Ten (i,1)+ Ftf3(i,1);
else
    Comp (i,1) = Comp (i,1)+ Ftf3(i,1);
end

%%% Force in FRP sandwich panel
strsssw (i,1) = (M(i,1)*(PNA(i,1)-Ysw)/I(i,))+
N(i,1)/A(i,);
strsswse (i,1) = strthsw(i,1)+(M(i,1)*(PNA(i,1)-Ysw)/I(i,))+
N(i,1)/A(i,);
if strsssw (i,1)>54 || strsssw (i,1)<-20
    Fsw(i,1)=0;
else
    Fsw(i,1) = strsssw (i,1)*Asw;
end

if Fsw(i,1)>0
    Ten (i,1) = Ten (i,1) + Fsw(i,1);
else
    Comp (i,1) = Comp (i,1) + Fsw(i,1);
end

%%% Force in (strands)
Epsstr = M(i,1)*(PNA(i,1)-Ys)/I(i,+)/Ew11 +
N(i,1)/A(i,+)/Ew11 ;
strnstr (i,1) = M(i,1)*(PNA(i,1)-Ys)/I(i,+)/Ew11 +
N(i,1)/A(i,+)/Ew11 ;
strnstrse (i,1) = strthstr(i,1)/Ep+M(i,1)*(PNA(i,1)-
Ys)/I(i,+)/Ew11 + N(i,1)/A(i,+)/Ew11 ;

if Epsstr > 0.0076
    Fstr (i,1) = (250 - (0.04/(Epsstr-0.0064)))*Astr;
end
if Epsstr < -0.0076
    Fstr (i,1) = -Astr*(250 - (0.04/(-1*Epsstr-0.0064)));
end
if Epsstr<= 0.0076 && Epsstr>= -0.0076
    Fstr (i,1) = Ep*Epsstr*Astr;
end

```

```

if Fstr(i,1)>0
    Ten (i,1) = Ten (i,1)+ Fstr(i,1);
else
    Comp (i,1) = Comp (i,1)+ Fstr(i,1);
end

%%% Force in FRP Webs
strsslw (i,1) = M(i,1)* PNA(i,1)/I(i,:)+ N(i,1)/A(i,:);
strsslwse (i,1) = strthw(i,1)+M(i,1)* PNA(i,1)/I(i,:)+
N(i,1)/A(i,:);
strssuw (i,1) = M(i,1)* (PNA(i,1)-h)/I(i,:)+
N(i,1)/A(i,:);
strssuwse (i,1) = strthw(i,1)+M(i,1)* (PNA(i,1)-h)/I(i,:)+
N(i,1)/A(i,:);
strnuw (i,1) = M(i,1)* (PNA(i,1)-h)/I(i,+)/Ew11+
N(i,1)/A(i,+)/Ew11;
Fw (i,1) = (strsslw (i,1) + strssuw (i,1))*h*2*tw;
if strsslw (i,1)> 54 && strssuw (i,1)> 54
    Fw (i,1) = 0;
end
if strsslw (i,1)< -20 && strssuw (i,1)< -20
    Fw (i,1) = 0;
end

%%%%%%%%%%%%%%%%%%%%%%%%%%%%%%%%%%%%%%%%%%%%%%%%%%%%%%%%%%%%%%%%%%%%%%%%
%%%%%%%%%%%%%%%%%%%%%%%%%%%%%%%%%%%%%%%%%%%%%%%%%%%%%%%%%%%%%%%%%%%%%%%%
%%% The other possible cases have been ignored due to the low
probability %%%
%%% that they take place
%%%

%%%%%%%%%%%%%%%%%%%%%%%%%%%%%%%%%%%%%%%%%%%%%%%%%%%%%%%%%%%%%%%%%%%%%%%%
%%%%%%%%%%%%%%%%%%%%%%%%%%%%%%%%%%%%%%%%%%%%%%%%%%%%%%%%%%%%%%%%%%%%%%%%

if Fw(i,1)>0
    Ten (i,1) = Ten (i,1)+ Fw(i,1);
else
    Comp (i,1) = Comp (i,1)+ Fw(i,1);
end

%%% Force in Deck Rft
Epslb = M(i,1)*(PNA(i,1)-Ylb)/I(i,+)/Ew11 +
N(i,1)/A(i,+)/Ew11;
Epsub = M(i,1)*(PNA(i,1)-Yub)/I(i,+)/Ew11 +
N(i,1)/A(i,+)/Ew11;
strnub (i,1) = M(i,1)*(PNA(i,1)-Yub)/I(i,+)/Ew11 +
N(i,1)/A(i,+)/Ew11;
if Epslb > (Fb/Eb) && Epslb <= 0.02
    Flb (i,1) = Fb*Nlb*Ab;
end
if Epslb < -1*(Fb/Eb) && Epslb >= -0.02

```



```

    Flb    (i,1) = -Fb*Nlb*Ab;
end
if Epslb > 0.02 && Epslb <= 0.09
    Flb    (i,1) = ((30/0.07)*(Epslb-0.02)+Fb)*Nlb*Ab;
end
if Epslb < -0.02 && Epslb >= -0.09
    Flb    (i,1) = -Nlb*Ab*((30/0.07)*(-1*Epslb-0.02)+Fb);
end
if Epslb < -0.09 || Epslb > 0.09
    Flb    (i,1) = 0;
else
    Flb(i,1) = Epslb*Eb*Nlb*Ab;
end

if Epsub > (Fb/Eb) && Epsub <= 0.02
    Fub(i,1) = Fb*Aub;
end
if Epsub < -1*(Fb/Eb) && Epsub >= -0.02
    Fub(i,1) = -Fb*Aub;
end
if Epsub > 0.02 && Epsub <= 0.09
    Fub(i,1) = (((30/0.07)*(Epsub-0.02)+Fb))*Aub;
end
if Epsub < -0.02 && Epsub >= -0.09
    Fub(i,1) = (-1*((30/0.07)*(-1*Epsub-0.02)+Fb))*Aub;
end
if Epsub < -0.09 || Epsub > 0.09
    Fub(i,1) = 0;
else
    Fub(i,1) = Epsub*Eb*Nub*Ab;
end

if Fub(i,1)>0
    Ten (i,1) = Ten (i,1)+ Fub(i,1);
else
    Comp (i,1) = Comp (i,1)+ Fub(i,1);
end

if Flb(i,1)>0
    Ten (i,1) = Ten (i,1)+ Flb(i,1);
else
    Comp (i,1) = Comp (i,1)+ Flb(i,1);
end

%%% Force in Conc Arch

y1          = Yca (i,1)- (tca/2);
y2          = Yca (i,1)+ (tca/2);
strnlca    (i,1) = M(i,1)*(PNA(i,1)-y1)/I(i,+)/Ew11 +
N(i,1)/A(i,+)/Ew11;
strnlcase  (i,1) = strthlca(i,1)/Eca + M(i,1)*(PNA(i,1)-
y1)/I(i,+)/Ew11 + N(i,1)/A(i,+)/Ew11;

```

```

        strnuca      (i,1) = M(i,1)*(PNA(i,1)-y2)/I(i,+)/Ew11 +
N(i,1)/A(i,+)/Ew11;
        strnucase   (i,1) = strthuca(i,1)/Eca + M(i,1)*(PNA(i,1)-
y2)/I(i,+)/Ew11 + N(i,1)/A(i,+)/Ew11;
        strsslca    (i,1) = M(i,1)*(PNA(i,1)-y1)/I(i,+) *nca +
N(i,1)*nca/A(i,+);
        strsslcase  (i,1) = strthlca(i,1) + M(i,1)*(PNA(i,1)-
y1)/I(i,+) *nca + N(i,1)*nca/A(i,+);
        strssuca    (i,1) = M(i,1)*(PNA(i,1)-y2)/I(i,+) *nca +
N(i,1)*nca/A(i,+);
        strssucase  (i,1) = strthuca(i,1) + M(i,1)*(PNA(i,1)-
y2)/I(i,+) *nca + N(i,1)*nca/A(i,+);
        ca          (i,1) = (strnlcase (i,1)-strnucase
(i,1))*0.8+strnucase (i,1);

        Fca        (i,1) = (strssuca(i,1)+strsslca(i,1))*tca*bca;

        if Fca(i,1)>0
            Ten      (i,1) = Ten (i,1) + Fca(i,1);
        else
            Comp     (i,1) = Comp(i,1) + Fca(i,1);
        end

        %%% Force in Conc Deck

        y1          = Yd - (ts/2);
        y2          = Yd + (ts/2);
        strnlcd     (i,1) = M(i,1)*(PNA(i,1)-y1)/I(i,+)/Ew11 +
N(i,1)/A(i,+)/Ew11;
        strnucd     (i,1) = M(i,1)*(PNA(i,1)-y2)/I(i,+)/Ew11 +
N(i,1)/A(i,+)/Ew11;
        strssucd   (i,1) = M(i,1)*(PNA(i,1)-y2)/I(i,+) *nd +
N(i,1)*nd/A(i,+);
        strssucdse (i,1) = (strthucd1(i,1) +
strthucd2(i,1)+strthucd3(i,1))/3+M(i,1)*(PNA(i,1)-y2)/I(i,+) *nd +
N(i,1)*nd/A(i,+);
        strsslcd   (i,1) = M(i,1)*(PNA(i,1)-y1)/I(i,+) *nd +
N(i,1)*nd/A(i,+);
        strsslcdse (i,1) = (strthlcd1(i,1)+ strthlcd2(i,1)+
strthlcd3(i,1))/3 + M(i,1)*(PNA(i,1)-y1)/I(i,+) *nd + N(i,1)*nd/A(i,+);
        strnucdse (i,1) = strssucdse (i,1)/Ed;

        Fd          (i,1) = bs*(strssucd(i,1)+strsslcd(i,1))*ts/2;

        if Fd(i,1)>0
            Ten      (i,1) = Ten (i,1)+ Fd(i,1);
        else
            Comp     (i,1) = Comp (i,1)+ Fd(i,1);
        end

        %%% Force in Conc Web

```

```

        y1                = Ycw (i,1)- (hcw(i,1)/2);
        y2                = Ycw (i,1)+ (hcw(i,1)/2);
        strnlcw          (i,1) = M(i,1)*(PNA(i,1)-y1)/I(i,+)/Ew11 +
N(i,1)/A(i,+)/Ew11;
        strnlcwse       (i,1) = strthlcw (i,1)/Eca+M(i,1)*(PNA(i,1)-
y1)/I(i,+)/Ew11 + N(i,1)/A(i,+)/Ew11;
        strnucw         (i,1) = M(i,1)*(PNA(i,1)-y2)/I(i,+)/Ew11 +
N(i,1)/A(i,+)/Ew11;
        strnucwse       (i,1) = strthucw (i,1)/Eca+M(i,1)*(PNA(i,1)-
y2)/I(i,+)/Ew11 + N(i,1)/A(i,+)/Ew11;
        strsslcw        (i,1) = M(i,1)*(PNA(i,1)-y1)/I(i,+)nca +
N(i,1)nca/A(i,);
        strsslcwse     (i,1) = strthlcw (i,1)+ M(i,1)*(PNA(i,1)-
y1)/I(i,+)nca + N(i,1)nca/A(i,);
        strssucw        (i,1) = M(i,1)*(PNA(i,1)-y2)/I(i,+)nca +
N(i,1)nca/A(i,);
        strssucwse     (i,1) = strthucw (i,1)+ M(i,1)*(PNA(i,1)-
y2)/I(i,+)nca + N(i,1)nca/A(i,);
        cw              (i,1) = (strnlcwse (i,1)+ strnucwse (i,1))/2;

        Fcw             (i,1) = tcw*(strssucw(i,1)+strsslcw(i,1))*hcw(i,1);

        if Fcw(i,1)>0
            Ten          (i,1) = Ten (i,1)+ Fcw(i,1);
        else
            Comp          (i,1) = Comp (i,1)+ Fcw(i,1);
        end

        Dif              (i,+) = abs((N(i,1)-
(Ten(i,1)+Comp(i,1)))/N(i,1))*100;

end

```

BIBLIOGRAPHY

- Ahsan, S. (2012). "Evaluation of Hybrid-Composite Beam for Use in Tide Mill Bridge." M. S. thesis, Virginia Polytechnic Institute and State University, Blacksburg, VA.
- Ansys 13.0. [computer software], Canonsburg, PA, Ansys.
- Ansys 14.0. [computer software], Canonsburg, PA, Ansys.
- Aref, A. J., Kitane, Y. and Lee, G. C. (2005). "Analysis of hybrid FRP-concrete multi-cell bridge superstructure." *Composite Structures*, Vol. 69, No. 3, pp. 346-359.
- Bank, L. C. (2006). "Composites for construction: Structural design with FRP materials." Wiley, Hoboken, NJ, 1-27.
- Benmokrane, B., Wang, P., Pavate, T. and Robert, M. (2006). "Durability of FRP composites for civil infrastructure applications." *Durability of Materials and Structures in Building and Civil Engineering*, pp. 300-343.
- Connolly, Michael, King, JP, Shidaker, TA and Duncan, AC. (2006). "Processing and characterization of pultruded polyurethane composites." *Proceedings of the 8th World Pultrusion Conference*, European Pultruders Technical Association.
- Deskovic, N., Triantafillou, T. C. and Meier, U. (1995). "Innovative design of FRP combined with concrete: Short-term behavior." *Journal of Structural Engineering*, Vol. 121, No. 7, pp. 1069-1078.
- Dickson, R. F., Fernando, G., A., T., Reiter, H. and Harris, B. (1989). "Fatigue behaviour of hybrid composites." *Journal of Materials Science*, Vol. 24, No. 1, pp. 227-233.
- Hai, N. D., Mutsuyoshi, H., Asamoto, S. and Matsui, T. (2010). "Structural behavior of hybrid FRP composite I-beam." *Construction and Building Materials*, Vol. 24, No. 6, pp. 956-969.
- Hawileh, R. A., Naser, M., Zaidan, W. and Rasheed, H. A. (2009). "Modeling of insulated CFRP-strengthened reinforced concrete t-beam exposed to fire." *Engineering Structures*, Vol. 31, No. 12, pp. 3072-3079.
- Hayashi, T., Koyama, K., Yamazaki, A. and Kihira, M. (1972). "Development of new material properties by hybrid composition." *Fukugo Zairyo (composite materials)*, Vol. 1, No. 1, pp. 18-20.

- Hillman, J. R. (2003). "Investigation of a Hybrid-Composite Beam System." High Speed Rail IDEA Program, Transportation Research Board of National Academies, Chicago, HSR Project Report 23.
- Hillman, J. R. (2008). "Product Application of a Hybrid-Composite Beam System". IDEA Program Final Report, Transportation Research Board of National Academies, Chicago, HSR - 43.
- Hillman, J. R. (2012). "Hybrid-Composite Beam (HCB®) Design and Maintenance Manual." The Missouri Department of Transportation, Jefferson City, Mo.
- Imbsen, R. A., Vandershaf, D. E., Schamber, R. A. and Nutt, R. V. (1985). "Thermal effects in concrete bridge superstructures, NCHRP report 276." Transportation Research Board, Washington, DC.
- Keller, T. (2002). "Overview of fibre-reinforced polymers in bridge construction." Structural Engineering International, Vol. 12, No. 2, pp. 66-70.
- Mascaro, M. G., and Moen, C. D. (2012). "Out-of-Plane Web Deformation and Relative Arch Movement of Hybrid-Composite Beams Based on Photogrammetry." Virginia Polytechnic Institute and State University, Report CE/VPI-ST-12/08, Blacksburg, VA.
- Mirmiran, A. (2001). "Innovative combinations of FRP and traditional materials". FRP Composites in Civil Engineering. Proceedings of the International Conference on FRP Composites in Civil Engineering.
- Mohamed, M., Vuppalapati, R. R., Bheemreddy, V., Chandrashekhara, K., and Schuman, T. (2014). "Characterization of polyurethane composites manufactured using vacuum assisted resin transfer molding." Advanced Composite Materials, (ahead-of-print), 10.1080/09243046.2014.909975.
- Myers, J. J., Aboelseoud, M. A., Earley, C. R. and Washer, G. (2014). "Field evaluation of hybrid-composite girder bridges in missouri." Missouri Department of Transportation, Jefferson City, MO.
- Nosdall, S. V. (2013). "Experiments on a hybrid composite beam for bridge applications". Master of Science, faculty of the Virginia Polytechnic Institute and State University, Blacksburg, VA.
- Sap2000 14.2 [computer software], Berkeley, CA, Computers and Structures.
- Shan, Y. and Liao, K. (2002). "Environmental fatigue behavior and life prediction of unidirectional glass-carbon/epoxy hybrid composites." International Journal of Fatigue, Vol. 24, No. 8, pp. 847-859.

- Snape, T., and Lindyberg, R. (2009). "Test Results: HC Beam for the Knickerbocker Bridge." Advanced Structures & Composites Center conducts, AEWG Report 10-16, University of Maine, Orono, ME.
- Sonawala, S. P. and Spontak, R. J. (1996). "Degradation kinetics of glass-reinforced polyesters in chemical environments." *Journal of materials science*, Vol. 31, No. 18, pp. 4745-4756.
- Summerscales, J. and Short, D. (1978). "Carbon fibre and glass fibre hybrid reinforced plastics." *Composites*, Vol. 9, No., pp. 157-166.
- Tuwair, H., Hopkins, M., Volz, J., ElGawady, M., Mohamed, M., Chandrashekhara, K. and Birmand, V. (2014). "An experimental study on static behavior of structural polyurethane foam infill for GFRP bridge deck panels." 1st International Conference on Mechanics of Composites, Long Island, New York.
- Van, E. G., Heldt, T., McCormick, L., Carter, D. and Tranberg, C. (2002). "An Australian approach to fibre composite bridges." *Proceedings of the International Composites Conference ACUN4, Composite Systems: Macro Composites, Micro Composites, Nano Composites*, UNSW Sydney.

VITA

Mohamed Abdelkhalik Aboelseoud was born on March 24th, 1979 in Cairo, Egypt. He was admitted to the Military Technical College in Cairo in 1995. He got his Bachelor degree in Civil Engineering with grade excellent with honor in 2000. He received his master degree from the Military Technical College in 2007 in structural health monitoring. Mohamed became a PhD candidate in civil engineering since December 2012 at Missouri University of Science and Technology. In May 2015, he received his PhD in civil engineering from Missouri University of Science and Technology.